Synthesis and Novel Attributes of Metal Chalcogenides

A Thesis
Submitted for the Degree of

Doctor of Philosophy

By
MANOJ KUMAR JANA

New Chemistry Unit
Jawaharlal Nehru Centre for Advanced Scientific Research
(A Deemed University)
Bangalore – 560 064

September 2017

Dedication

I dedicate this thesis to my late grandparents, the amazing people who raised me amidst their struggle with utmost love and affection that cannot be worded but can only be felt in my heart. I dedicate this thesis to my lovely parents and my ever understanding little sister for standing by me through ups and downs, and for all their support, love, and prayers. I dedicate my thesis to the omnipresent divine force that prompts me from within and keeps me going unfazed despite the odds. I dedicate this thesis to every single person, dear or distant, who made me a better person in some way or the other.

DECLARATION

I hereby declare that the matter presented in the thesis titled, "**Synthesis and Novel Attributes of Metal Chalcogenides**", is a result of studies carried out by me at the New Chemistry Unit, Jawaharlal Nehru Centre for Advanced Scientific Research, Bangalore, India, under the supervision of Prof. C. N. R. Rao, FRS and Dr. Kanishka Biswas, and it has not been submitted elsewhere for the award of any degree or diploma.

In keeping with the general practices of reporting scientific observations, due acknowledgements have been made wherever the work described is based on the findings of other investigators in a collaborative pursuit. Any omission which might have occurred by oversight or error in judgment is regretted.

Bangalore

Manoj Kumar Jana

CERTIFICATE

We hereby certify that the matter presented in the thesis titled "**Synthesis and Novel Attributes of Metal Chalcogenides**" is a result of investigations carried out by Mr. Manoj Kumar Jana at the New Chemistry Unit, Jawaharlal Nehru Centre for Advanced Scientific Research, Bangalore, India, under our supervision, and that it has not been submitted elsewhere for the award of any degree or diploma.

Bangalore

Prof. C. N. R. Rao, FRS
(Research supervisor)

Dr. Kanishka Biswas
(Research supervisor)

ACKNOWLEDGEMENTS

First and foremost, I express my sincere and heartfelt gratitude to my research supervisors, Prof. C. N. R. Rao, FRS and Dr. Kanishka Biswas for providing me the opportunity to work under their supervision. I am ever grateful to Bharat Ratna Prof. C. N. R. Rao for his constant guidance and support. His enthusiasm, dedication and relentless pursuit of science even in his eighties are truly inspiring and motivating. I am ever grateful to Dr. Kanishka Biswas for his constant guidance and personal training during several occasions. I thank him for all the valuable suggestions, freedom and motivating words in the times of need.

I thank Prof. U. V. Waghmare, Prof. A. J. Bhattacharyya, Prof. S. B. Krupanidhi, Prof. M. K. Sanyal, Prof. C. Felser, Dr. S. Maiti, Dr. D. J. Late, Dr. A. Singh, Dr. K. Pal, Dr. P. Mandal, Dr. M. Banavoth, Mr. A. Warankar, Mr. Rajendra and Ms. C. Rajamathi for the fruitful scientific collaborations and all the insightful discussions.

I thank my course work instructors: Prof. S. M. Shivaprasad, Prof. A. Sundaresan, Dr. R. Viswanatha and Dr. Sebastian C. Peter.

I thank all my beloved lab mates: Dr. Guin, Arindom, Dr. P. Chithaiah, Dr. Pal, Dr. Perumal, Subhajit, Ananya, Manisha, Ekashmi, Sujoy, Moinak, Arka, Tanmoy, Sushmita and Parivesh at the solid state chemistry lab, and Dr. Maitra, Dr. Nitesh, Dr. Saha, Dr. Gopal, Dr. Dey, Dr. Kumar, Dr. Pramoda, Dr. Vishnoi, Dr. Narang, Dr. Manjunath, Dr. Jaiswal, Sreedhara, Gupta, Roy, Chhetri, Manaswee, Monis, Amit, Rajesh and Manjunatha at the water splitting lab.

I thank Mr. Somnath Ghora and Mr. Chandan De (JNCASR) for help with low-temperature resistivity measurements, and Mr. Rajasekhar (IISc.) for various fruitful discussions.

I thank all the technical staff members: Mr. Anil, Mr. Vasu, Ms. Selvi, Mr. Mahesh, Ms. Usha, Mr. Jagadeesh, Mr. Shivkumar, Mr. N. Kishore, Mr. M. Gowda, Mr. Dileep, Mr. Peer and others.

I thank all the staff members associated with Academic, Admin, NCU, ICMS, Library, Hostel, Mess, Security, Utility, Gardening, Cleaning, Dhanvantari and other depts.

I thank the Dept. of science and technology (India) and JNCASR for funding, and CSIR (India) for the research fellowship.

I am forever indebted to my alma mater, Sri Sathya Sai Institute of Higher Learning for providing value-based free education. I am grateful to all my teachers for inspiring and shaping me to become what I am today.

I express my love and affection to my best buddies, Swathi, Shashi Kiran, and Susheela who have always been there to share my happiness as well as sorrow. I shall miss their physical company, but my thoughts will always hold them dear and near.

I thank all my batch mates: Swathi, Sreedhara, Sanjay, Satya, Dheeraj, Sunil and Papri, and all the seniors for their lovable company and support.

I thank all the past members of Ugadi committee at JNCASR for organizing the Ugadi celebrations, the sumptuous dinner, and the fun-filled cultural events.

I thank all the members of my volleyball team: Swathi, Sumukh, Apoorva, Anaranya, Dr. Suman, Dr. Prashanth and many others for all the fun and memorable times.

I thank all the highly talented artists who I had accompanied during cultural fests at JNCASR, especially the members of 'Game of Pirates' Symphony band for leaving me some wonderful experiences to cherish.

My special thanks to Mrs. Indumati Rao and Mr. Sanjay Rao for all the warmth, affection and excellent hospitality they extended during several occasions.

Last but not least, I thank my dearest parents and my little sister for always believing in me and continually praying for my well-being. I thank the almighty force that prompts me from within and keeps me going no matter what.

PREFACE

Metal chalcogenides constitute one of the most important classes of materials with a rich structural diversity on par with oxides and a plethora of significant properties and applications. This Ph.D. thesis presents the novel synthesis, structure-property relationships and other aspects of various heavy metal chalcogenides. I have divided my thesis into five parts containing two chapters each.

Part 1 gives a brief introduction to the chemistry of metal chalcogenides covering some of their important properties and applications. Besides, I have elaborated the essential basics of heat capacity and thermal conduction in solids and described the experimental details of high-temperature thermoelectric properties.

Part 2 discusses the ionothermal synthesis of some layered chalcogenides of p-block metals using an ionic liquid as the green solvent. **Chapter 2.1** discusses the ionothermal synthesis and characterization of ultrathin nanosheets of Bi_2Se_3, and of other related materials. I have investigated the high-temperature thermoelectric properties of compacted Bi_2Se_3 nanosheets between 300 K and 673 K which show relatively large electrical conductivity and very low thermal conductivity thereof owing to enhanced contribution from metallic surface states, and phonon scattering by a variety of defects respectively. **Chapter 2.2** discusses the ionothermal synthesis and characterization of hierarchical nanostructures of SnS_2. I have examined the electrochemical Li-ion storage properties of SnS_2 hierarchical nanostructures synthesized at two different temperatures and developed an understanding of their relative electrochemical performances through various studies including electrochemical impedance.

Part 3 deals with the facile and cost-effective room-temperature synthesis of heavy metal chalcogenides by employing the toluene-water fluid-interface as the reaction medium. In **chapter 3.1**, I have discussed the interfacial synthesis, characterization and near infrared detection properties of HgSe and $Hg_{0.5}Cd_{0.5}Se$ quantum dots. We have also probed the growth and self-organization of HgSe interfacial film by synchrotron based in-situ X-ray

reflectivity and ex-situ grazing incidence small angle X-ray scattering studies. In **chapter 3.2**, I have discussed the interfacial synthesis, characterization, and factors affecting the growth and morphology of PbSe nanocrystalline films. I have also examined the photodetection properties of as-synthesized PbSe nanocrystalline film in the near infrared region.

Part 4 deals with the structure-property relationships in a couple of layered transition metal ditellurides. In **chapter 4.1**, I have studied the structural aspects, magnetoresistance and thermoelectric properties of bulk Td-WTe_2. Besides, I have investigated in detail the Raman vibrational modes of bulk Td-WTe_2. I have examined the effect of thickness (i.e., number of layers) on the frequencies of Raman bands by carrying out Raman spectroscopy on mechanically exfoliated few-layers of Td-WTe_2. I have also determined the temperature-induced anharmonic red shifts in Raman frequencies as a function of temperature in the 123-623 K range in bulk as well as few-layer Td-WTe_2. In **chapter 4.2**, I have synthesized polycrystalline bulk 2H- and 1T'-phases of $MoTe_2$, and studied their temperature-dependent Raman vibrations and high-temperature thermoelectric properties. I have investigated the effect of defects such as Te-vacancies on the electronic structure and observed temperature-dependence of electronic transport properties.

Part 5 discusses the origin of ultralow thermal conductivity in a couple of Zintl phases. In **chapter 5.1**, I have investigated the intrinsic origin of observed ultralow lattice thermal conductivity (ca. 0.5 W/m.K at 300 K) of $TlInTe_2$ with the help of structure-refinement of powder X-ray diffraction, low-temperature specific heat capacity and terahertz time domain spectroscopy complemented by the first-principles study. In **chapter 5.2**, I have investigated the high-temperature thermoelectric properties of InTe polycrystalline ingots. Through optimal In-deficiencies, I have tuned the hole-carrier concentrations and thereby enhanced the power factor. As a result, I have increased the thermoelectric figure of merit (zT) to a maximum value close to unity in the 0.3 mol. % In-deficient InTe at 650 K which is promising for mid-temperature thermoelectric applications.

TABLE OF CONTENTS

PART 1

A brief introduction to the chemistry of metal chalcogenides.

A brief introduction to the chemistry of metal chalcogenides

1.1 Metal chalcogenides

Chalcogenides constitute one of the most important classes in the field of chemistry, exhibiting rich compositional and structural diversity on par with oxides and organic compounds. Chalcogenides are compounds that contain at least one chalcogen Q atom (Q = S, Se, Te) in a chemically reduced state compared to its elemental form. Chalcogenides bear few chemical resemblances to oxides, but there are also big dissimilarities in chemical character and physical properties among them which are significant enough to warrant a separate treatment of the chalcogenides as a distinct class of materials. One of the most striking differences between oxides and chalcogenides is the facile ability of the chalcogen to form stable Q—Q bonds: catenation. For instance, there are many allotropes of sulfur, owing to the ability of sulfur to form chains of singly-bonded atoms. This catenation is also observed in metal chalcogenides, for example, in pyrite where S-S (S_2^{2-}) units are found. Similarly, selenides and tellurides also exhibit Q-Q bonding as in Se_2^{2-} and Te_2^{2-} units of pyrite-type structures but in contrast with sulfides, they can form solid-state structures that contain Q_n rings or chains with $n>2$ as exemplified by Se_5 moiety in Nb_2Se_9[1] and Te_6 group in $Re_6Te_{16}Cl_6$.[2] In general, as we move from sulfides to selenides to tellurides, the degree of covalent bonding, delocalization of electrons and metallic behaviour increase, and the importance of long range Q-Q interactions (i.e., less than single bond) increases.[3] Te-Te single bonds are ca. 275 pm in length, but in a large number of telluride compounds, Te-Te bonds with distances intermediate between single bonds and van der Waals interactions (ca. 420 pm) exist. These bonds are energetically weak but are structurally important; they also manifest as Te...Te interlayer interactions that essentially stabilize the structures of layered tellurides such as $TaIrTe_4$ and $NbIrTe_4$.[4]

Besides, catenation can produce stable complex polychalcogenide anions (Q_x^{2-}, where x is up to 7 or 8). These anions serve as reactive building blocks for molecules and solid-state materials. Chalcogenides are similar to oxides in that there are as many chalcoanions, particularly with the main-group and early-transition metal atoms (e.g. $[PS_4]^{3-}$, $[P_2S_7]^{4-}$, $[SiS_4]^{4-}$, $[GeS_4]^{4-}$, $[MoS_4]^{2-}$, $[VS_4]^{3-}$ etc.), as there are oxyanions (e.g.

$[PO_4]^{3-}$, $[P_2O_7]^{4-}$, $[SiO_4]^{4-}$, $[Si_2O_7]^{6-}$, $[MoO_4]^{2-}$, $[VO_4]^{3-}$ etc.). In fact, chalcogens can form many other chalcoanions which do not have analogous oxyanions, few examples being $[P_2Se_6]^{4-}$, $[P_3Se_7]^{3-}$, $[P_2Se_8]^{2-}$, $[P_8Se_{18}]^{6-}$, $[GeS_4]^{4-}$, $[GeSe5]^{4-}$, $[Ge_2Se_6]^{6-}$etc. [5-7]

Metal oxides are usually ionic in character, and they resemble fluorides more than they do chalcogenides. For instance, dioxides such as VO_2, CrO_2, and MnO_2 crystallize in a rutile-type (TiO_2) structure similar to the corresponding fluorides viz. VF_2, CrF_2 and MnF_2. On the other hand, while VS_2 and CrS_2 are not known, MnS_2 has a pyrite-type structure characterized by S_2^{2-} units, which is rarely found in oxides. Similarly, $MnSe_2$ and $MnTe_2$ also crystallize in pyrite-type structures. It is noteworthy that although Mn metal atoms have octahedral coordination in both MnO_2 and MnQ_2, the overall structures are significantly different. Besides, layered structures are very common among metal dichalcogenides but seldom found among oxides. The structures of most oxides are well represented by models that treat atoms as hard, charged spheres with ionic radii specific to a given element. The constant-radius approximation is, however, not accurate for metal chalcogenides because of their more covalent character.[3] Some of the important distinctions between metal oxides and metal chalcogenides are summarized in table 1.1

Table 1.1 *Some important distinctions between metal oxides and metal chalcogenides*

Feature	Oxides	Chalcogenides
Close packing	Usually	Sometimes
Octahedral/tetrahedral metal-coordination	Yes	Usually
Trigonal prismatic metal-coordination	Very rarely	Groups 5 and 6
Layered structures	Rarely	Usually
Q-Q bonds	Peroxides	Common
Bonding	Ionic	Covalent

Many metal chalcogenides are central to many important technologies. They exhibit a broad range of chemical and physical properties associated with diverse scientific phenomena and enable a plethora of applications.[8-15] For example, CdTe and $CuInSe_2$ are high-performing materials for thin-film solar photovoltaics; PbTe and $Bi_2Te_{3-x}Se_x$ are the champion thermoelectric materials; Co(Ni)/Mo/S composites are

the best available catalysts for hydro-desulphurization of crude oil; $Ge_2Sb_2Te_5$ is a high-density memory material; CdHgTe is the key infrared detector material in night-vision cameras etc.

Metal chalcogenides are at the cutting edge of many research areas. Some examples include, nonlinear optics,[16] optical information storage,[17] photovoltaic energy conversion,[18] thermoelectric energy conversion,[13, 19, 20] radiation detectors,[21] thin-film electronics,[22] spintronics,[23] fast-ion conductivity,[24] rechargeable batteries,[25] catalysis,[26] novel magnetism,[27] unconventional superconductivity[28] and science in two dimensions.[14, 29] In the recent times, the scientific community has witnessed sensational discoveries pertinent to metal chalcogenides such as quantum spin Hall Effect,[30] topological insulators,[31-34] non-saturating magnetoresistance[35] and many others which will have huge implications, especially in the fields of spintronics and (Opto) electronics. We are currently in the midst of an impressive expansion in solid-state chalcogenide chemistry with emphasis on the synthesis of materials with new compositions and structures on the one hand, and exploration of their novel properties on the other. Most of the aforementioned applications and phenomena are associated with chalcogenides of transition metals and main group p-block metals. The following sections will brief structural aspects and novel properties pertinent to these metal chalcogenides along with some relevant basics at the end to provide a background to my thesis work.

1.1.1 Chalcogenides of p-block elements

The p-block metal chalcogenides exhibit rich structural diversity. Wurtzite and zincblende structures are prevalent in quasi-binary III_2-VI_3 metal chalcogenides. Anisotropic layered structures are also found in III-VI compounds with covalently bonded layers stacked via weak van der Waals interactions. For instance, GaQ (Q=S, Se, Te) and InSe are all found in layered structures stabilized by cation-cation bonds. InTe, TlS and TlSe crystallize in a tetragonal TlSe-type structure [i.e., $Tl^{1+}Tl^{3+}(Se^{2-})_2$] with monovalent and trivalent cations, characterized by anionic and cationic substructures similar to Zintl compounds. The underpinning causes of ultralow thermal conductivity in two such isostructural compounds viz. InTe and $TlInTe_2$ have been investigated in detail in **part 5** of the thesis. TlTe, on the other hand, doesn't occur in

a mixed valent Zintl structure but in a tetragonal polyanionic structure of type, $Tl^{+}(Te_n)^{-}_{1/n}$.

Among IV-VI metal chalcogenides, GeQ and SnQ (Q=S, Se) exhibit orthorhombic puckered layered structure similar to black phosphorous, which can be derived from three-dimensional distortion of the rock salt (NaCl) structures. GeTe and SnTe have rocksalt (NaCl) structures with slight deformations due to phase transitions. The high-temperature phase shows the perfect NaCl-structure, stable above 670 K and 100 K for GeTe and SnTe, respectively. SnQ_2 (Q=S and Se) crystallizes in layered CdI_2-type structure. PbQ (Q=S, Se, Te) crystallizes in cubic rock-salt structure.

Among group V-VI chalcogenides, Sb_2S_3, Sb_2Se_3, and Bi_2S_3 have orthorhombic Sb_2S_3-type stibnite structure with one-dimensional connectivity. Sb_2Te_3, Bi_2Se_3, and Bi_2Te_3 are found in rhombohedral layered structures comprised of covalently bonded Q-M-Q-M-Q (M=Sb/Bi; Q=Se/Te) quintuple layers stacked via weak van der Waals interactions along the c-axis.

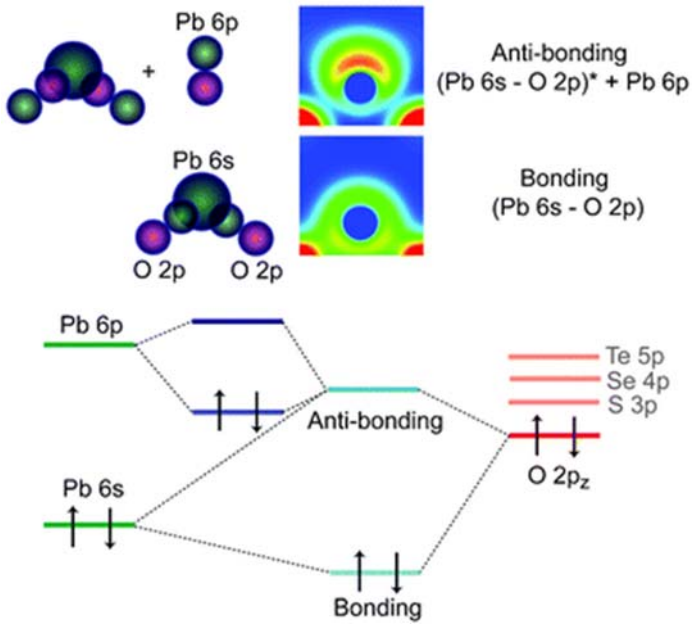

Figure 1.1*. Illustration of orbital interactions leading to stereochemical active lone pair in PbO (upper panel) and the corresponding energy level diagram (lower panel). The cation s and anion p orbital-interaction leads to formation of bonding and antibonding states which appear at the bottom and top of the upper valence band, respectively. The empty cation p states then interact with the filled antibonding state, resulting in stabilization of the cation ns^2 electrons. This interaction becomes symmetry-allowed by lattice distortion accompanied by an asymmetric electron density that is projected into the structural void. Reproduced with permission from ref. 37 © 2011 RSC.*

It is interesting to note the effect of cation lone pair on the structural stability of group 13-15 metal chalcogenides. The valence ns^2 lone pairs on the cations in these compounds play a key role in their structural, chemical and electronic properties. For example, as the metal becomes heavier on going down the group 13, the lone pair becomes increasingly stable in the order: $Ga^+ < In^+ < Tl^+$ and the same applies to groups 14 and 15 where the Pb^{2+} and Bi^{3+} cations possess stable lone pairs. The large stability of ns^2 lone pairs in the heavier elements of the main group is ascribed to relativistic effects that contract the s-orbital and bring it closer to the nucleus thereby lowering its energy. The cation ns^2 lone pair behaves in different ways depending on the local coordination environment as well as the metal and chalcogen atoms involved.[36, 37] It can either express stereochemically by occupying a distinct space around the metal atom or effectively remain 'quenched'. When expressed stereochemically, the ns^2 lone pair can cause lattice distortion accompanied by lowering of ns^2 energy. The formation of a stereochemically active lone pair (distortion) depends on the strength of interaction between cation *s* states and the anion *p* states; the stronger the interaction, the more contribution of cation *s* states to the upper valence band (Figure 1.1).[37] Down the group 16, the p-orbital energies increase on going from O to Te. As mentioned above, cation ns^2 energy decreases down the groups 13-15. Therefore, PbO exhibits low-symmetry litharge structure (distorted rocksalt structure) with stereochemically active ns^2 lone pairs whereas PbQ (Q=S, Se, Te) occurs in the symmetric rocksalt structure. Similar arguments hold true for orthorhombic Sb_2S_3, Sb_2Se_3 and Bi_2S_3 versus rhombohedral Bi_2Se_3 and Bi_2Te_3, orthorhombic SnSe versus cubic SnTe, and rhombohedral GeTe versus cubic SnTe and PbTe. As the stereochemical expression stabilizes the ns^2 pair which lies above or near the highest occupied state, the energy band gaps are usually higher in the low-symmetry structures relative to symmetric structures.[38] In the latter, the 'quenched' cationic lone pair may experience repulsion from the surrounding anions unlike the former where the structural distortion relieves this repulsion. The structural strain associated with the lone pair repulsion can result in highly anharmonic phonons as in the case of PbTe, Bi_2Se_3 and rocksalt I-V-VI compounds such as $AgSbSe_2$ causing low lattice thermal conductivity. The electronic origin to phonon anharmonicity in $AgSbSe_2$ has been ascribed to the deformation of the lone pair by lattice vibrations.[36] It is also worth noting that in PbTe, the stereochemical expression of ns^2 lone pair increases with temperature, a phenomenon

dubbed 'emphanisis'.[39] As a consequence, off-centering of Pb atoms occurs from their ideal octahedral sites at high temperatures. The structural and electronic links to the observed low thermal conductivity in InTe and $TlInTe_2$ are investigated in **part 5** of my thesis.

1.1.2 Chalcogenides of transition metals

A vast number of transition metal chalcogenides are known, but I shall restrict the discussion to layered transition metal dichalcogenides (TMDCs) that are relevant to my thesis. Layered TMDCs with the general formula MQ_2 (M= transition metal, Q=chalcogen) are solids with strong intralayer covalent bonding and weak interlayer van der Waals interaction. An individual layer of TMDCs typically has a thickness of 6-7 Å and comprises of hexagonally packed M atoms sandwiched between two layers of Q atoms. Group 4–7 TMDCs are predominantly layered, while some of group 8–10 TMDCs are prevalent in non-layered structures.

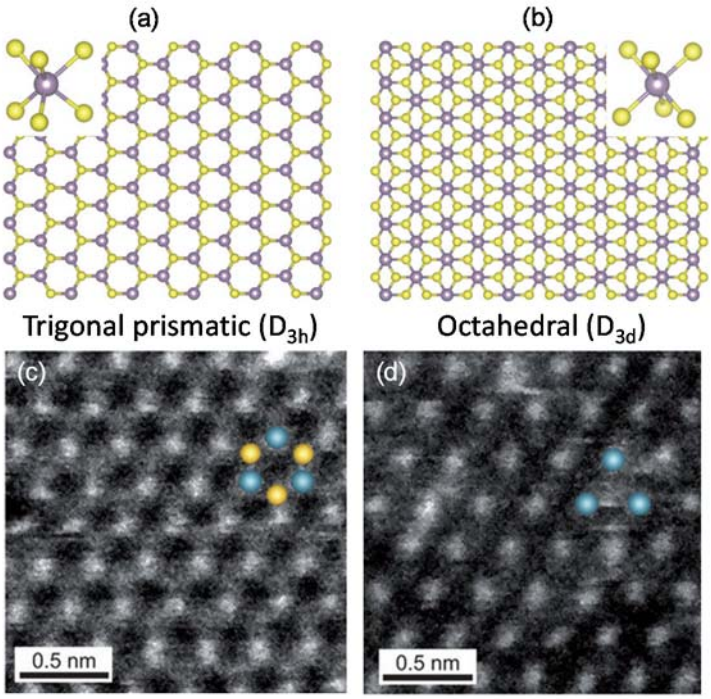

Figure 1.2*. (a,b) c-axis and [11–20] section view of single-layer TMDC with trigonal prismatic (a) and octahedral (b) coordination. Metal atoms: purple spheres; chalcogen atoms: yellow spheres. The labels AbA and AbC denote the stacking sequence (c,d) Dark-field scanning transmission electron microscopy image of single-layer MoS_2 showing the atomic arrangement of 1H (c) and 1T (d) phases. Blue and yellow spheres denote metal and chalcogen atoms respectively. (a) and (b) are adapted from ref. 9 © 2013 NPG; (c) and (d) are reproduced from ref. 15 © 2012 ACS.*

The metal (M) atoms provide four electrons to fill the bonding states of MQ_2 such that the oxidation states of M and Q atoms are +4 and –2, respectively. The metal coordination of layered TMDCs can either be trigonal prismatic or octahedral (sometimes referred to as trigonal-antiprismatic). Depending on the combination of the metal and chalcogen elements, one of the two coordination modes is thermodynamically preferred (Figure 1.2). In contrast to graphite, bulk TMDCs exhibit a variety of polymorphs. The most commonly encountered ones are 1T, 2H, and 3R where the letters stand for trigonal, hexagonal and rhombohedral, respectively, and the digit indicates the number of X–M–X units in the unit cell (i.e., the number of layers in the stacking sequence). A single TMDC can be found in multiple polymorphs depending on the history of its formation. For example, natural MoS_2 is commonly found in the '2H phase' (Figure 1.2) where the stacking sequence is AbA BaB (The capital and lower case letters denote chalcogen and metal atoms, respectively). Synthetic MoS_2, however, often contains the 3R phase where the stacking sequence is AbA CaC BcB. In both cases, the metal coordination is trigonal prismatic. Group 4 TMDs such as TiS_2 assume the 1T phase where the stacking sequence is AbC AbC and the coordination of metal atom is octahedral.[9] Metastable 1T phase is also found in Li-intercalated group 6 TMDCs such as MoS_2 and WS_2. (Figure 1.2).

The electronic structure of TMDCs strongly depends on the coordination environment of the transition metal and its d-electron count thus giving rise to an array of electronic and magnetic properties.[9] In 2H (or 1H in the case of the monolayer) as well as 1T phases of TMDCs, the nonbonding d-bands reside within the gap between the bonding (σ) and antibonding (σ*) bands of M–Q bonds as illustrated in figure 1.3. Octahedrally coordinated transition metal centers (D_{3d} point group) of TMDCs form degenerate $d_{x^2-y^2,z^2}$ (e_g) and $d_{xy,yz,xz}$ (t_{2g}) orbitals that can together accommodate a maximum of six d-electrons (for group 10 TMDCs). On the other hand, the d-orbitals of transition metals with trigonal prismatic coordination (D_{3h} point group) split into three groups, d_{z^2} (a_1), $d_{x^2-y^2,xy}$ (e), and $d_{xz,yz}$ (e′), with a sizeable gap of ca. 1 eV between the first two groups of orbitals. The diverse electronic properties of TMDCs arise from the progressive filling of the nonbonding d-bands from group 4 to group 10 species. When the orbitals are partially filled as, for instance, in 2H-$NbSe_2$, TMDCs exhibit metallic conductivity. When the orbitals are fully occupied, such as in 1T-HfS_2,

2H-MoS_2 and 1T-PtS_2, the materials are semiconductors. Besides, the d-bands broaden with a decrease in band gap with increasing atomic number of the chalcogen. Consequently, the band gap of 2H-phases of MoS_2, $MoSe_2$ and $MoTe_2$ decreases gradually from 1.3 to 1.0 eV.[40]

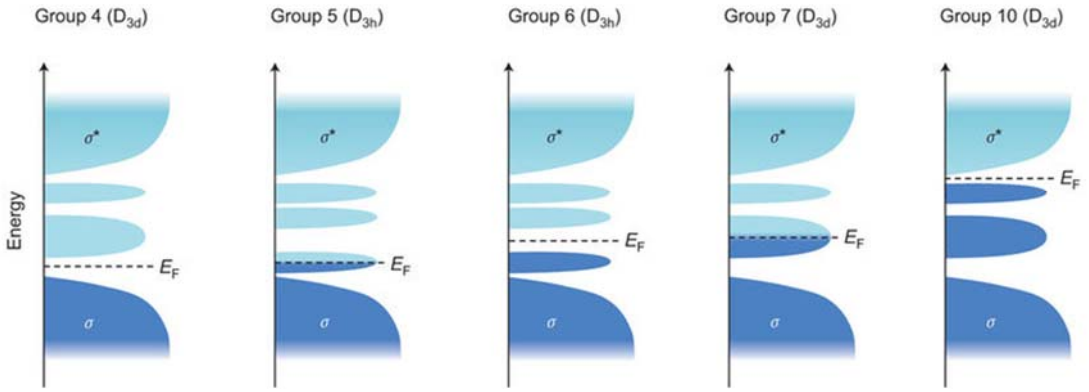

Figure 1.3. *A schematic showing progressive filling of nonbonding d-orbitals located within the energy gap in TMDCs of groups 4-10, assuming an ideal coordination. According to ligand field theory, D_{3d} compounds form two sets of nonbonding d orbitals: $d_{xy,yz,xz}$ (bottom) and $d_{x^2-y^2,z^2}$ (top), whereas D_{3h} compounds exhibit three sets of d orbitals: d_{z^2}, $d_{x^2-y^2,xy}$, and $d_{xz,yz}$ (from bottom to top). When an orbital is partially filled (e.g., group 5 and 7 TMDCs), the Fermi level (E_F) is within the band, and the compound exhibits metallic behavior. When an orbital is fully filled (e.g., group 6 TMDCs), E_F is in the energy gap, and the compound is a semiconductor. Reproduced with permission from ref. 9 © 2013 NPG.*

The preferred phase adopted by a TMDC depends primarily on the d-electron count of the transition metal. Group 4 TMDCs featuring d^0 transition metal centers are found in the octahedral phase whereas both octahedral and trigonal prismatic phases are found in group 5 TMDCs (d^1). Group 6 TMDCs (d2) are primarily found in trigonal prismatic geometry while group 7 TMDs (d^3) usually exhibit distorted octahedral structure. Group 10 TMDCs (d^6) are all found in octahedral structure (Figure 1.3).[9] It is also noted that charge density waves cause lattice distortions, and Li-insertion can produce metastable phases of TMDCs (discussed below).

The degree of quantum confinement and changes in interlayer coupling and symmetry elements cause dramatic differences in the electronic structure of monolayer TMDCs compared with their bulk counterparts. This effect is particularly prevalent for semiconducting TMDCs.[9, 41-43] An indirect-to-direct band gap transition occurs upon going from bulk to monolayer 2H-MoS_2 due to quantum confinement effects, and

indeed manifests as enhanced photoluminescence in monolayers of MoS_2 as well as those of $MoSe_2$, WS_2, and WSe_2 whereas only weak emission is observed in their multi-layered counterparts.[41, 42, 44] In the case of group 6 TMDCs, the size of band gap in the monolayer is typically about 50% larger than that of bulk materials.[42, 45]

1.2 Novel properties of metal chalcogenides

1.2.1 Valleytronics

Electronic and spintronics devices exploit the charge and spin of electrons respectively whereas valleytronics relies on the fact that the valence (conduction) bands of some materials have two or more degenerate valleys separated in the momentum space.[46] To realize a valleytronic device, a valley-polarization has to be achieved by controlling the number of carriers in these valleys.

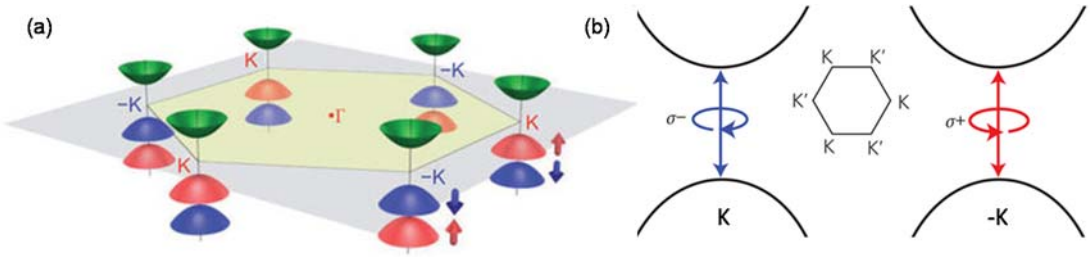

Figure 1.4*. a) Schematic illustration of the electronic structure of monolayer MoS_2 showing opposite spin-orbit splitting of valence band maxima at the K and -K points in the hexagonal Brillouin zone. Green surfaces represent conduction band valleys whereas red and blue surfaces represent spin-up and spin-down valence band valleys respectively. b) valley-dependent optical selection rule at the K and -K points. Interband optical transitions couple exclusively with left (σ^-) and right (σ^+) circularly polarized light at K and -K points, respectively. (a) is reproduced with permission from ref. 45 © 2012 APS and (b) is adapted from ref. 47 © 2012 NPG.*

Single-layer of 2H-MoS_2 is ideal for valleytronics with conduction and valence band edges having two degenerate valleys at the corners (K and K' points) of the 2D hexagonal Brillouin zone (Figure 1.4(a)). The direct band gap of ca. 1.9 eV at these two valley points allow for valley-polarization by optical pumping.[45-47] Owing to the broken inversion symmetry, spin–orbit interactions split the valence bands by ca. 0.160 eV and the spin projection (Sz) is well defined along the c-axis of the crystal with the two bands being of spin down (E↓) and spin up (E↑) in character (Figure 1.4(a)).[45, 48, 49] This broken spin degeneracy together with time-reversal symmetry leads to inherent coupling of the valley and the spin of the valence bands in monolayer MoS_2 leading to

a valley-dependent optical selection rule.[46, 47] Consequently, inter-band transitions in the vicinity of the K or K′ valleys couple exclusively to left or right circularly polarized light respectively (Figure 1.4(b)). The circular component of the band edge luminescence is of the same polarization as that of the circularly polarized excitation.[47] On the other hand, inversion symmetry is preserved in bi-layer MoS_2, which in combination with time reversal symmetry, restores the spin-degeneracy by splitting the 4-fold degenerate valence bands into two spin-degenerate valence bands. As valley and spin are decoupled in bi-layer MoS_2, the valley-dependent selection rule is not allowed, and therefore negligible circular polarization is exhibited by bi-layer MoS_2 under the same conditions.[47]

1.2.2 Charge Density Waves and Superlattices

Charge density waves (CDW) are periodic modulation of charge density accompanied by periodic lattice distortions (PLD), found in quasi-1-D or quasi-2-D layered metallic crystal. The electrons in such a CDW, like those in a superconductor, can move in a highly correlated fashion. Rudolf Peierls first predicted the existence of CDW in the 1930s. He argued that a 1-D metal would be unstable to the formation of energy gaps at the Fermi wavevectors $\pm k_F$, which reduce the energies of the filled electronic states at $\pm k_F$. The temperature below which such gaps form is known as the Peierls transition temperature. The distortion can cause an increase in elastic energy, but this can be compensated by the reduction of electronic energy induced by the CDW. CDWs in most materials arise conventionally due to the nesting of 1D and quasi 2D Fermi surfaces while band-type Jahn-Teller mechanism and excitonic-condensate mechanism have also been linked with CDW formation in 1T-$TiSe_2$ although the exact origin of CDW in 1T-$TiSe_2$ seems to be not settled yet.

The d^1 layered TMDCs such as TaS_2, $TaSe_2$, $NbSe_2$ in all their various polymorphic modifications, acquire below some appropriate temperature, CDW with concomitant PLDs manifesting as superlattices. These superlattices have been experimentally observed by advanced techniques such as scanning tunneling microscopy (STM)[50] and high angle annular dark field scanning transmission electron microscopy (HAADF-STEM)[51], and the CDW band gaps, through angle resolved photo emission spectroscopy (ARPES)[52]. Bulk 2H-$NbSe_2$ exhibits a unique ground state in which an incommensurate CDW and superconductivity coexist below 7 K.[53, 54]

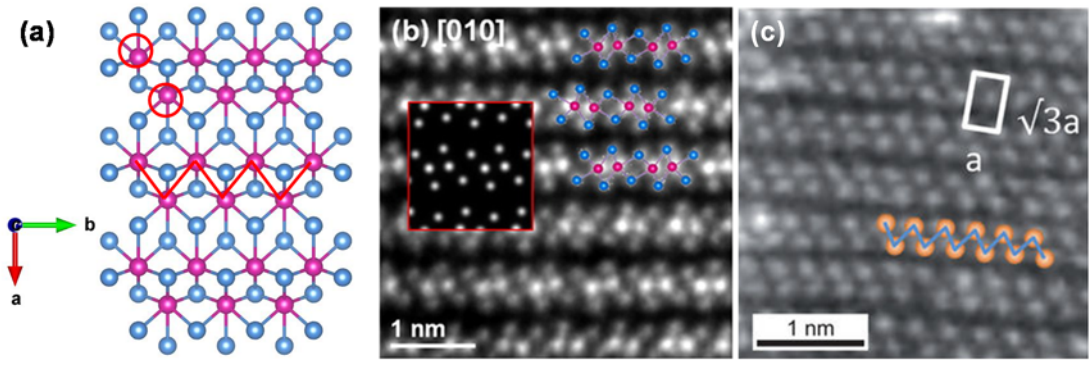

Figure 1.5. *a) A schematic showing the zigzag chain-clusterization of W atoms in Td-WTe_2 (indicated by red arrows). b) HAADF-STEM images of CVT grown Td-WTe_2 in the [010] orientation. Simulated STEM image (red box) and the corresponding calculated atomic model are given as insets. Blue and pink spheres in (a, b) denote Te and W atoms respectively. c) HAAD-STEM image showing zigzag clusterization of W atoms (indicated as orange spheres) in a monolayer WS_2 due to Jahn–Teller distortion. The √3a×a unit cell of the superstructure is indicated with a white rectangle. (b) and (c) are reproduced with permission from ref. 51 © 2016 ACS and ref. 9 © 2013 NPG respectively.*

Other layered TMDCs such as orthorhombic Td-WTe_2 (a distorted variant of centrosymmetric 1T phase) and monoclinic 1T'-$MoTe_2$ (distorted 1T) exhibit CDW-like superlattices at room temperature, formed by zigzag dimerization of off-centered metal atoms.[55] The metal atoms are displaced from their ideal sites at the centers of MTe_6 (M=Mo or W) octahedrons, and move towards each other to form buckled M-M zigzag chains running along the crystallographic a-axis (Figure 1.5(a)). This lattice distortion renders the Td-WTe_2 and 1T'-$MoTe_2$ semimetallic. The origin of distortion and its consequences in these ditellurides are discussed in detail in **part 4** of my thesis. A recent report of Lu *et al.* reveals the subtle distortions of Td-WTe_2 using atom resolved HAADF-STEM (Figure 1.5(b)).[51] Similarly, ReS_2 exists in a distorted 1T-structure (or 1T') with the formation of superlattice due to dimerized zigzag Re–Re chains.[56] Peierls distortion of the 1T structure of ReS_2 prevents ordered stacking and minimizes the interlayer overlap of wavefunctions. As a result, bulk 1T-ReS_2 behaves as electronically and vibrationally decoupled monolayers stacked together.[57] Bulk and monolayer 1T'-ReS_2 have nearly identical band structures with a direct-band gap as large as ca. 1.5 eV due to strong lattice distortion although the otherwise undistorted 1T-ReS_2 (d^3) is expected to be metallic with partially filled d-bands. CDW-like lattice distortions have also been observed at room temperature in some Li-intercalated TMDCs such as MoS_2 and WS_2 (Figure 1.5(c)), the driving force being the 'Jahn–

Teller instability' which splits the partially filled degenerate orbitals causing a reduction of the free energy[58]. Such metallic, distorted 1T phase in MoS_2 and WS_2 is induced through charge-transfer from Li to the TMDCs which causes a local atomic rearrangement from the otherwise 2H structure to the distorted 1T phase. The properties of such distorted TMDCs are expected to be significantly different from those of their undistorted counterparts.

1.2.3 Weyl Semimetals

A Weyl semimetal (WS) is a unique condensed phase of matter where the quasiparticle excitation is the massless Weyl fermion, a particle that played a crucial role in quantum electrodynamics but has not been observed as a fundamental particle in nature. One can realize a WS from a 3D Dirac semimetal either by breaking the inversion symmetry or by breaking the time-reversal symmetry using a magnetic field (B). Thereby, each bulk Dirac node splits into a pair of Weyl nodes with opposite chiralities (i.e., left- or right-handed), separated in the momentum space and connected by exotic arc-like surface states (Figure 1.6(a)). The populations of chiral charges are separately conserved but this chiral symmetry is, however, ruined in the presence of an electric field (E) and a chiral charge is pumped from one Weyl node to the other corresponding to a chiral anomaly. Owing to the chiral anomaly, a WS, unlike an ordinary metal, can exhibit anomalous negative magnetoresistance when E is parallel to B.[59] Weyl fermions are robust while carrying currents, giving rise to exceptionally high mobilities. A WS is, therefore, a topologically nontrivial metallic phase of matter holding promise for realizing unique transport properties with novel device applications.

WS phase is identified in a class of materials with broken inversion symmetry such as TaAs, TaP, NbAs, and NbP. Weyl nodes and Fermi arcs were later realized experimentally, for the first time, in TaAs which is now referred to as a type-I WS (Figure 1.6(b)).[60] Recently type-II WS is proposed where the Weyl points emerge at the contact points of the electron and hole pockets, resulting in a highly tilted Weyl cone (Figure 1.6(c)). TMDCS such as orthorhombic Td-WTe_2, Td-$MoTe_2$, and $Mo_xW_{1-x}Te_2$ with broken inversion symmetry were theoretically predicted to be type-II WS. More recently, the topological Fermi surface arcs were experimentally realized in Td-WTe_2[61] and Td-$MoTe_2$[62] through ARPES.

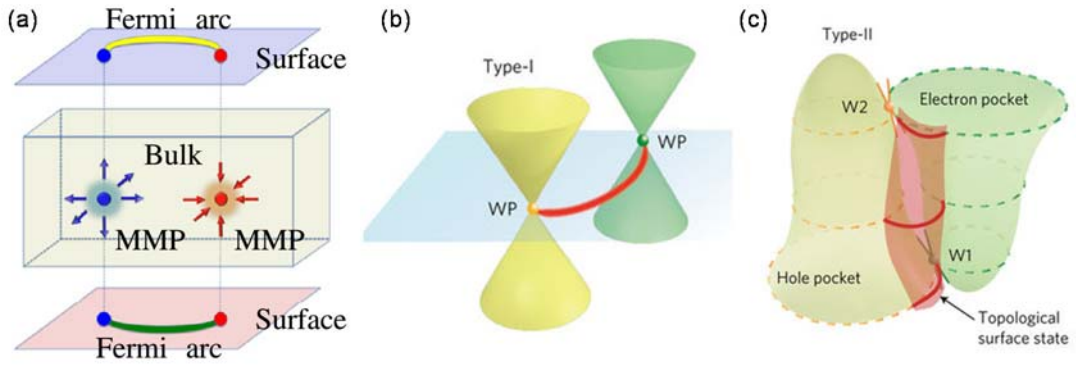

Figure 1.6*. Schematic illustration of Weyl semimetals. a) A Weyl semimetal has Fermi arcs on its surface connecting two Weyl nodes with opposite chirality. Each Weyl node behaves as a magnetic monopole (MMP) in the momentum (k) space, and its chirality corresponds to the charge of the MMP. b) Energy dispersion for type-I Weyl fermion near* E_F*. The two Weyl nodes (WP) are labeled by yellow and green dots. c) Weyl Fermions (W1 and W2) in a Type-II Weyl semimetal, at the boundary between electron and hole pockets at two different energies. (b) and (c) are reproduced with permission from ref. 62 © 2016 NPG.*

1.2.4 Topological insulators

In a 2D electron gas, an intense perpendicular magnetic field (B) drives the bulk electrons to circulate in quantized Landau levels. However, electrons along the opposite edges counter-flow unimpeded by impurities due to strong magnetic field. Such dissipationless edge-current is described as quantum Hall (QH) effect.

In a unique class of materials termed as topological insulators (TIs), an intrinsic strong spin-orbit interaction locks the spin of an electron at right angles with its momentum leading to spin-polarized current along the edges and surface of 2D and 3D TIs respectively. The forward- and backward-moving electrons with a given spin (i.e., up or down) along the edges or surface have different channels for transport and their backscattering ('U-turn') at the non-magnetic defect or impurity is prohibited by time reversal symmetry (TRS) in the absence of a magnetic field (Figure 1.7(c)), leading to low-dissipation metallic transport along the edges or surface.[32] In a 2D TI, this field-free effect is termed as quantum spin Hall (QSH) effect (Figure 1.7(a)), and is experimentally discovered first in HgTe quantum wells sandwiched between CdTe wells.[30, 63] Field-free QSH effect in TIs is practically more attractive than QH effect as very high magnetic fields are required for the latter. TIs are characterized by TRS-protected, spin-polarized edge or surface states coexistent with insulating bulk states;

the former are linearly dispersed and cross at Dirac point corresponding to massless Dirac fermion state.

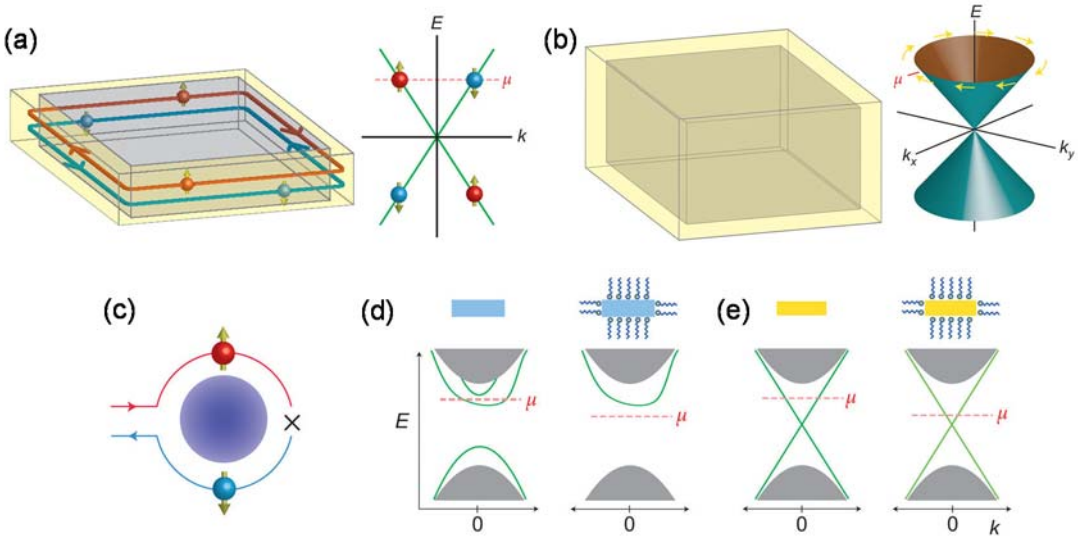

Figure 1.7 *(a) The metallic edge (shown in yellow) of a 2D TI in which spin-up and spin-down electrons counter-propagate (left), and the respective spin-resolved band structure of the edge states (right). The chemical potential is denoted by μ. (b) Metallic surface of a 3D TI (left), and the band structure of the surface states (right) revealing how the electron spin rotates as its momentum moves on the Fermi surface. (c) Backscattering on a TI surface at a non-magnetic impurity (purple sphere) is prohibited due to the conservation of spin angular momentum. (d) An ordinary insulator and its band diagram (left) with the coexistent surface (green lines) and bulk states (gray region). After surface modification, μ shifts and surface states are modified (right). The latter no longer contribute to the transport process as no surface states are available at μ. (e) Band structure of a TI (left). After surface functionalization, μ shifts but the surface states remain intact (right). Adapted from ref. 32 © 2011 NPG.*

Chalcogenides of p-block heavy metals such as Bi_2Se_3, Bi_2Te_3, and Sb_2Te_3 with rhombohedral layered structures exhibit strong spin-orbit interaction leading to inverted electronic structures. They are predicted and experimentally found to be 3D TIs at ambient conditions with linearly dispersed 2D Dirac cones of surface states (Figures 1.7(b) and 8).[31, 32, 34] On the other hand, the lighter members such as stibnite-type Bi_2S_3, Sb_2S_3 and Sb_2Se_3 are topologically trivial at ambient conditions. The gapless metallic surface states appear at the interface between TI and ordinary insulating media (e.g., vacuum) for the property called 'topological invariant' to smoothly change across the interface.[32] The existence of metallic surface states in TIs are robust to any surface modification (Figure 1.7(d)) owing to topological invariant

property, and are therefore, practically attractive for low-dissipation electronic devices. Synthesis of ultrathin TIs such as Bi_2Se_3 with the high surface-to-volume ratio is crucial to realize the full potential of dissipationless transport at the surface. In **chapter 2.1 (part 2),** I have discussed a novel ionothermal synthesis of ultrathin few-layer Bi_2Se_3 Tl.

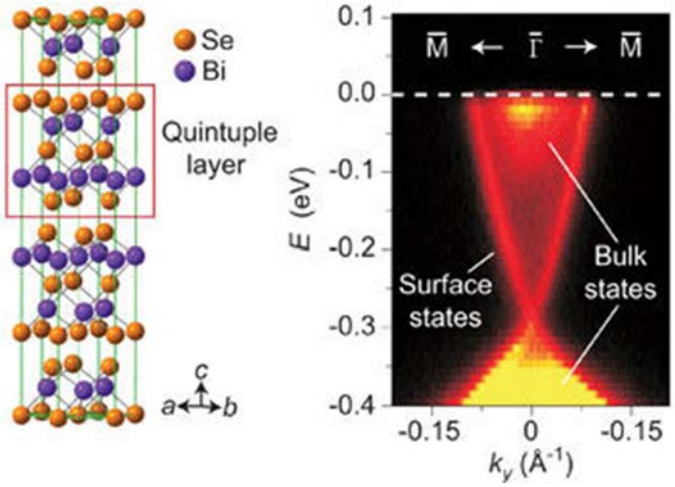

Figure 1.8. *Layered crystal structure of a 3D TI, Bi_2Se_3 (left) comprised of quintuple layers stacked along c-axis via weak van der Waals interaction. The electronic structure of Bi_2Se_3 determined by spin-resolved ARPES (right), revealing the surface states that form a quasi-linear, V-shaped band (i.e., Dirac cone) inside the bulk band gap. Adapted from ref. 34 © 2009 NPG.*

The TIs are found in systems containing heavy elements where the strength of spin-orbit coupling is strong. Interestingly, most of the TIs are also good thermoelectric materials owing to narrow band gaps and large atomic mass which result in high electrical conductivity and low thermal conductivity respectively.[32, 33]

1.2.5 Thermoelectrics

Thermoelectric (TE) materials, by virtue of a unique combination of electrical and thermal properties, are capable of converting thermal gradients into electrical energy or vice versa, and are posited to play a significant role in the energy management.[13, 19, 20, 64] Given the current global energy crisis and the dwindling non-renewable resources, capturing and converting the otherwise wasted heat back into useful electrical power will have a huge impact. When a temperature gradient (ΔT) is applied to a TE couple consisting of n-type and p-type elements, the mobile charge carriers (electrons in n-type and holes in p-type) at the hot end diffuse to the cold end, producing a potential difference (ΔV). This effect known as Seebeck effect, where

$S = \Delta V/\Delta T$ is defined as the Seebeck coefficient, forms the basis of TE power generation. (Figure 1.9(a)). Conversely, when a potential difference is applied to a TE couple, carriers bring heat from one side to the other so that one side gets cooler while the other gets hotter, an effect known as the Peltier effect (Figure 1.9(a)) which forms the basis of TE refrigeration.[65]

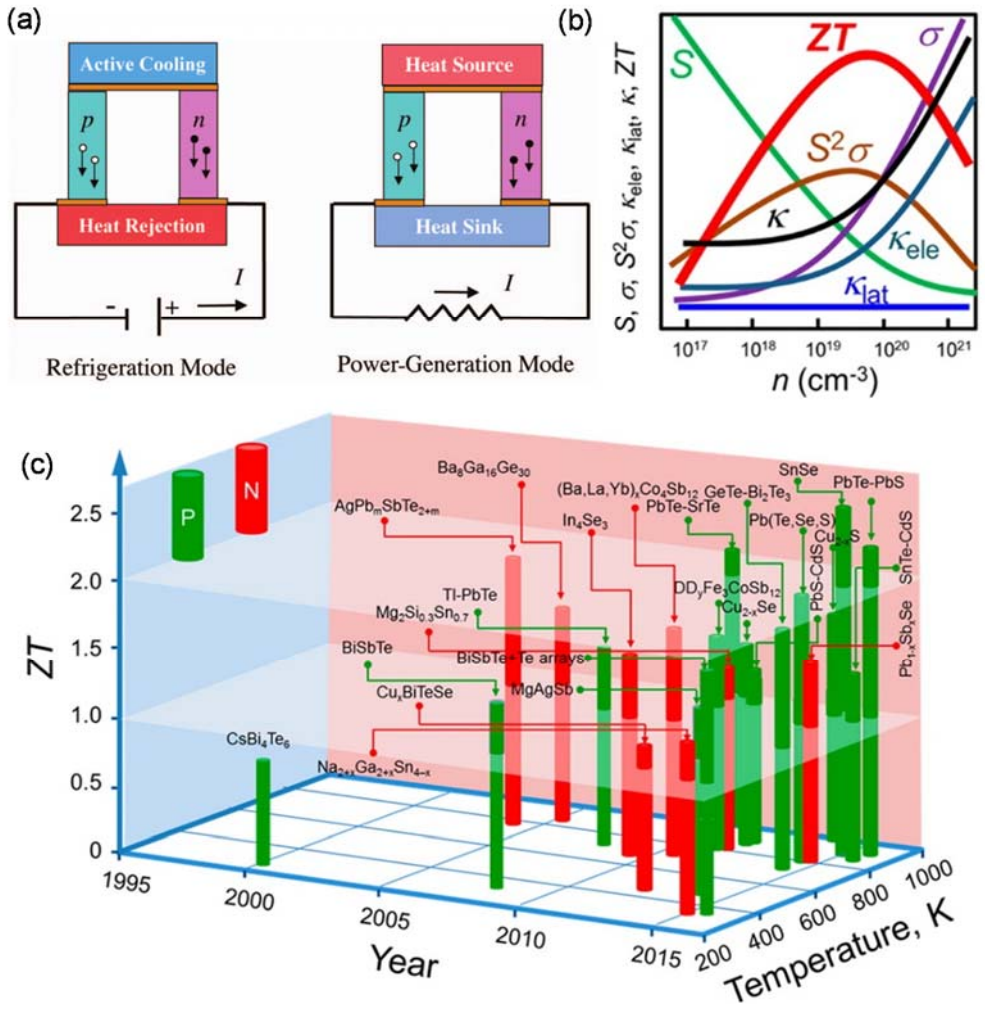

Figure 1.9. *a) Schematic illustrations of a thermoelectric (TE) module for active refrigeration-Peltier effect (left) and power generation-Seebeck effect (right). (b) Schematic diagram showing the variation of zT and related TE parameters (electrical conductivity (σ), Seebeck coefficient (S), power factor ($S^2\sigma$), electronic thermal conductivity (κ_{ele}), lattice thermal conductivity (κ_{lat}), and total thermal conductivity (κ), as a function of carrier concentration (n). The TE parameters are highly correlated thereby limiting the maximum zT. c) TE figure-of-merit (zT) as a function of temperature and year illustrating important milestones. (b) and (c) are reproduced with permission from ref. 19 © 2016 ACS.*

The TE conversion efficiency of a TE material is a function of a dimensionless figure of merit, zT, given by:

$$zT = \left(\frac{\sigma S^2}{\kappa_e + \kappa_L}\right) T \tag{1.1}$$

where σ is the electrical conductivity, S is the Seebeck coefficient, κ_e and κ_L are the electronic and thermal conductivities respectively, and T is the absolute temperature. A good TE material must possess simultaneously, a high σ (corresponding to low Joule heating), a large S (corresponding to large potential difference) and low κ_L (corresponding to a large temperature difference) to realize high TE efficiency. It is challenging to design a single TE material that meets all the above criteria; moreover, the high interdependence of all the above properties poses an inherent limit to the maximum zT that can be attained in a given material (Figure 1.9(b)). Figure 1.9(c) shows the evolution of zT over the past two decades and it clearly shows that the state-of-art TE materials are found among heavy metal chalcogenides, especially those based on Bi and Pb such as Bi_2Te_3, PbTe, and PbSe.[19]

Two approaches are employed to boost zT viz. enhancement of power factor (σS^2) and reduction of thermal conductivity. Some strategies to enhance power factor include: a) engineering of carrier-concentration through chemical doping, b) enhancement of effective carrier mass (m^*) and hence, the Seebeck coefficient either via convergence of multiple valence/conduction band extrema, or distortion of density of states near Fermi level by resonant impurity levels, and c) enhancement of carrier mobility by modulation-doping.[19] On the other hand thermal conductivity is supressed traditionally through a) point defects, b) endotaxial nanoscale precipitates in the host matrix and c) mesoscale grain boundaries. Sometimes all the above three are incorporated in what are referred to as hierarchical architectures where the atomic scale, nanoscale and mesoscale defects would scatter phonons with a broad range of wavelengths (Figure 1.10).[19, 64] The All-scale hierarchical architecting has been shown to be promising especially for the lead chalcogenides. However, in addition to scattering of phonons, an undesirable scattering of carriers can occur limiting the overall zT in most other TE materials. In this respect, materials with intrinsically low thermal conductivity are, therefore, practically more attractive being robust to impurities, doping, grain sizes etc.

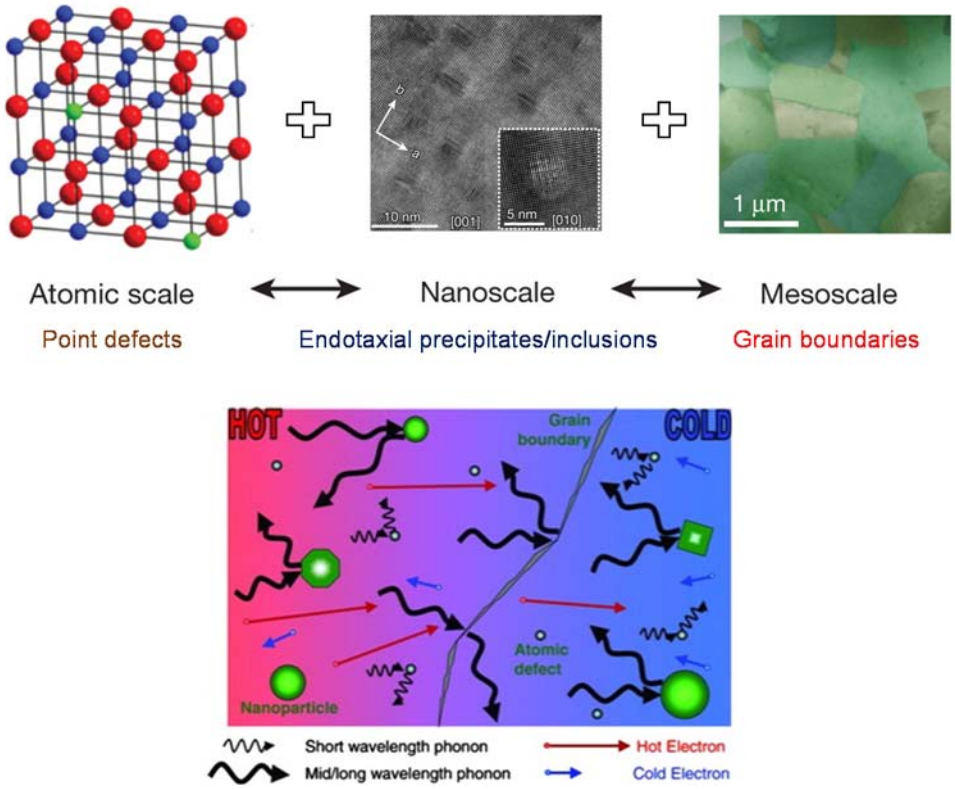

***Figure 1.10**. Illustration of atomic scale point defects, endotaxial nanostructures and mesoscale grain boundaries in hierarchical architectures based on PbTe that lead to an all-scale phonon scattering (upper panel). Point defects scatter short-wavelength phonons. Nanoparticles are effective at scattering mid-long wavelength phonons while grain boundaries predominantly scatter the long wavelength phonons. Schematic illustration of phonon-scattering by atomic defects, nanoparticles and grain boundaries in a solid (lower panel). The upper panel is adapted from ref. 64 © 2012 NPG and the lower panel is reproduced with permission from ref. 20 © 2010 Wiley.*

Slack had originally proposed 'phonon-glass electron-crystal' (PGEC) where the electron and phonon transport channels are decoupled, thus facilitating an independent control of electronic and thermal properties. As the name suggests, a PGEC crystal should possess glass-like low thermal conductivity coexistent with crystal-like high electrical conductivity. PGEC concept has inspired several investigations and led to significant increase in zT in several classes of compounds such as skutterudites,[66] clathrates[67] etc. The latter can be doped with guest-fillers that preferably occupy the intrinsic over-sized structural voids. These guest atoms, not being bonded to the host matrix, randomly rattle within the voids producing localized low-frequency optical vibrations. The latter can couple with the heat-carrying acoustic phonons of the host and lead to ineffective thermal transport via 'phonon resonant scattering'[68] or lowering of acoustic phonon group velocities.

Other intrinsic factors leading to low thermal conductivity include large unit cells,[69] complex crystal structures,[70] cation-disorder,[71] liquid-like atomic motion,[72] and weak multicentre bonds.[73] Lattice anharmonicity is a universal feature that leads to low lattice thermal conductivity due to anharmonic phonon-phonon scattering. An elaborate discussion on lattice anharmonicity is given below. As mentioned before, in certain lone pair containing compounds (e.g., $AgSbSe_2$), the lattice vibrations can be rendered strongly anharmonic by deformation of electron lone pairs. In **part 5** of the thesis, I have investigated the origins of an intrinsically low thermal conductivity in two Zintl compounds viz. InTe and $TlInTe_2$. I have ascribed the observed ultralow lattice thermal conductivity to the intrinsic lone-pair induced anharmonic rattling vibrations of cations.

1.3 Heat capacity and thermal conduction

In most of my thesis, I have studied the electrical and thermal transport properties of various metal chalcogenides. In particular, **part 5** of thesis majorly deals with the underlying causes of intrinsically low lattice thermal conductivity in a couple of Zintl compounds. It is therefore instructive to review some essential basics of how heat is stored and transported in crystalline solids including the effect of lattice anharmonicity, to appreciate our findings better. I have also elaborated the experimental details of thermoelectric measurements in the following section. I have made appropriate references to some of the following, wherever essential, in the subsequent parts of my thesis.

1.3.1 Basics of heat capacity

1.3.1.1 Dulong-Petit law

Dulong-Petit law is a classical expression for molar specific capacity (J/K/mole) of certain elements, proposed by French physicists, Pierre Louis Dulong and Alexis Thérèse Petit in 1819.[74] It is based on their empirical observation that mass-specific heat capacity (J/K/g) of various elements, when multiplied with respective atomic weights, approached a value close to 3R where R is the gas constant (8.314 J/K/mole). This law can be justified by the classical equipartition theorem which states that energy stored per degree of freedom is $1/2k_BT$. In a crystal, each atom will have 6 degrees of freedom - one translational and one vibrational degree of freedom along each spatial

dimension - and the total energy per atom is, therefore, $3k_BT$. The molar specific heat capacity at constant volume, $C_V = \frac{\partial}{\partial T}(3k_BTN_A) = 3k_BN_A/\text{mole} = 3\text{R/mole}$. While Dulong-Petit law holds true at sufficiently high temperatures, it does not explain the observed T^3-dependence of C_V at very low temperatures. This deviation calls for the quantum theory of lattice vibrations.

1.3.1.2 Einstein's model

Einstein's model of specific heat in 1907 offered a microscopic explanation of physical origins of the Dulong-Petit limit.[75] Einstein treated a solid lattice as an ensemble of N number of quantum oscillators coupled by harmonic forces and all vibrating at the same frequency (ω_0). With the total degrees of freedom being 3N, by recalling the energy of a quantum harmonic oscillator, the average energy of the Einstein lattice can be expressed as:

$$\langle U \rangle = 3N\hbar\omega_0 \left(\frac{1}{2} + \frac{1}{exp(\hbar\omega_0/k_BT - 1)} \right) \tag{1.2}$$

The specific heat capacity at constant volume can be obtained as:

$$C_V = \left(\frac{\partial U}{\partial T} \right)_V = 3Nk_B \frac{x^2 e^x}{(e^x - 1)^2} \tag{1.3}$$

where $x = \hbar\omega_0/k_BT$. By defining the Einstein temperature of a materials as $\theta_E = \hbar\omega_0/k_B$, equation 1.3 can be rewritten as :

$$C_V^{(E)}\ (T) = 3Nk_B \left(\frac{\theta_E}{T} \right)^2 \frac{e^{\theta_E/T}}{(e^{\theta_E/T} - 1)^2} \tag{1.4}$$

In the context of phonon dispersion relations, the Einstein's model of harmonic oscillators vibrating with a constant frequency is applicable to optical phonon branch as the latter is often dispersionless (nearly independent of k, the wave vector) and all the phonon modes for this optical branch can be assumed to possess the same frequency. Equation 1.4, therefore, gives the optical mode contribution to total specific heat capacity.

In the high-temperature limit (T→∞), $e^{\frac{\theta_E}{T}} \approx 1 + \frac{\theta_E}{T}$ and $C_V = 3Nk_B$ which agrees well with the Dulong-Petit law. In the low-temperature limit (T→0), $e^{\frac{\theta_E}{T}} - 1 \approx e^{\frac{\theta_E}{T}}$ and C_V decays exponentially as $exp\left(-\frac{\theta_E}{T}\right)$. Physically, the higher energy phonon modes are difficult to excite at very low temperatures thus leading to an abrupt decay

in C_V. The exponential decay predicted by Einstein's model, however, contradicts the observed T^3-dependence of C_V at low temperatures.

1.3.1.3 Debye's model

To account for the observed temperature dependence of C_V at low temperatures, Debye modelled atomic vibrations as normal modes confined in a box[76]. Whereas the Einstein model assumed that each oscillator has the same frequency, Debye theory accounts for different possible modes each with a different frequency (ω) and wave vector (k). Modes with low ω are excited at low temperatures and contribute to the heat capacity. Therefore, heat capacity varies less abruptly at low T compared with the Einstein model. Debye assumed a linear dispersion ($\omega(k) = vk$) for phonons whose frequency must satisfy $0 \leq \omega \leq \omega_D$ where the maximum frequency, ω_D, is called the Debye frequency. Since the acoustic phonon branches obey the said conditions, Debye's model essentially gives the acoustic mode contribution to specific heat capacity. With the above assumptions, the total energy of the Debye lattice can be calculated using the following equation:

$$\langle U \rangle = 9Nk_BT\left(\frac{T}{\theta_D}\right)^3 \int_0^{\frac{\theta_D}{T}} dx \frac{x^3}{e^x - 1} \tag{1.5}$$

The specific heat capacity is then given by:

$$C_V^{(D)}(T) = \frac{\partial U}{\partial T} = 9Nk_B\left(\frac{T}{\theta_D}\right)^3 \int_0^{\frac{\theta_D}{T}} dx \frac{x^4 e^x}{(e^x - 1)^2} \tag{1.6}$$

In equations 1.5 and 1.6, $x = \hbar\omega/k_B\,T$, θ_D is the mode Debye temperature given as $\theta_D = \hbar\omega_D/k_B$, and ω_D is the Debye frequency given as $\omega_D = (6\pi^2 \frac{N}{V})^{\frac{1}{3}}\, v_S$ where N/V is the number density of atoms and v_S is the speed of sound in the material. In the high-temperature limit, x is small, so $e^x \approx 1 + x$ and $C_{Debye} = 3Nk_B$ which agrees with the Dulong-Petit law. In the low-temperature limit, the integral's upper limit in equation 1.6 can be set to infinity so that it becomes:

$$C_V^{(D)}(T) = \frac{12\pi^4}{5} Nk_B\left(\frac{T}{\theta_D}\right)^3 = \beta T^3 \tag{1.7}$$

As seen from equation 1.7, heat capacity (from acoustic phonons) varies as T^3 at low temperatures, which is consistent with the experimental trend. This is due to the fact that Debye model predicts the exact phonon dispersion at sufficiently low temperatures

where only long wavelength acoustic phonon modes are activated. In the intermediate temperatures, however, both the Debye and Einstein models are not accurate owing to limitations of basic assumptions used in the derivation of C_V .

1.3.1.4 Electronic heat capacity

In real crystals, in addition to the lattice vibrations, heat can also be stored by excitations of free carriers. To account for the contribution of free carriers to the heat capacity, we begin with the following expression for the internal energy of a Fermi sea of electrons (holes):

$$U = \int_0^\infty \epsilon D(\epsilon) f(\epsilon) d(\epsilon) = U_0 + \frac{\pi^2}{6} (k_B T)^2 D(\epsilon_F) \tag{1.8}$$

where $D(\epsilon)$ is the electronic density of states and $f(\epsilon)$ is the Fermi-Dirac distribution. The carrier contribution to specific heat capacity in the low-temperature limit can be calculated using the equation below:

$$C_V = \frac{\partial U}{\partial T} = \frac{\pi^2}{3} g(\epsilon_F) k_B^2 T = \frac{\pi^2}{2} n k_B \left(\frac{k_B T}{\epsilon_F} \right) = \gamma T \tag{1.9}$$

Accounting for the electronic and Debye lattice contributions to specific heat capacity, the total specific heat capacity of a solid material in the low-temperature limit is given as:

$$C_V = C_{V,carrier} + C_{V,Debye} = \gamma T + \beta T^3 \tag{1.10}$$

1.3.1.5 Debye-Einstein model

In general, the optical modes are higher in energy (ω) compared to acoustic modes so that at very low temperatures, the total heat capacity is dominated by the acoustic modes since $C_V^{(D)} \gg C_V^{(E)}$. Few exceptions are noted, for instance, clatharates or filled-skutterudites wherein the low-energy optical modes induced by randomly rattling guest atoms also contribute to heat capacity at low temperatures. The rattling guest atoms are treated as independent harmonic oscillators (Einstein oscillators) and the remaining lattice is treated within the Debye model.[67] Specific heat capacity of the these compounds has been successfully interpreted considering Einstein modes in a Debye host.[67]

So far, the entire discussion deals with specific heat capacity at constant volume (C_V). However, specific heat capacity at constant pressure (C_p) is experimentally more

feasible and includes an additional contribution from thermal expansion. The difference between C_p and C_V is a measure of anharmonicity which is an important topic when thermal conductivity is concerned. At low temperatures ($T \ll \theta_D$), however, C_p can be approximated to C_V due to negligible thermal expansion.

1.3.2 Basics of thermal conductivity

Thermal conductivity is defined as the energy transmitted per unit time across unit area per unit temperature gradient. Using kinetic theory of phonon 'gas', the lattice thermal conductivity of a solid material can be described as [77]

$$\kappa_{Lat} = \frac{1}{3} C_V v^2 \tau = \frac{1}{3} C_V v l \tag{1.11}$$

where C_V is the specific heat at constant volume, v is the velocity of sound in the material, τ is the effective relaxation time, and l is the phonon mean free path. Unlike C_V and l, the velocity of sound is material-dependent and varies very little with changes in temperature, morphology, or doping.

Phonon mean free path is determined by a) rate of scattering with other phonons and (b) scattering with grain-boundaries or static impurities. In case of insulators and semiconductors with less than ca. 10^{19}-10^{20} free carriers per cm^3, κ_{Lat} usually dominates the total κ. Moreover, acoustic phonons usually dominate κ_{Lat} over optical phonons because of their higher group velocities, $v_i = \partial\omega/\partial k$ (here i refers to polarization of acoustic phonons i.e., longitudinal (LA) or transverse (TA1, TA2)).

1.3.2.1 Phonon-phonon interactions

Phonon-phonon scattering can be classified into two types: N-process and U-process[77]. Consider a three-phonon scattering process described by:

$$k_1 + k_2 = k_3 + g \tag{1.12}$$

In equation 1.12, k is the propagation wavevector inside the first Brillouin zone (BZ), bound by one-half of the reciprocal lattice vector, $g = 2\pi/a$ where a is the lattice constant of crystal lattice. The acoustic phonon energy, $E_i = \hbar\omega_i$, has an upper bound of $k_B\,\theta_i$, the zone-boundary energy of mode, where θ_i is the mode-dependent Debye temperature corresponding to the Debye frequency (ω_D). When $T \ll \theta_i$, only long-wavelength phonons with $k \ll g/2$ exist and collisions between two such phonons (k_1, k_2) give rise to a third phonon (k_3) in such a way that $|k_1 + k_2| = |k_3| < |g/2|$, and

g is zero in equation 1.12. Such a process is called 'Normal' process or N-process where there is no net loss of momentum (Figure 1.11(a)). When T exceeds 1/3 to 1/2 of θ_i, population of phonons with $|k|$ in the vicinity of BZ boundary increases and collision between two such phonons whose wavevectors are of the order of $g/2$ often gives rise to a third phonon whose wavevector is beyond the first BZ. This, however, is not physical as such a phonon would correspond to wavelength that is shorter than twice the lattice spacing. So, any longer k produced during collision should be brought back into first BZ by an addition of $g \neq 0$. This process is discovered by Peierls and is called 'Umklapp' process or U-process, where a collision of two phonons with negative k_x creates a third phonon with a positive k_x accompanied by a net loss of momentum of $\hbar g$ to transport (Figure 1.11(b)). Therefore, while N-processes do not directly contribute to thermal resistance, U-processes impede thermal conductivity. The effectiveness of U-processes in inhibiting heat transfer depends on a) the scattering cross-section or frequency of collisions and b) the amount of momentum loss during each collision. In both N- and U-processes, energy must be conserved i.e. $\hbar\omega_1 + \hbar\omega_2 = \hbar\omega_3$ where ω is the angular frequency of phonons.

1.3.2.2 Temperature-dependence of lattice thermal conductivity

High-temperature limit ($T \gg \theta$): The probability of phonon collision is directly proportional to average number of phonons present. The equilibrium number of phonons at a given temperature is governed by 'Planck distribution' and in the high-temperature limit ($T \gg \theta$),

$$\langle n \rangle = \frac{1}{\left(e^{\frac{\hbar\omega}{k_B T}} - 1\right)} \cong \frac{k_B T}{\hbar\omega} \tag{1.13}$$

Therefore, the mean free path of phonons (l) should go as 1/T. As C_V is nearly constant in this regime, the temperature-dependence of κ_{Lat} obeys that of l. Thus, $\kappa_{Lat} \sim 1/T$ at very high temperatures.

Low-temperature limit ($T \ll \theta$): Thermal conductivity is finite in a crystal owing to U-processes. For the U-process to occur, at least one of the initial phonons must have energy comparable to $k_B\theta$ and number of such phonons is:

$$\langle n \rangle = \frac{1}{\left(e^{\frac{\hbar\omega}{k_B T}} - 1\right)} \cong \frac{1}{(e^{\theta/T} - 1)} \sim e^{-\theta/T} \tag{1.14}$$

As T decreases, the number phonons participating in U-process decays exponentially. Hence the effective relaxation time for phonon scattering (τ) goes as $e^{\frac{\theta}{T}}$ and as T decreases, κ_{Lat} shows an exponential increase till the mean free path becomes comparable to that due to grain boundaries or static imperfections. Below this temperature, κ_{Lat} obeys the temperature dependence of C_V and goes as T^3. As temperature increases, U-processes begin to appear thereby decreasing the l. At this point κ_{Lat} reaches a maximum beyond which it falls exponentially as $e^{-\frac{\theta}{T}}$. At higher temperatures, the exponential decay of κ_{Lat} is replaced by a slower 1/T decay with temperature (Figure 1.11(c)).[78]

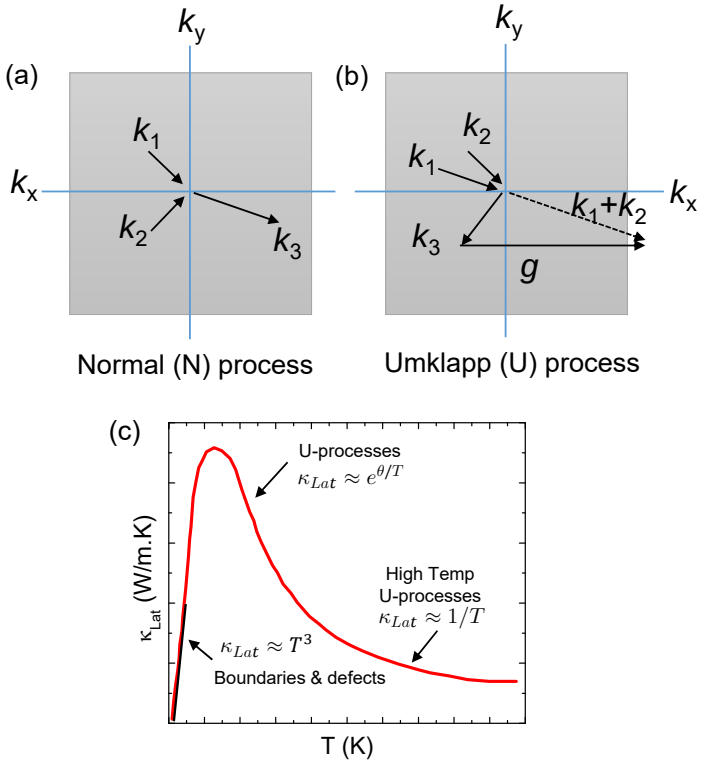

Figure 1.11. *Schematic of a) Normal and b) Umklapp phonon collision processes in a two-dimensional square lattice. Typical temperature dependence of lattice thermal conductivity (κ_{Lat}) for a crystalline solid due to different phonon scattering processes. Image in (c) is adapted from ref. 78 © 2004 Springer.*

1.3.2.3 Cahill's model for minimum thermal conductivity

In 1989, Cahill and Pohl proposed a model to describe the thermal conductivity in amorphous materials which has been more recently used to describe the minimum

lattice thermal conductivity in crystalline materials.[79] The model is an extension of the Debye's model for specific heat capacity and describes thermal transport in amorphous materials as 'a random walk of energy between localized oscillators of varying sizes and frequencies'. Within the framework of this model, the amorphous limit (κ_{min}) to lattice thermal conductivity is given as:[79]

$$\kappa_{min} = \left(\frac{\pi}{6}\right)^{1/3} k_B n_a^{2/3} \sum_i v_i \left(\frac{T}{\theta_i}\right)^2 \int_0^{\theta_i/T} \frac{x^3 e^x}{(e^x - 1)^2} dx \tag{1.15}$$

where the summation is taken over three acoustic modes (one longitudinal (LA) and two transverse (TA) modes), k_B is the Boltzmann constant, n_a is the number density of atoms, θ_i is the cut-off frequency (in the units of K) for each polarization branch, v_i is the sound velocity for each polarization branch and i is the polarization index (TA_1, TA_2 and LA).

1.3.2.4 Anharmonicity

Earlier discussion on heat capacity has assumed harmonic forces connecting the atoms in a solid where the lattice potential energy has only quadratic terms. Such a perfectly harmonic lattice would, however, imply that phonons do not interact with one another, the consequences being zero thermal expansion of solids with temperature, and infinite thermal conductivity. But in a real crystal, thermal expansion and thermal conductivity are finite quantities owing to anharmonic phonon interactions. The potential energy of a real lattice has higher order terms related to probabilities of anharmonic phonon interactions, and the lattice thermal conductivity is indeed limited by such interactions as evident by several experimental observations.

In 1970's, Slack developed a formalism for lattice thermal conductivity at high temperatures where heat transport is solely by the acoustic phonons, and anharmonic Umklapp processes are dominant:[80]

$$\kappa_{Lat} = \frac{A\overline{M}\theta^3\delta}{\gamma^2 n^{2/3}\ T} \tag{1.16}$$

In the above phenomenological equation, n is the number of atoms per primitive unit cell, γ is the Grüneisen parameter, δ^3 is the volume per atom, θ is the Debye temperature, $\overline{M}$ is the average mass of the atoms in the crystal and A is a collection of physical constants (A$\approx$ 3.1x10^{-6} if κ_{Lat} is in W/m.K, $\overline{M}$ is in amu, and δ is in

Angstroms). Grüneisen parameter (γ) is an estimate of strength of anharmonicity (i.e., phonon-phonon interactions) in a solid and from the above equation, κ_{Lat} goes as γ^{-2} at high temperatures where the U-processes are dominant. Since most thermoelectric power generators operate in this temperature regime, the strength of anharmonicity is the key 'intrinsic' factor in suppressing κ_{Lat} of a material. With reference to phonon dispersions, the mode-Gruneisen parameter (γ_i) is defined for each phonon mode as the negative of the logarithmic derivative of its frequency ω_i with respect to the crystal volume V:

$$\gamma_i = -\frac{\partial \ln(\omega_i)}{\partial \ln(V)} \tag{1.17}$$

1.4 Thermoelectric measurements

1.4.1 The Seebeck coefficient

The Seebeck coefficient (S) is the ratio of a resulting voltage gradient (ΔV) to an applied temperature gradient (ΔT). For the Seebeck measurement, temperature is varied around a constant base temperature, and the slope of ΔV vs. ΔT plot gives the Seebeck coefficient at a given base temperature (the slope method). Bar-shaped sample is held vertically between the top and bottom Ni electrodes. Two R-type thermocouples are pressed against the sample for probing ΔT and ΔV simultaneously. The base temperature of the sample-chamber is maintained by an infrared-furnace while ΔT values of 5, 10 and 15 K at each of the base temperatures is achieved by a joule-heater attached to the bottom electrode.

1.4.2 Electrical conductivity

For measuring electrical resistivity, a constant current (I) is passed along the length of the bar-shaped sample (i.e., along the hot-pressing direction) between the Ni electrodes. From the voltage drop across the sample (V), resistance (R=V/I) can be obtained, and one can calculate the resistivity (ρ) using $\rho = R.\frac{A}{l}$ where A is the sample's cross-sectional area and l is the separation between the two voltage probes (R-type thermocouples). Electrical conductivity is calculated as $\sigma = 1/\rho$. A schematic showing the sample-chamber and four-probe configuration for measuring the Seebeck coefficient and electrical conductivity in a commercial ULVAC-RIKO ZEM3 apparatus is shown in figure 1.12(b).

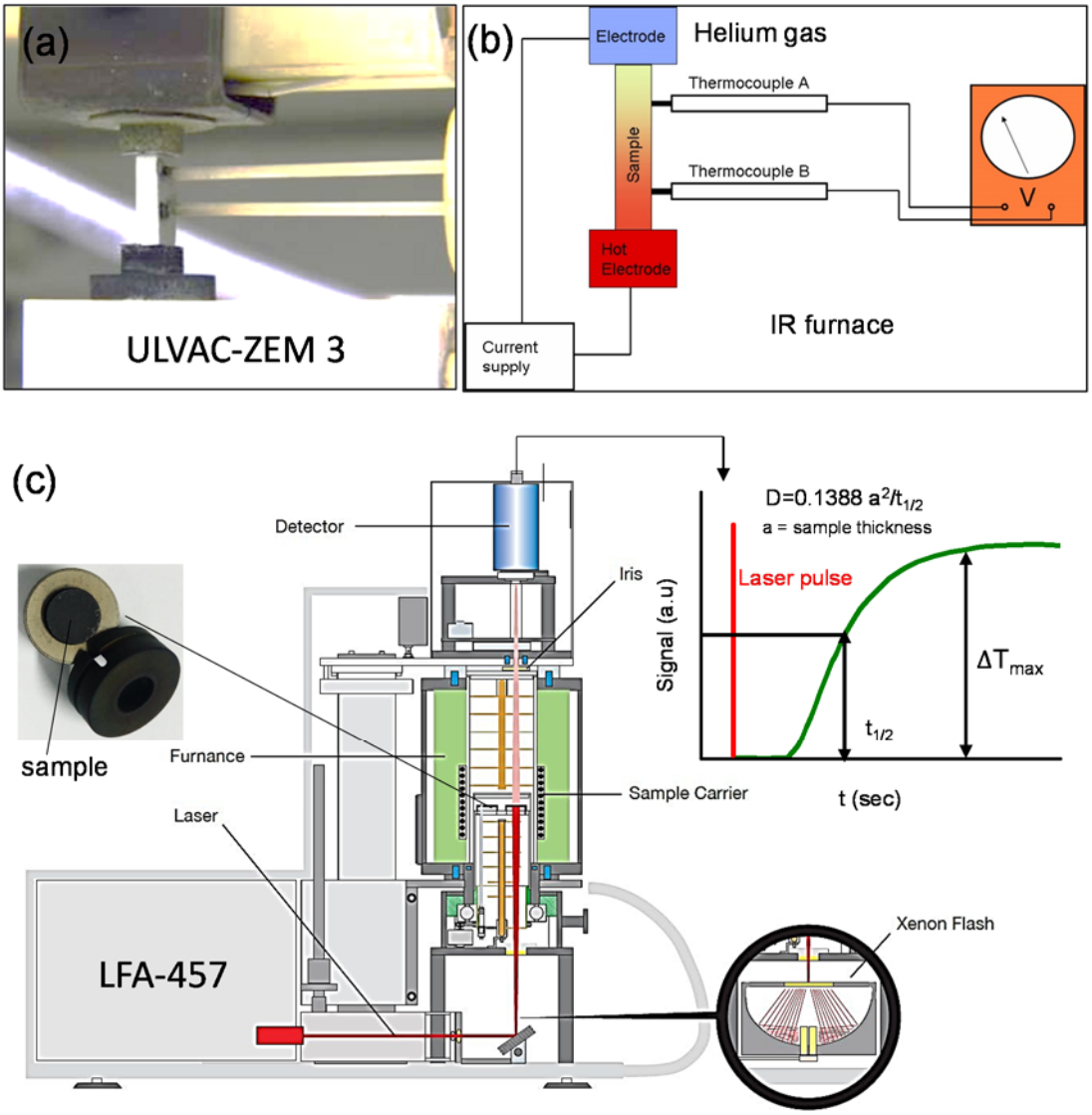

Figure 1.12 *a) Photograph of sample-chamber in ULVAC-ZEM 3 apparatus, b) schematic of UlVAC-ZEM 3 four-probe measurement system and c) schematic of LFA-457 diffusivity measurement apparatus*

1.4.3 Thermal conductivity

The thermal diffusivity, D, was measured in the N_2 atmosphere using the laser flash diffusivity technique in Netzsch LFA-457 instrument. In this technique, a short pulse of energy is applied to one side of a thin sample by a laser flash, while the temperature of the other side is monitored continuously by an infrared (IR) detector. The temperature will rise to a maximum, after which it will decay. The time taken for the temperature to rise to half-maximum ($t_{1/2}$) is used to calculate the thermal diffusivity as $D = 1.38\ d^2/\pi t_{1/2}$ (where d is the sample-thickness),[81] assuming an axial flow of

heat in the sample whose thickness is smaller than the diameter. Samples are loaded in SiC holders. An Nd-Glass pulsed laser (of 1054 nm wavelength) is used as the source of energy pulse and liquid N_2 cooled InSb is used as the IR detector. Both faces of the sample were coated with a thin layer of graphite to ensure good absorption of laser pulse and maximum signal-to-noise ratio at the detector. A correction proposed by Cowan was employed to account for the heat-losses on the sample-faces.[82] A schematic of laser flash apparatus is shown in figure 1.12(c). Owing to the instrumental factors, the percent error in the measured data is 5% each for electrical conductivity, Seebeck coefficient, and thermal diffusivity.

Total thermal conductivity (κ_{tot}) was estimated using the relation, $\kappa_{tot} = D.C_p.\rho$, where ρ is the sample's density and C_p is the specific heat capacity obtained indirectly with respect to a standard pyroceram reference. Lattice thermal conductivity (κ_{Lat}) is extracted by subtracting the electronic thermal conductivity (κ_{el}) from total thermal conductivity. κ_{el} is estimated using the Wiedemann Franz law, $\kappa_{el} = L\sigma T$, where σ is the electrical conductivity and L is the temperature-dependent Lorentz number. L is estimated from the reduced chemical potential and temperature-dependent Seebeck coefficient assuming single parabolic band conduction and dominant acoustic phonon scattering of carriers using: [64, 83]

$$S = \frac{k_B}{e}\left(\frac{2F_1(\eta)}{F_0(\eta)} - \eta\right) \tag{1.18}$$

$$L = \left(\frac{k_B}{e}\right)^2 \frac{3F_0(\eta)F_2(\eta) - 4F_1(\eta)^2}{F_0(\eta)^2} \tag{1.19}$$

$$F_j(\eta) = \int_0^\infty \frac{x^j}{1 + e^{x-\eta}}\, \mathrm{d}x \tag{1.20}$$

where η is the reduced Fermi energy ($E_F/k_B\,T$); $F_j(\eta)$, the j$^{\text{th}}$ order Fermi integral; k_B, the Boltzmann constant; e, the absolute electron charge; h, the Planck constant, and x, the reduced carrier energy. Experimental S vs. T data is fitted with equation 1.18 to obtain η. L is estimated as a function of temperature using the calculated values of $F_j(\eta)$ (see equations 1.19 and 1.20).

1.5 Scope of the thesis

As a part of my thesis work, I have synthesized and studied various heavy metal based chalcogenides of varied structures and dimensionality. Apart from the present introductory part, my thesis work is divided into four parts **(2-5)**, containing two chapters each.

In **part 2**, I have discussed a novel ionothermal route to synthesize few-layer nanosheets of 2D chalcogenides of main group metals viz. Bi_2Te_3 and SnS_2. Bi_2Se_3 is known to be a topological insulator (TI) with insulating bulk and metallic surface states. The fact that these metallic surface states are robust to surface modification or disorder is practically expedient for electronic applications. Synthesis of such TIs in nanoscale is extensively sought after, as the surface-to-volume ratio can be significantly enhanced in nano dimensions. A few reports at that time employed either chemical vapor deposition or chemical exfoliation to obtain few-layer Bi_2Se_3 Tl. In **chapter 2.1**, I have employed an ionothermal route to synthesize ultra-thin Bi_2Se_3 nanosheets down to 3-4 layers using a room-temperature ionic liquid as a green solvent. In general, as TIs are characterized by heavy constituents and a strong spin orbit coupling, they are also expected to possess low thermal conductivity-a crucial criterion for being a good thermoelectric material. I have investigated the thermoelectric properties of as-synthesized Bi_2Se_3 nanosheets in compacted form. I have extended the ionothermal route to synthesizing various other materials such as Bi_2S_3, Sb_2Se_3, and SnS_2. In **chapter 2.2**, I have studied the evolution of morphology, and the Li-ion storage properties of ionothermally obtained hierarchical structures of SnS_2 nanosheets.

Part 3 presents a facile bottom-up synthesis of thin films of heavy metal chalcogenides by employing a toluene-aqueous interface as the reaction medium. Films of nanocrystal granular solids are becoming increasingly relevant for several electronic and optoelectronic applications owing to their low-cost fabrication and facile processability. In **chapter 3.1**, I have discussed the room temperature synthesis of HgSe and HgCdSe quantum dot films by employing the toluene-water interface and studied their photodetection properties in the near-infrared region. Confinement-induced self-organization at the liquid-liquid interfaces is an interesting subject, and several interesting phenomena have been unraveled previously. We have probed the growth kinetics and self-organization of HgSe films at the toluene-water interface through in-

situ X-ray reflectivity and ex-situ grazing incidence X-ray scattering studies. In **chapter 3.2**, I have discussed the synthesis of PbSe nanocrystalline films, the evolution of morphology as a function of various parameters, and the photodetection properties in the near-infrared region.

Part 4 discusses the structure-property relationships in two layered transition metal ditellurides viz. $MoTe_2$ and WTe_2. The more covalent character of tellurium compared with its lighter congeners, bestows its compounds with structures and properties that are often strikingly distinct from the sulfides and selenides. Although numerous studies were carried out on disulfides and diselenides of Mo and W, the ditellurides are relatively less studied. Significant attention was renewed in WTe_2 following the recent discovery of its non-saturating giant magnetoresistance (GMR). In **chapter 4.1**, I have discussed the structural, vibrational and thermoelectric properties of Td-WTe_2. Despite numerous investigations on GMR in Td-WTe_2, vibrational properties in bulk and few-layer Td-WTe_2 have not been studied at that time. I have investigated in detail the Raman vibrational modes in Td-WTe_2 and determined the effect of thickness (i.e., the number of layers) and temperature on the former. I have gained an insight into the observed thickness-dependent Raman shifts in Td-WTe_2 which are found to be anomalous as compared to the well-studied disulfides and diselenides of Mo or W in 2H-structures. **In chapter 4.2**, I have synthesized polycrystalline $MoTe_2$ in 2H as well as 1T' structures and studied their electronic and thermal transport properties. The intrinsic defects such as anion deficiencies are found to govern the temperature-dependence of their electronic transport properties as particularly evident for 2H-$MoTe_2$, and also seem to affect the structural transition from 1T'- to Td-$MoTe_2$ at low temperatures as indicated by the electrical conductivity as well as temperature-dependent Raman spectra of 1T'-$MoTe_2$.

Understanding of intrinsic mechanism(s) affecting the phonon transport is not only of fundamental interest but also indispensable to explore and design new materials with ultralow thermal conductivity central to various applications including thermoelectrics. In **part 5**, I have studied two quasi-1D Zintl compounds viz. $TlInTe_2$ (**chapter 5.1**) and InTe (**chapter 5.2**) featuring chain-type rigid anionic and weakly bound cationic substructures. I have found both the compounds to exhibit ultralow lattice thermal conductivity (ca. 0.5-0.8 W/m.K) near room temperature that decays

close to the theoretical amorphous-limit at elevated temperatures. I have investigated the causes underpinning such intrinsically low lattice thermal conductivity in these compounds by probing into the underlying correlation among structure, chemical bonding, and lattice dynamics with the help of structure-refinement of X-ray diffraction patterns, low-temperature specific heat capacity, and terahertz time domain spectroscopy complemented by first-principles studies. Furthermore, I have demonstrated the concept of 'PGEC' in the case of InTe ingots wherein, by tuning the carrier concentration via optimal indium deficiencies, I have enhanced the thermoelectric figure of merit (zT) in InTe to a maximum value close to unity, which is promising for mid-temperature thermoelectric applications. In this study, we show that compounds where the spherically localized ns^2 lone pairs lead to a local disorder rather than a complete structural distortion, can exhibit strong lattice anharmonicity and hence low lattice thermal conductivity.

To summarize, in the early work of my thesis (**Parts 2 and 3**), I have employed synthesis routes, previously unexplored, to synthesize some important heavy metal chalcogenides and examined their properties. In the rest of my thesis (**Parts 4 and 5**), I have strived to understand the correlation between the crystal structure and the observed vibrational, electronic and phonon properties in select heavy metal chalcogenides.

1.6 References

1. A. Meerschaut, L. Guémas, R. Berger and J. Rouxel, *Acta Cryst.*, 1979, **B35**, 1747-1750.
2. Y. V. Mironov, M. A. Pell and J. A. Ibers, *Angew. Chem. Int. Ed. Engl.*, 1996, **35**, 2854-2856.
3. in *Transition Metal Sulfides: Chemistry and Catalysis*, eds. T. Weber, R. Prins and R. A. v. Santen, Kluwer Academic Publishers, 1998.
4. A. Mar, S. Jobic and J. A. Ibers, *J. Am. Chem. Soc.*, 1992, **114**, 8963-8971.
5. S. Dehnen and M. Melullis, *Coord. Chem. Rev*, 2007, **251**, 1259-1280.
6. M. G. Kanatzidis, *Curr. Opin. Solid State Mater. Sci.* , 1997, **2**, 139-149.
7. M. G. Kanatzidis, *Inorg. Chem.*, 2017, **56**, 3158-3173.
8. M. K. Jana and C. N. R. Rao, *Phil. Trans. R. Soc. A*, 2016, **374**, 20150318.
9. M. Chhowalla, H. S. Shin, G. Eda, L.-J. Li, K. P. Loh and H. Zhang, *Nat. Chem*, 2013, **5**, 263-275.
10. C. N. R. Rao, U. Maitra and U. V. Waghmare, *Chem. Phys. Lett.*, 2014, **609**, 172-183.
11. C. N. R. Rao, H. S. S. Ramakrishna Matte and U. Maitra, *Angew. Chem. Int. Ed.*, 2013, **52**, 13162-13185.
12. Q. Si, R. Yu and E. Abrahams, *Nat. Rev. Mater*, 2016, **1**, 16017.
13. J. R. Sootsman, D. Y. Chung and M. G. Kanatzidis, *Angew. Chem. Int. Ed.*, 2009, **48**, 8616-8639.
14. Q. H. Wang, K. Kalantar-Zadeh, A. Kis, J. N. Coleman and M. S. Strano, *Nat Nanotechnol.*, 2012, **7**, 699-712.
15. G. Eda, T. Fujita, H. Yamaguchi, D. Voiry, M. Chen and M. Chhowalla, *ACS Nano*, 2012, **6**, 7311-7317.
16. H. Lin, L. Chen, L.-J. Zhou and L.-M. Wu, *J. Am. Chem. Soc.*, 2013, **135**, 12914-12921.
17. S. Hudgens and B. Johnson, *MRS Bulletin*, 2004, **29**, 829-832.
18. S. C. Riha, B. A. Parkinson and A. L. Prieto, *J. Am. Chem. Soc.*, 2009, **131**, 12054-12055.
19. G. Tan, L.-D. Zhao and M. G. Kanatzidis, *Chem. Rev.*, 2016, **116**, 12123-12149.

20. C. J. Vineis, A. Shakouri, A. Majumdar and M. G. Kanatzidis, *Adv. Mater.*, 2010, **22**, 3970-3980.
21. A. Rogalski, *Rep. Prog. Phys.* , 2005, **68**, 2267.
22. B. Radisavljevic, A. Radenovic, J. Brivio, V. Giacometti and A. Kis *Nat. Nanotechnol.*, 2011, **6**, 147-150.
23. J. J. Cha, J. R. Williams, D. Kong, S. Meister, H. Peng, A. J. Bestwick, P. Gallagher, D. Goldhaber-Gordon and Y. Cui, *Nano Lett.*, 2010, **10**, 1076-1081.
24. N. Kamaya, K. Homma, Y. Yamakawa, M. Hirayama, R. Kanno, M. Yonemura, T. Kamiyama, Y. Kato, S. Hama, K. Kawamoto and A. Mitsui, *Nat. Mater.*, 2011, **10**, 682-686.
25. F. Cheng, J. Liang, Z. Tao and J. Chen, *Adv. Mater.*, 2011, **23**, 1695-1715.
26. D. Merki and X. Hu, *Energy Environ. Sci.*, 2011, **4**, 3878-3888.
27. J. M. Caron, J. R. Neilson, D. C. Miller, K. Arpino, A. Llobet and T. M. McQueen, *Phys. Rev. B* 2012, **85**, 180405.
28. S. Medvedev, T. M. McQueen, I. A. Troyan, T. Palasyuk, M. I. Eremets, R. J. Cava, S. Naghavi, F. Casper, V. Ksenofontov, G. Wortmann and C. Felser, *Nat. Mater.*, 2009, **8**, 630-633.
29. H. S. S. Ramakrishna Matte, A. Gomathi, A. K. Manna, D. J. Late, R. Datta, S. K. Pati and C. N. R. Rao, *Angew. Chem. Int. Ed.*, 2010, **49**, 4059-4062.
30. M. König, S. Wiedmann, C. Brüne, A. Roth, H. Buhmann, L. W. Molenkamp, X.-L. Qi and S.-C. Zhang, *Science*, 2007, **318**, 766.
31. D. Hsieh, Y. Xia, D. Qian, L. Wray, J. H. Dil, F. Meier, J. Osterwalder, L. Patthey, J. G. Checkelsky, N. P. Ong, A. V. Fedorov, H. Lin, A. Bansil, D. Grauer, Y. S. Hor, R. J. Cava and M. Z. Hasan, *Nature*, 2009, **460**, 1101-1105.
32. D. Kong and Y. Cui, *Nat. Chem.*, 2011, **3**, 845-849.
33. L. Müchler, F. Casper, B. Yan, S. Chadov and C. Felser, *Phys. Status Solidi RRL*, 2013, **7**, 91-100.
34. Y. Xia, D. Qian, D. Hsieh, L. Wray, A. Pal, H. Lin, A. Bansil, D. Grauer, Y. S. Hor, R. J. Cava and M. Z. Hasan, *Nat. Phys.*, 2009, **5**, 398-402.
35. M. N. Ali, J. Xiong, S. Flynn, J. Tao, Q. D. Gibson, L. M. Schoop, T. Liang, N. Haldolaarachchige, M. Hirschberger, N. P. Ong and R. J. Cava, *Nature*, 2014, **514**, 205-208.

36. M. D. Nielsen, V. Ozolins and J. P. Heremans, *Energy Environ. Sci.*,, 2013, **6**, 570-578.

37. A. Walsh, D. J. Payne, R. G. Egdell and G. W. Watson, *Chem. Soc. Rev.*, 2011, **40**, 4455-4463.

38. W. G. Zeier, A. Zevalkink, Z. M. Gibbs, G. Hautier, M. G. Kanatzidis and G. J. Snyder, *Angew. Chem. Int. Ed.*, 2016, **55**, 6826-6841.

39. E. S. Božin, C. D. Malliakas, P. Souvatzis, T. Proffen, N. A. Spaldin, M. G. Kanatzidis and S. J. L. Billinge, *Science*, 2010, **330**, 1660.

40. J. A. Wilson and A. D. Yoffe, *Adv. Phys.*, 1969, **18**, 193–335.

41. G. Eda, H. Yamaguchi, D. Voiry, T. Fujita, M. Chen and M. Chhowalla, *Nano Lett.*, 2011, **11**, 5111-5116.

42. A. Splendiani, L. Sun, Y. Zhang, T. Li, J. Kim, C.-Y. Chim, G. Galli and F. Wang, *Nano Lett.*, 2010, **10**, 1271-1275.

43. H. Zeng, J. Dai, W. Yao, D. Xiao and X. Cui, *Nat Nanotechnol.*, 2012, **7**, 490-493.

44. K. F. Mak, C. Lee, J. Hone, J. Shan and T. F. Heinz, *Phys. Rev. Lett.*, 2010, **105**, 136805.

45. D. Xiao, G.-B. Liu, W. Feng, X. Xu and W. Yao, *Phys. Rev. Lett.*, 2012, **108**, 196802.

46. K. F. Mak, K. He, J. Shan and T. F. Heinz, *Nat. Nanotehnol.*, 2012, **7**, 494-498.

47. H. Zeng, J. Dai, W. Yao, D. Xiao and X. Cui, *Nat. Nanotechnol.*, 2012, **7**, 490-493.

48. Z. Y. Zhu, Y. C. Cheng and U. Schwingenschlögl, *Phys. Rev. B*, 2011, **84**, 153402.

49. T. Cheiwchanchamnangij and W. R. L. Lambrecht, *Phys. Rev. B*, 2012, **85**, 205302.

50. S. Yan, D. Iaia, E. Morosan, E. Fradkin, P. Abbamonte and V. Madhavan, *Phys. Rev. Lett.*, 2017, **118**, 106405.

51. N. Lu, C. Zhang, C.-H. Lee, J. P. Oviedo, M. A. T. Nguyen, X. Peng, R. M. Wallace, T. E. Mallouk, J. A. Robinson, J. Wang, K. Cho and M. J. Kim, *J. Phys. Chem. C*, 2016, **120**, 8364-8369.

52. K. Sugawara, Y. Nakata, R. Shimizu, P. Han, T. Hitosugi, T. Sato and T. Takahashi, *ACS Nano*, 2016, **10**, 1341-1345.

53. J. A. Wilson, F. J. Di Salvo and S. Mahajan, *Adv. Phys.*, 1975, **24**, 117-201.

54. X. Xi, Z. Wang, W. Zhao, J.-H. Park, K. T. Law, H. Berger, L. Forro, J. Shan and K. F. Mak, *Nat Phys*, 2016, **12**, 139-143.

55. B. Brown, *Acta Cryst.*, 1966, **20**, 268-274.

56. S. Tongay, H. Sahin, C. Ko, A. Luce, W. Fan, K. Liu, J. Zhou, Y.-S. Huang, C.-H. Ho, J. Yan, D. F. Ogletree, S. Aloni, J. Ji, S. Li, J. Li, F. M. Peeters and J. Wu, *Nat. commun.*, 2014, **5**, 3252.

57. S. Tongay, H. Sahin, C. Ko, A. Luce, W. Fan, K. Liu, J. Zhou, Y.-S. Huang, C.-H. Ho, J. Yan, D. F. Ogletree, S. Aloni, J. Ji, S. Li, J. Li, F. M. Peeters and J. Wu, *Nat Commun*, 2014, **5**, 3252.

58. A. H. Castro Neto, *Phys. Rev. Lett.*, 2001, **86**, 4382-4385.

59. H.-J. Kim, K.-S. Kim, J. F. Wang, M. Sasaki, N. Satoh, A. Ohnishi, M. Kitaura, M. Yang and L. Li, *Phys. Rev. Lett.*, 2013, **111**, 246603.

60. B. Q. Lv, H. M. Weng, B. B. Fu, X. P. Wang, H. Miao, J. Ma, P. Richard, X. C. Huang, L. X. Zhao, G. F. Chen, Z. Fang, X. Dai, T. Qian and H. Ding, *Phys. Rev. X*, 2015, **5**, 031013.

61. C. Wang, Y. Zhang, J. Huang, S. Nie, G. Liu, A. Liang, Y. Zhang, B. Shen, J. Liu, C. Hu, Y. Ding, D. Liu, Y. Hu, S. He, L. Zhao, L. Yu, J. Hu, J. Wei, Z. Mao, Y. Shi, X. Jia, F. Zhang, S. Zhang, F. Yang, Z. Wang, Q. Peng, H. Weng, X. Dai, Z. Fang, Z. Xu, C. Chen and X. J. Zhou, *Phys. Rev. B*, 2016, **94**, 241119.

62. K. Deng, G. Wan, P. Deng, K. Zhang, S. Ding, E. Wang, M. Yan, H. Huang, H. Zhang, Z. Xu, J. Denlinger, A. Fedorov, H. Yang, W. Duan, H. Yao, Y. Wu, S. Fan, H. Zhang, X. Chen and S. Zhou, *Nat. Phys.*, 2016, **12**, 1105-1110.

63. X.-L. Qi and S.-C. Zhang, *Physics Today*, 2009, **63**, 33-38.

64. K. Biswas, J. He, I. D. Blum, C.-I. Wu, T. P. Hogan, D. N. Seidman, V. P. Dravid and M. G. Kanatzidis, *Nature*, 2012, **489**, 414-418.

65. J.-F. Li, W.-S. Liu, L.-D. Zhao and M. Zhou, *NPG Asia Mater.*, 2010, **2**, 152-158.

66. X. Shi, J. Yang, J. R. Salvador, M. Chi, J. Y. Cho, H. Wang, S. Bai, J. Yang, W. Zhang and L. Chen, *J. Am. Chem. Soc.*, 2011, **133**, 7837-7846.

67. T. Takabatake, K. Suekuni, T. Nakayama and E. Kaneshita, *Rev. Mod. Phys.*, 2014, **86**, 669-716.

68. H. Euchner, S. S. Pailhès, L. T. K. Nguyen, W. Assmus, F. Ritter, A. Haghighirad, Y. Grin, S. Paschen and M. de Boissieu, *Phys. Rev. B*, 2012, **86**, 224303.

69. S. R. Brown, S. M. Kauzlarich, F. Gascoin and G. J. Snyder, *Chem. Mater.*, 2006, **18**, 1873-1877.

70. G. J. Snyder and E. S. Toberer, *Nat. Mater.*, 2008, **7**, 105-114.

71. S. N. Guin, A. Chatterjee, D. S. Negi, R. Datta and K. Biswas, *Energy Environ. Sci.*, 2013, **6**, 2603-2608.

72. W. Qiu, L. Xi, P. Wei, X. Ke, J. Yang and W. Zhang, *PNAS*, 2014, **111**, 15031-15035.

73. S. Wang, J. Yang, L. Wu, P. Wei, J. Yang, W. Zhang and Y. Grin, *Chem. Mater.*, 2015, **27**, 1071-1081.

74. A. Petit and P. Dulong, *Ann. Chim. Phys.*, 1819, **14**, 189-198.

75. A. Einstein, *Annalen der Physik*, 1907, **22**, 180-190.

76. P. Debye, *Ann. Phys. (Leipzig)*, 1912, **39**, 789.

77. C. Kittel, in *Introduction to Solid State Physics*, John Wiley and Sons, New York, 2005.

78. in *Thermal Conductivity: Theory, Properties, and Applications*, ed. T. M. Tritt, Springer US, 2004.

79. D. G. Cahill, S. K. Watson and R. O. Pohl, *Phys. Rev. B*, 1992, **46**, 6131-6140.

80. G. A. Slack, in *The Thermal Conductivity of Nonmetallic Crystals*, eds. H. Ehrenreich, F. Weitz and D. Turnbull, Academic Press, New York, 1979.

81. W. J. Parker, R. J. Jenkins, C. P. Butler and G. L. Abbott, *J. Appl. Phys.*, 1961, **32**, 1679-1684.

82. R. D. Cowan, *J. Appl. Phys.*, 1963, **34**, 926-927.

83. A. Zevalkink, E. S. Toberer, W. G. Zeier, E. Flage-Larsen and G. J. Snyder, *Energy Environ. Sci.*, 2011, **4**, 510-518.

PART 2

Ionothermal synthesis of few-layer nanostructures of 2D metal chalcogenides and their thermoelectric and Li-ion storage properties.

CHAPTER 2.1

Ionothermal synthesis of few-layer nanostructures of Bi_2Se_3 and related materials*

Summary

Topological insulators (TI) are novel quantum phases of matter exhibiting metallic surface states embedded within insulating bulk states. Ultrathin few-layered Bi_2Se_3 TI has been successfully synthesized in an ionic liquid solvent which also acts as an intercalating and stabilizing agent. Thermoelectric properties of compacted few-layer Bi_2Se_3 nanosheets have been investigated. The latter exhibited high electrical conductivity at room temperature which is ascribed to the presence of high mobility carriers in the topologically robust metallic surface states, given the high surface-to-volume ratio in the few-layered sample. Moreover, the surface defects, nanoscale grain boundaries, and interfaces efficiently scatter the heat carrying phonons and suppress the lattice thermal conductivity to as low as ca. 0.4 $Wm^{-1}K^{-1}$ near room temperature. Further, few-layered nanostructures of Bi_2Se_3 and nanowires of Sb_2Se_3 have also been synthesized ionothermally by the decomposition of single-source precursors.

A paper based on this study has appeared in* ***Chem. Eur. J.* 2013, *19*, 9110.

2.1.1 Introduction

Topological insulators (TIs) are novel spin Hall quantum phases with a gapless Dirac cone of surface states, embedded within an insulating bulk band gap. These metallic surface states, being topologically protected by time reversal symmetry, are robust to surface modification and can resist electron back-scattering even at the defects or impurities thereby offering low-dissipation channels for charge-transport at the surface.[1, 2] These exotic surface states were experimentally realized in Bi_2Se_3 and Bi_2Te_3 in the form of a gapless single Dirac cone using angle resolved photoelectron spectroscopy.[3, 4] Owing to strong spin-orbit coupling and heavy mass of constituent elements, these TIs are also good thermoelectric materials which can directly convert untapped heat into electricity and vice versa.[5-11]

Bi_2Se_3 is a TI with a two-dimensional anisotropic structure (R-3m space group) with strong covalent bonding within the layers and weak van der Waals interactions perpendicular to layers. Atomically thin layers of Bi_2Se_3 TI are attractive for electronic devices and thermoelectric applications. Mechanical exfoliation, chemical vapour transport, vapour-solid synthesis and molecular beam epitaxy have been employed for the synthesis of few-layer Bi_2Se_3.[12-15] Mention must be made of the intercalation route of Sun *et al.* to obtain five atom thick layers,[16] and the surfactant-assisted solution growth to obtain nanodiscs and nanosheets of Bi_2Se_3.[17, 18] Polyol method has also been used to prepare few QL Bi_2Se_3.[19]

In search of a simple chemical method for generating ultra-thin few-layered nanostructures of Bi_2Se_3 and related chalcogenides, we have explored a green ionothermal synthesis in the water soluble, room-temperature ionic liquid, 1-ethyl-3-methyl imidazolium tetrafluoroborate ([EMIM]BF_4). Ionic liquids, due to their desirable properties such as negligible vapor pressure, high thermal stability, broad liquidus domain and tunable solubility of both inorganic and organic compounds, have been extensively employed in the inorganic syntheses [20-25] including metal chalcogenide nanostructures. [26-29]

We have found that the ionothermal reaction of bismuth acetate and selenourea in [EMIM]BF_4 yields ultrathin few-layer (ca.3-5) Bi_2Se_3

nanostructures. The few-layer nature was established by atomic force microscopy (AFM), transmission electron microscopy (TEM) and Raman spectroscopy, and the electronic and phonon transport properties investigated. We have also carried out thermal decomposition of the single-source precursor, $Bi(Se\text{-}C_6H_6N)_3$, in $[EMIM]BF_4$ to obtain few-layer Bi_2Se_3 nanodiscs.

2.1.2 Methods

2.1.2.1 Synthesis

In a Teflon-lined autoclave of 7 ml capacity, 100 mg (0.26 mmol) of bismuth acetate and 47.6 mg (0.39 mmol) of selenourea were ultrasonicated in 3 ml of $[EMIM]BF_4$ ionic liquid for 10 min. The autoclave was maintained at a temperature of 180 °C for 4 hrs in a hot-air oven. After natural cooling, the product was washed thoroughly with water and ethanol several times to remove the excess ionic liquid. After drying at 60 °C, the black powder of few-layer Bi_2Se_3 obtained was used for other characterizations. The samples obtained from different batches were finely ground together and compacted in steel dies for thermoelectric measurements (see below).

A similar procedure was followed using 25 mg (0.06 mmol) of bismuth acetate and 7.4 mg (0.09 mmol) of thioacetamide to synthesize Bi_2S_3 nanorods. A similar procedure was followed using 0.025 g of single source precursor, $M(Se\text{-}C_6H_6N)_3$ (M=Sb/Bi)[15] to obtain nanostructures of Sb_2Se_3 or Bi_2Se_3.

2.1.2.2 Characterizations

Powder X-ray diffraction was recorded on Bruker D8 Advance diffractometer using Cu Kα radiation. TEM images were obtained using JEOL TEM-3010 electron microscope at an operating accelerating voltage of 300 kV. AFM was carried out on Bruker Innova Microscope instrument in tapping mode using antimony doped silicon tip with 10 nm resolution. Raman spectra were recorded in Jobin Yvon LabRam HR spectrometer using Ar laser (514 nm wavelength).

2.1.2.3 Thermoelectric measurements

To study the temperature-dependence of electronic and thermal transport properties, a $2\times2\times8$ mm^3 rectangular bar and a coin of 8 mm diameter and

0.85 mm thickness (see figure 2.1.5(a)) were molded in steel dies by pressing the finely powdered sample of few-layer Bi_2Se_3 under 75 kN/m^2 load for 30 minutes. The above pellets were sealed within an evacuated quartz tube (10^{-5} torr), sintered at 450 °C for 1 hr and cooled to room temperature. The intercalated ionic liquid was seen to stick on the sides of ampoule as tiny droplets indicating the removal of any residual ionic liquid in the sintered sample. Electrical conductivity (σ) and Seebeck coefficient (S) for the bar were measured between 300 and 700 K in He-atmosphere using ULVAC-RIKO ZEM3 instrument. The thermal diffusivity (D) for the disc was also measured between 300 and 700 K using the laser flash diffusivity method in Netzsch LFA-457 instrument. Total thermal conductivity (κ_{tot}) was estimated using the relation, $\kappa_{tot} = D.C_p.\rho$, where ρ is the sample's density and C_p is the specific heat capacity reported for the standard Bi_2Se_3. Lattice thermal conductivity (κ_{Lat}) is extracted by subtracting the electronic thermal conductivity (κ_{el}) from total thermal conductivity. κ_{el} is estimated using the Wiedemann Franz law, $\kappa_{el} = L\sigma T$, where σ is the electrical conductivity and L is the temperature-dependent Lorentz number estimated by fitting the temperature-dependent Seebeck coefficient assuming the single parabolic conduction and dominant acoustic phonon scattering (refer to part 1 for more details). Owing to the instrumental factors, the percent error in the measured data is 5% each for electrical conductivity, Seebeck coefficient and thermal diffusivity.

2.1.3 Results & discussion

The crystal structure of Bi_2Se_3 is comprised of quintuple layers (QL) each of ca. 1 nm thickness and constituting five covalently bonded atomic planes [Se(2)-Bi-Se(1)-Bi-Se(2)]. These QLs are periodically stacked along the crystallographic c-axis via weak van der Waals interactions as shown in figure 2.1.1. The powder X-ray diffraction (PXRD) pattern for the sample synthesized by the reaction of bismuth acetate and selenourea in ionic liquid could be indexed on the rhombohedral structure with R-3m space group (Figure 2.1.2). The low intensity of (006) and (003) reflections relative to those of bulk counterpart indicate reduced periodicity along the crystallographic c-direction

suggesting the few-layer nature of the sample. The low-angle PXRD pattern in the inset shows a shift in the (003) reflections to lower angles, indicating an expansion in the interplanar spacing due to intercalation of the ionic liquid.

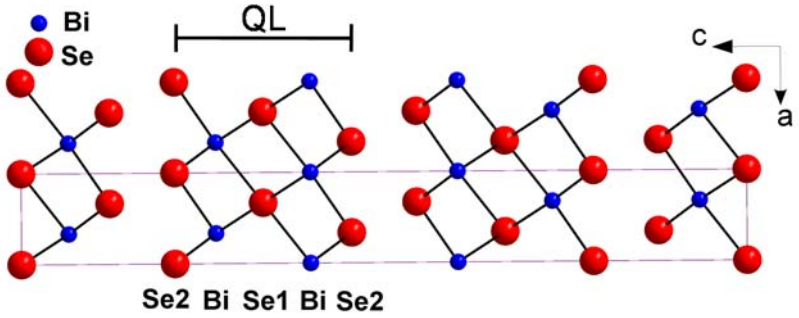

Figure 2.1.1 *Crystal structure of Bi_2Se_3 viewed down b-axis. Each QL constitutes five covalently bonded atomic planes.*

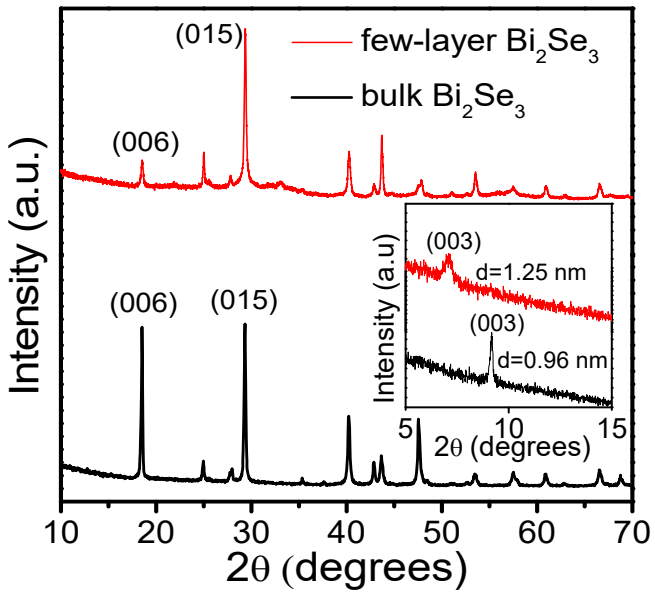

Figure 2.1.2 *PXRD patterns of few-layer Bi_2Se_3 nanosheets (red) and reference bulk Bi_2Se_3 (black). The low-angle PXRD patterns in the inset reveal a shift in the (003) peak in the few-layer Bi_2Se_3 sample to lower 2θ angles due to an interlayer expansion.*

Figure 2.1.3(a) shows a low-resolution TEM image of ultrathin nanostructures of Bi_2Se_3 with bent edges. The high-resolution TEM image (HRTEM) of the bent edges shows an interlayer spacing of ca. 1.23 nm (Figure 2.1.3(b)), as expected in the case of (003) lattice planes. The HRTEM image in figure 2.1.3(c) shows (110) planes of a hexagonal nanodisc (lower inset in figure 2.1.3(b)) with a d-spacing of 0.21 nm. An edge of the same hexagonal

nanodisc is shown in the right inset. The selected area electron diffraction pattern (SAED) given in the left inset of figure 2.1.3(c) could be indexed on the basis of a 6-fold symmetry [0001] zone axis, in agreement with the layered structure along the crystallographic c-axis. Figure 2.1.3(d) shows an AFM image of a free-standing Bi_2Se_3 nanostructure of ca. 4 QL thickness.

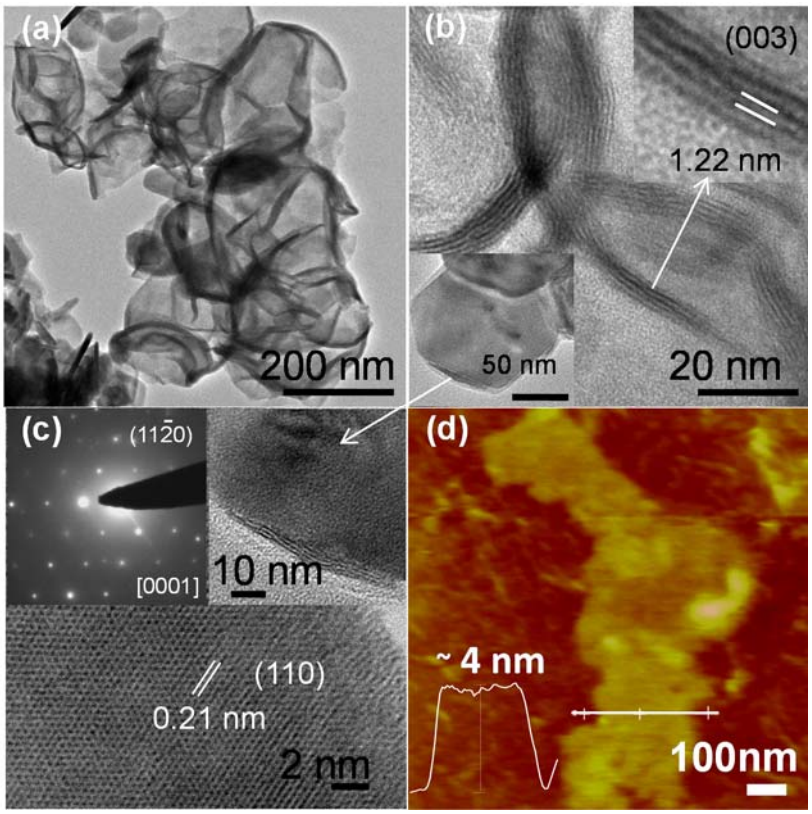

Figure 2.1.3 *a) TEM image of Bi_2Se_3 nanosheets. b) HRTEM image of bent edges of nanosheets, upper inset is a magnified image of the indicated region and the lower inset is a TEM image of a hexagonal nanosheet. c) HRTEM lattice image of a hexagonal nanosheet shown in the lower inset of (b) with the right inset showing an edge of the same nanosheet. The left inset is the corresponding SAED pattern projecting [0001] zone view. d) AFM image of Bi_2Se_3 nanosheet.*

We have examined the few-layer Bi_2Se_3 nanostructures by Raman spectroscopy (Figure 2.1.4). Bi_2Se_3 has 15 lattice modes at the center of Brillouin zone: 12 optical and 3 acoustic modes. Of the 12 Optical modes, A_{1g}^1, A_{1g}^2 (out-of-plane modes) and E_g^1, E_g^2 (in-plane modes) are Raman active.[19] Two representative areas were analysed. In one case (a), E_g^2 and A_{1g}^2 were observed at 122 cm^{-1} and 168 cm^{-1} and in the other case (b), at 126 cm^{-1} and 169 cm^{-1} respectively. In the bulk counterpart (c), these modes were observed at 129

cm^{-1} and 171 cm^{-1} respectively (see figure 2.1.4, left image). Clearly, in the case of few-layer Bi_2Se_3, there is a red shift in the frequencies of above modes due to phonon-softening (Figure 2.1.4, left image). The softening of out-of-plane phonon is ascribed to the smaller number of layers along the *c*-axis, resulting in a reduced effective restoring force. The softening of in-plane mode reflects the impact of inter-layer stacking on the intra-layer bonding. Significant broadening of the E_g^2 mode is indicative of the few-layer regime, where there is a decrease in the phonon life-time due to strong electron-phonon coupling.[19] Comparison of the full-width-at-half-maximum (FWHM) of the E_g^2 mode with the previously reported curve [19] of thickness-dependent FWHM of E_g^2 indicates that the nanostructures under observation are about 4-5 QL thick (Figure 2.1.4, right image) which is consistent with the AFM height profiles.

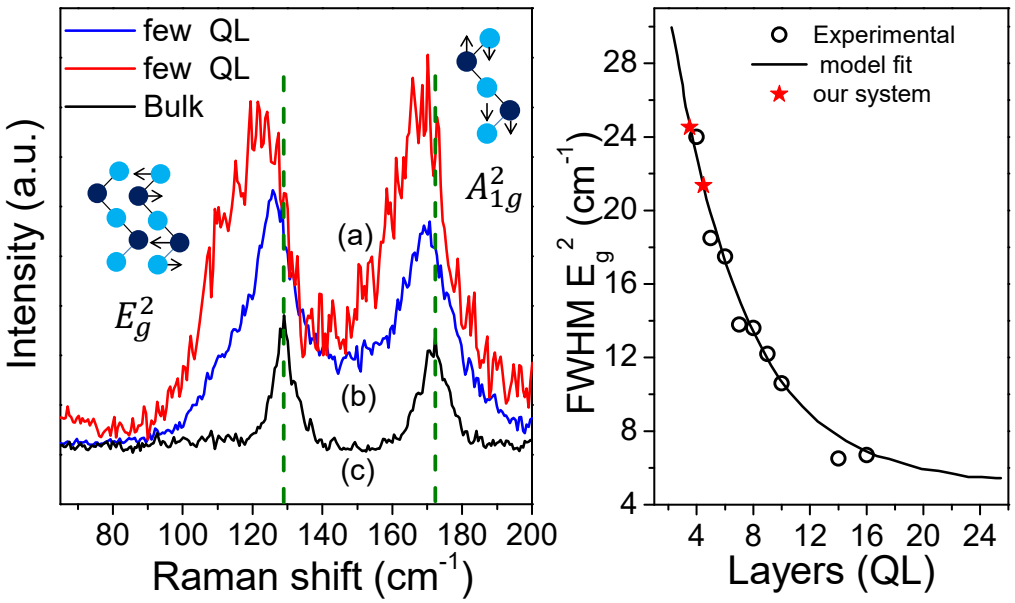

Figure 2.1.4 *The left image shows Raman spectra of two representative regions (a, b) of Bi_2Se_3 nanosheets along with (c) bulk Bi_2Se_3. Left and right insets show schematics of in-plane and out-of-plane vibrational modes respectively. The right image shows the experimental curve of FWHM of E_g^2 mode as a function of the number of QLs in Bi_2Se_3 nanoplates (taken from reference 19). Our experimental FWHM points (red stars) are superimposed on this curve.*

The intrinsic tendency for structural anisotropy in Bi_2Se_3 stems from the differential bonding along different crystallographic directions. After nucleation, hexagonal close packing of atoms gives rise to QLs which are stacked along crystallographic *c*-axis via weak van der Waals interactions.

Based on low-angle PXRD and HRTEM, it is quite clear that an expansion in d-spacing of (003) planes is possible due to intercalation of the ionic liquid. The expansion is ca. 0.29 nm which can accommodate the substituted imidazolium ring of ionic liquid with its plane parallel to QLs.[30] Two plausible factors can result in the formation of few-layer Bi_2Se_3 nanostructures in the ionic liquid. Firstly, the growth along the c-axis is hindered due to the minimization of surface energy by the surrounding ionic liquid. Secondly, as the QLs are being stacked along c-direction, the ionic liquid can intercalate into van der Waals gaps and expand the interlayer distance to the extent of exfoliation. The random exfoliation may thus give rise to few-layer Bi_2Se_3 fragments. It is known that ionic liquids intercalate into layered materials[31-33] and the driving force for the intercalation is the preference for ion-dipole interactions over weak inter layer van der Waals interactions. The stabilizing surface capped ionic liquid refrains the restacking of the as-formed fragments.

The electrical conductivity (σ) increases linearly with temperature from 223 Scm^{-1} at 300 K to 400 Scm^{-1} at 700 K, with a typical semiconducting behaviour (Figure 2.1.5(b)). It is noteworthy that compacted powders of commercial bulk Bi_2Se_3 showed a much lesser σ of ca. 120 Scm^{-1} at 300 K.[16] The reasonably high σ of the present Bi_2Se_3 sample is by the virtue of ultra-thin nature of the nanostructures down to few QL in which the dominant surface states can offer high mobility, scattering-resistant carriers to enhance σ relative to bulk. Greater electronic density of states at the conduction band of few-layer Bi_2Se_3 can further increase the σ compared to bulk.[16] The negative sign of Seebeck coefficient (S), indicates dominant n-type conduction in few-layer Bi_2Se_3 (Figure 2.1.5(c)). S varies linearly with temperature, ranging from -75 μVK^{-1} at 300 K to -42 μVK^{-1} at 700 K. The decreasing S with temperature is due to concomitantly increasing σ, in accordance with semiclassical Mott-Jones formula, which shows that S is inversely proportional to the carrier density, n ($S \sim n^{-2/3}$).[34] This behaviour is usual for traditional thermoelectric materials. The room temperature value of power factor (σS^2) is about 1.25 $\mu Wcm^{-1}K^{-2}$ (Figure 2.1.5(d)) which is comparable to that of single layer based Bi_2Se_3 composite, reported previously.[16]

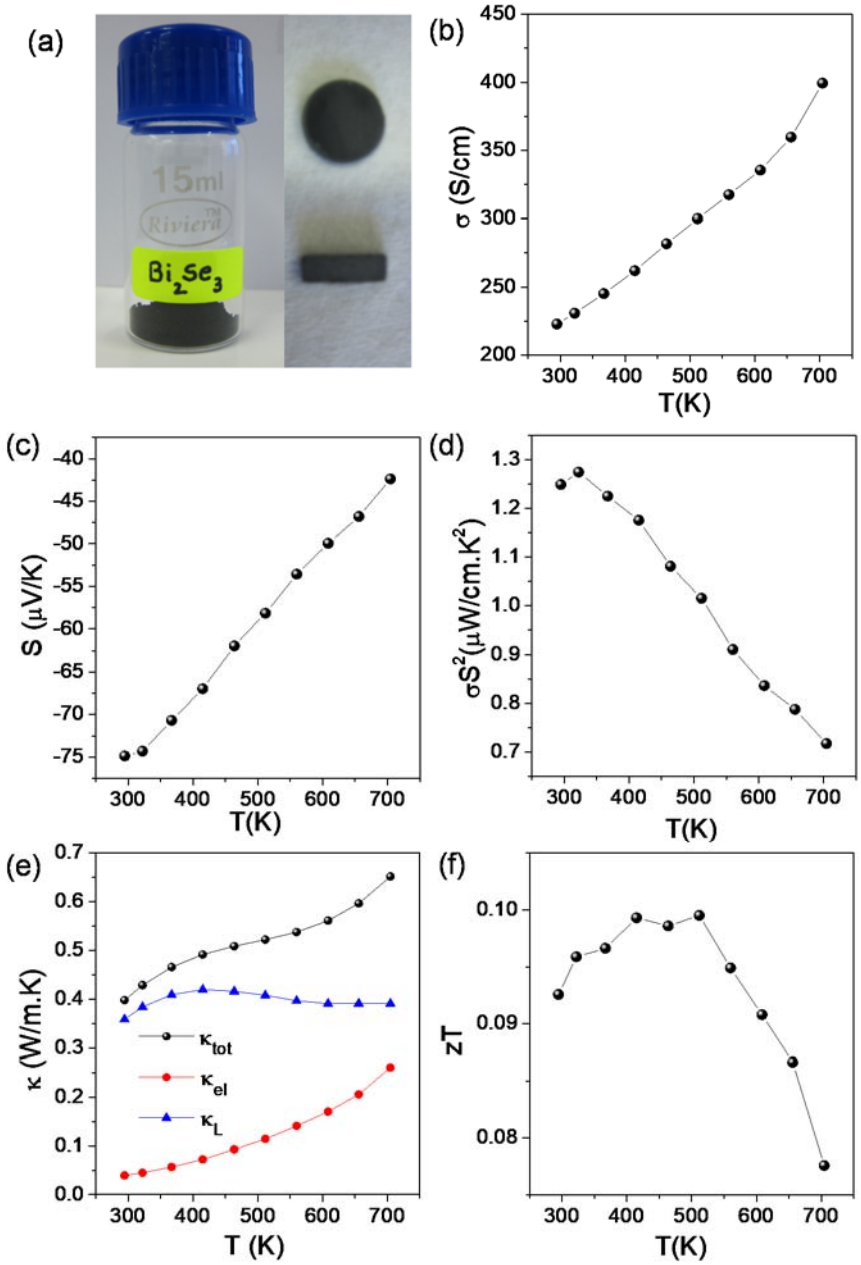

Figure 2.1.5 *a) Photograph showing the annealed few-layer Bi_2Se_3 powder (left) which is compacted into pellet- and bar-shaped samples (right). Temperature-dependence of b) electrical conductivity (σ), c) Seebeck coefficient (S), d) power factor (σS^2), e) total thermal conductivity (κ_{tot}) along with lattice (κ_L) and electronic thermal conductivities (κ_{el}), and f) thermoelectric figure of merit (zT) of compacted few-layer Bi_2Se_3 nanosheets.*

Temperature-dependent total thermal conductivity (κ_{tot}) along with lattice (κ_L) and electronic thermal conductivities (κ_{el}) are shown in figure 2.1.5(e). κ_{tot} ranges from ca.0.4 $Wm^{-1}K^{-1}$ at 300 K to 0.65 $Wm^{-1}K^{-1}$ at 700 K (Figure 2.1.5(e)). κ_{tot} has dominant contribution from κ_L especially near room temperature. κ_{el}, however, increases with temperature due to thermal-

excitation of carriers causing an upturn of κ_{tot} at elevated temperatures. The considerably low κ_L in few-layer Bi_2Se_3 is due to enhanced scattering of short-wavelength phonons by surface defects and of mid/long-wavelength phonons by numerous nanoscale grain boundaries and interfaces in the compacted samples.[5, 11] Few-layer Bi_2Se_3 exhibited a maximum thermoelectric figure of merit (zT) of ca. 0.1 at 510 K and stays nearly flat in the range of 300-550 K (Figure 2.1.5(f)). Thermoelectric transport measurements provide clear evidence of phonon localization (i.e., reduced κ_L) and high σ, reminiscent to topological insulator.

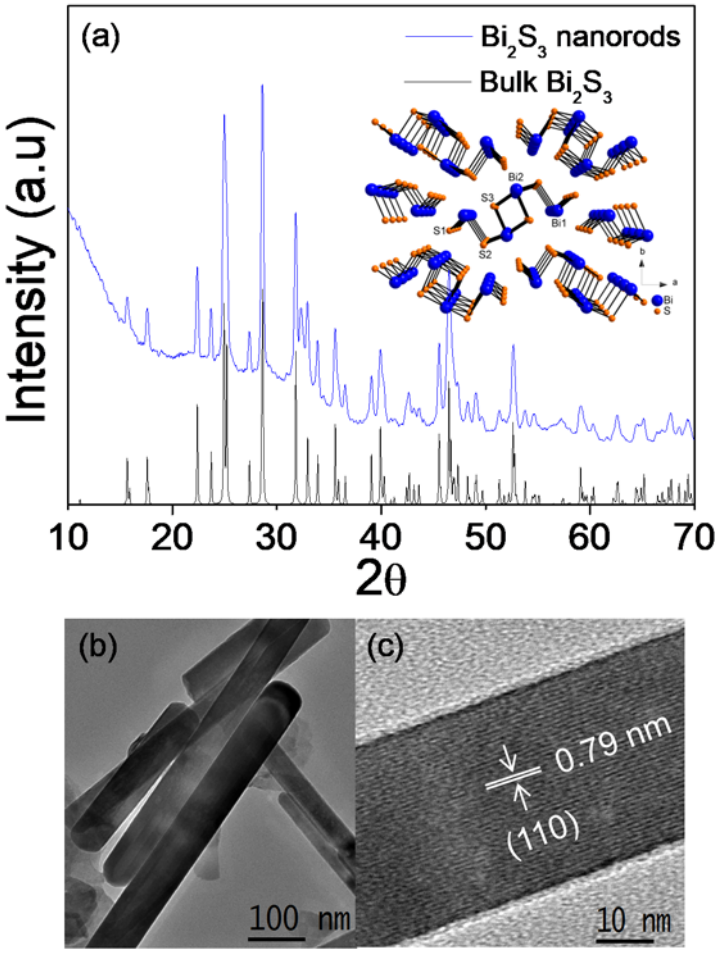

Figure 2.1.6 *a) PXRD patterns of Bi_2S_3 nanorods synthesized by the reaction of bismuth acetate and thioacetamide in [EMIM]BF_4 ionic liquid, and reported bulk Bi_2S_3. The inset shows the one-dimensional orthorhombic crystal structure of Bi_2S_3 viewed down the crystallographic c-axis. b) TEM image of Bi_2S_3 nanorods and c) HRTEM image of a Bi_2S_3 nanorod showing the (110) lattice planes.*

I have also synthesized nanorods of Bi_2S_3 by the reaction of bismuth acetate and thioacetamide in [EMIM]BF_4 ionic liquid (see methods). The

PXRD pattern of the as-synthesized Bi_2S_3 sample can be indexed on pure orthorhombic crystal structure with P*nma* space group (Figure 2.1.6(a)). Low-resolution TEM image in figure 2.1.6(b) reveals nanorods of Bi_2S_3. The anisotropic growth leading to nanorod-like morphology is favored owing to the intrinsic one-dimensional connectivity along the c-axis of the orthorhombic crystal structure of Bi_2S_3 (inset of figure 2.1.6(a)). The high-resolution TEM (HRTEM) image of a Bi_2S_3 nanorod in figure 2.1.6(c) reveals a lattice-spacing of ca. 0.79 which corresponds to d-spacing of (110) crystal lattice planes.

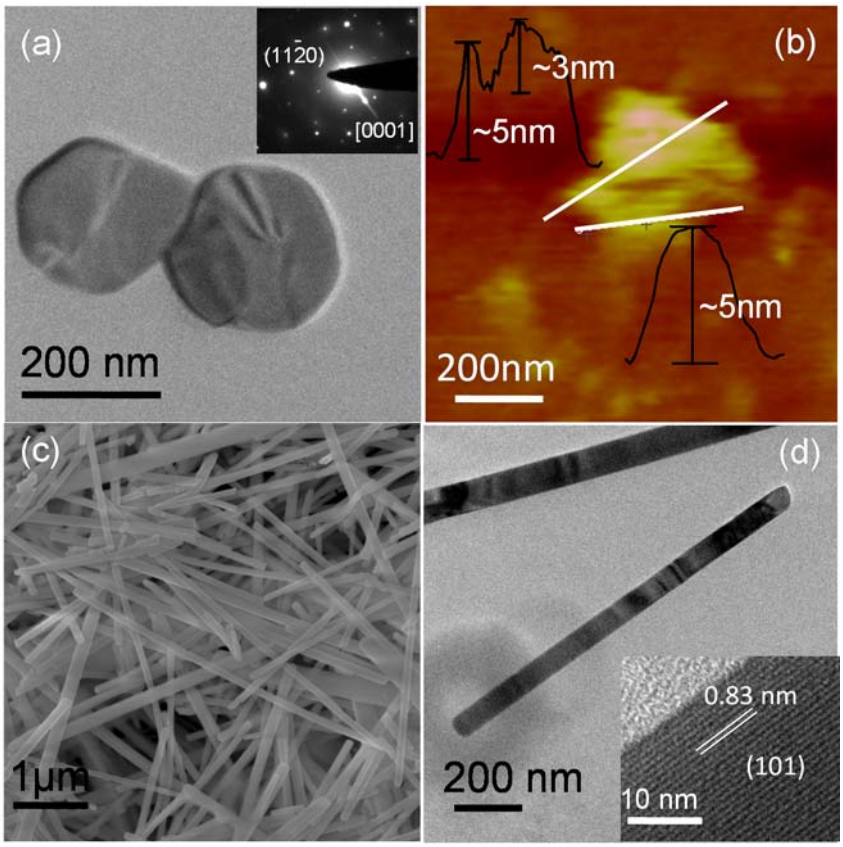

Figure 2.1.7 *a) TEM and b) AFM image of Bi_2Se_3 nanodiscs synthesized by ionothermal decomposition of single source precursor. The inset in (a) shows SAED pattern along [0001] zone axis. c) FESEM and d) TEM images of Sb_2Se_3 nanowires synthesized by ionothermal decomposition of single source precursor. Inset in (d) is a HRTEM image of the nanowire.*

I have also obtained few-layer nanodiscs of Bi_2Se_3 by the ionothermal decomposition of a single source precursor, $Bi(Se\text{-}C_6H_6N)_3$, in $[EMIM]BF_4$ ionic liquid (see methods). Figure 2.1.7(a) shows the TEM image along with an indexed selected area electron diffraction (SAED) pattern showing a projection down the [0001] zone axis. The AFM image confirms the four-layered nature

of this sample (Figure 2.1.7(b)). I have synthesized nanowires of Sb_2Se_3 by a similar ionothermal decomposition of the single source precursor, $Sb(Se\text{-}C_6H_6N)_3$, in $[EMIM]BF_4$ ionic liquid (see methods). Low-resolution TEM images in figures 2.1.7(c) and (d) reveal the nanowire morphology of the as-synthesized Sb_2Se_3. HRTEM image in the inset of figure 2.1.7(d) confirms the single crystalline nature of nanowires; an observed d-spacing of ca. 0.83 nm corresponds to (101) crystal lattice planes.

2.1.4 Conclusions

In conclusion, ultrathin few-layer (3-5) Bi_2Se_3 nanosheets have been successfully synthesized in an ionic liquid for the first time. The ionic liquid acts as an intercalating and stabilizing agent in addition to being a green solvent for the synthesis of few-layer Bi_2Se_3. Few-layer nanostructures of Bi_2Se_3 and one-dimensional nanowires of Sb_2Se_3 have also been synthesized by the thermal decomposition of single source precursors in the ionic liquid. Thus the present work shows the versatility of ionothermal synthesis. The relatively high electrical conductivity of the current ultrathin Bi_2Se_3 nanosheets is attributed to the enhanced contribution from the surface states which can offer highly mobile and scattering-resistant carriers. Low-dimensional nanostructures of TIs with a large surface-to-volume ratio provide attractive systems for transport studies as the contribution from surface carriers is much higher than that from bulk carriers. Moreover, the surface defects, nanoscale grain boundaries, and interfaces efficiently scatter the heat carrying phonons thereby decreasing κ_L in the present Bi_2Se_3 nanosheets to as low as ca. 0.4 $Wm^{-1}K^{-1}$ near room temperature.

2.1.5 References

1. D. Hsieh, D. Qian, L. Wray, Y. Xia, Y. S. Hor, R. J. Cava and M. Z. Hasan, *Nature*, 2008, **452**, 970-974.
2. D. Kong and Y. Cui, *Nat Chem*, 2011, **3**, 845-849.
3. Y. L. Chen, J. G. Analytis, J. H. Chu, Z. K. Liu, S. K. Mo, X. L. Qi, H. J. Zhang, D. H. Lu, X. Dai, Z. Fang, S. C. Zhang, I. R. Fisher, Z. Hussain and Z. X. Shen, *Science*, 2009, **325**, 178.
4. Y. Xia, D. Qian, D. Hsieh, L. Wray, A. Pal, H. Lin, A. Bansil, D. Grauer, Y. S. Hor, R. J. Cava and M. Z. Hasan, *Nat. Phys.*, 2009, **5**, 398-402.
5. K. Biswas, J. He, I. D. Blum, C.-I. Wu, T. P. Hogan, D. N. Seidman, V. P. Dravid and M. G. Kanatzidis, *Nature*, 2012, **489**, 414-418.
6. R. J. Mehta, Y. Zhang, C. Karthik, B. Singh, R. W. Siegel, T. Borca-Tasciuc and G. Ramanath, *Nat Mater*, 2012, **11**, 233-240.
7. L. Müchler, F. Casper, B. Yan, S. Chadov and C. Felser, *Phys. Status Solidi RRL*, 2013, **7**, 91-100.
8. B. Poudel, Q. Hao, Y. Ma, Y. Lan, A. Minnich, B. Yu, X. Yan, D. Wang, A. Muto, D. Vashaee, X. Chen, J. Liu, M. S. Dresselhaus, G. Chen and Z. Ren, *Science*, 2008, **320**, 634.
9. J. S. Son, M. K. Choi, M.-K. Han, K. Park, J.-Y. Kim, S. J. Lim, M. Oh, Y. Kuk, C. Park, S.-J. Kim and T. Hyeon, *Nano Lett.*, 2012, **12**, 640-647.
10. A. Soni, Z. Yanyuan, Y. Ligen, M. K. K. Aik, M. S. Dresselhaus and Q. Xiong, *Nano Lett.*, 2012, **12**, 1203-1209.
11. J. R. Sootsman, D. Y. Chung and M. G. Kanatzidis, *Angew. Chem. Int. Ed.*, 2009, **48**, 8616-8639.
12. D. Kong, W. Dang, J. J. Cha, H. Li, S. Meister, H. Peng, Z. Liu and Y. Cui, *Nano Lett.*, 2010, **10**, 2245-2250.
13. D. Kong, J. C. Randel, H. Peng, J. J. Cha, S. Meister, K. Lai, Y. Chen, Z.-X. Shen, H. C. Manoharan and Y. Cui, *Nano Lett.*, 2010, **10**, 329-333.
14. D. Teweldebrhan, V. Goyal and A. A. Balandin, *Nano Lett.*, 2010, **10**, 1209-1218.

15. G. Zhang, H. Qin, J. Teng, J. Guo, Q. Guo, X. Dai, Z. Fang and K. Wu, *Appl. Phys. Lett.*, 2009, **95**, 053114.
16. Y. Sun, H. Cheng, S. Gao, Q. Liu, Z. Sun, C. Xiao, C. Wu, S. Wei and Y. Xie, *J. Am. Chem. Soc.*, 2012, **134**, 20294-20297.
17. Y. Min, G. D. Moon, B. S. Kim, B. Lim, J.-S. Kim, C. Y. Kang and U. Jeong, *J. Am. Chem. Soc.*, 2012, **134**, 2872-2875.
18. Y. Min, J. W. Roh, H. Yang, M. Park, S. I. Kim, S. Hwang, S. M. Lee, K. H. Lee and U. Jeong, *Adv. Mater.*, 2013, **25**, 1425-1429.
19. J. Zhang, Z. Peng, A. Soni, Y. Zhao, Y. Xiong, B. Peng, J. Wang, M. S. Dresselhaus and Q. Xiong, *Nano Lett.*, 2011, **11**, 2407-2414.
20. E. Ahmed, J. Beck, J. Daniels, T. Doert, S. J. Eck, A. Heerwig, A. Isaeva, S. Lidin, M. Ruck, W. Schnelle and A. Stankowski, *Angew. Chem. Int. Ed.*, 2012, **51**, 8106-8109.
21. K. Biswas, Q. Zhang, I. Chung, J.-H. Song, J. Androulakis, A. J. Freeman and M. G. Kanatzidis, *J. Am. Chem. Soc.*, 2010, **132**, 14760-14762.
22. D. Freudenmann, S. Wolf, M. Wolff and C. Feldmann, *Angew. Chem. Int. Ed.*, 2011, **50**, 11050-11060.
23. J.-R. Li, Z.-L. Xie, X.-W. He, L.-H. Li and X.-Y. Huang, *Angew. Chem. Int. Ed.*, 2011, **50**, 11395-11399.
24. Y. Lin, W. Massa and S. Dehnen, *J. Am. Chem. Soc.*, 2012, **134**, 4497-4500.
25. Z. Ma, J. Yu and S. Dai, *Adv. Mater.*, 2010, **22**, 261-285.
26. K. Biswas and C. N. R. Rao, *Chem. Euro. J.*, 2007, **13**, 6123-6129.
27. J. Jiang, S.-H. Yu, W.-T. Yao, H. Ge and G.-Z. Zhang, *Chem. Mater.*, 2005, **17**, 6094-6100.
28. Y. Jiang, Y.-J. Zhu and G.-F. Cheng, *Cryst. Growth Des.*, 2006, **6**, 2174-2176.
29. J. Ma, Z. Liu, J. Lian, X. Duan, T. Kim, P. Peng, X. Liu, Q. Chen, G. Yao and W. Zheng, *CrystEngComm*, 2011, **13**, 3072-3079.
30. H. Hu, J. C. Martin, M. Xiao, C. S. Southworth, Y. Meng and L. Sun, *J. Phys. Chem. C*, 2011, **115**, 5509-5514.

31. M. Acik, D. R. Dreyer, C. W. Bielawski and Y. J. Chabal, *J. Phys. Chem. C*, 2012, **116**, 7867-7873.

32. Q. Ji, I. Honma, S.-M. Paek, M. Akada, J. P. Hill, A. Vinu and K. Ariga, *Angew. Chem. Int. Ed.*, 2010, **49**, 9737-9739.

33. T. E. Sutto and T. T. Duncan, *Electrochim. Acta*, 2012, **77**, 204-211.

34. M. Jonson and G. D. Mahan, *Phys. Rev. B*, 1980, **21**, 4223-4229.

CHAPTER 2.2

Green ionothermal synthesis of hierarchical nanostructures of SnS_2 and their Li-ion storage properties*

Summary

Flower-like hierarchical architectures of layered SnS_2 have been synthesized ionothermally for the first time, using water soluble [EMIM]BF_4 ionic liquid (IL) as the solvent medium. At lower reaction temperatures, the hierarchical structures are formed of few-layered polycrystalline 2D nanosheet-petals composed of randomly oriented SnS_2 nanoparticles. The supramolecular networks of IL would serve as templates on which the nanoparticles of SnS_2 are glued together by combined effects of hydrogen bonding, electrostatic, hydrophobic and imidazolium stacking interactions of the IL, giving rise to polycrystalline 2D nanosheet-petals. At higher reaction temperatures, single crystalline plate-like nanosheets with well-defined crystallographic facets are obtained due to rapid inter-particle diffusion across the IL. Efficient surface charge-screening by the IL favors the aggregation of individual nanosheets to form hierarchical flower-like architectures of SnS_2. Li-ion storage properties of the present SnS_2 samples have been examined, and the electrochemical performance of the sample synthesized at higher temperatures is found to be comparable to that reported for pristine SnS_2 samples in the literature.

*A paper based on this study has appeared in **CrystEngComm,** 2014, *16*, 3994.

2.2.1 Introduction

Ionic liquids (ILs) have emerged to be powerful, eco-friendly solvents, attracting interest in areas ranging from inorganic synthesis to energy related applications. The unique physicochemical properties of ILs, seldom found in traditional solvents, such as low melting point, negligible vapor pressure, broad liquidus range, high thermal stability and tunable solubility of both inorganic and organic compounds make them excellent green solvents for the synthesis of a variety of compounds including zeolites, open framework compounds, nanostructures of chalcogenides and metal nanoparticles.[1-15] Due to their excellent solvent characteristics that extend to biomaterials such as cellulose, IL's can have useful biofuel-cell applications.[16] Due to their electrochemical stability and negligible vapor pressure, ILs have been used for the electrodeposition of reactive metals (even above 100°C) which would otherwise be difficult to deposit from aqueous or organic solvents.[17] Non-flammability and high ionic conductivities coupled with chemical and electrochemical stabilities allow ILs to be employed as electrolytes in electrochemical energy devices such as Li-ion batteries, fuel cells, supercapacitors and thermo-electrochemical cells.[16, 18]

1,3-dialkyl imidazolium IL's organize into supramolecular polymeric networks in both solid and molten states via hydrogen bonding, electrostatic and hydrophobic interactions.[19] Long-range spatial correlations are an interesting feature of molten ILs in contrast to van der Waals organic liquids. When used as solvents, ILs can stabilize nanostructures through electrostatic and steric factors and affect their growth and organization, to yield novel morphologies. The role of ILs in the self-assembly of nanowires and nanorods has been pointed out earlier.[10, 20] Micellar vesicles formed of hydrophilic and hydrophobic constituents of IL in aqueous media serve as templates for the growth of spherical Bi_2S_3 flowers composed of nanowires.[21]

Motivated by our earlier work on the ionothermal synthesis of few-layered Bi_2Se_3 nanosheets with enhanced electronic transport properties (chapter 2.1),[7] I have employed the ionothermal approach to synthesize layered SnS_2 in a water soluble ionic liquid, 1-ethyl-3-methyl imidazolium

tetrafluoroborate ([EMIM]BF_4), as the solvent medium. Layered chalcogenides of transition metals, as well as group 14 and 15 metals such as SnS_2 and Bi_2Se_3, have shown promise in applications ranging from optoelectronics to energy generation and storage.[22-24] Layered SnS_2, constituting non-toxic and abundant elements, shows a rich portfolio of applications as photocatalysts, photoelectrodes, photoconductors and importantly as anode materials for Li-ion batteries.[25-31] I have found that the ionothermal reactions at 180 °C and 240 °C yielded hierarchical flower-like assemblies composed of 2D nanosheets of SnS_2. Through electron microscopy investigation, I have gained insights into mechanistic aspects of the IL-assisted hierarchal assembly of SnS_2 nanostructures. Supramolecular assemblies of molten IL serve as templates for the formation of 2D nanosheets and drive their assembly to form hierarchical flower-like nanostructures. I have obtained polycrystalline nanosheet-petals at lower reaction temperatures and single crystalline nanosheet-petals at higher reaction temperatures. I have also examined the Li-ion storage performance of the present SnS_2 samples. The electrochemical performance of the SnS_2 sample synthesized at higher temperatures is found to be superior to that of sample synthesized at low temperature owing to a greater degree of crystallinity in the former. I must point out that the present ionothermal synthesis of self-assembled structures of SnS_2 is first of its kind though there are reports on the synthesis of hierarchical nanostructures of SnS_2, based on either conventional solvothermal or hydrothermal synthesis.[25, 32-35]

2.2.2 Methods

2.2.2.1 Synthesis

In a typical synthesis of hierarchical nanostructures of SnS_2, $SnCl_2.2H_2O$ (50 mg, 0.22 mmol) and thioacetamide (33.3 mg, 0.44 mmol) were dissolved by ultrasonication in 3 ml of 1-ethyl-3-methyl imidazolium tetrafluoroborate ([EMIM]BF_4) ionic liquid taken in a Teflon lined autoclave of 7 ml capacity. The autoclave was maintained at 180 °C or 240 °C in a preheated hot air-oven for 12 hrs after which the autoclave was allowed to cool to the ambient temperature. The yellow colored product obtained was thoroughly centrifuged

several times with water to remove the residual ionic liquid and dried in a vacuum oven at 60 °C for 6 hrs.

2.2.2.2 Characterizations

Powder X-ray diffraction patterns of the samples were recorded using Bruker D8 Advance diffractometer using Cu Kα radiation source. Atomic force microscopy (AFM) was performed in tapping mode with antimony doped silicon tip (10 nm resolution) using Bruker Innova Microscope instrument. Transmission electron microscopy (TEM) was performed on JEOL TEM-3010 electron microscope at an accelerating voltage of 300 kV. Field emission scanning electron microscopy (FESEM) was performed on NOVA NANO SEM 600 (FEI, Germany) at an operating voltage of 15 kV.

2.2.2.3 Electrochemical measurements

For fabricating the working electrode, SnS_2 samples were mixed into a slurry with polyacetylene conducting additive and polyvinylidene fluoride (PVDF) binder in a weight ratio of 7.5:1.5:1 in 1-methyl-2-pyrrolidinone (NMP) solvent. The above slurry was coated on a disc shaped copper foils and dried overnight at 100°C in a vacuum oven. Cyclic voltammetry (CV) was performed at a scan rate of 0.25 mV s^{-1} in a potential range of 0.01-2 V *vs.* Li^+/Li, on half cells assembled of SnS_2 as working electrode, Li-metal as counter electrode and 1M $LiPF_6$ solution in a mixture of diethylene carbonate (DEC) and ethylene carbonate (EC) (1:1 vol %) as electrolyte solution. For charge-discharge cycling studies, the half cells were initially discharged from open circuit voltage and cycled between 0.01 V and 2 V *vs.* Li^+/Li at a constant current density of 100 mA g^{-1} (0.155 C, 1 C= 645 mA g^{-1}). Electrochemical impedance spectroscopy (EIS) measurements were performed on the electrodes extracted after twenty charge-discharge cycles at an applied a.c signal of 50 mV amplitude within a frequency range of 1 MHz to 1 Hz.

2.2.3 Results & discussion

α-SnS_2 adopts a CdI_2-type layered structure with a hexagonal unit cell (P-*3*m1 space group), where the octahedrally coordinated tin atoms are sandwiched

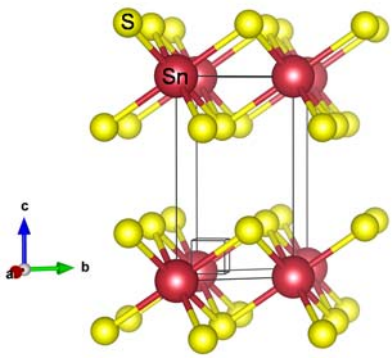

Figure 2.2.1 *CdI_2-type hexagonal crystal structure of SnS_2. The yellow and red spheres denote S and Sn atoms respectively.*

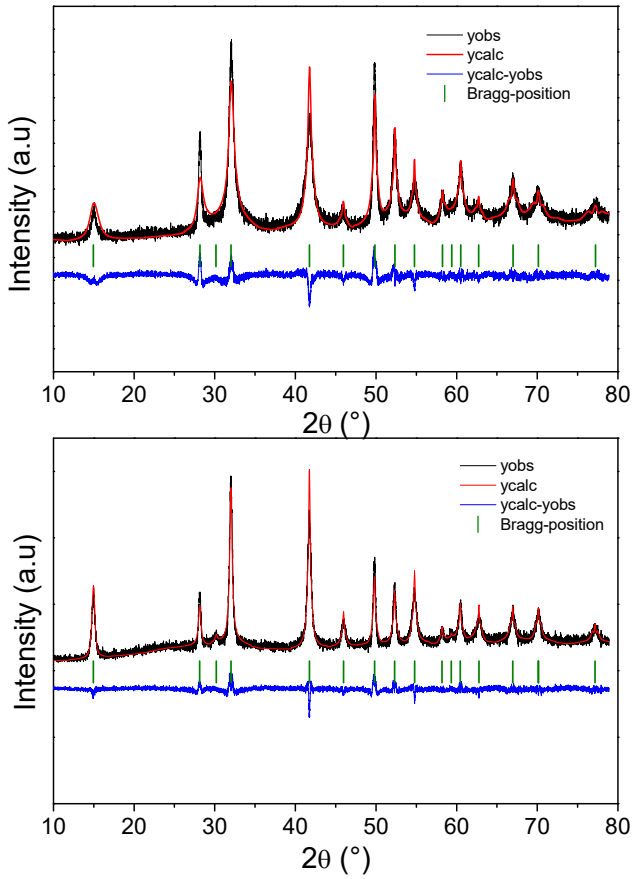

Figure 2.2.2 *Rietveld refinement of powder XRD patterns of SnS_2 flowers synthesized at (a) 180 °C (**I**) and (b) 240 °C (**II**).*

between two layers of hexagonally close packed sulfur atoms to form triple layers as shown in figure 2.2.1 with the tin and sulfur atoms having coordination numbers of 6 and 3 respectively. The triple layers are held by weak van der Waals interactions along the crystallographic *c*-direction. Figure 2.2.2 shows Rietveld refined powder X-ray diffraction (PXRD) patterns of the

samples synthesized in [EMIM]BF_4 IL at 180 °C (**I**) and 240 °C (**II**). PXRD patterns can be indexed on the pure hexagonal SnS_2 structure with no detectable impurities. The lattice parameters obtained from Rietveld refinement are a=b=3.6579(3) Å and c= 5.9249(3) Å for **I** and a=b=3.6586(4) Å and c= 5.9170(4) Å for **II**. It is to be noted that the ratio of relative intensities of (001) and (101) crystallographic planes (I_{001}/I_{101}) is 0.25 and 0.42 for **I** and **II** respectively.

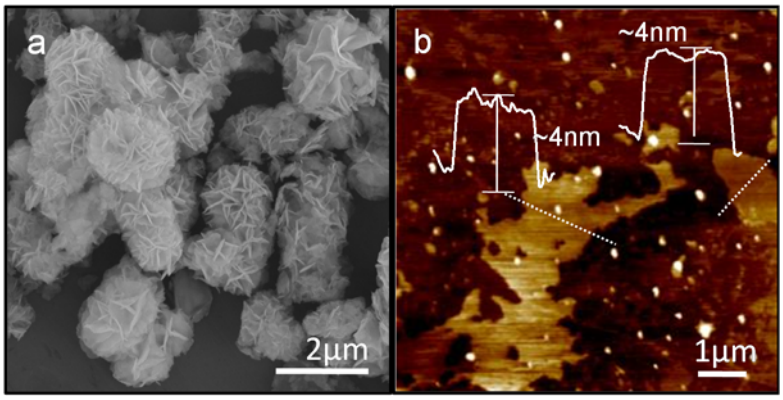

Figure 2.2.3 *(a) Low-magnification FESEM image of SnS_2 flower-like structures synthesized at 180 °C and (b) AFM image of SnS_2 petals peeled off the flower-like assembly.*

Figure 2.2.3(a) shows a field emission scanning electron microscopy (FESEM) image of SnS_2 flower-like structures synthesized at 180 °C (**I**). Figure 2.2.3(b) shows the atomic force microscope (AFM) image of the sample synthesized at 180 °C (**I**). The height profiles of fragments peeled off the flowers are found to be about 4 nm thick indicating the few-layered nature of the nanosheet-petals. Figure 2.2.4(a) shows the high magnification FESEM image of a SnS_2 flower-like structure. Flower-like morphology of self-assembled nanosheets is also revealed by the transmission electron microscopy (TEM) image in figure 2.2.4(b). The high-resolution TEM (HRTEM) image in figure 2.2.4(c) shows a bent edge of a nanosheet-petal. From the magnified view in the inset, the edge is ca. 2.4 nm thick with an average inter-layer spacing of ca. 0.59 nm which is close to the d-spacing of (002) crystallographic planes of SnS_2. The HRTEM image in figure 2.2.4(d) projects the in-plane view of a

nanosheet-petal. The nanosheet is seen to be composed of randomly oriented SnS_2 nanocrystals. The corresponding fast Fourier transformation diffraction pattern (FFTD) in the lower inset reveals the polycrystalline nature of the nanosheet. The upper inset in figure 2.2.4(d) gives a magnified view of a single nanocrystal, showing a lattice fringe-spacing of ca. 0.34 nm which corresponds to the d-spacing of crystallographic (100) planes of SnS_2.

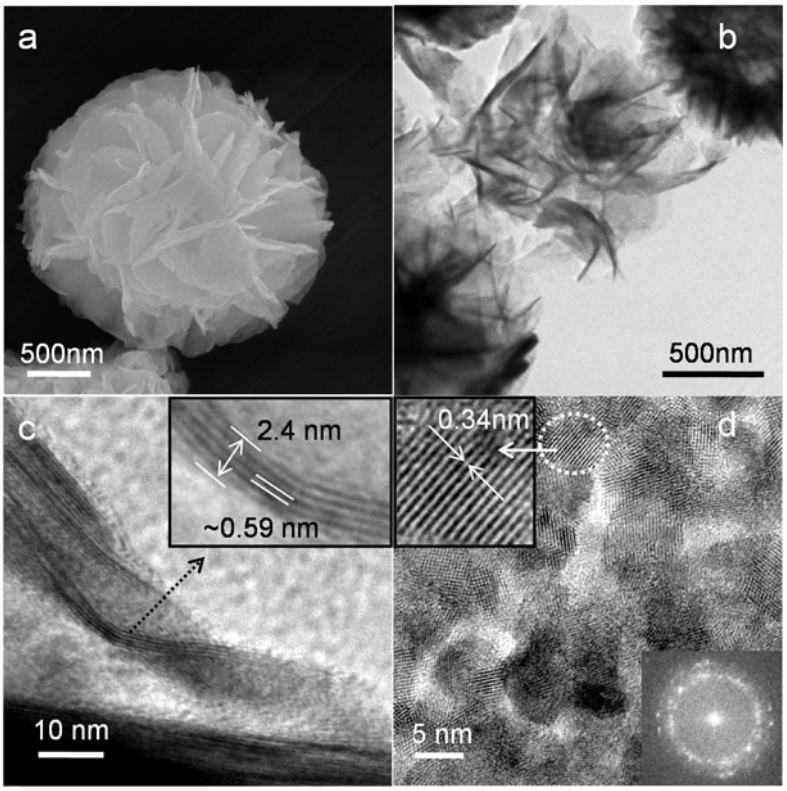

Figure 2.2.4 *(a) High-magnification FESEM and (b) low-magnification TEM images of SnS_2 flowers synthesized at 180 °C. (c) High-magnification TEM image showing a bent edge of a nanosheet-petal which is magnified in the inset. (d) HRTEM image with the indicated region magnified in the upper-left inset and the respective FFTD pattern given in the lower-right inset.*

Figures 2.2.5(a) and (b) show respectively, the FESEM and TEM images of SnS_2 sample synthesized in IL at 240 °C (**II**). The flower-like structures are seen to be formed of plate-like nanosheets as building blocks. The hexagonal edge of a protruding nanoplate is marked by a dotted line in figure 2.2.5(b). The HRTEM image in figure 2.2.5(c) gives the in-plane view of the region indicated by an arrow. The corresponding FFTD pattern in the lower inset projects a view along the [001] zone axis with the bright diffraction

spots indexed onto the (100) crystal plane. In figure 2.2.5(d), the line-profile of the boxed region in figure 2.2.5(c) shows a lattice fringe spacing of 0.31 nm corresponding to the d-spacing of (100) planes in agreement with the FFTD pattern. As apparent from the HRTEM image, the plate-like nanosheet is single crystalline with (100) planes. No intercalation of IL in-between the SnS_2 layers is observed either from PXRD or HRTEM unlike in the case of ionothermally synthesized Bi_2Se_3 nanosheets in chapter 2.1. An interlayer spacing of ca. 0.58 nm in SnS_2 (Figure 2.2.4(c), inset) is too small for intercalation of IL as compared to that of ca. 0.96 nm in Bi_2Se_3.

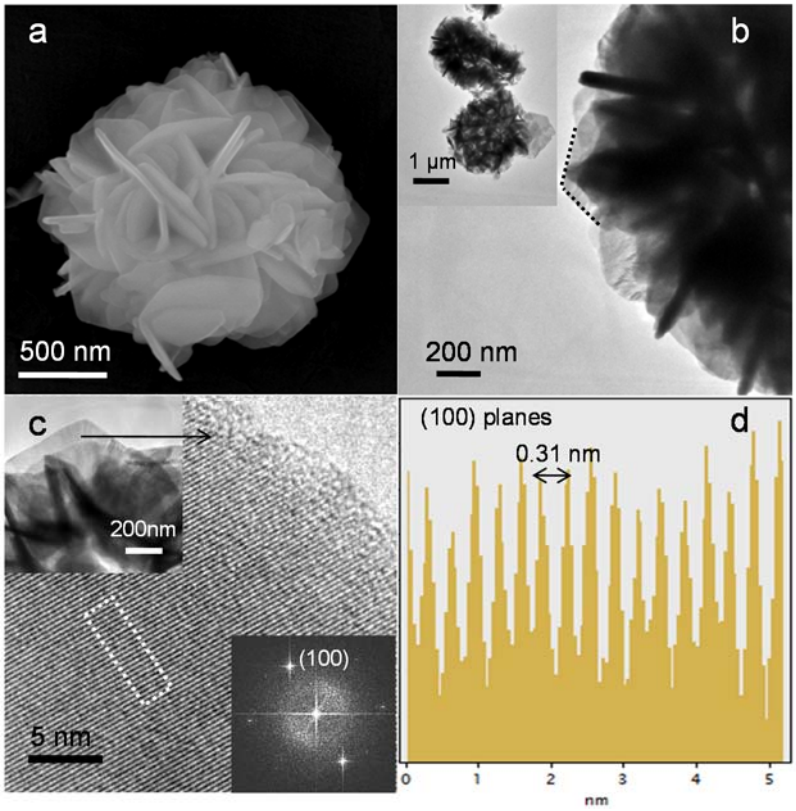

Figure 2.2.5 *(a) FESEM and (b) low-magnification TEM images of SnS_2 flowers synthesized at 240 °C; (c) high-magnification TEM image of the region indicated by an arrow along with the indexed FFTD pattern given in the lower-right inset and (d) line-profile of the boxed area in (c) showing the d-spacing of (100) lattice planes.*

In the ionothermal synthesis carried out at a lower temperature (180 °C), we have obtained few-layered polycrystalline nanosheets composed of small nanocrystals without any particular orientation (Figure 2.2.4(d)). The

question pertaining as to how nanocrystals would assemble into few-layered polycrystalline nanosheets instead of randomly agglomerating into 3D aggregates would seem intriguing at first. The traditional growth mechanisms dictating the formation of long-range architectures are based on particle-aggregation via oriented attachment and Ostwald's ripening. Schliehe *et al.* [36] have reported oriented attachment of nanocrystals to form 2D sheets of PbS. The small PbS nanocrystals attach via high energy (110) facets in an oriented fashion, resulting in single crystalline sheets. In the present synthesis at 180 °C, the oriented attachment does not seem to be the underlying mechanism of self-assembly as we have obtained polycrystalline nanosheets composed of randomly oriented nanocrystals lacking directionality. Tang *et al.* [37] have earlier reported free-floating polycrystalline CdTe sheets, self-assembled from CdTe nanocrystals. These authors suggest that self-assembly is mainly driven by dipolar and electrostatic interactions besides ligand-induced hydrophobic attractions. Xu *et al.* [23] reported the synthesis of polycrystalline nanosheets of FeS, assisted by dodecanethiol serving as a soft-template.

Molten ILs based on 1, 3-dialkyl imidazolium (DAI) cations associated with different anions (X) have been experimentally shown to form stable supramolecular assemblies of the type $[(DAI)_x(X)_{x-n})]^{n+}[(DAI)_{x-n}(X)_x)]^{n-}$ (x, n = 1, 2, 3,...and x > n) through hydrogen bonding.[19] The infrared spectrum of the neat [EMIM]BF_4 ionic liquid clearly exhibits characteristic stretching frequencies due to hydrogen bonding between imidazolium-hydrogen atoms (H2, H4, H5) and fluorine atoms of BF_4^- anion in the 3100-3200 cm^{-1} region [19, 38] These IL supramolecular networks can, therefore, act as templates to assist the nanocrystals with inherent layered structure to assemble into nanosheets. Due to the high ionic strength of ILs, the solubility of precursors is enhanced, and the tin-thioacetamide complexes can electrostatically interact with the IL assemblies. After the subsequent reaction, the SnS_2 nanoparticles formed on these planar assemblies would be held together by surrounding ionic species to organize into nanosheet-petals (Figure 2.2.4 and 2.2.6). The IL can serve as a complexing agent and alter the kinetics of nucleation and growth in favor of nucleation to give rise to small nanoparticles with inherent layered structure. The surrounding cationic and anionic aggregates of IL may passivate the

surface-dangling bonds through electrostatic stabilization and present a steric hindrance to particle coalescence at a lower reaction temperature (180 °C). It was suggested earlier that the hydrogen bonded-network in ILs is disrupted upon introduction of nanocrystals (or molecules) with an effect of formation of inclusion-type complexes where the nanocrystals are stabilized by electrostatic, and steric-effects of surrounding hydrogen bonded aggregates of IL.[19, 39] Such inclusion-type compounds of Pt(0) nanocrystals embedded in 1-butyl-3-methyl imidazolium hexafluorophosphate IL have been found by the TEM studies.[40] Through similar interactions with the surrounding IL, the so formed SnS_2 nanocrystals would be embedded in the IL network and thus held together into polycrystalline nanosheets. Resulting grain boundaries and voids are seen in the TEM image (Figure 2.2.4(d)). Furthermore, π-π stacking interactions between the imidazolium rings of IL molecules can direct the particles to assemble into a layered sheet. We conjecture that the combined effects of hydrogen bonding, electrostatic, hydrophobic and π-π stacking interactions of the IL can drive the assembly of nanoparticles into few-layered polycrystalline nanosheets. Essentially, the well-organized IL molecules serve as an ionic glue to assist the assembly of nanocrystals into nanosheets. Besides the interactions above, due to efficient electrostatic screening by the surrounding IL, surface-to-surface and edge-to-surface attachments become energetically allowed as the charge differences between the edges and surfaces of nanosheet-petals are minimized.[10] The nanosheet building blocks, therefore, tend to aggregate into flower-like assemblies, thereby completing the hierarchy.

When the reaction temperature is increased to 240 °C, apart from the increased growth rate, the interparticle diffusion across the IL polymeric network and grain boundaries becomes rapid, leading to single crystalline plate-like nanosheets (Figures 2.2.5(c) and 2.2.6). From the FESEM image in figure 2.2.5(a), we see that the plate-like nanosheets are relatively thicker with an average edge-thickness of about 32 nm owing to the increased growth rate in accordance with the higher I_{001}/I_{101} ratio in PXRD pattern. Again, due to the stabilizing effects of IL, the energy differences between the facets are minimized, favoring the aggregation of plate-like nanosheets to form flower-like assemblies. The temperature-dependent morphogenesis of flower-like

assemblies of SnS_2 is depicted schematically in figure 2.2.6. Such temperature-dependent evolution from polycrystalline nanosheets to single crystalline nanoplates has been earlier reported for FeS by Xu *et al.* where the dodecanethiol as the sulfur source also served as a bilayer lamellar template.[23]

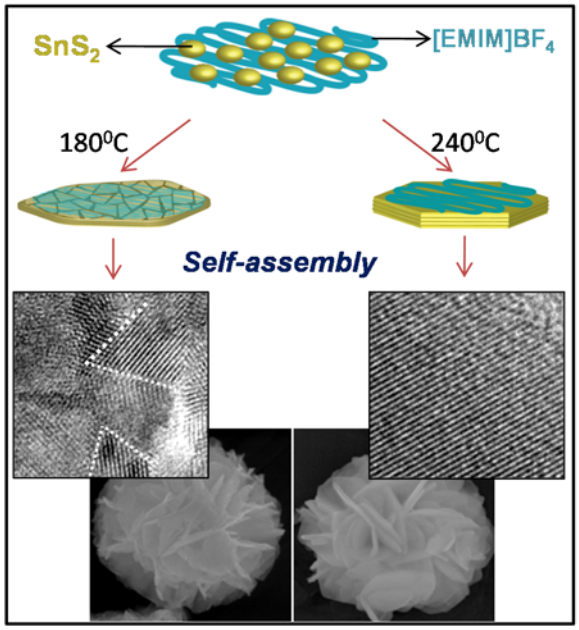

Figure 2.2.6 *Schematic depiction of ionic liquid assisted bottom-up hierarchical assembly of SnS_2 flowers at 180 °C and 240 °C.*

SnS_2 is practically superior to commercial graphite (372 mAh g^{-1}) as an anode material for Li-ion battery applications due to its higher theoretical capacity (645 mAh g^{-1}).[41] In principle, owing to higher volumetric energy density, hierarchical architectures organized from nanoscale building blocks could be superior to free standing nanosheets and nanoplates for Li-ion battery applications. It has been shown that hierarchical structures of SnS_2 are favorable hosts for Li-intercalation/deintercalation as they can accommodate concomitant large volume changes and mitigate the fracture and capacity degradation.[32] The high collective electroactive surface area and percolation networks in the hierarchical architectures can facilitate efficient Li-ion insertion and shorten the Li-ion diffusion lengths.[25] We have examined the Li-ion storage properties of the as-prepared pristine SnS_2 samples. The proposed electrochemical reactions between SnS_2 and lithium ions are as follows: [42, 43]

$$SnS_2 + 4Li^+ + 4e^- \rightarrow Sn + 2Li_2S \quad 2.2.1$$

$$Sn + xLi^+ + xe^- \leftrightarrow Li_xSn\ (0 \leq x \leq 4.4) \quad 2.2.2$$

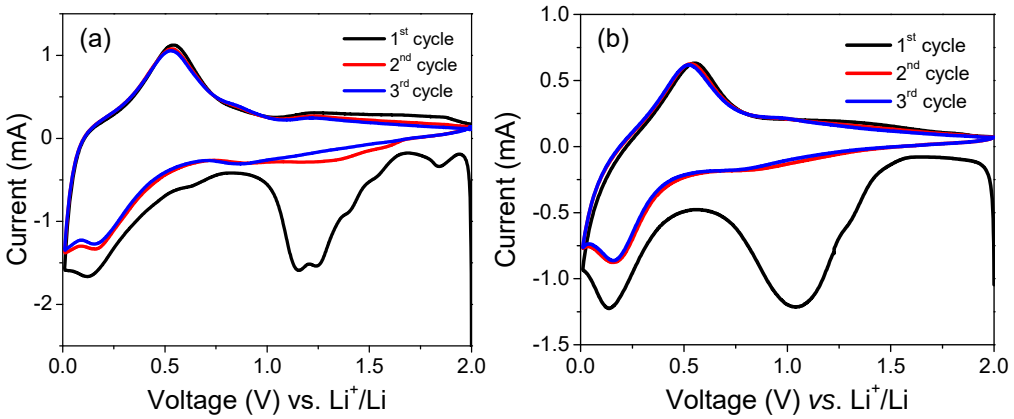

Figure 2.2.7 *Cyclic voltammograms of SnS_2 flowers synthesized at a) 180 °C (**I**) and b) 240 °C (**II**).*

Figures 2.2.7(a) and (b) show the cyclic voltammograms (CV) of SnS_2 samples synthesized at 180 °C and 240 °C respectively, measured at a scan rate of 0.25 mV s^{-1} in the voltage range of 0.01-2 V *vs.* Li^+/Li. A broad irreversible cathode peak in the first scan between 1.1-1.3 V is ascribed to the irreversible decomposition of SnS_2 into metallic Sn and Li_2S (Equation 2.2.1).[44] The reversible cathodic peak in the 0.14-0.16 V range and anodic peak in the 0.5-0.6 V range correspond to the reversible alloying and dealloying reactions respectively as given by equation 2.2.2.[25, 32] The solid electrolyte interface (SEI) also forms around 1 V.[45] Cycling studies were performed on the SnS_2 samples synthesized at 180 °C (**I**) and 240 °C (**II**) with a lithium metal-counter electrode between 0.01 V and 2 V at a constant current density of 100 mA g^{-1} (0.155 C rate, 1 C= 645 mA g^{-1}). The charge-discharge curves (voltage vs. specific capacity) of samples **I** and **II** are shown in figures 2.2.8(a) and (b) respectively. The first discharge curve reveals a plateau at ca. 1.1 V corresponding to the irreversible decomposition of SnS_2 in agreement with the respective CV. The cycle-life behavior of the samples I and II is shown in figure 2.2.9(a). The first discharge cycle reveals a large discharge capacity of 1540 mAh g^{-1} for **I** and 1423 mAh g^{-1} for **II** due to contributions from the irreversible decomposition of SnS_2 into metallic tin and the subsequent formation of Li-Sn alloy (equations

2.2.1 and 2.2.2). [27, 39] These values are higher than the sum of the theoretical reversible capacity of 645 mAh g^{-1} and the irreversible capacity of 587 mAh g^{-1}.[41] Surface defects and dangling bonds in our flower-like SnS_2 samples can promote side reactions leading to additional irreversible trapping of lithium. In the presence of Li-ion salts, reduction of the alkyl carbonates in the electrolyte solution at about 1 V to form a passivating layer called solid electrolyte interface (of $ROCO_2Li$, ROLi moieties) also leads to excess irreversible capacity loss.[45] The discharge capacities of the second cycle are about 560 mAh g^{-1} and 557 mAh g^{-1} for **I** and **II** respectively, corresponding to ca. 87 % and 86.2 % respectively of the maximum theoretical reversible capacity. The average discharge capacity over 50 cycles is ca. 417 mAh g^{-1} for **I** and ca. 458 mAh g^{-1} for **II**.

Coulombic efficiency for both the samples is initially low due to the irreversible decomposition of SnS_2 and SEI formation during the first cycle but maintains above 96 % after the 10th cycle (Figure 2.2.9(a)). The discharge capacity was retained above 48 % and 65 % of the first reversible discharge capacity for **I** and **II** respectively, after 50 cycles.

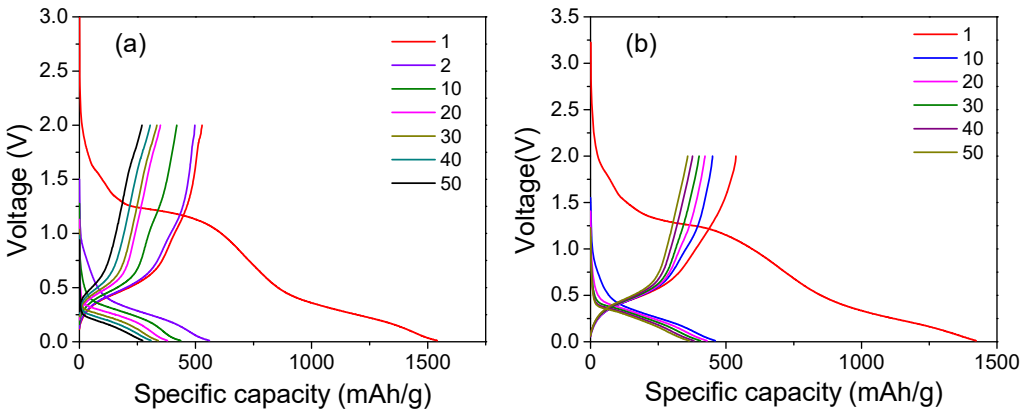

Figure 2.2.8 *Charge/discharge profiles of SnS_2 flowers synthesized at a) 180 °C and b) 240 °C; legends denote the number of charge/discharge cycles.*

The relative electrochemical performances can be explained by the degree of crystallinity which is higher for the sample synthesized at a higher temperature (**II**) compared to that of the sample synthesized at a lower temperature (**I**). Electron scattering at the grain boundaries and defects in the polycrystalline sample (**I**) can hamper the electronic conduction resulting in a

reduced cycle-life performance in this sample as compared to the sample **II** composed of single crystalline nanoplates. Electrochemical impedance spectroscopy (EIS) can probe the changes in the charge transfer resistance of the cell as a function of time. Figure 2.2.9(b) shows the Nyquist plots of working electrodes extracted after twenty charge-discharge cycles. The diameter of the semicircle in the Nyquist plot is, in general, proportional to the summation of charge transfer resistance, solid-electrolyte interfacial resistance and contact resistance.[44] As apparent from figure 2.2.9(b), the resistance of sample **I**-electrode is higher than that of sample **II**-electrode**.** The overall resistance depends partially upon morphological changes which may be induced due to changes in the volume during Li-intercalation and de-intercalation processes. The relatively large morphological changes and permanent Li-ion trapping in the voids of nanosheets can plausibly lead to rapid capacity fading in our polycrystalline sample synthesized at 180 °C (**I**) as compared to sample synthesized at 240 °C (II).The FESEM images of the spent electrodes extracted after twenty charge-discharge cycles reveal that the original flower-like morphology is retained to a larger extent in sample **II** as compared to sample **I** (Figure 2.2.10) leading to a better performance of the former compared to the latter.

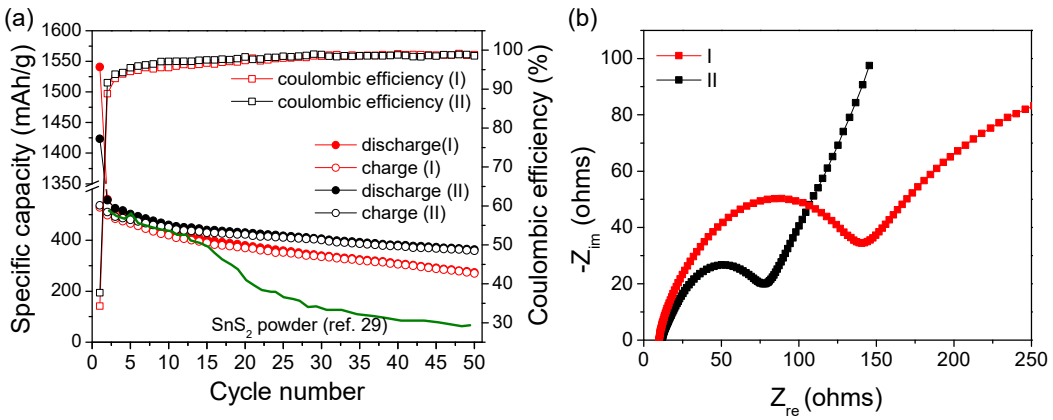

Figure 2.2.9 *(a) Cyclability and Coulombic efficiencies of SnS_2 flowers synthesized at 180 °C (**I**) and 240 °C (**II**). Discharge capacity of SnS_2 powders (ref. 29) as a function of number of cycles is also given for comparison (solid green curve). (b) Nyquist plots of SnS_2 flowers synthesized at 180 °C (**I**) and 240 °C (**II**) at the end of twenty charge-discharge cycles.*

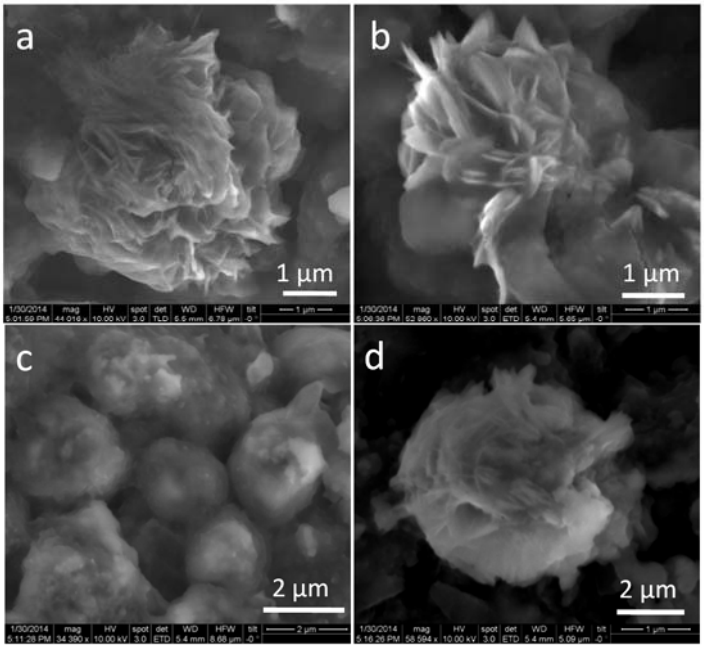

Figure 2.2.10 *FESEM images of spent electrodes comprising SnS_2 flowers synthesized at a) 180 °C and b) 240 °C after the first cycle of CV; (c, d) respective FESEM images of electrodes extracted after twenty charge-discharge cycles.*

A discharge capacity of 537 mAh g^{-1} with 69% capacity retention after 50 cycles at 0.1 C rate is previously reported for pristine flower-like SnS_2. [34] Under similar conditions, our sample synthesized at 240 °C (**II**) shows 557 mAh g^{-1} discharge capacity with 65 % retention after 50 cycles at 0.155 C rate. A higher discharge capacity is reported for SnS_2 microspheres, but the capacity retention is only ca. 52 % after 50 cycles. [35] Also, a reversible discharge capacity of 526 mAh g^{-1} with 63 % retention after 100 cycles at 0.6 C rate is reported for pristine SnS_2 flower-like structures.[25] On the other hand, in contrast with sample **II**, bare SnS_2 nanoplates showed an inferior performance with a reversible discharge capacity of 504 mAh g^{-1} and 54 % retention at 0.07 C rate[44] while SnS_2 powders exhibited a drastically decaying capacity due to severe pulverization[29] (see the solid green curve in figure 2.2.9(a)). It suggests the benefits of flower-like morphologies of the present samples. The large interlayer spacing of ca. 0.57 nm in SnS_2 nanosheets (see figure 2.2.4(c), inset) is advantageous for the diffusion of lithium ions in-between the layers, provides greater accessibility to the active sites, and facilitates the subsequent alloying

and dealloying processes. The hollow spaces in the flower-like assemblies can also cushion the volumetric strain during alloying and dealloying processes.

It is to be noted, however, that the hetero-composites of SnS_2 with conducting carbon or graphene exhibit higher conductivity and synergistic effects leading to greater capacity and durability. [25, 44-47] Incorporation of carbon into the active component (SnS_2) in a suitable configuration under the present ionothermal synthesis conditions is non-trivial as it involves several optimizations of synthesis parameters which would eventually have a tremendous impact on the electrochemical performance. Though the electrochemical performance of sample **II** is comparable to that of earlier reports based on hierarchical structures of pristine SnS_2, the present work primarily emphasizes the ionothermal route of synthesis and the role of eco-friendly IL solvent on the growth of anisotropic SnS_2. We believe that the ionothermal route can be extended to the synthesis of several other functional materials with novel morphologies.

2.2.4 Conclusions

Hierarchical nanostructures of layered SnS_2 have been ionothermally synthesized in the green IL solvent, [EMIM]BF_4. Supramolecular hydrogen bonded networks in IL assist the nanocrystals of SnS_2 in assembling into nanosheet-petals. Efficient charge-screening by IL favors the aggregation of nanosheets into flower-like assemblies of SnS_2. A temperature-dependent evolution from polycrystalline to single crystalline nanosheet building blocks occurs due to rapid inter-particle diffusion across the IL at higher temperatures. The pristine samples of SnS_2 have been tested for Li-ion storage performance. The relatively poor electrochemical performance of the polycrystalline sample (**I**) is attributed to the electron scattering and Li-ion trapping at the grain boundaries as well as defects, compounded by adverse morphological changes during cycling. The single crystalline sample (**II**), on the other hand, exhibits an overall performance comparable to that reported in the literature for pristine SnS_2. The present report primarily aims at drawing interest of a broader community to further explore the unique properties of

alternative IL-based green solvents in the inorganic synthesis of functional materials with novel morphologies.

2.2.5 References

1. J. Ma, X. Duan, J. Lian and W. Zheng, *CrystEngComm*, 2013.
2. D. Freudenmann, S. Wolf, M. Wolff and C. Feldmann, *Angew.Chem. Int. Ed.*, 2011, **50**, 11050-11060.
3. R. E. Morris, *Angew. Chem. Int. Ed.*, 2008, **47**, 442-444.
4. Z. Ma, J. Yu and S. Dai, *Adv. Mater*, 2010, **22**, 261-285.
5. E. Ahmed, J. Breternitz, M. F. Groh and M. Ruck, *CrystEngComm*, 2012, **14**, 4874-4885.
6. K. Biswas, Q. Zhang, I. Chung, J.-H. Song, J. Androulakis, A. J. Freeman and M. G. Kanatzidis, *J. Am. Chem. Soc.*, 2010, **132**, 14760-14762.
7. M. K. Jana, K. Biswas and C. N. R. Rao, *Chem. Eur. J.*, 2013, **19**, 9110-9113.
8. K. Biswas and C. N. R. Rao, *Chem. Eur. J.*, 2007, **13**, 6123-6129.
9. J. Dupont, G. S. Fonseca, A. P. Umpierre, P. F. P. Fichtner and S. R. Teixeira, *J. Am. Chem. Soc.*, 2002, **124**, 4228-4229.
10. N. Recham, L. Dupont, M. Courty, K. Djellab, D. Larcher, M. Armand and J. M. Tarascon, *Chem.Mater.*, 2009, **21**, 1096-1107.
11. Y. Lin, W. Massa and S. Dehnen, *J. Am. Chem. Soc.*, 2012, **134**, 4497-4500.
12. J.-R. Li, Z.-L. Xie, X.-W. He, L.-H. Li and X.-Y. Huang, *Angew.Chem. Int. Ed.*, 2011, **50**, 11395-11399.
13. E. Ahmed and M. Ruck, *Angew.Chem. Int. Ed.*, 2012, **51**, 308-309.
14. R. Li, J. Du, Y. Luan, H. Zou, G. Zhuang and Z. Li, *CrystEngComm*, 2012, **14**, 3404-3410.
15. K. Biswas, I. Chung, J.-H. Song, C. D. Malliakas, A. J. Freeman and M. G. Kanatzidis, *Inorg. Chem.*, 2013, **52**, 5657-5659.
16. M. Armand, F. Endres, D. R. MacFarlane, H. Ohno and B. Scrosati, *Nat. Mater*, 2009, **8**, 621 - 629.
17. Q. X. Liu, S. Z. El Abedin and F. Endres, *Surf. Coat.Tech.*, 2006, **201**, 1352-1356.

18. J. F. Wishart, *Energy Environ. Sci.*, 2009, **2**, 956-961.
19. J. Dupont, *J. Braz. Chem. Soc.*, 2004, **15**, 341-350.
20. S. S. Mali, C. A. Betty, P. N. Bhosale, R. S. Devan, Y.-R. Ma, S. S. Kolekar and P. S. Patil, *CrystEngComm*, 2012, **14**, 1920-1924.
21. J. Jiang, S.-H. Yu, W.-T. Yao, H. Ge and G.-Z. Zhang, *Chem.Mater.*, 2005, **17**, 6094-6100.
22. U. Maitra, U. Gupta, M. De, R. Datta, A. Govindaraj and C. N. R. Rao, *Angew.Chem. Int. Ed.*, 2013, **52**, 1-6.
23. C. Xu, Y. Zeng, X. Rui, N. Xiao, J. Zhu, W. Zhang, J. Chen, W. Liu, H. Tan, H. H. Hng and Q. Yan, *ACS Nano*, 2012, **6**, 4713-4721.
24. A. Soni, Z. Yanyuan, Y. Ligen, M. K. K. Aik, M. S. Dresselhaus and Q. Xiong, *Nano Lett.*, 2012, **12**, 1203-1209.
25. M. He, L.-X. Yuan and Y.-H. Huang, *RSC Adv.*, 2013, **3**, 3374-3383.
26. J. Ma, D. Lei, L. Mei, X. Duan, Q. Li, T. Wang and W. Zheng, *CrystEngComm*, 2012, **14**, 832-836.
27. J.-w. Seo, J.-t. Jang, S.-w. Park, C. Kim, B. Park and J. Cheon, *Adv. Mater*, 2008, **20**, 4269-4273.
28. Y. Sun, H. Cheng, S. Gao, Z. Sun, Q. Liu, Q. Liu, F. Lei, T. Yao, J. He, S. Wei and Y. Xie, *Angew. Chem. Int. Ed.*, 2012, **51**, 8727-8731.
29. C. Zhai, N. Du and H. Z. D. Yang, *Chem.Commun*, 2011, **47**, 1270-1272.
30. H. Zhong, G. Yang, H. Song, Q. Liao, H. Cui, P. Shen and C.-X. Wang, *J. Phys. Chem. C*, 2012, **116**, 9319-9326.
31. A. Kuhn, T. Holzmann, J. Nuss and B. V. Lotsch, *J. Mater. Chem. A*, 2013.
32. S. Liu, X. Yin, L. Chen, Q. Li and T. Wang, *Solid State Sciences*, 2010, **12**, 712-718.
33. J. Zai, K. Wang, Y. Su, X. Qian and J. Chen, *J. Power Sources.*, 2011, **196**, 3650-3654.
34. Y. Zou and Y. Wang, *Chemical Engineering Journal*, 2013, **229**, 183-189.
35. D. Lei, M. Zhang, B. Qu, J. Ma, Q. Li, L. Chen, B. Lu and T. Wang, *Electrochim. Acta*, 2013, **106**, 386-391.

36. C. Schliehe, B. H. Juarez, M. Pelletier, S. Jander, D. Greshnykh, M. Nagel, A. Meyer, S. Foerster, A. Kornowski, C. Klinke and H. Weller, *Science*, 2010, **329**, 550-553.

37. Z. Tang, Z. Zhang, Y. Wang, S. C. Glotzer and N. A. Kotov, *Science*, 2006, **314**, 274-278.

38. S. A. Katsyuba, P. J. Dyson, E. E. Vandyukova, A. V. Chernova and A. Vidis, *HELVETICA CHIMICA ACTA*, 2004, **87**, 2556-2565.

39. U. Schroder, J. D. Wadhawan, R. G. Compton, F. Marken, P. A. Z. Suarez, C. S. Consorti, R. F. de Souza and J. Dupont, *New J. Chem.*, 2000, **24**, 1009-1015.

40. C. W. Scheeren, G. Machado, J. Dupont, P. F. P. Fichtner and S. R. Texeira, *Inorg. Chem.*, 2003, **42**, 4738-4742.

41. T. Brousse, S. M. Lee, L. Pasquereau, D. Defives and D. M. Schleich, *Solid State Ionics*, 1998, **113-115**, 51-56.

42. T. Momma, N. Shiraishi, A. Yoshizawa, T. Osaka, A. Gedanken, J. Zhu and L. Sominski, *J. Power Sources*, 2001, **97-98**, 198-200.

43. T.-J. Kim, C. Kim, D. Son, M. Choi and B. Park, *J. Power Sources*, 2007, **167**, 529-535.

44. B. Luo, Y. Fang, B. Wang, J. Zhou, H. Song and L. Zhi, *Energy Environ. Sci.*, 2012, **5**, 5226-5230.

45. Y. Du, Z. Yin, X. Rui, Z. Zeng, X.-J. Wu, J. Liu, Y. Zhu, J. Zhu, X. Huang, Q. Yan and H. Zhang, *Nanoscale.*, 2013, **5**, 1456-1459.

46. L. Zhuo, Y. Wu, L. Wang, Y. Yu, X. Zhang and F. Zhao, *RSC Adv.*, 2012, **2**, 5084-5087.

47. X. Jiang, X. Yang, Y. Zhu, J. Shen, K. Fan and C. Li, *J. Power Sources.*, 2013, **237**, 178-186.

PART 3

Liquid-liquid interfacial synthesis of nanocrystalline films of heavy metal chalcogenides and their use as near-infrared photodetectors.

CHAPTER 3.1

Near infrared detectors based on HgSe and HgCdSe quantum dots generated at the liquid-liquid interface*

Summary

Thin-films of HgSe and $Hg_{0.5}Cd_{0.5}Se$ quantum dots (QDs) are synthesized at room temperature by a novel liquid-liquid interfacial reaction, and their photodetection properties in the near-infrared region are investigated. The photodetection properties of our Te-free systems are found comparable with those of the previously reported QD based visible-infrared detectors, especially HgTe. The present synthesis indicates the cost-effectiveness of selenium based near-infrared detectors owing to abundance and low cost of selenium relative to tellurium. In-situ X-ray reflectivity and ex-situ grazing incidence X-ray scattering studies were carried out on the interfacial HgSe films at different reaction times. These studies show that random HgSe clusters with an average diameter of ca. 4.4 nm are initially formed which subsequently self-organize into face-centered cubic superstructures giving rise to intense reflections normal to the interface. The large coherent domains of these reflections (> 100 nm) provide direct evidence for self-organization via contact-epitaxy.

*Papers based on this study have appeared in **J. Mater. Chem. C,** 2013, *1,* 6184 *and **J. Phys. Condense. Matter**,* 2017, *29*, 095101.

3.1.1 Introduction

Mercury cadmium telluride (HgCdTe) is one of the earliest known infrared (IR) photodetectors[1] with broad tunability in the IR absorption range.[2] It is used commercially in FTIR spectrophotometers, wireless communication and night surveillance. Epitaxial routes adopted for the synthesis of HgCdTe films and other photodetectors have some limitations besides being expensive. Problems such as lattice mismatch and substrate incompatibility have made it necessary to explore simple solution-processed photodetectors based on colloidal quantum dots (QDs).[3-6] Although bulk mercury chalcogenides in zinc blende structure are semimetals with inverted (negative) band gaps,[7] quantum confinement in the nano regime renders them narrow band gap semiconductors with tunable band structure.[8] The calculated exciton diameter is ca. 28 nm for HgSe which is significantly larger than that of ca. 6.7 nm for CdSe.[9] The large exciton diameter of HgSe in the nano regime enables the tailoring of IR absorption to suit specific interests in photodetection and imaging. Recently, a solution-processed PbS QD device has been shown to be superior to the state-of-art IR detectors based on epitaxial films of InGaAs.[10] Solution-grown HgTe QDs have been explored for near to mid-IR photodetection.[11-13] Te is scarce in the Earth's crust and is much more expensive than Se.[14] Replacing Te with abundant Se would be, therefore, desirable to produce cost-effective photodetectors. Solvothermal chemical synthesis of HgSe colloids has been reported,[9, 15] but to my knowledge, their photodetection properties have not been investigated hitherto.

In the present chapter, I have employed a novel strategy, i.e., liquid-liquid interfacial synthesis to obtain nanocrystalline films of HgSe and $Hg_{0.5}Cd_{0.5}Se$ at the toluene-water interface near room temperature, starting with selenourea in the aqueous phase, and Hg-cupferronate or a solid solution of Hg- and Cd-cupferronates in the toluene layer. The formation of the nanocrystalline film at the interface is very rapid and occurs within a few minutes. For the first time, we have investigated the near-IR detection properties of drop-casted devices based on HgSe and $Hg_{0.5}Cd_{0.5}Se$ QDs synthesized by this novel route. Furthermore, we have carried out synchrotron

X-ray reflectivity and grazing incidence X-ray scattering studies on interfacial HgSe films to probe the growth and self-organization at the toluene-water interface.

The following section briefs on the liquid-liquid interfacial synthesis and few aspects thereof and provides a necessary background for the current part of the thesis.

3.1.1.1 Liquid-liquid interfacial reactions

Interfaces between two immiscible liquids have emerged as novel non-homogeneous platforms for the synthesis of functional materials.[16-23] The thin emulsive region around the liquid interface with controlled super-saturation of precursors can serve as a constrained growth medium to give rise to unusual morphologies of the deposits.[24] The unique thermodynamic properties of liquid interfaces such as interfacial tension and viscosity can stabilize metastable phases under moderate conditions. For instance, hemihedral PbS crystallites bound by high energy (113) facets[25] and metastable phases such as zinc blend CdS and wurtzite ZnS could be deposited at the organic-aqueous interfaces.[26, 27] Significant efforts have gone into studying several phenomena associated with the liquid-liquid interfacial self-assembly such as dipolar repulsions induced by asymmetric charging of particulates, and capillary attractions engendered by contact angle hysteresis, electrical stresses, and electro-dipping forces.[28-33] Recently, in-situ x-ray scattering studies have been demonstrated to directly probe into the formation and temporal evolution of nanoscale aggregates at the organic-aqueous interface.[34-36]

Structure of liquid-liquid Interface

The interface between two immiscible liquids is difficult to illustrate for it is dynamic and time-dependent. With the help of advanced spectroscopic and diffraction techniques in combination with molecular dynamics and theoretical studies, the liquid-liquid interface can now be best viewed as a sharp boundary roughened by thermal capillary waves whose width is estimated from the expression:[37]

$$\sigma^2 \approx \frac{k_B\, T}{2\pi\gamma} log\left(\frac{q_{max}}{q_{min}}\right) \qquad 3.1.1$$

where γ is the interfacial tension, q is the plane wavevector of the capillary waves and T is the temperature. Equation 3.1.1 is phenomenological and includes the intrinsic width of the interface in addition to broadening caused by capillary waves. The widths obtained from equation 3.1.1 are dynamic and are dependent on timescale of observation.

Adsorption of solid particulates at the interface

Solid particles can act as conventional surfactants and form ''Pickering emulsions''. They adhere to the liquid-liquid interface and lower the area of unfavorable contact between the two immiscible liquids. The adsorption energy (ΔG) of a particle is dependent on it's a) surface area, b) contact angle (θ) between particle's surface and the two liquids and c) interfacial tension (γ). For a spherical particle, ΔG is given by:[22]

$$\Delta G = \pi r^2 \, \gamma(1 - cos\theta)^2 \qquad 3.1.2$$

From the above equation, strongest adsorption is obtained when $\theta = 90°$. Other factors that promote adsorption are larger interfacial tension between the two liquids and bigger particulates (limited by gravity). For a micrometer-sized particle, ΔG can exceed thermal energy (k_BT) by several orders of magnitude and that means, in principle, they can be irreversibly bound to the interface. On the other hand, the stability (ΔG) of non-spherical nanoparticles at the liquid-liquid interface is also strongly dependent on the geometry as well as orientation of particle.

Interaction between solid particles at the interface

Solid particles adsorbed at the oil-water interface are usually set upon by capillary, Coulomb and thermal forces. The overall strength and effectiveness of these forces are dependent on the properties of the interface as well as particles.

A) *Interface-deformation and capillary-attractions:* A spherical particle adopts an equilibrium position normal to the liquid-liquid interface to match the three-phase (liquid-liquid and particle-liquid) equilibrium contact line. The contact angle (θ) is a function of the surface energies of the particle–liquid and liquid-liquid interfaces. Changes in these surface energies will favour higher or lower

contact angles, and the spherical particle will adjust its height while the interface always remains flat. On the other hand, it is not possible for an anisotropic particle to satisfy the three-phase contact angle over its entire perimeter without deforming the interface. Such an interface-deformation creates excess surface area and hence, higher energy. The equilibrium position of such an anisotropic particle will reflect a minimization of the overall deformation, in which some areas bend down and others rise up. The consequence of this deformation is a long-range "capillary force" that brings particles together to minimize the local interfacial deformation and hence, the area of liquid–liquid interface.[38]

B) *Asymmetric charging and dipole-repulsion:* When there is a mismatch in the dielectric constants of the two adjacent fluids, asymmetric charging can occur leading to dipolar-repulsion of particles. Since a nonpolar solvent cannot sustain charges as much as a polar aqueous solvent, surface charges of adsorbed particles accumulate on the aqueous side and combine with the screening ions in the aqueous medium to produce an effective dipole moment in the particle. When the interface is confined, a strong long-range dipolar-repulsion between the particles leads to long-range ordered structures of the kind first reported by Pieranski.[33] Sometimes, for colloidal particles with size ranging from tens of nano meters to millimeters, a short- to medium-range capillary attraction can arise from the electro-dipping force.[32] The latter occurs due to the difference between integral electric forces at the oil-particle and particle-water interfaces and acts as a downward thrust to deform the interface.

C) At shorter ranges, Van der Waals attractive forces tend to dominate. Also, thermal fluctuations can cause interactions of the attractive type which lower the free energy of the interface when two particles approach. Although such thermal forces are thought to be too small for the larger particulates, they can be important particularly for very small nanoparticles.

Inexpensive fabrication, low temperature-processing, and compatibility with large-area and flexible substrates are becoming increasingly desirable for electronic and optoelectronic applications. Solution-processable colloidal

nanocrystal (CNC) granular solids have thus become extremely expedient over conventional epitaxial thin films owing to drawbacks associated with the latter such as high-cost, high deposition temperatures, and substrate-mismatch. Alternatively, liquid-liquid interfacial reactions can constitute a facile and efficient route to the bottom-up fabrication of granular and in some cases, single crystalline films[39] under ambient conditions without requiring a solid substrate. Large lateral dimensions may render interfacial films suitable for practical applications. Formation of thin films via reactions at liquid-liquid interfaces involves nucleation followed by simultaneous growth and assembly, unlike schemes where the self-assembly is achieved by either post-synthetic solvent evaporation[40] or pressure induced coalescence at elevated temperatures.[41] Liquid-liquid interfacial reactions and the self-assembly can occur even at room temperature, the driving force being the lowering of interfacial tension between the two immiscible liquids through formation of the so-called 'Pickering emulsions' with the particulates.[22] Nanocrystalline films of plasmonic metals, metal hydroxides, and a few transition metal chalcogenides have been successfully synthesized at the organic-aqueous interface.[28, 29]

3.1.2 Methods

3.1.2.1 Synthesis

Mercury cupferronate ($Hg(cup)_2$) or mercury cadmium cupferronate ($Hg_{0.5}Cd_{0.5}(cup)_2$) was used as Hg or Hg-Cd sources and selenourea, as the selenium source to prepare mercury selenide (HgSe) and mercury cadmium selenide ($Hg_{0.5}Cd_{0.5}Se$) QDs. $Hg(cup)_2$ was prepared by adding aqueous cupferron solution to the aqueous $HgCl_2$ solution at 0 °C with vigorous stirring. $Hg_{0.5}Cd_{0.5}(cup)_2$ (nominal composition) was prepared by adding cupferron solution to the stoichiometric amounts of $HgCl_2$ and $CdCl_2$ dissolved in water, at 0 °C. The products were collected by centrifugation, washed several times with distilled water and ethanol and dried in a vacuum desiccator.

For the synthesis of HgSe nanocrystalline films, 6.5 mg of selenourea was dissolved in 20 ml of water in a 50 ml beaker, and 25 mg of Hg $(cup)_2$ was

dissolved in a solution of 0.5 ml of n-octylamine in 20 ml of toluene by ultrasonication. For the similar synthesis of $Hg_{0.5}Cd_{0.5}Se$ films (nominal composition), 7.1 mg of selenourea and 25 mg of $Hg_{0.5}Cd_{0.5}(cup)_2$ were used. The toluene solution of $Hg(cup)_2$ or $Hg_{0.5}Cd_{0.5}(cup)_2$ was slowly added along the walls of the beaker containing an aqueous solution of selenourea. The interface starts appearing black within a few minutes. The reaction was left undisturbed for 24 hrs for the complete formation of nanocrystalline films. After removing the upper toluene layer carefully, the films were gently lifted on to glass or Si/SiO_2 substrates for further characterizations. HgS films can be synthesized similarly using 4.1 mg of Na_2S and 25 mg of Hg $(cup)_2$ while keeping the other conditions unchanged.

3.1.2.2 Characterizations

For powder X-ray diffraction (PXRD), the interfacial deposits were thoroughly washed with acetone by centrifugation and dried in an evacuated desiccator. PXRD patterns were recorded on Bruker D8 Advance diffractometer with CuK_α radiation (1.54 Å). The average crystallite sizes were estimated (from XRD) using the Scherrer-formula to be ca. 9.5 nm and 6 nm for HgSe and $Hg_{0.5}Cd_{0.5}Se$ respectively.

Transmission electron microscopy (TEM) and selected area electron diffraction (SAED) were performed on JEOL TEM-3010 electron microscope at an accelerating voltage of 300 kV. For TEM, the as-lifted films were washed several times with acetone by centrifugation, mildly ultrasonicated in ethanol and subsequently drop-casted on carbon-coated copper grids. The actual elemental composition of the nominal $Hg_{0.5}Cd_{0.5}Se$ powders was determined by energy dispersive X-ray spectroscopy (EDAX). For estimating the optical band gaps, diffuse reflectance measurements were performed on solid products using Perkin Elmer Lambda 900 UV-Vis-NIR spectrometer at room temperature. The reflectance was converted to absorbance by Kubelka Munk function using the relation, $\alpha/S=(1-R)^2/(2R)$, where R is the reflectance, α is the absorption coefficient, and S is the scattering coefficient. α/S is plotted as the y-axis while energy ($E = h\nu$, in the units of eV) is plotted as the x-axis. Optical band edge

was determined from α/S vs. E (eV) plots as the point of intersection of a tangential line on the energy axis.

3.1.2.3 Device-fabrication

For the fabrication of devices, two Au electrodes of 150 nm thickness were deposited on a pre-cleaned soda lime glass (SLG) by evaporating Au through electron-beam evaporation. During the deposition, a spacing of 70 μm was maintained in between the Au electrodes using a mask. The active layer was prepared by drop casting a toluene-dispersion of HgSe or $Hg_{0.5}Cd_{0.5}Se$ QDs into the channel between the Au electrodes, and the device was dried overnight in the vacuum. For studying the near IR detection properties, the IR source constituting a monochromatic laser diode with 1550 nm peak wavelength and a beam diameter of 400 μm was focused vertically on to the channel. The photocurrent measurements were performed under ambient conditions. The current-voltage characteristics of the devices were measured using Keithley 6430 meter and monitored through the LabVIEW program.

3.1.3 Results & discussion

3.1.3.1 Interfacial films

Figures 3.1.1(a) and (b) show photographs of the nanocrystalline films of HgSe and $Hg_{0.5}Cd_{0.5}Se$ QDs formed at the toluene-water interface. Powder X-ray diffraction (PXRD) patterns of the HgSe and $Hg_{0.5}Cd_{0.5}Se$ QDs in figure 3.1.1(c) could be indexed on the cubic system ($F\bar{4}3m$ space group) with no detectable impurities. To determine the actual composition of the nominal $Hg_{0.5}Cd_{0.5}Se$ film, EDAX was carried out on dried powder sample. A typical EDAX spectrum along with elemental mapping is shown in figure 3.1.2. The average elemental composition as determined from EDAX is Hg:Cd:Se = 0.48:0.52:1 which is close to the nominal composition.

Figures 3.1.3(a) and (c) show transmission electron microscope (TEM) images of HgSe and $Hg_{0.5}Cd_{0.5}Se$ QDs respectively along with the indexed selected area electron diffraction (SAED) patterns given as insets. High-resolution TEM (HRTEM) images of HgSe and $Hg_{0.5}Cd_{0.5}Se$ QDs are shown in

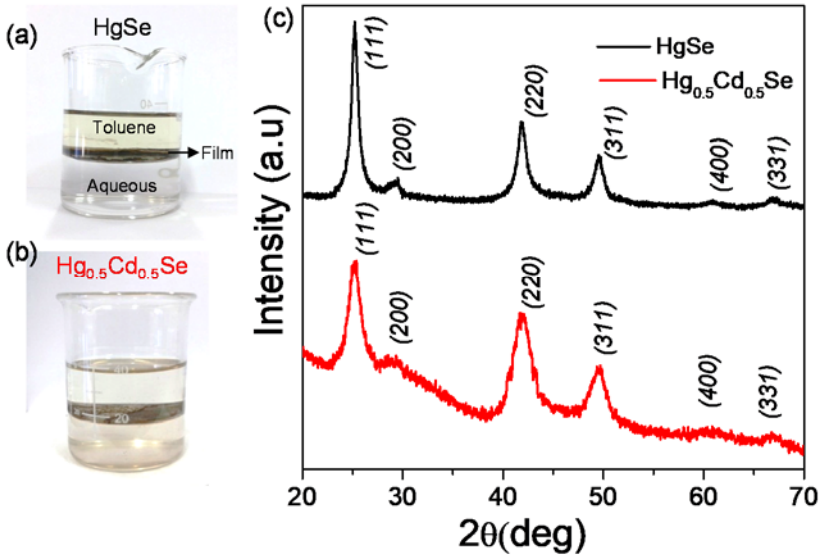

Figure 3.1.1 *Photographs showing interfacial films of (a) HgSe and (b) $Hg_{0.5}Cd_{0.5}Se$ QDs formed at the toluene-water interface. (c) Indexed PXRD patterns of HgSe and $Hg_{0.5}Cd_{0.5}Se$ QDs.*

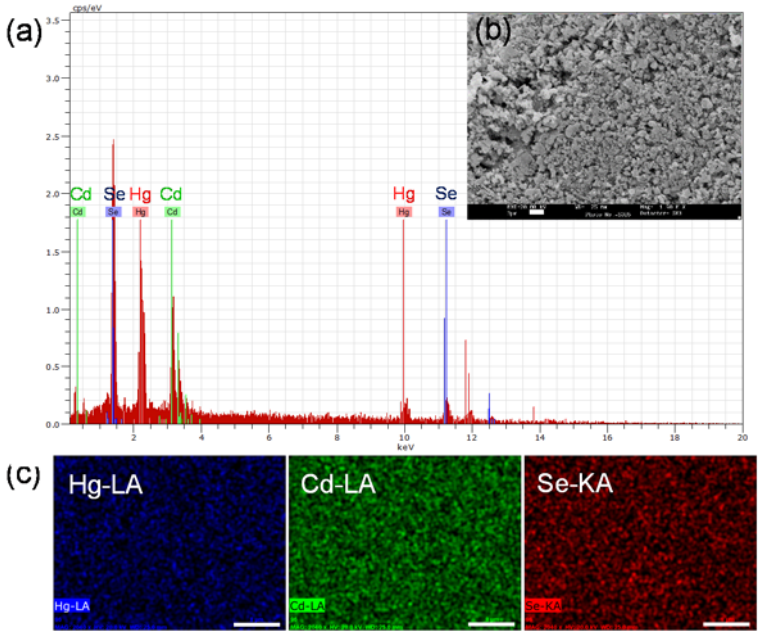

Figure 3.1.2 *(a) EDAX spectrum of $Hg_{0.5}Cd_{0.5}Se$ QDs (nominal composition) and (b) corresponding SEM image of the solid sample with a scale bar of 3 μm. (c) Elemental mapping of the image in (b), showing the distribution of elements. The scale bars are of 8 μm.*

figures 3.1.3(b) and (d) respectively. The d-spacing of 0.21 nm corresponds to the (220) crystal planes for HgSe and a d-spacing of 0.34 nm, to the (111) planes for $Hg_{0.5}Cd_{0.5}Se$. The size-distribution histograms shown as insets in figures 3.1.3(b) and (d) give the mean diameters of ca. 9 nm for HgSe QDs and

ca. 5 nm for $Hg_{0.5}Cd_{0.5}Se$ QDs. The as-synthesized nanocrystalline films are densely packed having a maximum coverage of interfacial area (Figures 3.1.1(a) and (b)). The dense nature of the films is also apparent from the TEM images, although fragmentation occurs due to ultrasonication, which can ensure good electronic coupling between the quantum dots and provide a continuous channel for the transport of carriers across the film.[11] Since the interfacial barriers across particles give rise to transport-noise decreasing the device performance, inter-particle connectivity is critical for good photoconduction.[10]

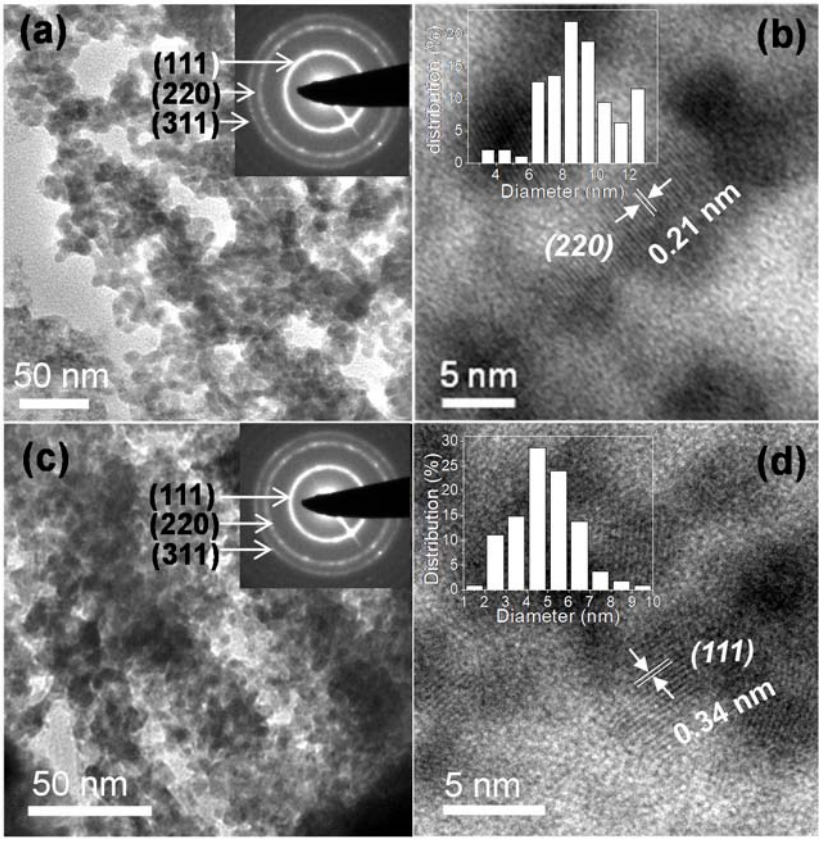

Figure 3.1.3 *(a) TEM and (b) HRTEM images of HgSe QDs. (c) TEM and (d) HRTEM images of $Hg_{0.5}Cd_{0.5}Se$ QDs. Insets in (a) and (c) are SAED patterns and insets in (b) and (d) are particle size histograms.*

3.1.3.2 Growth and self-organization

To directly probe into the growth and self-organization of interfacial films, we have carried out *in-situ* X-ray reflectivity (XRR) and *ex-situ* grazing incidence small angle X-ray scattering (GISAXS) measurements on HgSe films in collaboration with Prof. Milan K. Sanyal's group at SINP, Kolkata.

Synchrotron X-ray sources at P08 beamline in PETRA-III (25 KeV) and Indian beamline in photon factory (18 KeV) were used for the XRR and GISAXS measurements respectively. For the *in-situ* XRR measurements, incident x-ray beam size is of 0.05×0.10 mm^2 (V×H) which was defined using a conventional slit. For the *in-situ* XRR measurements, a custom-built Teflon cell (1.5×3.0 cm^2) was used with its two rectangular windows sealed with 25 μm thick Kapton sheets on the opposite walls. The angle of incidence was set to 0.03° for GISAXS measurements with an x-ray beam size of 50×100 (V×H) μm^2. We used a Perkin Elmer 2D detector of 0.2 μm pixel size for the grazing incidence x-ray scattering and a 1D MYTHEN detector for the reflectivity measurements.

For the *in-situ* XRR measurements, I have synthesized thin interfacial film of HgSe at room temperature by a dropwise addition of a solution of 4.4 mg of $Hg(cup)_2$ and 50 μl of octylamine in 5ml of toluene to an aqueous solution of 1.4 mg of selenourea in 5 ml of water. The above Teflon cell was used for the synthesis. The above concentrations were chosen to slow down the interfacial-reaction and facilitate the *in-situ* XRR study. The interface gradually turns black over time due to the formation of HgSe nanoparticles and their self-organization at the interface. Complete details of methods can be found in reference 36.

X-ray Reflectivity (XRR)

XRR provides information on electron density, thickness, and roughness of interfacial films as a function of depth during formation. In the XRR technique, the intensity of scattered x-rays normalized to the intensity of incident beam is measured as a function of $q_z = 2\pi/\lambda(sin\theta_i + sin\theta_f)$ keeping q_{xy}=0 where q is the wave-vector and θ_i and θ_f are the incident and final angles respectively. *In-situ* XRR measurements were carried out at different stages of reaction by varying angles θ_i and θ_f under specular condition (i.e., with θ_i=θ_f) and keeping the azimuth angle $\varphi = 0$ (see figure 3.1.4(a)). The measured reflectivity is modelled using Parratt formalism by incorporating roughness values of water-HgSe as well as HgSe-toluene interfaces (for more details, refer to reference 36).

Measured XRR data of HgSe film (R) is normalized with that for the pure water–toluene interface (R_W), obtained before initiating the chemical reaction. Figure 3.1.4(b) shows representative (R/R_W) data as a function of q_z collected at different time intervals after initiating the interfacial reaction. The different electron density profiles (EDPs) of toluene, water and HgSe allowed us to determine the thickness of HgSe film at the toluene-water interface. Figure 3.1.4(c) shows the roughness-convoluted EDPs obtained from the fitted reflectivity curves at different time intervals. The thickness of HgSe film is determined from the derivative plots of EDP and is found to be 8.8, 9.7, 10.8, 12.5, 13, 13.6 and 15 nm for reaction times of 20, 50, 80, 110, 140, 170 and 200 min respectively, giving a constant growth rate of 0.034 nm min^{-1} (Figure 3.1.4(d)). For more details, refer to reference 36.

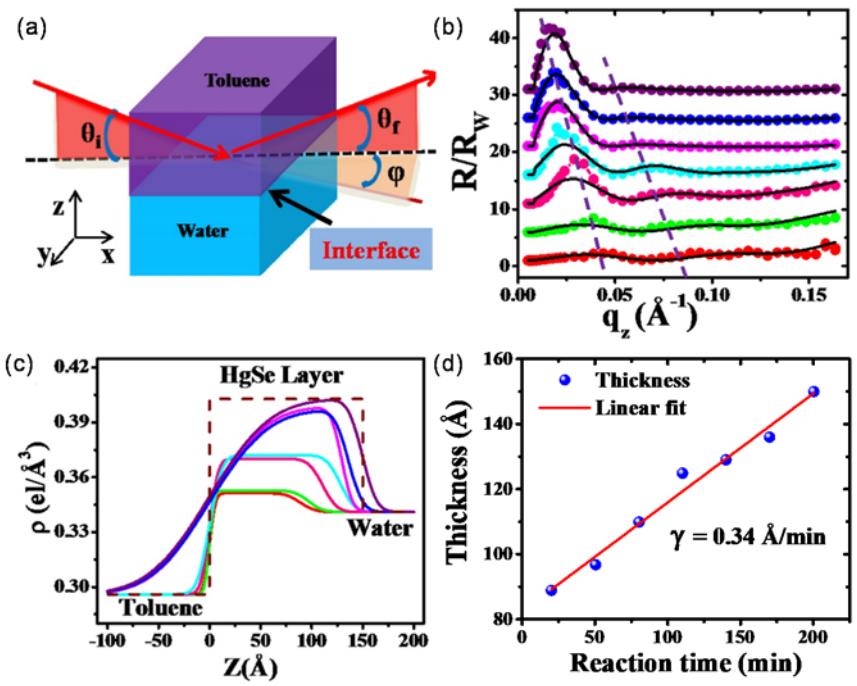

Figure 3.1.4 *(a) Schematic of in-situ synchrotron XRR measurement indicating the X-ray beam directions. b) XRR as a function of q_z during the formation of HgSe film at the toluene-water interface at different time intervals (red: 20 min, green: 50 min; pink: 80 min; cyan: 110 min; magenta: 140 min; blue: 170 min; purple: 200 min and fits (solid black lines)). The XRR data were normalized with measured reflectivity from the toluene-water interface (R_W) and shifted vertically for clarity. The q_z positions corresponding to first and second maxima of each reflectivity curve are shown by violet dotted lines. c) The extracted electron density profiles (EDPs) as a function of depth (Z) from toluene to water at different reaction times; color codes are same as in (b). c) Evolution of HgSe film-thickness with reaction time.*

Grazing incidence small angle x-ray scattering (GSAXS)

GISAXS technique is extremely surface-sensitive as the incident angle is kept very low (close to the critical angle of 0.03° for the toluene-water interface). Hence it gives a footprint over the entire sample along the x-ray beam. It can provide detailed information about the ordering along in-plane and out-of-plane directions of the film with respect to the substrate. The high x-ray absorption factor and bulk scattering of the liquids, and the lack of crystalline orientation of films did not allow us to investigate *in-situ* the in-plane ordering using GISAXS. Therefore, we have carefully lifted the interfacial films at specific intervals (6 and 12 hr) onto Si substrate such that the orientation of the film on Si substrate remains similar to that at the liquid-liquid interface.

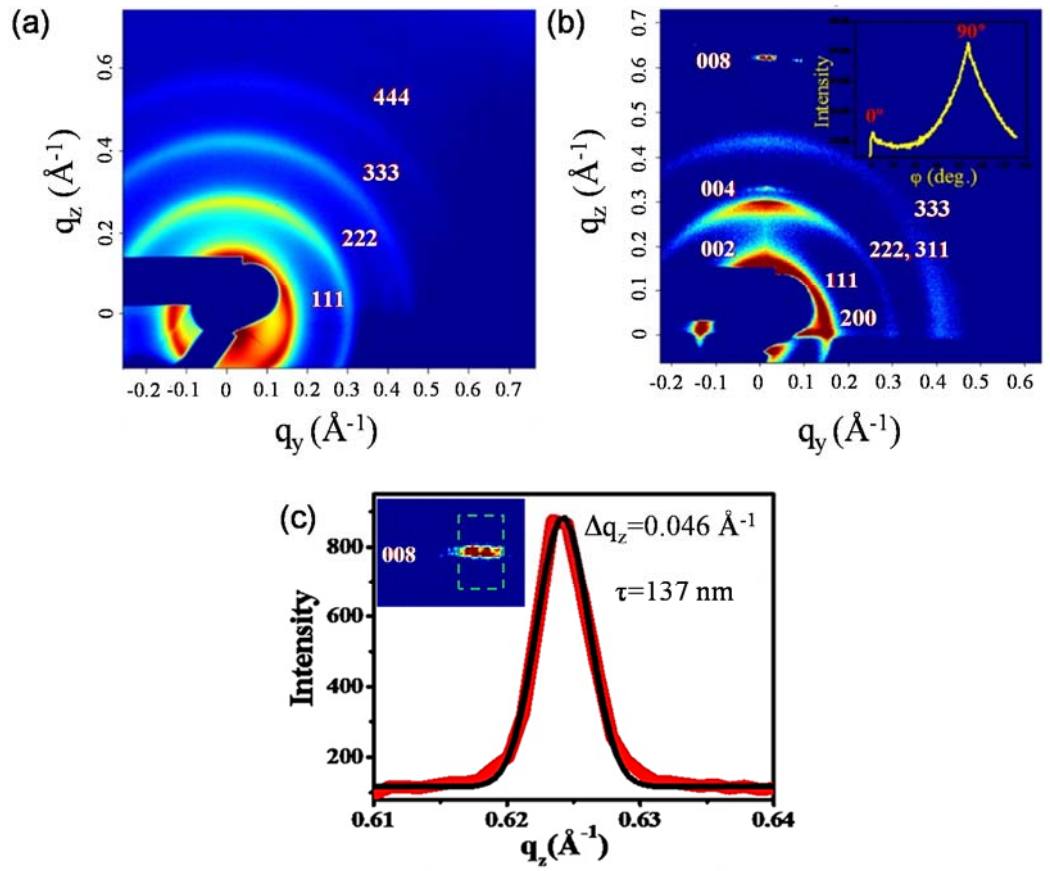

Figure 3.1.5 *(a) GSAXS data from the interfacial HgSe films lifted on to Si substrate at the end of a) 6 hr and b) 12 hr of the reaction. The dark blue region is due to the specular beam-stop. c) The expanded GISAXS region of (008) reflection (inset) and the corresponding line profile (red curve) along the q_z direction; the solid black line is the Lorentzian fit.*

The obtained *ex-situ* GSAXS data at the end of 6 hr exhibits (Figure 3.1.5(a)) equidistant arc-like peaks at q ($= \sqrt{(q_z^2 + q_y^2)}$) values of 1.44, 2.86, 4.36 and 5.75 nm^{-1}. The equal separation of the peaks (1.44 nm^{-1}) corresponds to a center-to-center distance of 4.4 nm, giving an average cluster-radius (r) of 2.2 nm. GISAXS measurement at the end of 12 hr is shown in figure 3.1.5 (b). The GISAXS pattern exhibits superlattice peaks at 1.44, 1.57, 2.86, 3.31, 4.36, 5.75, 6.25 and 7.4 nm^{-1}, and all the obtained peaks could be indexed to a face-centered cubic (f.c.c) superstructure. The lattice parameter of this f.c.c superstructure (a) and the corresponding cluster radius ($a/2\sqrt{2}$) were found to be 7.55 nm and 2.7 nm, respectively. In addition to the observed equidistant peaks in the 6 hr-sample, we found intense single crystal-like reflections in the 12 hr-samples along the q_z direction (normal to the liquid–liquid interface) at 6.25 and 3.31 nm^{-1}, indexed as the (008) and (004) planes, respectively. The peak at 1.57 nm^{-1} clearly exhibits strong intensity variation (figure 3.1.5(b)) at 90° azimuth separation, indexed as (002) and (200), giving clear evidence of the four-fold symmetry of the superstructure. The coherent domain size of the sharp (008) superlattice peak is 137 nm (figure 3.1.5(c)) which is significantly larger than the observed cluster size of 4.4 nm. This observation provides a clear signature of contact epitaxy, i.e., multiple clusters orient along a crystal plane and the capillary-wave fluctuations at the liquid–liquid interface promote such confinement-induced ordering. An elaborate discussion on our findings can be found in reference 36.

3.1.3.3 Near-IR photodetection

The absorption band edge for the HgSe QDs is at ca. 0.7 eV (Figure 3.1.6) which falls in the near-infrared (NIR) region. For investigating the NIR detection properties, devices were illuminated using a monochromatic laser of 1550 nm wavelength as the IR source (see methods). Figure 3.1.7(a) shows the I-V characteristics of the HgSe QDs under dark conditions and illumination intensities of 80 mW/cm^2 and 100 mW/cm^2. As the external bias was swept from 0 V to 2 V, a linear photo-response is observed suggesting an Ohmic contact between the HgSe QDs and the gold electrodes. The Ohmic behavior is expected since the electron affinity of HgSe particles (ca. 5.1 eV)[42] matches

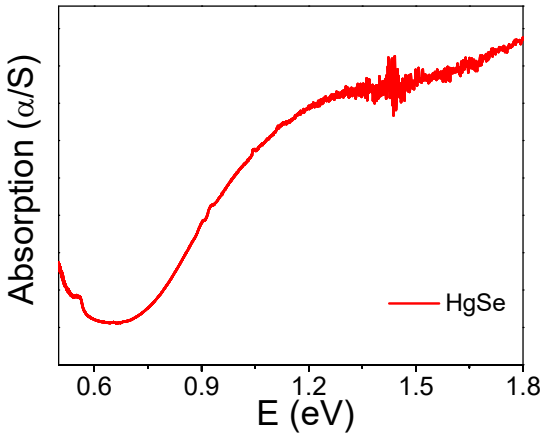

Figure 3.1.6 *Kubelka-Munk absorbance spectrum of HgS QDs synthesized at the toluene-water interface.*

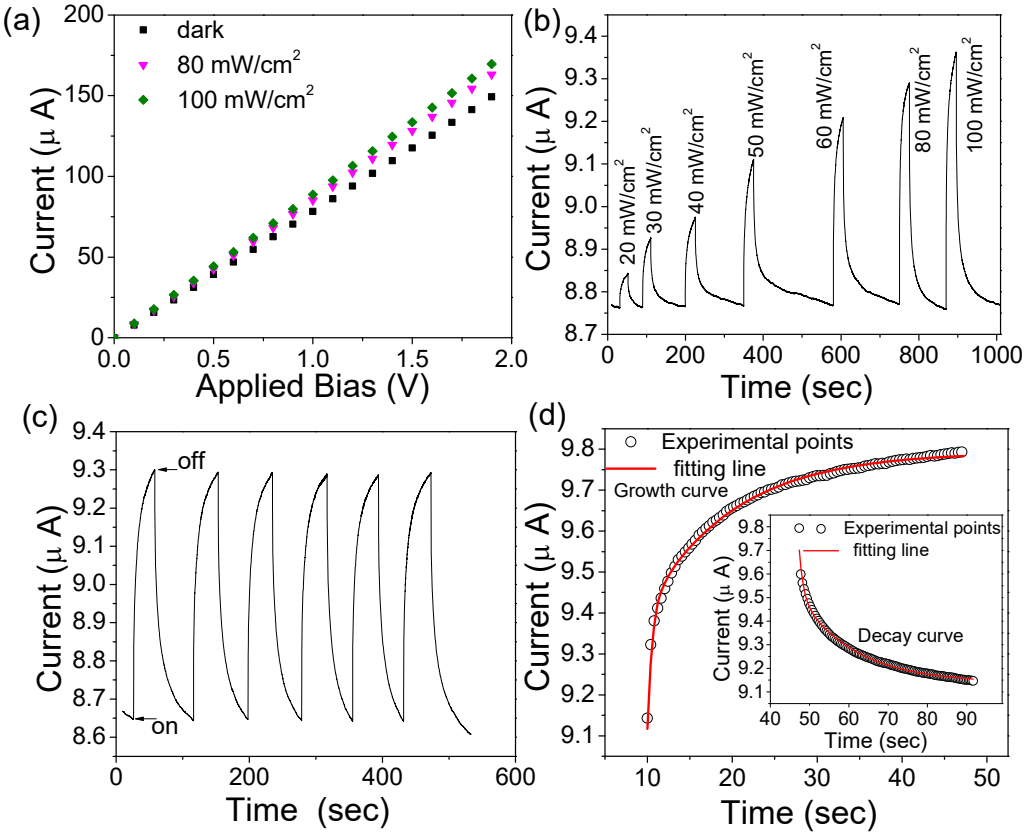

Figure 3.1.7 *(a) I-V characteristics of HgSe QDs in the dark and under 1550 nm-laser illumination intensities of 80 mW/cm² and 100 mW/cm². (b) The plot of photocurrent versus time as a function of different laser intensities. (c) On–off curves of photocurrent with time at 0.1 V bias and 80 mW/cm² intensity, showing the reproducibility. (d) Time-resolved photocurrent growth and decay (inset) curves.*

with the work function of gold (5.1 eV). Figure 3.1.7(b) shows the photocurrent as a function of time at different optical intensities when the applied bias is 0.1 V. The photocurrent increases with increasing intensities as more excitons are

generated with increasing photon flux density. In figure 3.1.7(c), we show the photocurrent as a function of time at an external bias of 0.1 V and irradiance of 80 mW/cm^2, with periodic exposure to the laser for 30 sec to demonstrate the reproducibility and stability of the device over cycles.

In figure 3.1.7(d), we show the time-resolved photocurrent response. The dynamic response of the HgSe QD device to laser illumination can be described for the rise and decay respectively by the following exponential equations:

$$I(t) = I_{dark} + A[exp\left(\frac{t}{\tau_1}\right)] + B[exp\left(\frac{t}{\tau_2}\right)] \quad 3.1.3$$

$$I(t) = I_{dark} + A[exp\left(-\frac{t}{\tau_1}\right)] + B[exp\left(-\frac{t}{\tau_2}\right)] \quad 3.1.4$$

where τ_1 and τ_2 are the time constants; t, the time when the laser was turned on or off; A and B, the scaling constants and I_{dark}, the dark current. The time constants (τ) for the faster and slower components from the above fits are 0.6 and 10 sec respectively for the rise and 1.1 and 14.3 sec respectively for the decay (Figure 3.1.7(d)). The dynamic response is, however, slower compared to HgTe QD detector.[12] Room temperature synthesis would have generated defects in the QDs and the electron charging at these defects might have plausibly led to the observed slow photo-response. The responsivity (R_λ), defined as the photocurrent per unit power, and the external quantum efficiency (EQE), defined as the number of excitons generated per photon absorbed are key parameters for photoconductors. R_λ and EQE can be calculated respectively from the following equations: [43]

$$R_\lambda = (I_p - I_{dark})/(P_\lambda S) \quad 3.1.5$$

$$EQE = hcR_\lambda/(q.\lambda) \quad 3.1.6$$

where I_p is the current upon illumination; I_{dark}, the dark current; P_λ, the illumination intensity; S, the effective area under illumination; h, the Planck's constant; q, the absolute electronic charge (1.6 x 10^{-19} C) and λ, the wavelength of the incident light. The photocurrent response of the HgSe device at 2 V bias is presented in figure 3.1.8. For the HgSe device, room-temperature values of R_λ and EQE at an external bias of 2 V and 80 mW/cm^2 intensity of the 1550 nm laser are found to be 0.45 A/W and 35.74 % respectively. Detectivity (D^*)

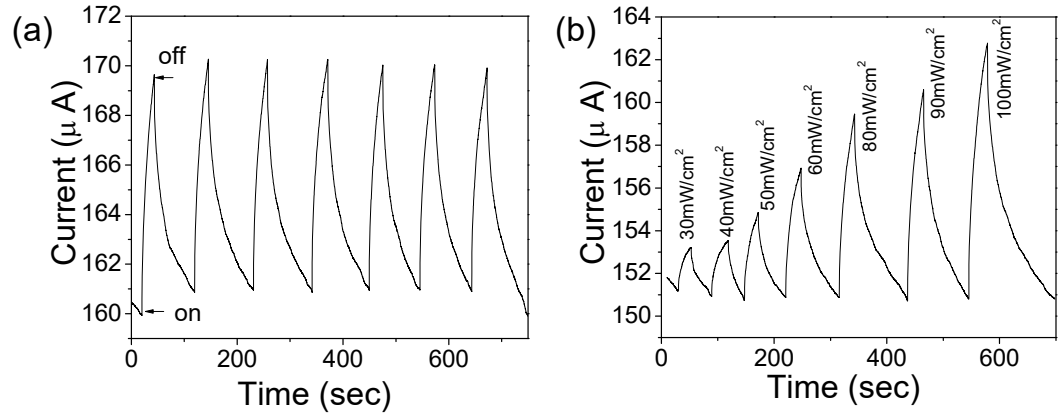

Figure 3.1.8 *(a) On–off curves of photocurrent with time at 2 V bias and 80 mW/cm² irradiance for the HgSe QDs. (b) The plot of photocurrent versus time at different laser intensities.*

is the standard figure of merit expressed as [43]

$$D^* = (S\Delta f)^{\frac{1}{2}} \, (R_\lambda / I_n) \qquad 3.1.7$$

where Δf is the electrical bandwidth (Hz) and I_n, the noise current. Assuming that the shot noise from the dark current is the major contribution, the normalized detectivity can be defined as:[6, 44]

$$D^* = R_\lambda \left(\frac{S}{2qI_{dark}} \right)^{\frac{1}{2}} \qquad 3.1.8$$

The room-temperature value of D^* for the HgSe device is calculated to be 1.1×10^9 Jones.

Figure 3.1.9(a) shows the I-V characteristics of the $Hg_{0.5}Cd_{0.5}Se$ QDs. Figure 3.1.9(b) shows the dependence of the photocurrent on illumination intensities and the reproducibility of this device is demonstrated in figure 3.1.9(c). The dynamic photoresponse in the $Hg_{0.5}Cd_{0.5}Se$ QD device to IR illumination is shown in figure 3.1.9(d). The time constants for the faster and slower components are ca. 1.6 and 17 sec respectively for the rise and ca. 1 and 19 sec respectively for the decay. The photocurrent response in the $Hg_{0.5}Cd_{0.5}Se$ QD device measured at 2 V bias and 80 mW/cm² irradiance is presented in figure 3.1.10. The room-temperature values of R_λ, EQE and D^* for $Hg_{0.5}Cd_{0.5}Se$ QD device at 2 V bias and 80 mW/cm² intensity are 0.91 A/W, 72% and 3.3×10^{10} Jones respectively.

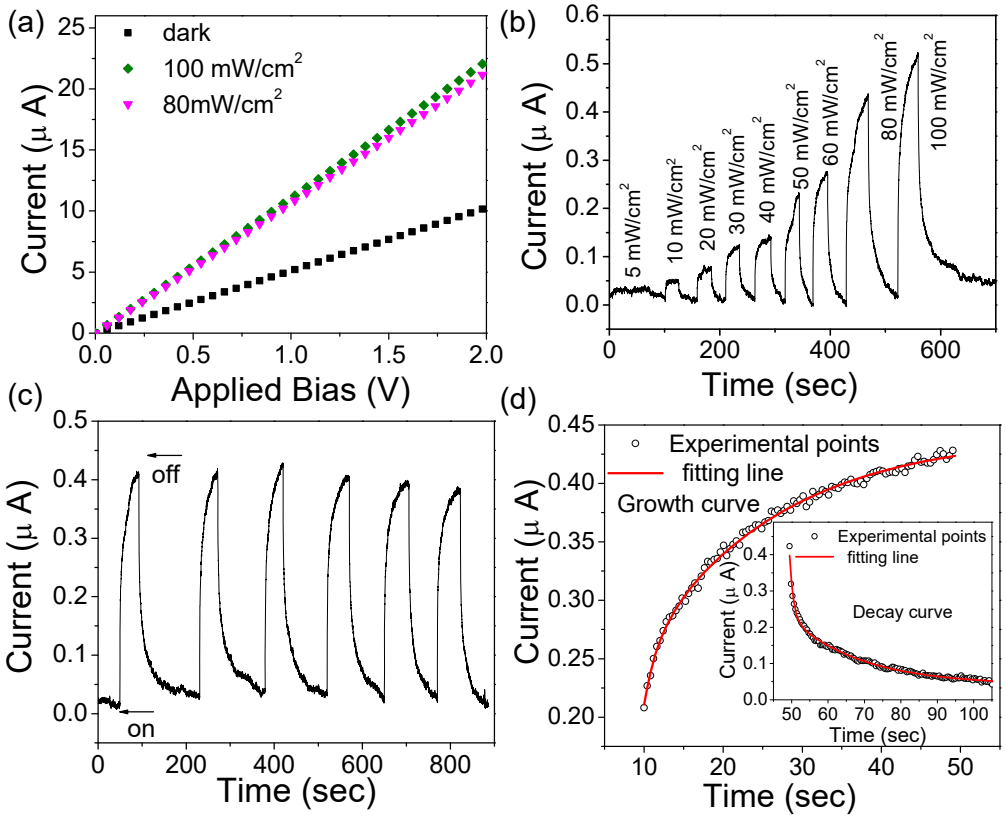

Figure 3.1.9 *(a) I-V characteristics of $Hg_{0.5}Cd_{0.5}Se$ QDs in the dark and under 1550 nm-laser illumination intensities of 80 mW/cm² and 100 mW/cm². (b) The plot of photocurrent versus time as a function of different laser intensities. (c) On–off curves of photocurrent with time at 0.1 V bias and 80 mW/cm² intensity showing the reproducibility. (d) Time-resolved photocurrent growth and decay (inset) curves.*

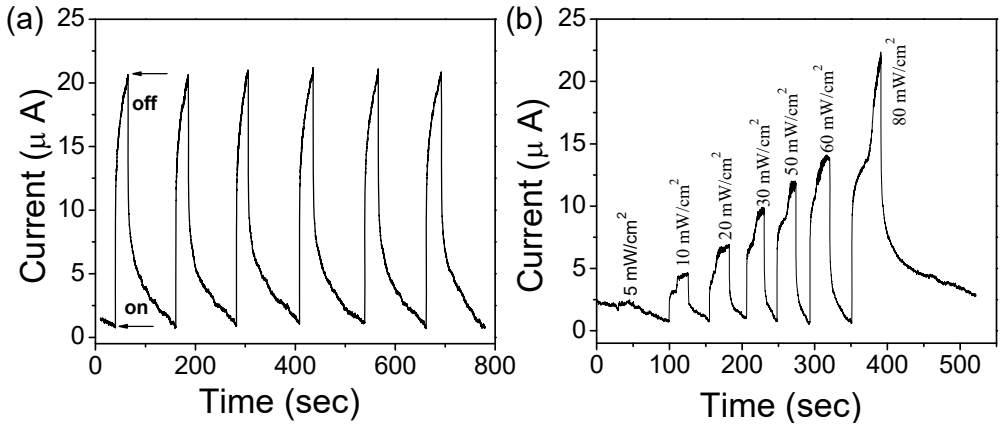

Figure 3.1.10 *(a) On–off curves of photocurrent with time at 2 V bias and 80 mW/cm² irradiance for $Hg_{0.5}Cd_{0.5}Se$ QDs. (b) The plot of photocurrent versus time at different laser intensities.*

Our present studies indicate that the HgSe and $Hg_{0.5}Cd_{0.5}Se$ QD devices are comparable with some of the previously reported QD based vis-IR detectors (Table 3.1.1). The R_λ and D^* values of our HgSe and $Hg_{0.5}Cd_{0.5}Se$ QD devices

are reasonably comparable to those of HgTe QDs synthesized by Keuleyan *et al* (R_λ and D^* values of 0.25 A/W and 2×10^9 Jones respectively)[11] and by Böberl *et al* (R_λ and D^* values of 4.4 A/W and 3×10^{10} Jones respectively),[3] indicating the potential of our Te-free devices as NIR detectors.

Table 3.1.1 *Summary of photodetection properties of various Vis-IR photodetectors in the literature along with the present interfacial films.*

Compound	Responsivity (A/W)	Detectivity (Jones)	Operating range	Reference
PbS QDs	2700	1.8×10^{13}	Vis-NIR	10
PbS QDs	0.225	10^{12}	Vis-NIR	45
CdSe	9.1-31	6.9×10^{10}	Vis	6
CdSe NWs	1.30×10^{-2}	3.7×10^{9}	Vis	46
CdSe QDs	1.80×10^{-3}	10^{7}	Vis	47
Bi_2S_3 NCs	20	10^{11}	Vis-900nm	4
HgTe QDs	4.4	3×10^{10}	Mid-IR	3
HgTe QDs	0.15-0.25	2×10^{9}	Mid-IR	11
HgCdTe bulk		10^{10}-10^{11}	NIR-LWIR	2
$Hg_{0.5}Cd_{0.5}Se$ film	0.91	3.3×10^{10}	Vis-NIR	Our work
HgSe film	0.45	1.1×10^{9}	NIR	Our work

3.1.4 Conclusions

Interfacial films of HgSe and $Hg_{0.5}Cd_{0.5}Se$ QDs were successfully synthesized at room temperature through a facile and cost-effective bottom-up synthesis employing the organic-aqueous interface. *In-situ* XRR measurements revealed a linear growth in thickness of HgSe film with reaction time, and *ex-situ* GSAXS measurements performed on the HgSe film revealed the self-organization of HgSe clusters into face centered cubic superstructures at the toluene-water interface. The NIR photodetection properties of HgSe and $Hg_{0.5}Cd_{0.5}Se$ QDs have been examined. The R_λ and D^* values of the present Se-based devices are comparable to some of the previously reported QD based IR detectors, especially those based on HgTe QDs.

3.1.5 References

1. P. Norton, *Opto-Electron. Rev.*, 2002, **10**, 159-174.
2. A. Rogalski, *Rep. Prog. Phys.*, 2005, **68**, 2267.
3. M. Böberl, M. V. Kovalenko, S. Gamerith, E. J. W. List and W. Heiss, *Adv. Mater*, 2007, **19**, 3574-3578.
4. G. Konstantatos, L. Levina, J. Tang and E. H. Sargent, *Nano Lett.*, 2008, **8**, 4002-4006.
5. G. Konstantatos and E. H. Sargent, *Nat. Nanotechnol.*, 2010, **5**, 391-400.
6. W. Xing, S.-C. Kung, W. E. van der Veer, W. Yan, T. Ayvazian, J. Y. Kim and R. M. Penner, *ACS Nano*, 2012, **6**, 5627-5634.
7. A. Svane, N. E. Christensen, M. Cardona, A. N. Chantis, M. van Schilfgaarde and T. Kotani, *Phys. Rev. B*, 2011, **84**, 205205.
8. M. V. Kovalenko, E. Kaufmann, D. Pachinger, J. Roither, M. Huber, J. Stangl, G. Hesser, F. Schäffler and W. Heiss, *J. Am. Chem. Soc.*, 2006, **128**, 3516-3517.
9. P. Howes, M. Green, C. Johnston and A. Crossley, *J. Mater. Chem.*, 2008, **18**, 3474-3480.
10. G. Konstantatos, I. Howard, A. Fischer, S. Hoogland, J. Clifford, E. Klem, L. Levina and E. H. Sargent, *Nature*, 2006, **442**, 180-183.
11. S. Keuleyan, E. Lhuillier, V. Brajuskovic and P. Guyot-Sionnest, *Nat Photon*, 2011, **5**, 489-493.
12. H. Kim, K. Cho, B. Park, J.-H. Kim, J. W. Lee, S. Kim, T. Noh and E. Jang, *Solid State Commun.*, 2006, **137**, 315-319.
13. H. Kim, K. Cho, H. Song, B. Min, J.-S. Lee, G.-T. Kim, S. Kim, S. H. Kim and T. Noh, *Appl. Phys. Lett.*, 2003, **83**, 4619-4621.
14. Z. C. Hu and S. Gao, *Chem. Geol.*, 2008, **253**, 205.
15. M. Kuno, K. A. Higginson, S. B. Qadri, M. Yousuf, S. H. Lee, B. L. Davis and H. Mattoussi, *J. Phys. Chem. B*, 2003, **107**, 5758-5767.
16. S. Deki, A. Nakata, Y. Sakakibara and M. Mizuhata, *J. Phys. Chem. C*, 2008, **112**, 13535-13539.

17. L. Hou, Q. Zhang, L. Ling, C.-X. Li, L. Chen and S. Chen, *J. Am. Chem. Soc.*, 2013, **135**, 10618-10621.
18. M. K. Jana, P. Chithaiah, B. Murali, S. B. Krupanidhi, K. Biswas and C. N. R. Rao, *J. Mater. Chem. C*, 2013, **1**, 6184-6187.
19. S. N. Mlondo, P. J. Thomas and P. O'Brien, *J. Am. Chem. Soc.*, 2009, **131**, 6072-6073.
20. N. Nuraje, K. Su, N.-l. Yang and H. Matsui, *ACS Nano*, 2008, **2**, 502-506.
21. C. N. R. Rao and K. P. Kalyanikutty, *Acc. Chem. Res.*, 2008, **41**, 489-499.
22. P. J. Thomas, E. Mbufu and P. O'Brien, *Chem. Commun.*, 2013, **49**, 118-127.
23. X. Wang, Q. Peng and Y. Li, *Acc. Chem. Res.*, 2007, **40**, 635-643.
24. Q. Han, Y. Yuan, X. Liu, X. Wu, F. Bei, X. Wang and K. Xu, *Langmuir*, 2012, **28**, 6726-6730.
25. D. Fan, P. J. Thomas and P. O' Brien, *J. Am. Chem. Soc.*, 2008, **130**, 10892-10894.
26. D. Fan, P. J. Thomas and P. O'Brien, *J. Mater. Chem*, 2007, **17**, 1381-1386.
27. X. Liang, L. Xing, J. Xiang, F. Zhang, J. Jiao, L. Cui, B. Song, S. Chen, C. Zhao and H. Sai, *Cryst. Growth Des.*, 2012, **12**, 1173-1179.
28. K. D. Danov, P. A. Kralchevsky and M. P. Boneva, *Langmuir*, 2004, **20**, 6139-6151.
29. E. P. Lewandowski, J. A. Bernate, A. Tseng, P. C. Searson and K. J. Stebe, *Soft Matter*, 2009, **5**, 886-890.
30. E. P. Lewandowski, M. Cavallaro, L. Botto, J. C. Bernate, V. Garbin and K. J. Stebe, *Langmuir*, 2010, **26**, 15142-15154.
31. J. C. Loudet, A. M. Alsayed, J. Zhang and A. G. Yodh, *Phys. Rev. Lett.*, 2005, **94**, 018301.
32. M. G. Nikolaides, A. R. Bausch, M. F. Hsu, A. D. Dinsmore, M. P. Brenner, C. Gay and D. A. Weitz, *Nature*, 2002, **420**, 299-301.
33. P. Pieranski, *Phys. Rev. Lett.*, 1980, **45**, 569-572.

34. M. K. Bera, M. K. Sanyal, L. Yang, K. Biswas, A. Gibaud and C. N. R. Rao, *Phys. Rev. B*, 2010, **81**, 115415.

35. M. Santanu, M. K. Sanyal, N. Varghese, B. Satpati, D. Dipak, J. Daillant, D. Carriere, O. Konovolov and C. N. R. Rao, *J. Phys.: Condens. Matter*, 2013, **25**.

36. M. Santanu, K. S. Milan, K. J. Manoj, R. Benjamin, M. M. Bridget, B. Kanishka and C. N. R. Rao, *J. Phys.: Condens. Matter*, 2017, **29**, 095101.

37. P. S. Pershan, *Faraday Discuss. Chem. Soc.*, 1990, **89**, 231-245.

38. E. M. Furst, *PNAS* 2011, **108**, 20853-20854.

39. U. K. Gautam, M. Ghosh and C. N. R. Rao, *Langmuir*, 2004, **20**, 10775-10778.

40. A. H. Khan, S. Maji, S. Chakraborty, N. B. Manik and S. Acharya, *RSC Adv.*, 2012, **2**, 186-191.

41. S. Acharya, B. Das, U. Thupakula, K. Ariga, D. D. Sarma, J. Israelachvili and Y. Golan, *Nano Lett.*, 2013, **13**, 409-415.

42. J. Yun, K. Cho and S. Kim, *ACS Appl. Mater. Interfaces*, 2012, **4**, 5839-5843.

43. E. H. Sargent, *Adv. Mater.*, 2005, **17**, 515-522.

44. X. Gong, M. Tong, Y. Xia, W. Cai, J. S. Moon, Y. Cao, G. Yu, C.-L. Shieh, B. Nilsson and A. J. Heeger, *Science*, 2009, **325**, 1665.

45. J. P. Clifford, G. Konstantatos, K. W. Johnston, S. Hoogland, L. Levina and E. H. Sargent, *Nat Nanotechnol.*, 2009, **4**, 40-44.

46. S.-C. Kung, W. Xing, W. E. van der Veer, F. Yang, K. C. Donavan, M. Cheng, J. C. Hemminger and R. M. Penner, *ACS Nano*, 2011, **5**, 7627-7639.

47. D. C. Oertel, M. G. Bawendi, A. C. Arango and V. Bulović, *Appl. Phys. Lett.*, 2005, **87**, 213505.

CHAPTER 3.2

Fabrication of large-area PbSe films at the organic-aqueous interface, and their near-infrared photoresponse*

Summary

Organic-aqueous interfacial reaction at room temperature has been employed to synthesize large-area self-assembled films consisting of PbSe single crystallites. The utility of the films for the low-cost fabrication of IR-photodetectors has been explored. (111)-Oriented single crystallites of PbSe self-assemble to form robust large-area films. The near-infrared photoresponse of the film measured at room temperature showed large responsivity and photoconductive gain owing to trap-associated mechanisms. The low-cost, mild reaction conditions and tunability of the nature of deposits make the present strategy useful for synthesizing large-area films of functional materials for possible optoelectronic applications.

A paper based on this study has appeared in* ***J. Mater. Chem. C*, 2014, *2*, 6283.

3.2.1 Introduction

In the present chapter, we have employed the liquid-liquid interface for the synthesis of lead selenide (PbSe) films and explored their utility for low-cost fabrication of IR photodetectors. Owing to the large Bohr radii (ca. 45 nm), widely tunable emission spanning from near to mid-IR region[1] and multiple exciton generation by single photons,[2] lead chalcogenide nanocrystals have drawn considerable attention as active materials in IR-detectors,[3-5] IR–emitting diodes,[6] lasers[7] field-effect transistors[8] and photovoltaic devices.[9] I have successfully obtained continuous and nearly-monolayer films comprising (111)-faceted single crystallites of PbSe at room temperature at the interface between a solution of lead cupferronate and octylamine in toluene and an aqueous solution of selenourea. I have also tuned the particle shape and size by varying parameters such as concentration, area, etc. I have characterized the films using electron microscopy, FTIR-absorption and Raman spectroscopy. The measured near-infrared photoresponse exhibited a significant responsivity of ca. 80 A/W and a photoconductive gain of ca. 90 owing to oxygen-induced electron trap states.

3.2.2 Methods

3.2.2.1 Synthesis

For the synthesis of PbSe films, lead cupferronate ($Pb(cup)_2$) was used as the lead precursor and selenourea as the source of selenium. To synthesize $Pb(cup)_2$, stoichiometric amounts of $Pb(NO_3)_2$ and cupferron ($C_6H_9N_3O_2$) were separately dissolved in deionized water. After cooling the solutions in an ice-bath for 10 min, $Pb(NO_3)_2$ solution was added drop-wise to the cupferron solution under vigorous stirring. The white precipitate obtained was washed thrice with deionized water and dried overnight in a vacuum desiccator.

In a typical room temperature (RT) synthesis of PbSe films, 0.5 ml of octylamine was added to 15 ml of 1.30 mM solution of $Pb(cup)_2$ in toluene and ultrasonicated for 3 min. The above solution was allowed to stand atop 15 ml of 2.60 mM aqueous solution of selenourea (degassed with N_2 for 5 min) for 4

hrs at RT in a glass beaker with 4.4 cm outer diameter. The resultant gray colored films are comprised of (111)-faceted PbSe single crystallites. When 3.90 mM aqueous solution of selenourea was used, large irregular crystallites were obtained. To obtain films comprising cuboctahedron-like crystallites, the reaction was performed in a glass beaker with 4.4 cm outer diameter for 4 hrs at RT using 0.25 ml of octylamine, 15 ml of 0.65 mM toluene solution of $Pb(cup)_2$ and 15 ml of 1.30 mM aqueous solution of selenourea. To obtain granular films comprising cube-like PbSe crystallites, the reaction was performed in a beaker with 3.4 cm outer diameter using 0.25 ml of octylamine, 15 ml of 0.65 mM toluene solution of $Pb(cup)_2$ and 15 ml of 1.30 mM aqueous solution of selenourea for 4 hrs at RT.

3.2.2.2 Characterizations

X-ray diffraction (XRD) patterns were recorded directly for the films lifted onto glass substrates using Bruker D8 Advance diffractometer with CuK_α radiation (1.54 Å); the films were first dried under N_2-purge before recording XRD. The TEM and SAED were performed on JEOL TEM-3010 electron microscope at an accelerating voltage of 300 kV. Samples for TEM were prepared by gently lifting the films onto carbon-coated copper grids. FESEM images were obtained for the films lifted onto Si/SiO_2 substrates using NOVA NANO SEM 600 (FEI, Germany) at an operating voltage of 15 kV.

To precisely determine the stoichiometry of the films, inductively coupled plasma-optical emission spectroscopy (ICP-OES) was performed on Perkin Elmer Optima 7000 DV instrument. For the ICP-OES analysis, PbSe films were first thoroughly washed with acetone by centrifugation and subsequently dried in vacuum. The dried samples are then digested in 1:1 HNO_3: HCl mixture and diluted with Millipore water. Standards of Pb and Se with different concentrations were prepared from the commercial ICP standards (1000 ppm each) by dilution, and ICP-OES was performed on these standards to obtain a calibration plot of concentration vs. intensity. The concentrations of Pb and Se in the unknown sample are determined by measuring the intensity through ICP-OES and reading the corresponding concentration in the linear regime of calibration plot.

Raman spectroscopy was performed on Jobin Yvon LabRam HR spectrometer using Argon laser excitation (632 nm) in back scattering mode. To estimate the band gap energy, Fourier Transform Infrared (FTIR) spectroscopy was performed in Kubelka-Munk mode on FT-IR Bruker TFS 66V/S instrument. X-ray photoelectron spectroscopy (XPS) was performed on Omicron nanotechnology ESCA instrument (model: EAC 2000 SPHERA 547) using monochromatic Mg Kα X-ray source. Spectra for Se-3d and Pb-4f were obtained with a pass energy of 25 eV and resolution of 0.5 eV. Washed and dried powder samples were used for all the above measurements.

3.2.2.3 Device fabrication

We have examined the near-infrared (NIR) detection of interfacial PbSe films synthesized with Pb:Se precursor ratio of 1:2. Firstly, the toluene layer was slowly removed with a dropper pipette, and the films were gently lifted onto pre-cleaned soda lime glass (SLG) substrates. The films were dried under nitrogen flow and stored in a nitrogen-filled glove box. 40 nm thick gold electrodes were vapor-deposited on the film under vacuum (base pressure of 10^{-6} mbar) with a shadow mask to create a channel spacing of 85 μm. A monochromatic, continuous-wave laser with a wavelength of 1064 nm and a spot diameter of 400 μm was used as a near-infrared source to illuminate the channel vertically. An area of 85 μm x 400 μm was taken as an effective area under illumination. Plots of current versus voltage and time were measured using Keithley source measurement unit (SMU model no. 2420) interfaced to a computer-controlled lab-view program. The optical powers of incident beams were calibrated using new port energy/power meter (model 842-PE).

3.2.3 Results & discussion

3.2.3.1 Interfacial films

Figure 3.2.1 shows the (XRD) pattern of a monolayer film formed at the toluene-water interface with $Pb(cup)_2$ and selenourea concentrations of 1.30 M and 2.6 M respectively (see the synthesis section). XRD pattern can be indexed

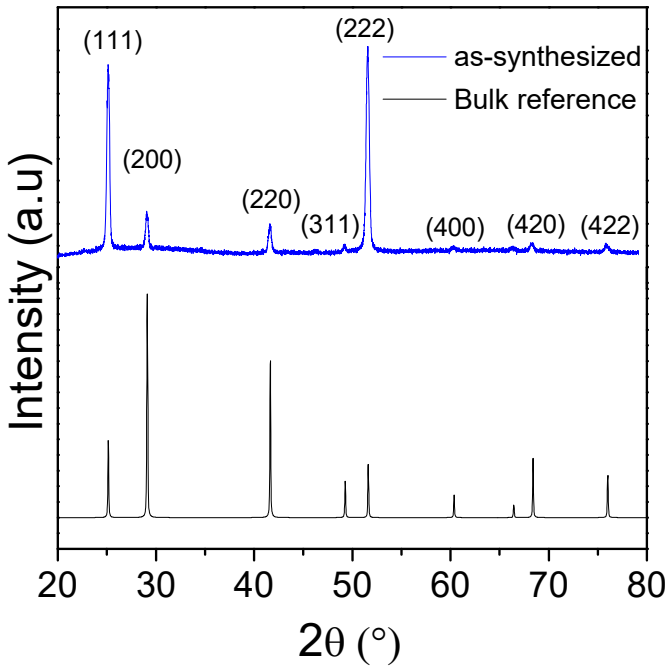

Figure 3.2.1*. XRD pattern of PbSe film lifted onto glass substrate revealing the preferred orientation along <111> direction.*

on rock salt phase of PbSe with *Fm-3m* space group. The film exhibits preferred orientation along (111) and (222) crystallographic planes. The field emission scanning electron microscope (FESEM) image in figure 3.2.2(a) reveals the continuous nature of the fragment with an area spanning tens of microns. Such large area-interfacial films can be readily lifted onto various substrates. The inset in figure 3.2.2(a) is a photograph showing centimeter-scale PbSe interfacial films prepared with Pb:Se precursor ratio of 1:2. Octahedron-like PbSe particles with an average edge-length of 175 nm are close-packed into nearly monolayer films with small randomly distributed overlying islands. The FESEM image of the boxed region of the film in figure 3.2.2(a) is given in figure 3.2.2(b) which shows that the octahedron–like PbSe particles are oriented upright along <111> direction (along the C_3 symmetry axis of an octahedron) while being laterally connected in accordance with the XRD pattern. The film is somewhat rough on the aqueous side (figure 3.2.2(c)) in contrast to the smooth surface on the toluene side. The particles at first appear to be randomly close-packed forming continuous films. Upon closer inspection, the particles are seen to be fused in many a place, along the vertices to form distorted arrays (see the dotted line in figure 3.2.2(b)). The loosely

held particles in some of the regions along the edges of the film are seen to attach along the vertices (Figure 3.2.2(d)).

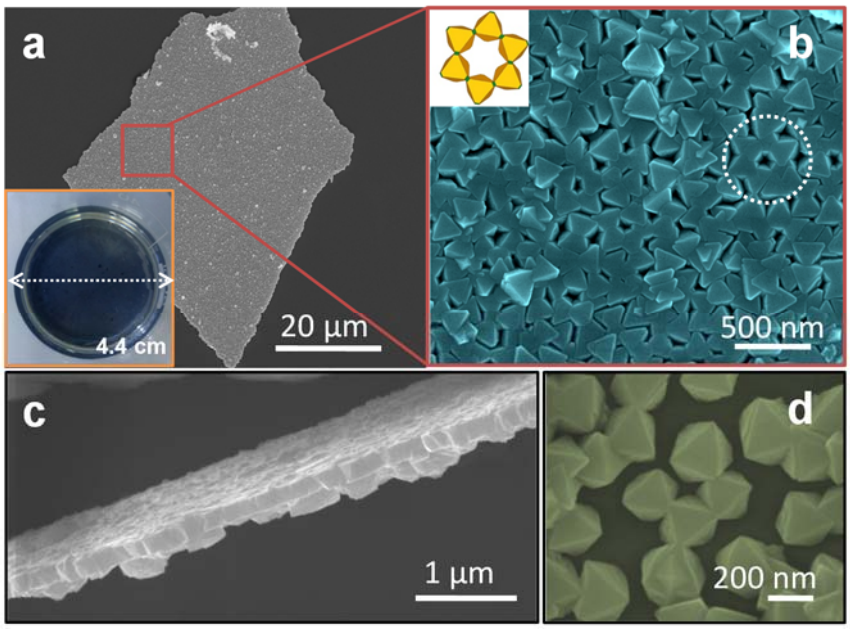

Figure 3.2.2*. a) Low-magnification FESEM image of a fragment of PbSe film obtained with a precursor ratio of Pb:Se=1:2. The inset shows a photograph of centimeter-scale PbSe film; b) magnified FESEM image of the indicated region and the inset is a schematic of the circled region; c) FESEM image projecting a cross-sectional view of the film and d) FESEM image showing the clustering of crystallites along vertices.*

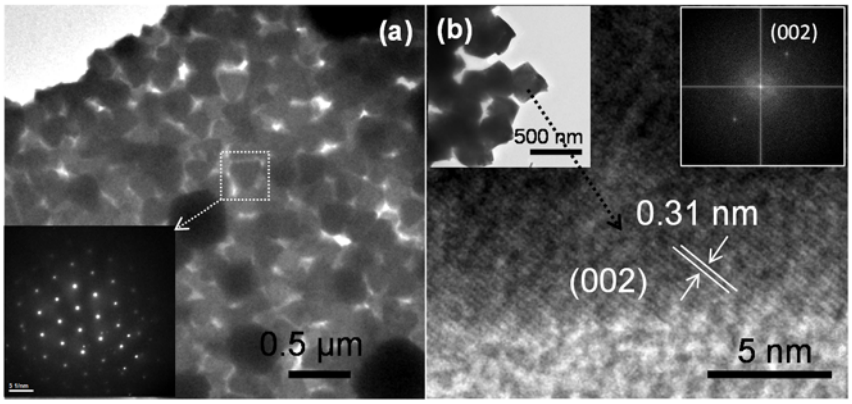

Figure 3.2.3 *a) Low-magnification TEM image of PbSe film obtained with a precursor ratio of Pb:Se=1:2. The inset is a SAED pattern. b) HRTEM image of the indicated region in the top-left inset showing d-spacing of (002) planes. The top-right inset shows the corresponding FFT diffraction pattern.*

The interfacial films remain intact despite ultra-sonication during sample preparation for transmission electron microscopy (TEM). Figure

3.2.3(a) shows a low-magnification TEM image of self-assembled PbSe film. The selected area electron diffraction (SAED) pattern in the inset reveals distinct spots due to the single crystalline nature of constituent particles of the film. High-resolution TEM image of a crystallite near an edge of the fragment in figure 3.2.3(b) shows a d-spacing of 0.31 nm corresponding to (002) crystallographic planes. The corresponding fast Fourier transform (FFT) diffraction pattern is given in the upper-right inset with the diffraction spots indexed on to (002) planes.

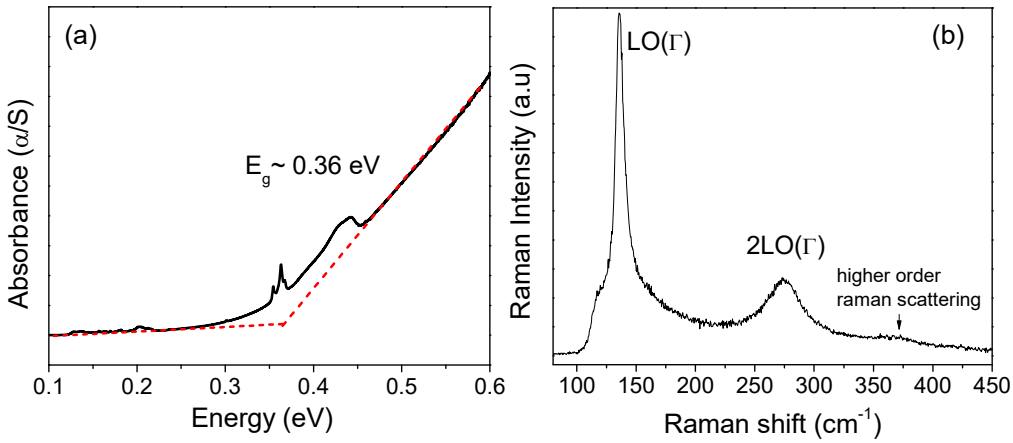

Figure 3.2.4*. a) FTIR absorption spectrum and b) Raman spectrum of PbSe film obtained with a precursor ratio of Pb:Se=1:2.*

The band gap absorption onset of as-synthesized PbSe films is estimated to be ca. 0.36 eV from the Kubelka-Munk FTIR spectrum given in figure 3.2.4(a). The features around 0.35-0.37 eV and 0.41-0.45 eV are due to the stretching frequencies associated with sp^3 C-H and primary N-H bonds of the residual octylamine, respectively. The Raman spectrum in figure 3.2.4(b) shows a prominent peak around 136 cm^{-1} associated with the first-order longitudinal optical phonon (LO(τ)) while the one at 274 cm^{-1} corresponds to the overtone, 2LO(τ). The weak hump beyond 350 cm^{-1} is due to higher order Raman scattering.[10] The electron-phonon coupling strength is characterized by Huang-Rhys parameter, S, which is strongly dependent on the ratio of intensities of first overtone to fundamental lines (I_{2LO}/I_{LO}).[11] The I_{2LO}/I_{LO} ratio from the background corrected Raman spectrum is calculated to be 0.17.

The formation of PbSe films at room temperature is favored by the lowering of interfacial tension between toluene and water through the formation

of so-called "Pickering emulsions" with the particulates.[12-14] The initial reaction between the precursors near the interface generates small PbSe seeds weakly adsorbed at the interface due to lower adsorption energy, ΔG. After they grow into critical dimensions, they firmly adhere to the interface with ΔG higher than thermal energy (kT) by several orders of magnitude. The particle growth is autocatalytic being driven by the lowering of interfacial tension as the particles emulsify the solvents, promoting the further reaction between precursors to result in self-assembled films over a period. Selenourea being a weak source of selenide ions, decomposition of selenourea to release selenide ions may be a rate-limiting process and the nature of films would depend on the concentration of aqueous selenourea. The concentration of selenourea in the aqueous phase is varied relative to that of $Pb(cup)_2$ in the toluene phase (i.e., 1.30 M). Keeping all the reaction parameters constant, when the ratio of concentrations of selenourea to $Pb(cup)_2$ is 1:1, the film is barely formed at the end of 4 h. When the ratio is 2:1, octahedron-like (111)-bound crystallites are formed which are strongly confined at the interface (Figure 3.2.2(b)). At a higher ratio of 3:1, irregular octahedrons are formed owing to an increased rate of reaction (Figure 3.2.5). Furthermore, no deposition occurs even after several hours in the absence of octylamine suggesting that octylamine aids the decomposition of selenourea to release the selenide ions near the interface. Replacing octylamine with the more hydrophobic oleylamine or oleic acid in the toluene phase did not result in the formation of films due to the lower proximity of the latter to the interface.

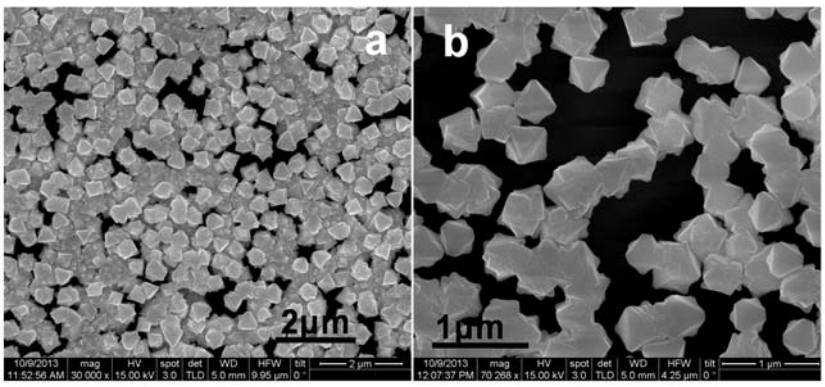

Figure 3.2.5 *(a, b) FESEM images of a fragment of PbSe film obtained with Pb:Se precursor ratio of 1:3.*

Based on the theoretical and experimental studies, it has been established that the surface energies of different crystallographic facets in the cubic rock-salt lead chalcogenide systems follow the order, {100} < {111} < {110}.[13, 15] Thus, under equilibrium growth conditions, PbSe with rock-salt structure would have {100} crystallographic planes as the dominant planes.[16] However, we have obtained octahedron-like PbSe crystallites bound by (111) planes as shown in figure 3.2.2(b). For cubic rock salt systems, the growth ratio along (100) and (111) planes defines the final morphology of the crystallites. (111) planes are polar as they are terminated by either Pb or Se atoms, while (100) planes are neutral containing both Pb and Se atoms. Under kinetic control, the ratio of relative growth rates along (100) and (111) planes can be altered if the latter are selectively blocked by polar capping agents like primary amines. As a result, the growth is retarded along <111> direction while the (100) planes grow faster resulting in crystallites bound by (111) facets.[16]

The size and morphology of the constituent crystallites in the deposits vary with the concentrations of the reagents and the interfacial area. When the reagent concentrations were halved keeping the rest of the parameters unchanged (see synthesis section), the rate of the reaction decreases. The kinetics of growth is altered to result in films comprising small cuboctahedron-like particles (mean size of ca. 70 nm) bound by both (111) and (100) planes (Figure 3.2.6(a)). Maintaining the above conditions, when the diameter of the beaker is decreased from 4.4 cm to 3.4 cm, granular films comprising highly aggregated particles with distorted cube-like morphology and small dimensions are formed as shown in figure 3.2.6(b). Decreasing the interfacial area by narrowing the diameter of the beaker can be treated analogously to lateral compression force exerted by the movable barriers which are employed in Langmuir-Blodgett (LB) trough to control the available surface area of the subphase.[17] As the amount of the toluene phase remains constant, reducing the interfacial area would essentially increase the weight exerted by toluene per unit area of the interface. These factors may lead to an increase in the rate of reaction. As the interfacial area is reduced, the growth of particles is constricted thereby forcing the particles to aggregate early after nucleation to result in granular films of small particles. A similar effect has been observed in the case

of PbS films deposited at the toluene-water interface when the amount of the upper toluene layer was increased.[13] Apart from van der Waals forces, interfacial deformations around the anisotropic particles can engender strong long-range capillary attractive interactions between particles [18] which together result in large-area self-assembled films (see figures 3.2.2(a) and (b)).

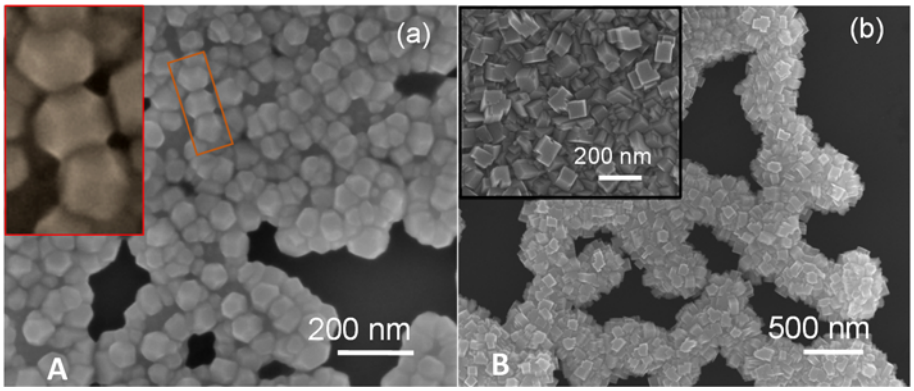

Figure 3.2.6 *FESEM images of films comprising a) cuboctahedron-like particles (inset is a magnified view of the boxed region) and b) distorted cube-like particles (inset is a high-magnification FESEM image).*

3.2.3.1 Near-Infrared photodetection

To investigate the NIR photoconductivity of PbSe films at room temperature, devices were fabricated of the films corresponding to figure 3.2.2(a). A monochromatic, continuous-wave laser of 1064 nm wavelength was used as NIR illumination source. Plots of dark current (I_d) and photocurrent (I_p) under incident optical powers (P_λ) of 86 mWcm^{-2} and 58 mWcm^{-2} as a function of applied bias were presented in figure 3.2.7(a). Responsivity (R_λ) is defined as the photocurrent generated per unit power and is given by: [19, 20]

$$R_\lambda = \frac{I_p - I_d}{P_\lambda S} \qquad 3.2.1$$

where S is the effective area of illumination. R_λ is plotted as a function of applied bias in figure 3.2.7(b). A maximum R_λ of 82 AW^{-1} was obtained at an applied bias of 2V and an incident optical power of 86 mWcm^{-2}. To demonstrate the stability of device, photocurrent is recorded as a function of time by switching the laser on and off alternately for a period of 30 sec at 2 V applied bias and an incident optical power of 86 mWcm^{-2} (Figure 3.2.7(c)). Time-resolved rise and decay for the normalized photocurrent corresponding to figure

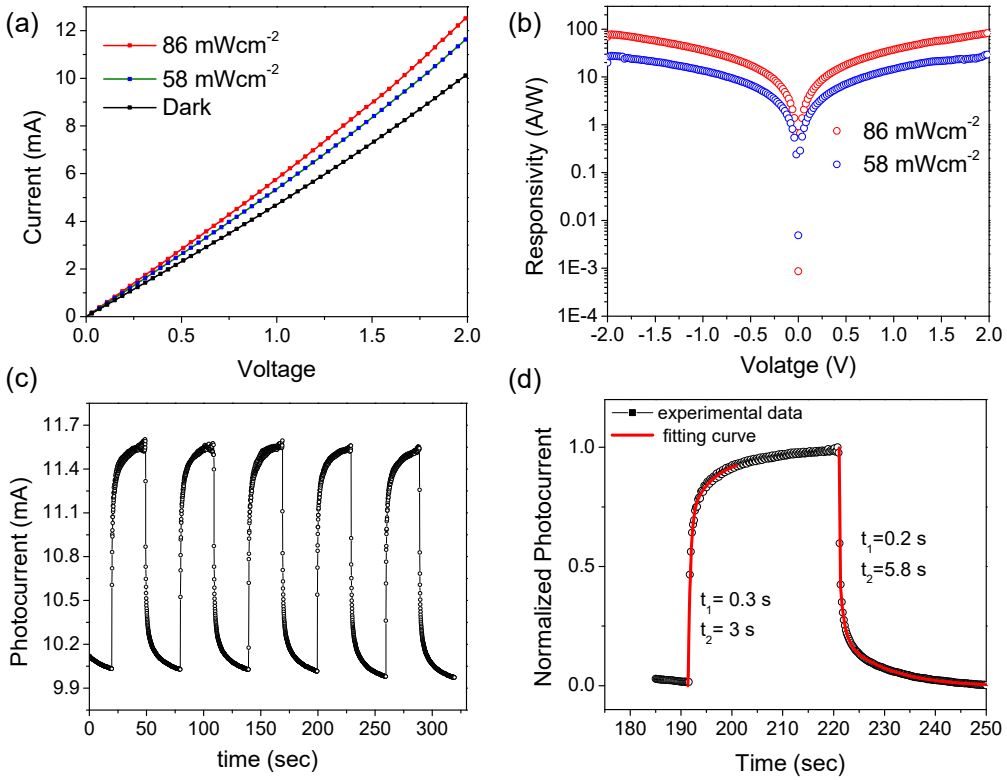

Figure 3.2.7 *Photoconduction properties of PbSe film using 1064 nm laser source. a) Current vs. applied bias in the dark and under incident laser powers of 80 mWcm^{-2} and 100 mWcm^{-2}. b) The plot of responsivity versus applied bias. c) Photocurrent as a function of time with the laser turned on and off at an applied bias of 2 V under incident laser power of 86 mWcm^{-2}. d) Time-resolved photocurrent under laser power of 86 mWcm^{-2} at 2 V bias.*

3.2.7(c) is shown in figure 3.2.7(d). Both the rise and decay in photocurrent can be fitted respectively using double-exponential equations:

$$I(t) = I_d + A[exp\left(\frac{t}{\tau_1}\right)] + B[exp\left(\frac{t}{\tau_2}\right)] \qquad 3.2.2$$

$$I(t) = I_d + A[exp\left(-\frac{t}{\tau_1}\right)] + B[exp\left(-\frac{t}{\tau_2}\right)] \qquad 3.2.3$$

where τ_1 and τ_2 are the time constants, t is the time when the laser was turned on or off, A and B are the scaling constants and I_d is the dark current. The faster (τ_1) and slower (τ_2) components are respectively 0.3 s and 3 s for the rise and 0.2 s and 5.8 s for the decay. Observation of two time constants for the photocurrent decay suggests a β-type photoconduction and the slowest component is associated with the longest-lived trap state.[4, 21] Plots of photocurrent versus time at different optical powers are shown in figure 3.2.8(a). The plot of photocurrent versus laser intensities is linear within the

range of intensities used (Figure 3.2.8(b)), conforming to the well-known power law. [22, 23]

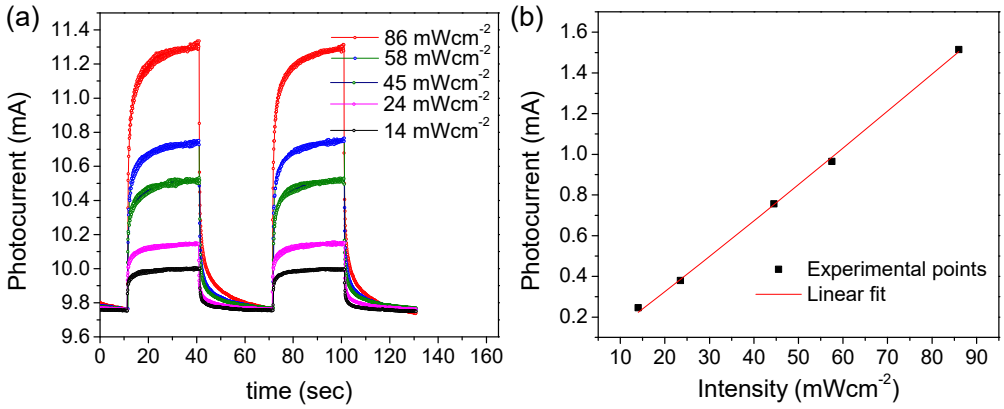

Figure 3.2.8 *a) Plots of photocurrent versus time at different laser powers and b) a linear dependence of photocurrent with laser powers.*

Gain (G) is an important performance metric, defined as the number of electrons (or holes) produced in the circuit per one photon absorbed. G is given by the ratio of life time of photoexcited carriers to the transit time of carriers:

$$G = \frac{\tau}{\tau_{\mathrm{tr}}} = \mu\tau V / L^2 \qquad 3.2.4$$

where μ is the carrier mobility, V is the applied bias, and L is the distance between the electrodes.[23] Gain is also given in terms of steady-state photocurrent: [21]

$$G = \frac{I_p}{e}\ \frac{h\nu}{p_\lambda}\ \frac{1}{\eta\ S} \qquad 3.2.5$$

where h is the Planck's constant, ν is the frequency, e is the absolute electronic charge and η is the effective photocarrier generation efficiency which accounts for the effects of scattering and reflection. For simplicity, if η is assumed to be unity, the calculated gain is about 90 at an applied bias of 2 V and an incident optical power of 86 mWcm^{-2}, which is an appreciably high value. Such high gain can be attributed to the presence of trap states in the PbSe crystallites. The impact of non-stoichiometry in PbSe nanocrystals on the electronic structure and properties via formation of mid-gap sates has been realized earlier.[24-26]

However, the as-synthesized PbSe crystallites are stoichiometric with Pb:Se ratio of 1.03:1 as analyzed by ICP-OES (Table 3.2.1). Films of PbSe nanocrystals exposed to oxygen are known to exhibit a shift in the polarity of

Table 3.2.1 *ICP-OES analysis of interfacial PbSe films*

Initial Pb : Se mole ratio of precursors	Concentration (mg/L)	Std. dev	Final Pb: Se mole ratio in the films
1 : 3	Pb : 16.061	0.039	1.02 : 1
	Se : 5.948	0.021	
1 : 2	Pb : 6.642	0.006	1.03 : 1
	Se : 2.461	0.017	
1 : 1	Pb : 8.540	0.076	1.05 : 1
	Se : 3.092	0.036	

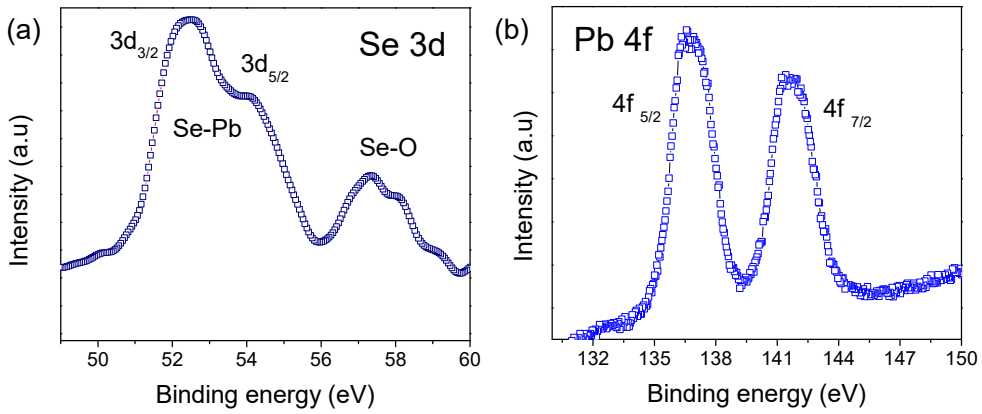

Figure 3.2.9 *XPS analysis of film exposed to oxygen for more than 45 days. a) Se 3d spectra. The peak in the region between 50 eV and 55 eV corresponds to Pb bound Se^{2-} (splitting is due to spin-orbit coupling), and the peak in the region between 56 eV and 60 eV corresponds to oxygen bound Se (IV); b) Pb-4f spectrum.*

transport from ambipolar or n-type to p-type behavior due to hole-doping.[27-29] Controlled doping by oxygen to result in unipolar p-type PbSe field effect transistors has also been demonstrated previously.[30] We ascribe the high dark current in our PbSe film to possible doping due to surface oxidation, and thermal activation of carriers owing to narrow band gap.[29, 31, 32] The high photoconductive gain observed in the present case is attributed to electron trapping in the acceptor levels created by surface oxidation.[29, 31] XPS data for the films exposed to oxygen for a prolonged period ($>$ 45 days) revealed a significant surface oxidation of selenium in agreement with reports in the literature (Figure 3.2.9).[26] Photoconductive gain (G) is usually associated with carrier trapping. Following the exciton-generation, if a carrier of a given type is trapped, the chemical potential for the transport of the opposite carrier is

lowered. If the life time of a given type of carrier in the trap state exceeds the transit time of the opposite carrier, then many carriers can traverse the circuit several times before recombining with the opposite carriers trapped within the photoconductor bulk. In the present case, the photoconductive gain is appreciably high due to trapping of photogenerated electrons in the oxidation-induced electron traps, resulting in a delayed response. Such a trade-off between gain and response/recovery speed is inevitable.[33] Indeed, a large photoconductive gain was achieved in the case of PbS colloidal nanocrystals with the aid of surface oxidation.[4]

Another important metric related to the sensitivity of the detector is the specific detectivity, D*, given by [34, 35]

$$D^* = (S\Delta f)^{\frac{1}{2}}/NEP \qquad 3.2.6$$

where NEP is the noise equivalent power and Δf the electrical bandwidth (Hz). NEP is the minimum optical power at which the signal to noise ratio is one and is given by I_n/R_λ where I_n is the noise current. If the shot noise from the dark current is assumed to be the major contribution to the noise, then the normalized detectivity can be defined as: [35, 36]

$$D^* = R_\lambda/(2.\,e.\,J_d)^{1/2} \qquad 3.2.7$$

where J_d is the dark current density in A cm^{-2}. The room-temperature value of D^* for the PbSe device illuminated with 86 mWcm^{-2} optical power at 2 V bias is estimated to be 2.5×10^{10} Jones.

3.2.4 Conclusions

I have synthesized large-area centimeter-scale PbSe films composed of self-assembled single crystallites of PbSe at the toluene-water interface at room temperature and explored their utility for near infrared photodetection. The PbSe interfacial film exhibited significant responsivity and appreciably high photoconductive gain due to trap-associated mechanisms. In the present work, I primarily emphasize the ability of the liquid-liquid interfacial reactions to generate large-area films suitable for practical applications. The low-cost, mild reaction conditions and the possibility of tuning the nature of deposits make the present strategy a useful alternative bottom-up approach for synthesizing

large-area films of functional materials. The liquid-liquid interfacial route to fabricating strongly interconnected films, particularly, of quantum confined nanocrystals with tunable properties will be of considerable interest and importance for electronic and optoelectronic applications.

3.2.5 References

1. J. M. Pietryga, R. D. Schaller, D. Werder, M. H. Stewart, V. I. Klimov and J. A. Hollingsworth, *J. Am. Chem. Soc.*, 2004, **126**, 11752-11753.
2. J. E. Murphy, M. C. Beard, A. G. Norman, S. P. Ahrenkiel, J. C. Johnson, P. Yu, O. I. Mićić, R. J. Ellingson and A. J. Nozik, *J. Am. Chem. Soc.*, 2006, **128**, 3241-3247.
3. N. Cho, K. Roy Choudhury, R. B. Thapa, Y. Sahoo, T. Ohulchanskyy, A. N. Cartwright, K. S. Lee and P. N. Prasad, *Adv. Mater.*, 2007, **19**, 232-236.
4. G. Konstantatos, I. Howard, A. Fischer, S. Hoogland, J. Clifford, E. Klem, L. Levina and E. H. Sargent, *Nature*, 2006, **442**, 180-183.
5. F. Prins, M. Buscema, J. S. Seldenthuis, S. Etaki, G. Buchs, M. Barkelid, V. Zwiller, Y. Gao, A. J. Houtepen, L. D. A. Siebbeles and H. S. J. van der Zant, *Nano Lett.*, 2012, **12**, 5740-5743.
6. L. Sun, J. J. Choi, D. Stachnik, A. C. Bartnik, B.-R. Hyun, G. G. Malliaras, T. Hanrath and F. W. Wise, *Nat Nano*, 2012, **7**, 369-373.
7. R. D. Schaller, M. A. Petruska and V. I. Klimov, *J. Phys. Chem. B*, 2003, **107**, 13765-13768.
8. M. Law, J. M. Luther, Q. Song, B. K. Hughes, C. L. Perkins and A. J. Nozik, *J. Am. Chem. Soc.*, 2008, **130**, 5974-5985.
9. W. Ma, S. L. Swisher, T. Ewers, J. Engel, V. E. Ferry, H. A. Atwater and A. P. Alivisatos, *ACS Nano*, 2011, **5**, 8140-8147.
10. F. S. Manciu, Y. Sahoo, F. Carreto and P. N. Prasad, *J. Raman Spectrosc.*, 2008, **39**, 1135-1140.
11. S. Acharya, D. D. Sarma, Y. Golan, S. Sengupta and K. Ariga, *J. Am. Chem. Soc.*, 2009, **131**, 11282-11283.
12. Y. Chevalier and M.-A. Bolzinger, *Colloid Surface A*, 2013, **439**, 23-34.
13. D. Fan, P. J. Thomas and P. O' Brien, *J. Am. Chem. Soc.*, 2008, **130**, 10892-10894.
14. P. J. Thomas, E. Mbufu and P. O'Brien, *Chem. Commun.*, 2013, **49**, 118-127.
15. J. M. García-Ruíz, *J. Cryst. Growth.*, 1986, **75**.

16. K.-S. Cho, D. V. Talapin, W. Gaschler and C. B. Murray, *J. Am. Chem. Soc.*, 2005, **127**, 7140-7147.
17. S. Acharya, B. Das, U. Thupakula, K. Ariga, D. D. Sarma, J. Israelachvili and Y. Golan, *Nano Lett.*, 2013, **13**, 409-415.
18. E. M. Furst, *PNAS*, 2011, **108**, 20853-20854.
19. Z. Jin, L. Gao, Q. Zhou and J. Wang, *Sci. Rep.*, 2014, **4**.
20. B. Murali, D. Sandra and S. B. Krupanidhi, *AIP Adv.*, 2013, **3**.
21. S.-C. Kung, W. Xing, W. E. van der Veer, F. Yang, K. C. Donavan, M. Cheng, J. C. Hemminger and R. M. Penner, *ACS Nano*, 2011, **5**, 7627-7639.
22. X. Wang, W. Song, B. Liu, G. Chen, D. Chen, C. Zhou and G. Shen, *Adv. Funct. Mater.*, 2013, **23**, 1202-1209.
23. W. Xing, S.-C. Kung, W. E. van der Veer, W. Yan, T. Ayvazian, J. Y. Kim and R. M. Penner, *ACS Nano*, 2012, **6**, 5627-5634.
24. D. Kim, D.-H. Kim, J.-H. Lee and J. C. Grossman, *Phys. Rev. Lett.*, 2013, **110**, 196802.
25. S. J. Oh, N. E. Berry, J.-H. Choi, E. A. Gaulding, T. Paik, S.-H. Hong, C. B. Murray and C. R. Kagan, *ACS Nano*, 2013, **7**, 2413-2421.
26. S. J. Oh, N. E. Berry, J.-H. Choi, E. A. Gaulding, H. Lin, T. Paik, B. T. Diroll, S. Muramoto, C. B. Murray and C. R. Kagan, *Nano Lett.*, 2014, **14**, 1559-1566.
27. D. M. Balazs, M. I. Nugraha, S. Z. Bisri, M. Sytnyk, W. Heiss and M. A. Loi, *App. Phys. Lett.*, 2014, **104**, 112104-112104-112104.
28. S. J. Oh, D. K. Kim and C. R. Kagan, *ACS Nano*, 2012, **6**, 4328-4334.
29. K. S. Leschkies, M. S. Kang, E. S. Aydil and D. J. Norris, *J. Phys.Chem. C*, 2010, **114**, 9988-9996.
30. D. K. Kim, T. R. Vemulkar, S. J. Oh, W.-K. Koh, C. B. Murray and C. R. Kagan, *ACS Nano*, 2011, **5**, 3230-3236.
31. C. M. Aguirre, P. L. Levesque, M. Paillet, F. Lapointe, B. C. St-Antoine, P. Desjardins and R. Martel, *Adv. Mater.*, 2009, **21**, 3087-3091.
32. E. I. Rogacheva, T. V. Tavrina, O. N. Nashchekina, V. V. Volobuev, A. G. Fedorov, A. Y. Sipatov and M. S. Dresselhaus, *Thin Solid Films*, 2003, **423**, 257-261.

33. C. Soci, A. Zhang, B. Xiang, S. A. Dayeh, D. P. R. Aplin, J. Park, X. Y. Bao, Y. H. Lo and D. Wang, *Nano Lett.*, 2007, **7**, 1003-1009.

34. R. Saran, M. N. Nordin and R. J. Curry, *Adv. Funct. Mater.*, 2013, **23**, 4149-4155.

35. G. Sarasqueta, K. R. Choudhury, J. Subbiah and F. So, *Adv. Funct. Mater.*, 2011, **21**, 167-171.

36. X. Gong, M. Tong, Y. Xia, W. Cai, J. S. Moon, Y. Cao, G. Yu, C.-L. Shieh, B. Nilsson and A. J. Heeger, *Science*, 2009, **325**, 1665-1667.

PART 4

Structure-property relationships in layered transition metal ditellurides, MTe_2 (M=Mo, W).

CHAPTER 4.1

A study of the structural, electronic and vibrational properties of Td-WTe_2*

Summary

The recent discovery of non-saturating giant positive magnetoresistance has aroused much interest in Td-WTe_2. We have investigated the structural, electronic and vibrational properties of Td-WTe_2. Spin-orbit coupling is found to govern the semi-metallic character of Td-WTe_2, and its structural link with the metallic 1T form provides an understanding of its structural stability. There is a metal to insulator cross-over in the electrical conductivity and a change in the sign of the Seebeck coefficient around 373 K in polycrystalline Td-WTe_2. We have analyzed the lattice vibrations of Td-WTe_2. Out of the 33 possible zone-center Raman active modes, five distinct Raman bands are observed around 112, 118, 134, 165 and 212 cm^{-1} in bulk Td-WTe_2. Based on symmetry analysis and calculated Raman tensors, we have assigned the intense bands at 165 cm^{-1} and 212 cm^{-1} to the A_1' and A_1'' modes respectively. The thickness-dependent Raman shifts are found to be anomalous as compared to 2H-MoS_2 and related dichalcogenides. Raman spectroscopy as a function of temperature reveals that the intense A_1'' mode is more anharmonic and sensitive to interlayer coupling whereas the other intense A_1' mode exhibits weak or no dependence on interlayer coupling.

A paper based on this study has appeared in* ***J. Phys.: Condense. Matter**,* 2015, *27*, 285401.

4.1.1 Introduction

Layered transition metal dichalcogenides (TMDCs) are inorganic analogs of graphene, with a broad range of electronic, optical, chemical, thermal and catalytic properties of fundamental and technological importance[1-4]. Among group VI dichalcogenides, the ditellurides exhibit eccentricity concerning structure and properties and are relatively less studied to date. The early electronic structure calculations by Dawson and Bullet [5] revealed that unlike Group VI disulfides and diselenides, the ditellurides deviate from a simple band model predicting a semiconducting behavior due to trigonal prismatic crystal-field splitting. Tungsten ditelluride (WTe_2) crystallizes in a distorted variant of the CdI_2-type structure with an octahedral coordination around the metal, referred to as Td-polytype [6]. The structure of Td-WTe_2 constitutes triple-layers of covalently bonded Te-W-Te atomic planes, stacked along the crystallographic c-axis through weak van der Waals interactions. The WTe_6 octahedra are strongly distorted due to off-centering of W atoms as the latter move towards each other to form slightly buckled W-W zigzag chains running along a-axis. Consequently, WTe_2 exhibits metallic bonding with a W-W bond distance of 2.849 Å - only about 0.13 Å longer than that in tungsten metal [7]. The reduced Madelung energy as compared to the hypothetical 2H-WTe_2 favors this configuration leading to a semimetallic ground state [5, 8]. The exact origin for the preference of the Td-structure instead of the 2H-polytype remains unclear. Earlier experiments on WTe_2 single crystals have revealed a metal-like behavior in the electrical resistivity below ca. 400 K beyond which the resistivity decreases slightly with temperature. The above together with temperature-dependent hall-coefficient and thermopower measurements were earlier interpreted by Kabashima using a three-carrier semimetallic band model.[9] There is, however, no precise identification of these three bands owing to complex band structure with many interwoven bands as revealed by a study of Augustin *et al.* based on angle resolved photoemission spectroscopy (ARPES) and density functional based augmented spherical wave calculations.[8] An extremely large unidirectional (along a-axis) positive magnetoresistance (MR) has been reported recently in single crystals of Td-WTe_2 [10]. MR in WTe_2

does not saturate even at very high applied magnetic fields, and this is considered to be due to a perfectly balanced electron-hole resonance in semimetallic WTe_2, as later complemented with high-resolution ARPES study of low energy electronic structure.[11] The pronounced anisotropy in MR is ascribed to the uniaxial character of the Fermi surface, and the proximity of balanced electron and hole Fermi pockets aligned along W-W chain direction in the k-space.

We have experimentally studied the electronic and thermal transport properties of bulk Td-WTe_2 as a function of temperature. The electronic transport shows a metal-to-insulator cross-over in the electronic conductivity and a change in the sign of Seebeck coefficient from negative (n-type) to positive (p-type) around 373 K. For the first time, we have investigated the phonons in Td-WTe_2 using Raman spectroscopy and examined the effect of temperature and layer-thickness on the Raman bands. To understand the origin for stabilization of Td-structure in WTe_2 and the experimentally observed features of electronic transport, we have also carried out first-principles calculations based on density functional theory.

4.1.2 Methods

4.1.2.1 Synthesis

Polycrystalline WTe_2 was synthesized by annealing finely ground stoichiometric amounts of W powder and Te pieces (total weight of 4g) in an evacuated quartz tube at 650 °C for 12.5 hr and further at 1200 °C for 15 hr followed by cooling slowly to the ambient temperature. Prof. Claudia Felser at the Max Planck Institute, Dresden, has kindly provided me single crystals of WTe_2 to carry out Raman spectroscopy as a function of layer-thickness and temperature. Single crystals of Td-WTe_2 were grown by chemical vapor transport (CVT) of polycrystalline WTe_2 powder using $TeCl_4$ as a transport agent.[12] Tungsten powder was ground together with purified tellurium pieces, pressed into a pellet, and heated in an evacuated quartz tube at 800 ^{0}C for 7 days. 1g of this powder and 0.075 g of $TeCl_4$ was then transferred into a quartz tube which was flushed with Argon thrice, evacuated, sealed and heated in a

two-zone furnace between 880 °C (T_{cold}) and 930 °C (T_{hot}) for seven days with a heating rate of 10 °C per hour. The crystals obtained were silvery–gray flakes and rectangular.

4.1.2.2 Characterizations

A small single crystal was isolated, and the crystal structure was validated by single crystal x-ray diffraction analysis. Data of WTe_2: $Pmn2_1$ (No. 31); a = 3.4950(2), b = 6.2700(4), c = 14.0280(9); Type of Diffractometer: Bruker D8 VENTURE SC X-ray Diffractometer; Mo-kα radiation at 295 K; $2.9 < \vartheta < 50.6$; crystal size = 1 x 0.45 mm; $\mu = 55.848 mm^{-1}$; $\rho = 9.487\ gcm^{-3}$; inversion twin; R = 0.03 and WR2 = 0.089 for all 24855 reflections and 38 variables. Powder X-ray diffraction (PXRD) patterns were recorded using Bruker D8 Advance diffractometer with Cu-Kα radiation.

For atomic force microscopy (AFM), I have mechanically exfoliated few-layer WTe_2 flakes using a scotch-tape and transferred them onto Si/SiO_2 (300 nm) wafers. AFM images and height profiles were obtained using Bruker Innova Microscope instrument in tapping mode with antimony doped silicon tip (10 nm resolution). For transmission electron microscopy (TEM), few-layer Td-WTe_2 flakes were first exfoliated using a scotch tape and then gently transferred onto carbon-coated grids. The low- and high-resolution TEM was performed on JEOL TEM-3010 electron microscope at an accelerating voltage of 300 kV.

Raman spectra of few-layer WTe_2 flakes deposited on Si/SiO_2 wafers and the disc-shaped compacted pellets were recorded on Jobin-Yvon LabRam HR800 microscope using Ar-laser (514.5 nm) excitation in a backscattering configuration. The detector is a Synapse charge-coupled device (CCD) with thermoelectric cooling to -70 °C. A 50× objective was used to focus the laser beam and collect the signal. The diameter of the laser spot is about 1 μm. The backscattered signal was dispersed by 1800 grooves/mm grating with a spectral resolution of about 1 cm^{-1}. The laser power reaching the sample was adjusted to below 2 mW using a neutral density filter to exclude laser-induced heating effects. All the spectra were recorded under identical experimental conditions.

The band positions and intensities were obtained by fitting the bands with a Lorentzian function. Raman spectra were recorded at various temperatures ranging from 123 K to 623 K using a THMS600 stage equipped with a liquid-N_2 cryostat.

4.1.2.3 Transport measurements

To measure the electronic and thermal transport properties of Td-WTe_2 between 300 K and 673 K, finely ground polycrystalline WTe_2 was cold-compacted into a bar- and disc-shaped samples under 30 MPa pressure. The samples were sintered at 500 °C for 10 hr in an evacuated quartz tube (10^{-5} torr). The density of samples was determined by Archimedes method to be ca. 8.6 g/cm^3, i.e., about 92% of the expected theoretical density.

Electrical transport: Electrical conductivity (σ) and Seebeck coefficient (S) for the bar-shaped sample were concurrently measured between room temperature and 673 K in Helium-atmosphere by a four-probe method using ULVAC-RIKO ZEM3 instrument (refer to part 1 for more details). For measuring the magnetoresistance (MR), electrical resistance with (R_H) and without (R_0) applied magnetic field (H) was measured along the length of the bar between 3 K and 300 K by a four-probe method using PPMS instrument. The applied magnetic field was perpendicular to the current direction in the bar. MR is then determined as $\mathrm{MR} = (R_H - R_0)/R_0$. MR measurements were similarly carried out on CVT-grown WTe_2 single crystal with the current-direction being in the a-b plane and magnetic field being normal to the a-b plane.

Thermal conductivity: The thermal diffusivity (D) for the disc-shaped sample was measured between 300 K and 623 K using laser flash diffusivity method in Netzsch LFA-457 instrument (refer to part 1 for more details) and the total thermal conductivity (κ_{tot}) was calculated from diffusivity using the formula, $\kappa_{tot} = Cp \times D \times \rho$ where ρ is the volumetric density and C_p is the heat capacity of sample derived indirectly with respect to a pyraceram reference standard.

4.1.2.4 Computational details

Prof. Waghmare's group at JNCASR has performed the first-principles calculations based on density functional theory (DFT) as implemented in Quantum ESPRESSO package,[13] in which the ionic and core-valence electron interactions are modeled with ultra-soft pseudopotentials.[14] The exchange-correlation energy of electrons is treated within a Generalized Gradient Approximation (GGA) with the functional parameterized by Perdew, Burke, and Ernzerhof. [15] An energy cutoff of 35 Ry was used to truncate the plane wave basis used in representing Kohn-Sham wave functions, and an energy cutoff of 280 Ry, for the basis set to represent charge density. Structures are relaxed to minimize energy till the Hellman-Feynman forces on each atom are less than 0.02 eV/A. A periodic supercell was used to simulate a 2D sheet, including vacuum of 15 Å to separate the adjacent periodic images of the sheet. In self-consistent Kohn-Sham (KS) calculations of configurations of WTe_2 with monolayered form and bulk Td-structure unit cell, the Brillouin zone (BZ) integrations are sampled over uniform meshes of 20×11×1 and 20×11×5 k-points respectively. The electronic structure is determined by including the spin-orbit interaction (SOI) through use of relativistic pseudopotentials using a second variational procedure.[16] Dynamical matrices and phonons at wave vectors on a 3x3x1 mesh in the BZ were determined using DFT linear response (Quantum ESPRESSO implementation based on Green's function method [13]). From these, dynamical matrices and phonons at arbitrary wave vectors in the BZ are obtained using Fourier interpolation. Boltztrap program [17] is used with input from first-principles calculations to understand the temperature-dependence of electronic properties. This program is based on the smoothened Fourier interpolation of the electronic band structure and used for calculating transport-coefficients within semi-classical treatment.

4.1.3 Results & discussion

A schematic of an orthorhombic unit cell of Td-WTe_2 in figure 4.1.1(a) shows the vertical stacking of covalently bonded Te-W-Te triple layers along the c-axis via weak van der Waals interactions. A schematic of the structure

viewed down the c-axis in figure 4.1.1(b) reveals the off-centering of W-atoms from their 'ideal' octahedral sites to form slightly buckled zig-zag W-W chains running along the a-axis. Each W atom is surrounded by eight neighbors: six

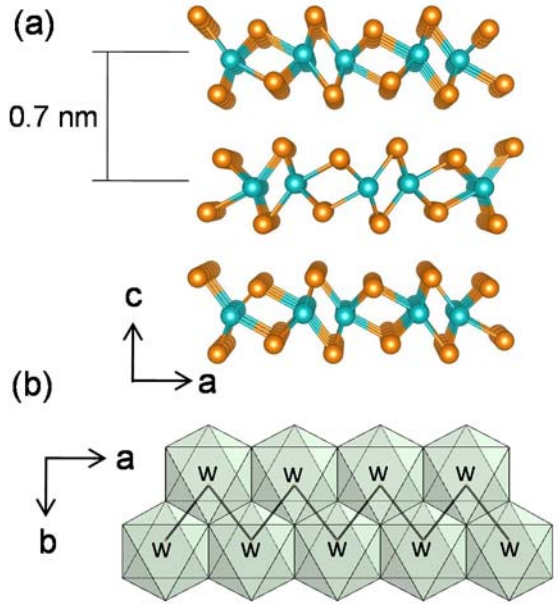

Figure 4.1.1*. a) The orthorhombic unit cell of Td-WTe_2 viewed down the b-axis. Orange and blue spheres denote Te and W atoms respectively. b) Polyhedral representation of a monolayer Td-WTe_2 viewed down the c-axis, showing the zigzag chains of W atoms along the a-axis.*

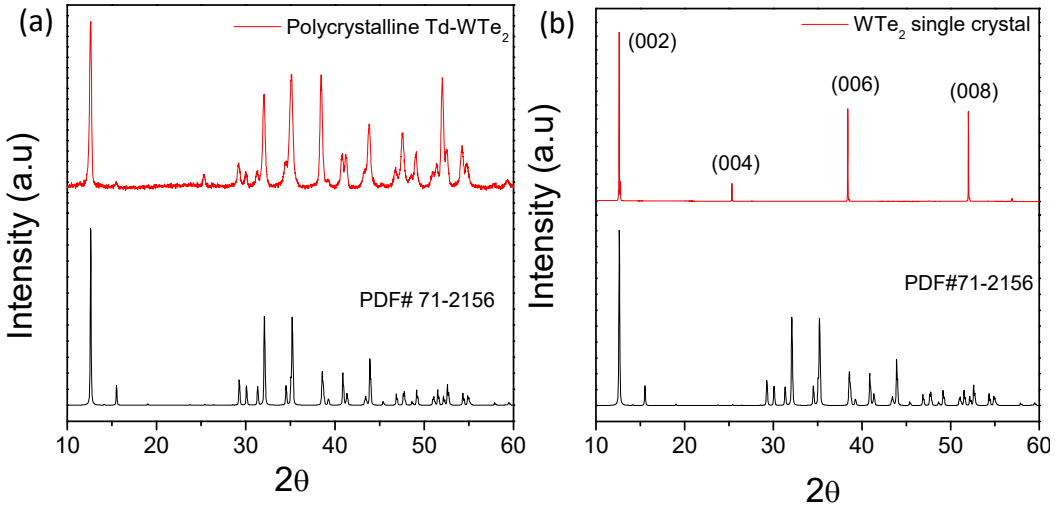

Figure 4.1.2 *Powder X-ray diffraction patterns of a) bulk polycrystalline Td-WTe_2 and b) CVT-grown single crystalline Td-WTe_2. A standard reference pattern of Td-WTe_2 (PDF# 71-2156) is also given for comparison.*

Te atoms and two W atoms. As seen from figure 4.1.1(a), the successive sandwich layers are sequentially rotated by 180^0. The powder X-ray diffraction (PXRD) patterns of the as-synthesized polycrystalline and single crystalline

WTe_2 samples can be indexed on pure orthorhombic Td-WTe_2 (space group $Pmn2_1$) with no detectable impurities (Figure 4.1.2). The PXRD pattern of single crystalline Td-WTe_2 reveals only (00l) peaks due to the preferred orientation of the crystal along [00l] direction, i.e., van der Waal's direction (Figure 4.1.2(b)).

4.1.3.1 Structural stability of Td-WTe_2

Though WTe_2 is known to adopt only Td-structure - a distorted variant of regular 1T structure - the stability of Td-structure has not been explained hitherto. In the following section, we discuss the structural stability of Td-WTe_2 through phonon dispersions.

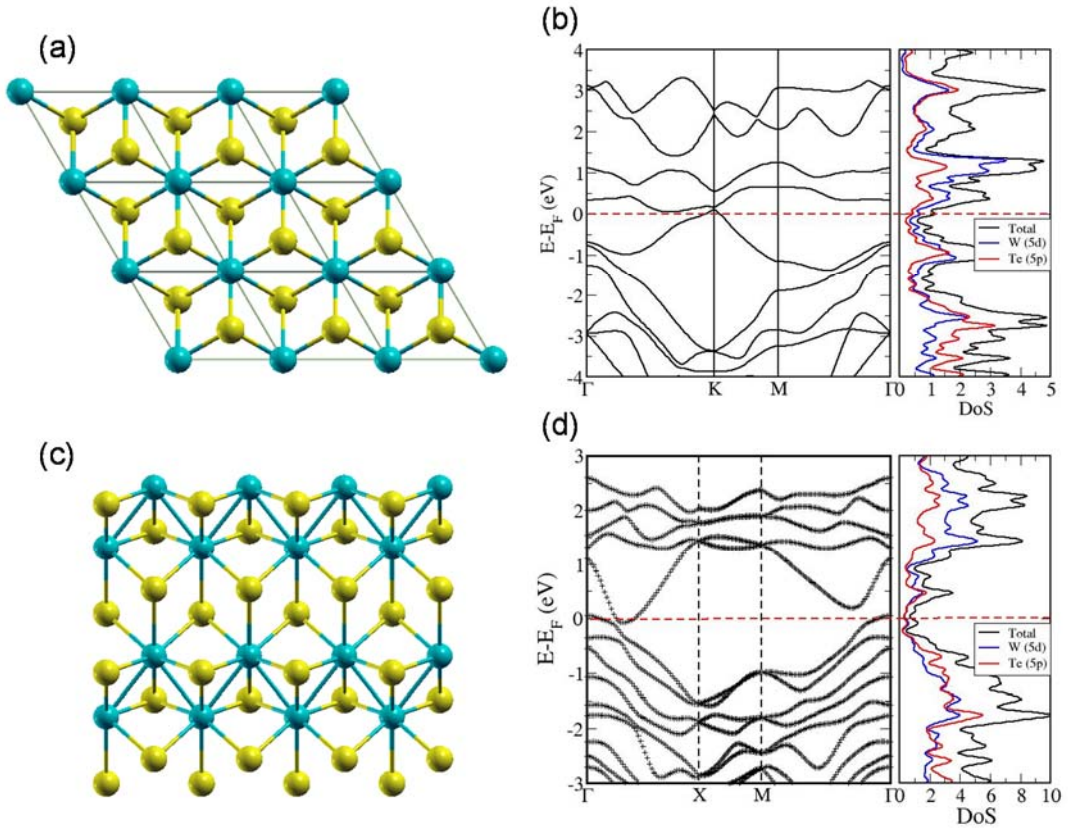

Figure 4.1.3*. Crystal (top-view) and electronic structures of monolayer WTe_2: (a, b) c1T and (c, d) Td forms of WTe_2. The c1T and Td-structures of WTe_2 are metallic and semimetallic respectively. Note that spin-orbit coupling included in these calculations is crucial even for these qualitative properties of the electronic structure. W and Te atoms are shown in cyan and yellow spheres respectively.*

We first note that the bulk Td-structure of WTe_2 is (a) layered and (b) closely related to centrosymmetric 1T structure (or c1T) shown in figure 4.1.3(a). The 1T structure of MX_2 (M= metal, X= chalcogen) has an ABC

stacking of the X-M-X planes with atoms arranged in a triangular lattice. The structure is essentially a close-packed network of regular MX_6 octahedra with M atoms positioned at the centers of octahedra as shown in figure 4.1.3(a). As it has an inversion symmetry, it is referred as the centrosymmetric 1T or *c*1T structure.[18] Due to regular octahedral coordination of W-atoms, the *c*1T structure is metallic with partially-filled t_{2g} orbitals as also revealed by its electronic structure (Figure 4.1.3(b)).

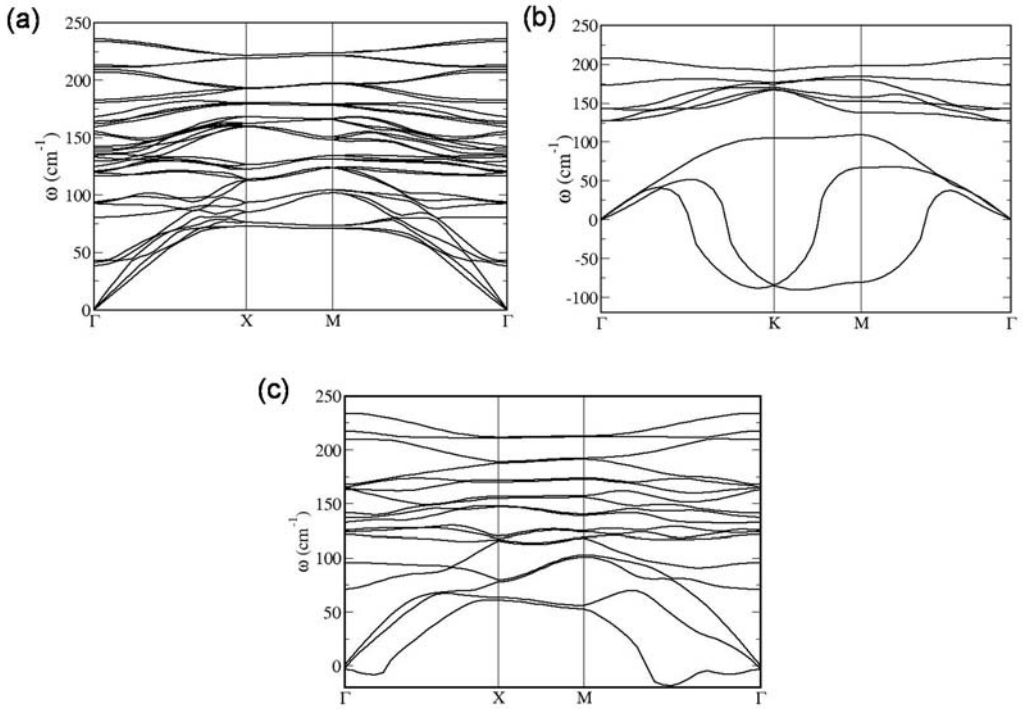

*Figure **4.1.4**. Phonon dispersion curves of (a) bulk Td-WTe_2 and of monolayer WTe_2 in (b) c1T and (c) Td-structures. Note that c1T-WTe_2 exhibits doubly degenerate and singly degenerate instabilities at K and M point respectively.*

We assess the structural stability of c1T monolayer and Td (bulk and monolayer) forms of WTe_2 through determination of their phonon spectra (Figure 4.1.4). If a phonon spectrum exhibits phonon modes with imaginary frequencies ($\omega^2 < 0$), the structure is locally unstable (*i.e.*, it is not a local minimum, but a saddle point in the energy landscape); otherwise it is stable. The eigen displacements of the unstable modes precisely give the structural distortions that lower energy often lowering the symmetry. Our results for phonons of the stable structural forms would be relevant and useful in Raman and infra-red (IR) characterization of these structures. Experimentally, bulk

WTe_2 is known to adopt the Td-structure [6, 7] and our calculated phonon spectrum of bulk WTe_2 exhibits no unstable modes, confirming its stability in the Td-structure (Figure 4.1.4(a)).

Our analysis of the phonon spectrum of the *c*1T polymorph reveals that *c*1T-WTe_2 is structurally unstable, exhibiting structural instabilities with imaginary frequencies of about 100i cm^{-1} (Figure 4.1.4(b)) at K and M points. The unstable mode at the high symmetry K-point of the BZ is doubly degenerate, while it is singly degenerate at the M-point of the BZ. We focus on the M-point instability and its consequences to the structure of the 1T form [18]. On distorting the *c*1T structure in the figure. 4.1.3(a)) with eigen-displacements of its unstable mode at M-point, we get a √3x1 superstructure (figure 4.1.3(c)) with zigzag chains of metal atoms. This distorted structure involving dimerization of metal atoms (where the M-M bonds are significantly contracted by 0.8 Å) is semimetallic (Figure 4.1.3(d)). This distorted √3x1 superstructure is similar to a monolayer of Td-structure though the b/a ratio of experimental lattice parameters is 1.80 (as opposed to 1.73 here) due to coupling with strain. It is evident from phonon spectrum that monolayered Td-structure is locally stable. Weak instabilities near Γ point along the Γ-X and Γ-M directions involve long wavelength rippling of the 2D planar structure (Figure 4.1.4(c)), prevalent in other 2D materials.[19, 20]

4.1.3.2 Electronic structures of bulk and monolayer Td-WTe_2

Group VI dichalcogenides with two nonbonding d-electrons adopt trigonal prismatic coordination (2H-structure) with filled dz^2 orbitals resulting in a semiconducting band gap. As mentioned above, WTe_2 adopts a Td-structure with a distorted octahedral coordination around metal atoms. From our first principles calculations, the energy difference between the 2H- and Td-structures of WTe_2, E_{2H}-$E_{Td,}$ (where E is the total energy of 2H/Td monolayer structure) is 99 meV/f.u showing that WTe_2 prefers Td-structure over 2H-structure. In the case of regular octahedral coordination (1T-structure), the t_{2g} metal orbitals would be partially filled leading to the metallic character. Owing to the off-centering of W-atoms, the nonbonding t_{2g} derived orbitals experience some σ-bonding and split into bonding and antibonding orbitals leaving the

density of states (DOS) minimum at the Fermi level and thus resulting in a semimetal.[8] The degree of distortion is proportional with the splitting of the otherwise degenerate t_{2g} derived orbitals.[21] ReS_2, a group VII dichalcogenide, with three nonbonding d-electrons, is expected to be metallic both in trigonal prismatic (2H) and regular octahedral (1T) structures. ReS_2, however, exists in the 1T-structure with a semiconducting band gap of about 1.55 eV due to the severe distortion of ReS_6 octahedra.[22] The distortion in Td-WTe_2 is, however, smaller compared to 1T-ReS_2 rendering the former semimetallic.

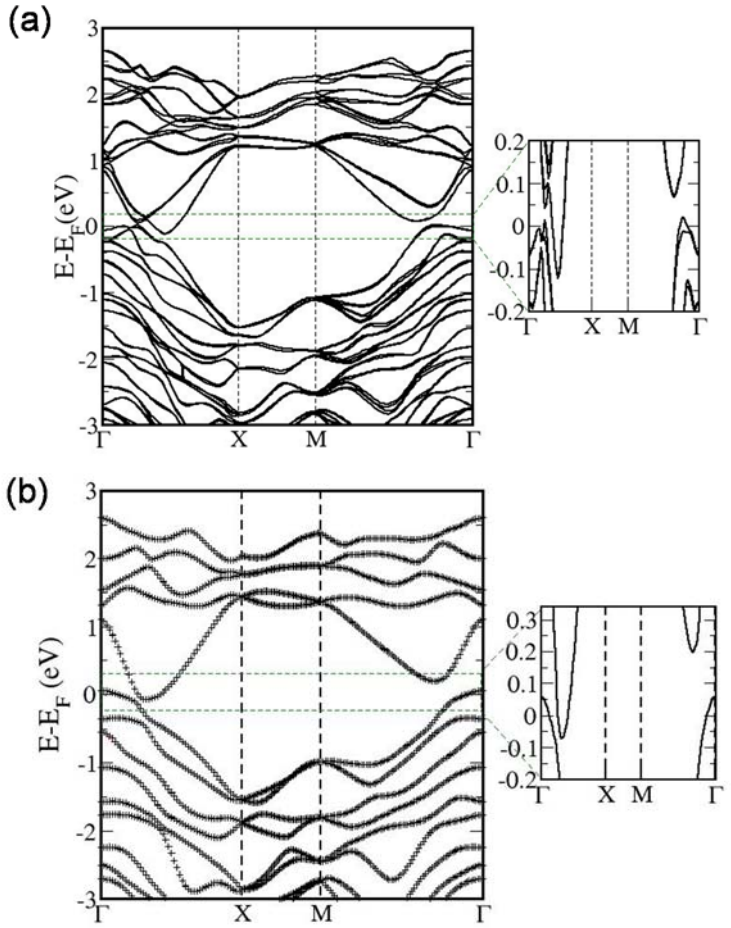

Figure 4.1.5 *Electronic structure of Td-WTe_2 in bulk (a) and monolayer (b) forms with spin-orbit coupling. The region of band structures highlighted in the green box is magnified on the right. Note that indirect band gap close to Γ point (along M-Γ path) in monolayer Td-WTe_2 is higher by 0.10 eV than that in bulk Td-WTe_2.*

Our calculations reveal that bulk and monolayer of Td-WTe_2 exhibit rather similar band structures (Figure 4.1.5), both being semimetallic in nature. As shown in figures 4.1.5(a) and (b), the electron and hole states form

small pockets whose centers are slightly displaced in k-space along Γ-X direction (W-W chain direction). These pockets cross the Fermi energy making Td-WTe_2 semimetallic in both bulk and monolayer forms. We note that the spin-orbit coupling is crucial to these features of the electronic structure and is probably a cause for magnetoresistance. This behavior is in contrast to other TMDCs, in which a strong dependence of their electronic structure on the number of layers is seen.[3] From the partial density of states (DoS), we see that both the valence and conduction bands near Fermi energy (E_F) are composed of W-5d and Te-5p states indicating the covalency in W-Te bonding (Figures 4.1.3 (b) and (d)). The spin-orbit coupling (SOC) included in calculations of electronic structure crucially influences even its qualitative features, for example, the spin-split bands. It is evident from the crystal structure that dimerized chain of W atoms along a-axis (Figure 4.1.1(b)) gives a semimetallic electronic structure along Γ-X direction in the BZ. Along M-Γ path, we find an indirect band gap close to Γ-point (see the zoomed image in figure 4.1.5). This indirect band gap increases from bulk to monolayer by 0.1 eV.

4.1.3.3 Electron transport properties

Figure 4.1.6(a) shows the electrical conductivity (σ) of compacted polycrystalline WTe_2 measured between 3 K and 673 K. The open squares correspond to low-temperature data obtained from PPMS while the closed squares correspond to high-temperature data obtained from ULVAC ZEM-3. σ decreases from 1040 S/cm at ca. 3 K to 740 S/cm at ca. 373 K, exhibiting metal-like behaviour. The metallic conductivity is due to the semimetallic nature of Td-WTe_2. Beyond 373 K, σ increases with temperature reaching 900 S/cm at ca. 673 K with semiconductor-like behaviour.[9, 10] The increase in conductivity above 373 K could arise from thermal excitation of carriers from the lower to the upper states. As seen from figure 4.1.5(a), the bulk Td-WTe_2 structure has a narrow indirect band gap of around 0.05 eV near Γ-point in the band structure seen along M-Γ path which allows thermal excitation of carriers leading to the observed increase in the electrical conductivity of Td-WTe_2 beyond 373 K. The activation energy (E_A) estimated from the Arrhenius plot

(inset of figure 4.1.6(a)) is ca. 0.03 eV which is roughly half of the calculated indirect energy gap of 0.05 eV.

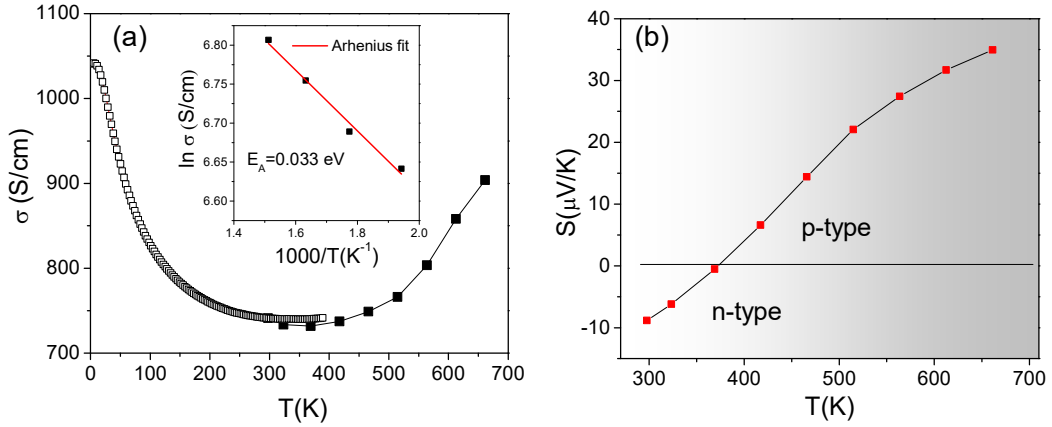

Figure 4.1.6*. Temperature-dependent (a) electrical conductivity, σ and (b) the Seebeck coefficient, S of bulk polycrystalline Td-WTe_2. The inset in (a) shows ln σ vs. 1000/T plot.*

Figure 4.1.6(b) shows the temperature-dependence of Seebeck coefficient (S) measured between 300 K and 673 K. S remains nearly linear throughout the temperature-range investigated which is characteristic of a semimetal. Interestingly, S varies from -9 μVK^{-1} at 300 K to 35 μVK^{-1} at 673 K with a change in its sign from negative (n-type) to positive (p-type) around the metal-to-insulator cross-over temperature of ca. 373 K. The change in the sign of S is consistent with the semimetallic band structure of Td-WTe_2.[23-26] It is to be noted that the Fermi surface in Td-WTe_2 semimetal has been experimentally observed to change with temperature - the relative sizes of electron and hole Fermi pockets vary with temperature, i.e., the position of Fermi level changes leading to n- or p-type conduction depending on relative sizes of electron and hole pockets.[11] In 1966, Kabashima observed a similar sign-change in S around 400 K in the sintered polycrystalline specimens of Td-WTe_2 and explained this behavior based on a three-carrier conduction by heavy holes, light electrons, and light holes. The change in the sign of S from negative to positive was attributed to the contribution of thermally excited light holes beyond 400 K. That said, we cannot entirely rule out the possible effect of innate defects and doping on the observed behavior of S in the present samples, and a further investigation is required to this end.

4.1.3.4 Thermal conductivity

Figure 4.1.7 shows the total thermal conductivity (κ) of polycrystalline bulk Td-WTe_2 measured between 300 K and 623 K. κ increases slightly from 0.96 W/mK near room temperature to 1.06 W/mK at 623 K due to contribution from thermally excited carriers at elevated temperatures. From the phonon dispersion in figure 4.1.4(a), we point out that there are several low frequency transverse acoustic phonon modes related to shear deformation that cause low κ which is proportional to the square of the group velocity of these modes.

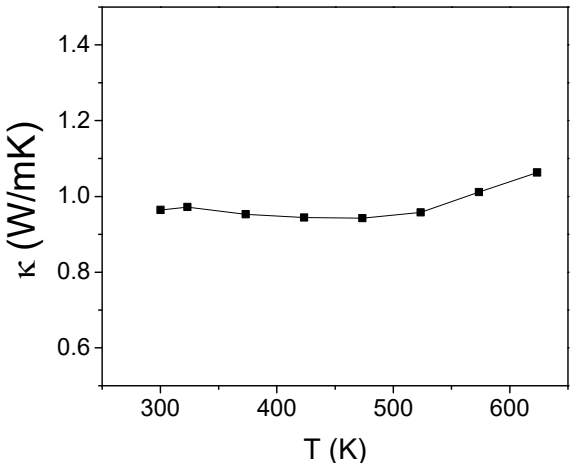

Figure 4.1.7 *Temperature-dependent thermal conductivity (κ) of bulk polycrystalline Td-WTe_2.*

4.1.3.5 Magnetoresistance (MR)

Figure 4.18(a) shows the temperature-dependent resistance of CVT grown Td-WTe_2 single crystal under various applied magnetic fields. When a magnetic field is applied, the resistance of the sample decreases following the zero-field resistance curve until it is cooled down to a 'turn-on' temperature (taken as the temperature where the first derivative of resistance vs. temperature is zero). Below this 'turn-on' temperature, the resistance begins to increase markedly (see figure 4.18(a)). This 'turn-on' temperature, where the metal-to-insulator transition occurs, increases with magnetic field strength from 8 K at 3 T to 45 K at 5 T and further to 65 K at 9 T. Figure 4.1.8(b) shows the field-dependent magnetoresistance (MR) of CVT-grown WTe_2 single crystal. A large MR of ca. 1800 % is obtained at 3 K under a magnetic field of 9 T for the CVT-grown Td-WTe_2 single crystal which, however, decreases drastically above

15 K. Shubnikov-de Haas (SdH) quantum oscillations (Figure 4.1.8(c)) are observed for the MR data at 3 K and 9 T. The SdH oscillations were extracted after fitting a third-order polynomial to the MR vs. 1/H data at 3 K and subtracting that as background. The SdH oscillations are found to vanish at and above 15 K. Preliminary MR measurements on the pellets of polycrystalline sample showed a much smaller MR of ca. 25 % at 3 K and 9 T field (Figure 4.1.8(d)) due to a) large zero-field resistance and b) the anisotropic nature of MR i.e, strong dependence of MR on the crystal-orientation.[10]

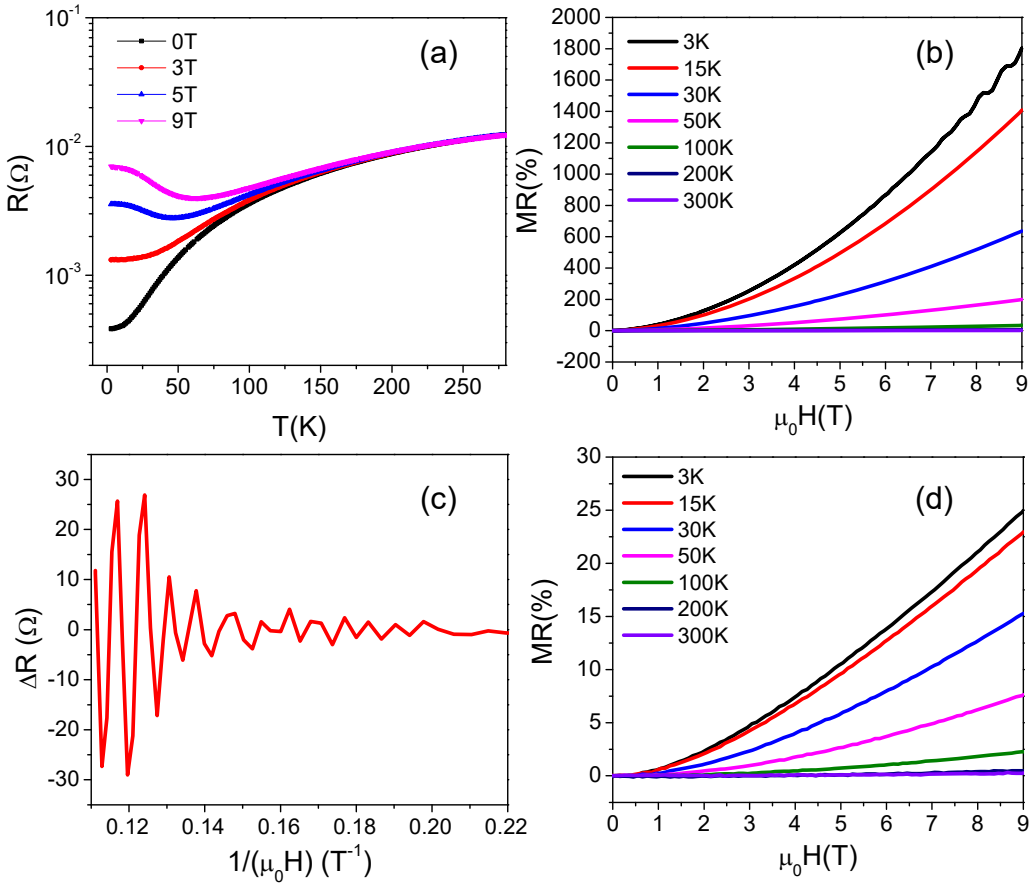

Figure 4.1.8 *a) Resistance of Td-WTe_2 single crystal as a function of temperature at various magnetic fields, showing the 'turn-on' behavior at low temperatures. b) Magnetoresistance (% MR) of Td-WTe_2 single crystal as a function of magnetic field ($\mu_0 H$) at different temperatures and c) corresponding Shubnikov-de Haas quantum oscillations extracted for the field-dependent MR data at 3 K and 9 T. d) MR vs. magnetic field data for the polycrystalline Td-WTe_2 at various temperatures.*

4.1.3.6 Lattice vibrations and Raman Spectroscopy

In the following section, we discuss the lattice vibrations of Td-WTe_2. Bulk Td-WTe_2 has a periodic unit cell containing 12 atoms and belongs to the point group C_{2v} and the space group $Pmn2_1$. There are 33 optically active modes at the Brillion zone center (at Γ-point) whose irreducible representations can be written as:

$$\Gamma_{bulk} \rightarrow 11A_1 + 6A_2 + 5B_1 + 11B_2$$

All the modes are Raman active because of the low crystal symmetry. According to the group theory, optical modes of A_1, B_1, and B_2 symmetry are Raman as well as IR active while the modes of A_2 symmetry are Raman active but IR inactive.

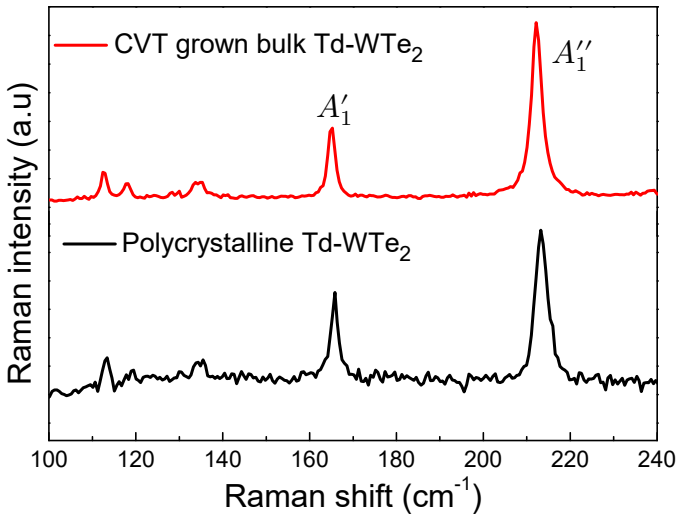

Figure 4.1.9 *Raman spectra of CVT-grown single crystalline Td-WTe_2 (top), and polycrystalline bulk Td-WTe_2 (bottom).*

The Raman spectra of both bulk polycrystalline Td-WTe_2 and CVT-grown single crystalline Td-WTe_2 excited with a 514.4 nm laser show five bands around 112, 118, 134, 165 and 212 cm^{-1} (Figure 4.1.9). The two prominent peaks are centered at ca. 165 cm^{-1} and 212 cm^{-1}. To assign the irreducible representations to calculated phonons at Γ, we obtained overlap (inner product) of a basis vector of an irreducible representation and Eigen vectors of phonon modes (obtained using density functional perturbation theory). There are many modes with frequencies (see Table 4.1.1) close to those of the experimentally observed Raman bands, and the assignment of the observed peaks is, therefore, non-trivial. For example, modes with frequencies of 162

cm^{-1}, 164 cm^{-1} and 168 cm^{-1} make the assignment of the observed intense peak at 165 cm^{-1} difficult, i.e., it can either be A_1 or A_2 or B_1 mode. Similarly, modes with frequencies of ca. 211 cm^{-1} and 213 cm^{-1} are close to the observed intense peak at ca. 212 cm^{-1} which can be assigned to either B_2 or A_1 irreducible representation. The Raman tensor of these possible modes can facilitate the differentiation between these modes. The Raman tensor is calculated as a slope of the linear changes in electronic dielectric constant (the second derivative of the electronic density matrix with respect to a uniform electric field[27]) with normal mode displacements. As bulk WTe_2 is semimetallic, its response to the macroscopic electric field is not finite or well defined, and it is not straightforward to determine the Raman tensor directly. To this end, we have estimated the Raman tensor by constraining the occupation numbers of electrons to treat Td-WTe_2 as an insulator (i.e., the number of occupied bands = number of electrons/2). We identify the modes around 168 cm^{-1} and 207 cm^{-1} as the ones with the largest Raman tensor, both belonging to A_1 symmetry. The observed intense Raman bands around 165 cm^{-1} and 212 cm^{-1} are in agreement with the theoretical estimates and hence designated as the A_1' and A_1'' modes respectively.

***Table 4.1.1**: Calculated phonon frequencies of Raman active modes of Td-WTe_2*

A_1	A_2	B_1	B_2
ν (cm^{-1})	ν (cm^{-1})	ν (cm^{-1})	ν (cm^{-1})
42	38	92	41
80	93	119	94
120	116	129	121
134	125	153	133
138	155	164	136
140	162		142
168			159
183			180
207			209
211			213
233			236

Raman Spectroscopy of few-layer Td-WTe_2

Atomically thin layers of TMDCs constitute a new class of graphene-like 2D electronic materials and promise to become next generation functional materials with unusual electronic, optical and mechanical properties and applications ranging from spin- and valleytronics to photocatalysis and flexible electronics[1-4]. Raman spectroscopy is a powerful analytical tool for determining thickness and stacking of 2D layered materials, [28] to study their thermal [29, 30] and mechanical properties, [31] and to directly probe and monitor the charge-doping.[32] Owing to low-temperature giant positive magnetoresistance and the ease of exfoliation of single crystals, few-layer Td-WTe_2 can be potential for thin-film device applications such as low-temperature field-sensing and high-field temperature-sensing in cryogenics. The van der Waals inter-layer coupling in the anisotropic layered materials has been shown earlier to affect the lattice vibrations by causing systematic shifts in the Raman peaks with varying layer-thickness. These changes can be useful to determine the number of layers in the sample and hence it is important to study the effect of layer-thickness on the lattice vibrations in Td-WTe_2.

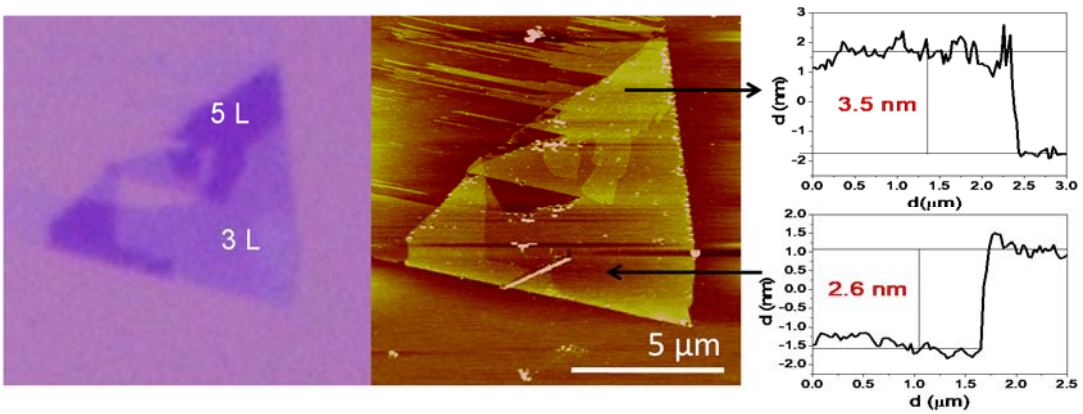

***Figure 4.1.10**. Optical microscope images of few-layer Td-WTe_2 flake deposited on Si/SiO_2 substrates (left) and the corresponding AFM image (middle) and height profiles (right).*

Few-layer WTe_2 flakes were mechanically exfoliated (using a scotch tape) from CVT-grown WTe_2 single crystals and deposited onto Si substrates coated with 300 nm thick SiO_2 layer. The few-layer WTe_2 flakes were first identified using optical microscopy, and the flake-thickness was precisely determined through atomic force microscopy (AFM). Figure 4.1.10 shows a

representative optical image of mechanically exfoliated WTe_2 flake deposited on Si/SiO_2 substrate and the corresponding AFM height profiles. A monolayer thickness of ca. 0.7 nm (Figure 4.1.1) was used for estimating the number of layers. Figure 4.1.11(a) shows transmission electron microscope (TEM) image of mechanically exfoliated few-layer WTe_2 flake deposited on a carbon-coated copper grid. The high-resolution TEM (HRTEM) image of a flake in figure 4.1.11(b) reveals an interlayer spacing of ca. 0.7 nm corresponding to the d-spacing of (002) planes. The HRTEM image of a flake with layers perpendicular to the electron beam is shown in figure 4.1.11(c). The fast Fourier transformation (FFT) electron diffraction pattern of the region indicated in figure 4.1.11(c) projects a view down the [-1 0 1] zone axis with (111), (101) and (212) reflections (Figure 4.1.11(d)).

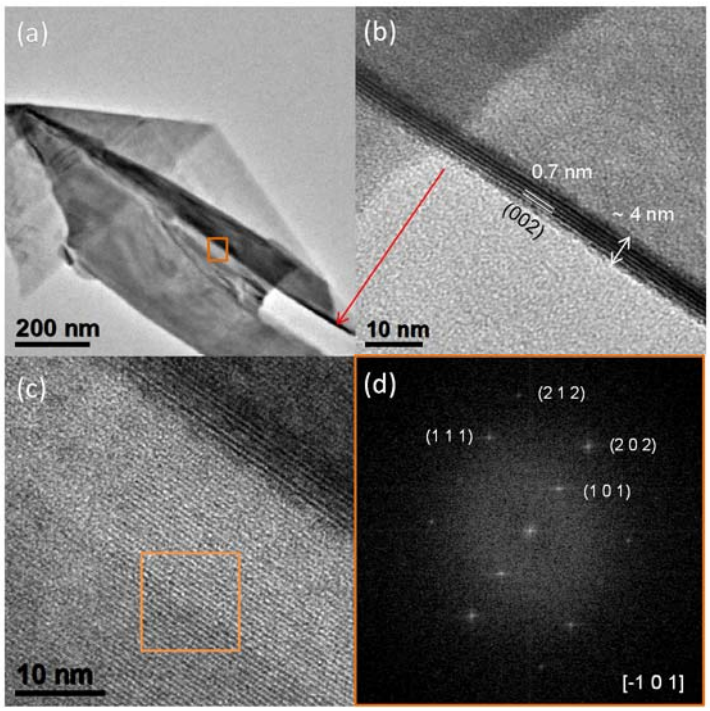

Figure 4.1.11*. a) TEM image of few-layer Td-WTe_2, b) HRTEM image of the region indicated by an arrow, revealing (002) planes with d-spacing of ca. 0.7 nm, c) HRTEM image of the boxed area in (a) and d) FFT image of the boxed region in (c).*

The Raman spectrum of 3-layer Td-WTe_2 recorded at room temperature under 514.5 nm laser excitation reveals six bands centered around 108, 120, 135, 164, and 216 cm^{-1}, the last two intense bands being assigned to A_1' and A_1'' respectively from the aforementioned analysis of Raman tensor. Figure 4.1.12(a) shows the Raman spectra recorded on exfoliated flakes of different

thicknesses (3, 4, 5, 6, 10 and 25 layers) at room temperature using 514.4 nm laser-excitation. The intensity of all the Raman peaks increase with decreasing thickness. The shifts in various Raman peaks are plotted as a function of thickness (Figure 4.1.12(b)). All the peaks stiffen with decreasing thickness except the intense A_1' peak which is nearly independent of thickness and the one at ca. 112 cm^{-1} which softens with decreasing thickness (Figure 4.1.12(b)).

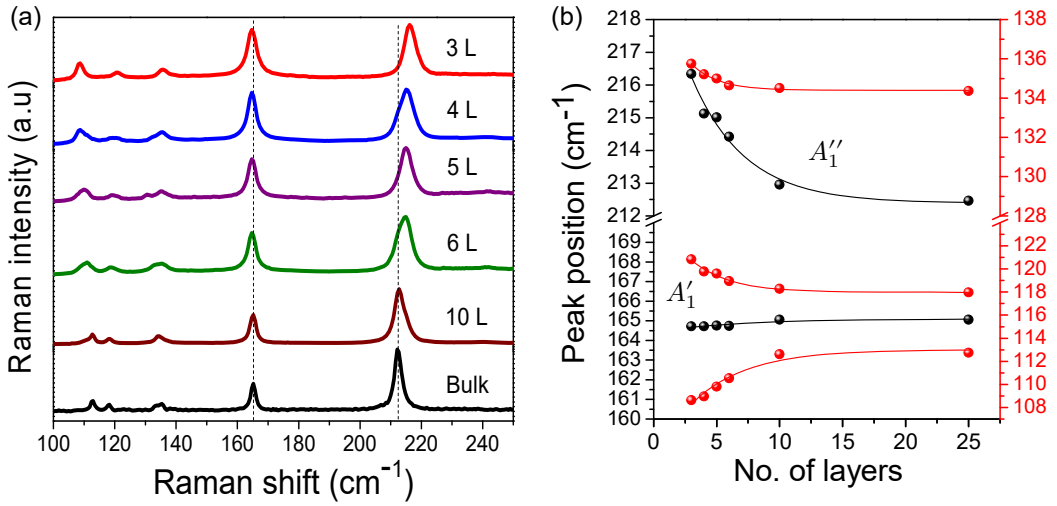

Figure 4.1.12. *a) Raman spectra of Td-WTe_2 layers with different thicknesses under 514.4 nm laser excitation and b) peak positions of various bands as a function of layer-thickness.*

In 2H-MoS_2 and the related TMDCs, the out-of-plane A_{1g} vibration softens with decreasing thickness which is justified as being a consequence of reducing interlayer van der Waals interactions and hence the effective restoring forces on atoms with decreasing thickness. The observed stiffening of the in-plane E_{2g} vibration with decreasing thickness has been attributed to stacking-induced changes in intralayer bonding .[33-37] On the other hand, in Td-WTe_2, we find that the intense A_1'' band is most sensitive to the number of layers, exhibiting an up-shift of about 4 cm^{-1} in a 3-layer flake relative to bulk Td-WTe_2 whereas the intense A_1' band does not change with the number of layers though both belong to the same A_1 symmetry. To understand such contrasting dependence on thickness, we first examine the displacements of W and Te in the eigenvectors of these modes (Figure 4.1.13). Firstly, it can be seen that (i) the A_1' mode involves out-of-plane (z-direction) displacements of Te atoms and in-plane (x-y) displacements of W atoms and (ii) the A_1'' mode involves out-of-plane displacements of W atoms and in-plane displacements of Te atoms. Such

complex mixing of in-plane and out-of-plane components of atomic displacements is a consequence of low crystal-symmetry due to distortion in Td-WTe_2 and has been recently reported for a similar strongly distorted structure of 1T-ReS_2 [22]. Secondly, the Te atoms of the same plane vibrate in-phase in the A_1' mode of vibration (Figure 4.1.13(a, b)), while their motion is out-of-phase in the A_1'' mode of vibration (Figure 4.1.13(c, d)).

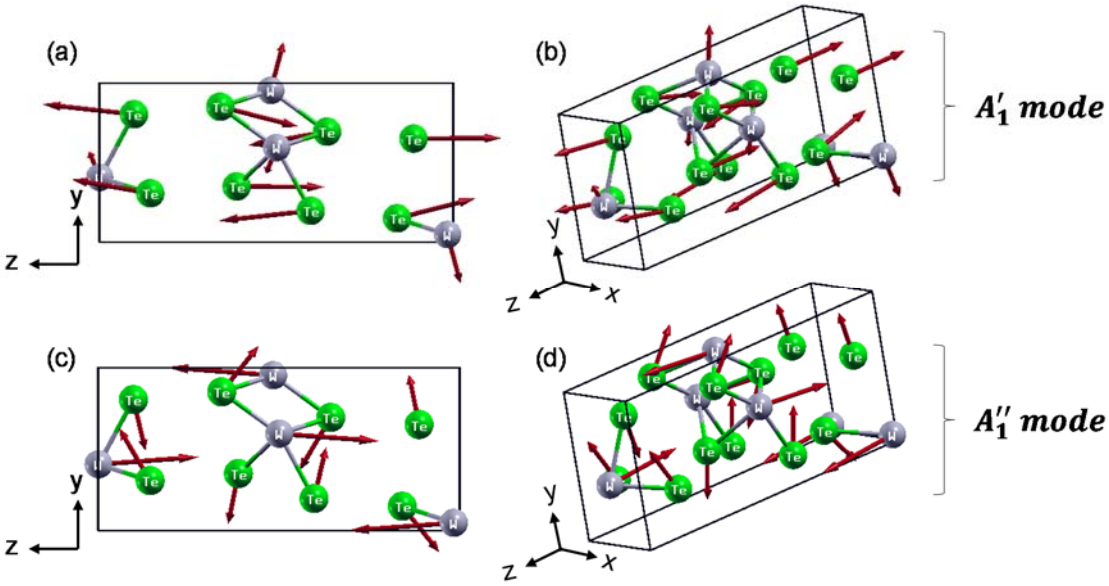

Figure 4.1.13 *Raman active phonon modes of bulk Td-WTe_2 with largest Raman tensor. (a, b) Two views of the atomic displacements of the A_1' mode observed at ca. 165 cm^{-1} in bulk Td-WTe_2; (c, d) Two views of the atomic displacements of A_1'' mode observed at ca. 212 cm^{-1} in bulk Td-WTe_2. W and Te atoms are represented by grey and green spheres respectively.*

To confirm the observed changes in Raman bands as a function of thickness, we compare the calculated Raman mode frequencies of monolayer Td-WTe_2 with those of the bulk Td-WTe_2. We find stiffening of the A_1'' mode by ca. 3 cm^{-1} and also softening of the A_1' mode by ca. 3 cm^{-1} in the monolayer with respect to bulk. While this is consistent with the observed trend in the A_1'' mode, it suggests an additional compensating mechanism that governs the thickness-dependence of the A_1' vibrational mode, which needs further investigation. The observed stiffening of A_1'' mode with decreasing thickness is plausibly due to modification of force constants through compression of bond lengths. As seen in figure 4.1.13(a), the Te-vibrations appear to be more localized within a Te-W-Te layer in the A_1' mode which explains in part the

observed insensitivity of this mode to the number of layers. Furthermore, the ratio of the observed integrated intensities of A_1'' to A_1' bands decreases from ca. 2 in the bulk to ca. 1 in 3-layer flake reflecting the thickness-dependence of relative oscillator strengths of these modes.

Temperature dependence of Raman Spectra

To gain further insights, we have investigated the temperature-dependence of phonons in bulk and few-layer Td-WTe_2. Anharmonic effects such as thermal expansion and thermal conductivity will have implications especially in devices fabricated of few-layer TMDCs. The thermally-induced anharmonic shifts in Raman peak frequencies are, therefore, important to study and are expected to be different for few-layers and bulk. Figure 4.1.14(a) shows the Raman spectra of bulk polycrystalline Td-WTe_2 recorded at various temperatures. All the Raman peaks are observed to soften with increasing temperature, and the line-shape doesn't deviate from a symmetric Lorentzian profile in the range of temperature studied, suggesting the absence of strong electron-phonon coupling. Figure 4.1.14(b) shows the temperature-dependence of the intense A_1' (165 cm^{-1}) and A_1'' (212 cm^{-1}) bands obtained by fitting the bands with a Lorentzian function. The phonon softening with temperature is ascribed to the thermal expansion (implicit contribution), and anharmonic phonon-decay process (explicit contribution) where an optical mode at the zone center decays into two or three acoustic modes with conservation of energy and momentum.[38, 39] Besides, the decreased van der Waals interlayer coupling at higher temperatures can also lead to phonon softening.[29] For simplicity, the present experimental data points are fitted considering only the linear implicit contribution using:

$$\omega\,(T) = \omega_0 - \alpha\,T \qquad (4.1.1)$$

where ω_0 is the peak position at 0 K and α is the first order temperature coefficient. α is proportional to mode Grüneisen parameter (γ_i) which is in turn commensurate with the strength of phonon anharmonicity. The experimental data can be well fitted with equation 4.1.1 and the linear temperature coefficients (α) for the A_1' (165 cm^{-1}) and A_1'' (212 cm^{-1}) bands are estimated to be 0.0060(4) $cm^{-1}K^{-1}$ and 0.0081(4) $cm^{-1}K^{-1}$ respectively. The

higher value of α for the A_1'' vibration relative to the A_1' vibration reflects higher sensitivity of the former to temperature (i.e., more anharmonic). Also, the ratio of integrated intensities of A_1'' to A_1' bands decreases with increasing temperature suggesting that the anharmonic A_1'' mode has increased phonon decay channels at elevated temperatures.

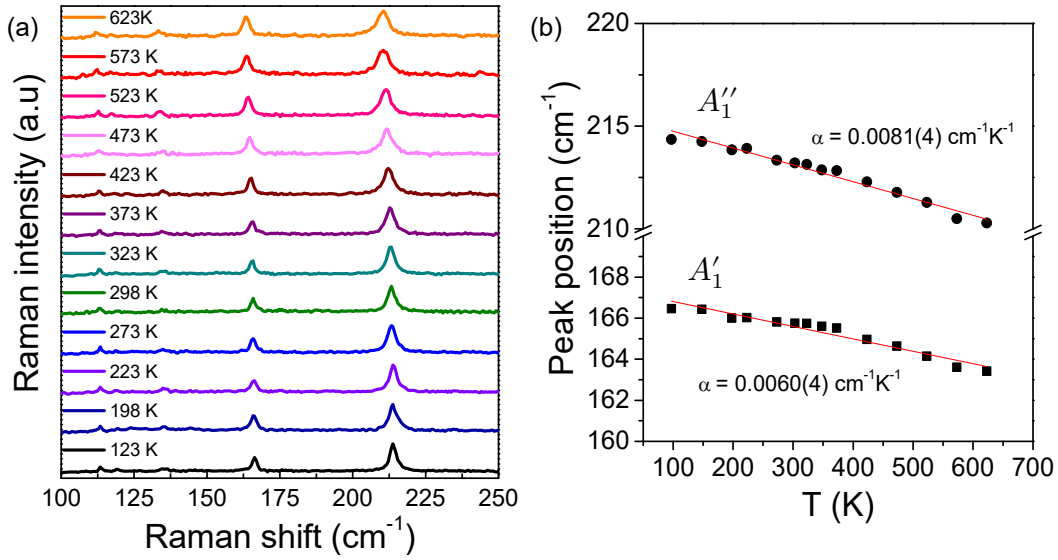

Figure 4.1.14. *a) Raman spectra of bulk polycrystalline Td-WTe_2 recorded at various temperatures under 514.4 nm laser excitation and b) peak positions of the two intense bands as a function of temperature.*

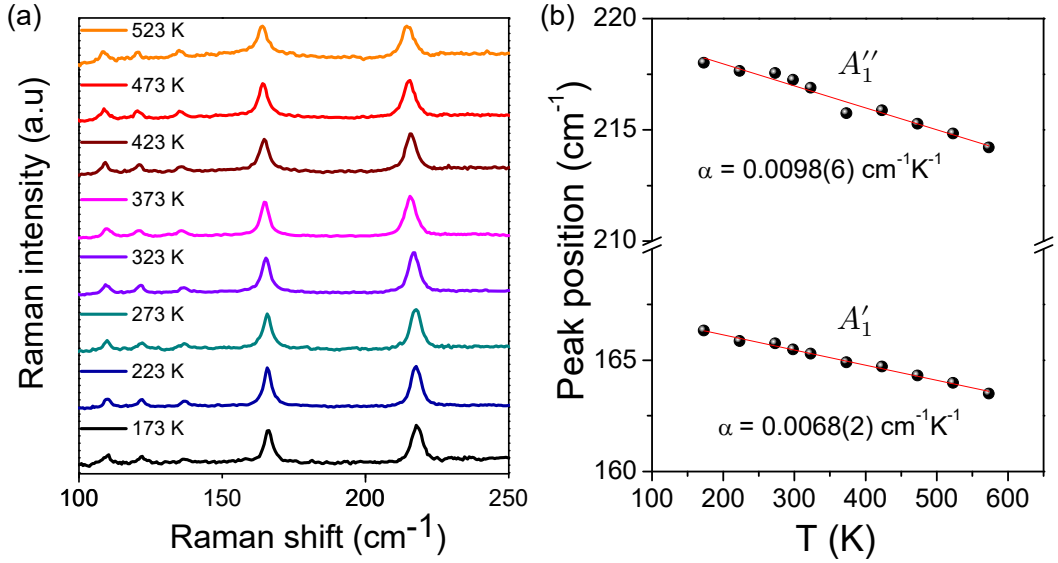

Figure 4.1.15. *a) Raman spectra of 3-layer Td-WTe_2 recorded at various temperatures under 514.4 nm laser excitation and b) peak positions of the two intense bands as a function of temperature.*

Figure 4.1.15(a) shows the Raman spectra of 3-layer Td-WTe_2 recorded at various temperatures. All the Raman peaks of the 3-layer sample soften with increasing temperature similar to the bulk counterpart. Figure 4.1.15(b) shows the temperature-dependence of the observed intense A_1' and A_1'' bands obtained by fitting the bands with a symmetric Lorentzian function. Similar to bulk Td-WTe_2, the estimated linear temperature coefficient (α) of 0.0098(6) $cm^{-1}K^{-1}$ for the A_1'' band is greater than that of 0.0068(2) $cm^{-1}K^{-1}$ for the A_1' band. The former being higher than that of bulk Td-WTe_2 and the latter being similar to that of bulk Td-WTe_2 necessarily suggest that A_1'' is more sensitive to thickness (and hence, interlayer coupling) while A_1' has weak or no dependence on thickness, which is in accord with the thickness-dependent Raman analysis. Besides, the temperature coefficients being distinct from those of bulk can also be useful to characterize few-layer samples.

4.1.4 Conclusions

We have studied the structural, electronic and vibrational properties of Td-WTe_2. We bring out the structural link between the Td-structure of WTe_2 and the *c*1T-structure found in other TMDCs and explain the stability of Td-structure through phonon instabilities in the metallic *c*1T form. The periodic distortions in Td-WTe_2 resemble charge density waves observed in a few other TMDCs (refer to part 1), and the associated increase in elastic energy is compensated by electronic stabilization at the Fermi level. As a result, bulk as well as monolayer Td-WTe_2 exhibit semimetallic electronic structures in contrast with 2H-MoS_2. From the electrical transport measurements, polycrystalline bulk Td-WTe_2 is found to exhibit a metal-to-insulator cross-over in the electrical conductivity around 373 K, along with a change in the sign of Seebeck coefficient from negative (n-type) to positive (p-type). The increase in conductivity beyond 373 K arises from the thermal excitation of carriers, and the sign-change in S is ascribed to the contribution of light holes to the conduction. The Raman spectrum of bulk Td-WTe_2 shows five distinct bands around 112, 118, 134, 165 and 212 cm^{-1}. We have assigned the intense bands at 165 cm^{-1} and 212 cm^{-1} to the A_1' and A_1'' modes respectively. I have

examined the effect of temperature and the number of layers on the Raman bands. Most of the Raman bands stiffen with decreasing thickness and the ratio of integrated intensities of the A_1'' to A_1' bands decreases in the few-layer sample while all the bands soften in both the bulk and few-layer samples with increasing temperature. Analysis shows that the A_1'' mode is more sensitive to interlayer coupling and is more anharmonic whereas the other intense A_1' mode exhibits weak or no dependence with layer thickness. The seemingly anomalous thickness-dependence of Raman bands as compared to 2H-MoS_2 is ascribed to the complex mixing of in-plane and out-of-plane atomic displacements in Td-WTe_2 arising from periodic distortions.

4.1.5 References

1. M. Chhowalla, H. S. Shin, G. Eda, L.-J. Li, K. P. Loh and H. Zhang, *Nat Chem*, 2013, **5**, 263-275.
2. V. Nicolosi, M. Chhowalla, M. G. Kanatzidis, M. S. Strano and J. N. Coleman, *Science*, 2013, **340**, 1226419.
3. C. N. R. Rao, U. Maitra and U. V. Waghmare, *Chem. Phys. Lett.*, 2014, **609**, 172-183.
4. Q. H. Wang, K. Kalantar-Zadeh, A. Kis, J. N. Coleman and M. S. Strano, *Nat Nanotech*, 2012, **7**, 699-712.
5. W. G. Dawson and D. W. Bullett, *J. Phys. C: Solid State Phys.*, 1987, **20**, 6159-6174.
6. B. Brown, *Acta Cryst.*, 1966, **20**, 268-274.
7. A. Mar, S. Jobic and J. A. Ibers, *J. Am. Chem. Soc.*, 1992, **114**, 8963-8971.
8. J. Augustin, V. Eyert, T. Boker, W. Frentrup, H. Dwelk, C. Janowitz and R. Manzke, *Phys. Rev. B*, 2000, **62**, 10812-10823.
9. S. Kabashima, *J. Phys. Soc. Jpn.*, 1966, **21**, 945-948.
10. M. N. Ali, J. Xiong, S. Flynn, J. Tao, Q. D. Gibson, L. M. Schoop, T. Liang, N. Haldolaarachchige, M. Hirschberger, N. P. Ong and R. J. Cava, *Nature*, 2014, **514**, 205-208.
11. I. Pletikosić, M. N. Ali, A. Fedorov, R. J. Cava and T. Valla, *Phys. Rev. Lett.* , 2014, **113**, 216601.
12. M. Binnewies, R. Glaum, M. Schmidt and P. Schmidt, 2010.
13. P. Giannozzi, S. Baroni, Nicola Bonini, Matteo Calandra, Roberto Car, C. Cavazzoni, Davide Ceresol, Guido L Chiarotti, Matteo Cococcioni, Ismaila Dabo, Andrea Dal Corso, Stefano de Gironcoli, Stefano Fabris, Guido Fratesi, Ralph Gebauer, Uwe Gerstmann, Christos Gougoussis, Anton Kokalj, Michele Lazzeri, Layla Martin-Samos, Nicola Marzari, Francesco Mauri, Riccardo Mazzarello, Stefano Paolini, Alfredo Pasquarello, Lorenzo Paulatto, Carlo Sbraccia, Sandro Scandolo, Gabriele Sclauzero, Ari P Seitsonen, Alexander Smogunov, P. Umari and R. M. Wentzcovitch, *J. Phys.: Condens. Matter*, 2009, **21**, 395502.

14. D. Vanderbilt, *Phys. Rev. B*, 1990, **41**, 7892-7895.
15. J. P. Perdew, K. Burke and M. Ernzerhof, *Phys. Rev.Lett.*, 1996, **77**, 3865-3868.
16. A. D. Corso and A. M. Conte, *Phys. Rev. B*, 2005, **71**, 115106.
17. G. K. H. Madsen and D. J. Singh, *Comput. Phys. Commun.*, 2006, **175**, 67-71.
18. A. Singh, S. N. Shirodkar and U. V. Waghmare, *2D Materials*, 2015, **2**, 035013.
19. S. N. Shirodkar and U. V. Waghmare, *Phys. Rev. B*, 2012, **86**, 165401.
20. A. Singh and U. V. Waghmare, *Phys. Chem. Chem. Phys*, 2014, **16**, 21664-21672.
21. J. A. Wilson and A. D. Yoffe, *Adv Phys*, 1969, **18**, 193-335.
22. S. Tongay, H. Sahin, C. Ko, A. Luce, W. Fan, K. Liu, J. Zhou, Y.-S. Huang, C.-H. Ho, J. Yan, D. F. Ogletree, S. Aloni, J. Ji, S. Li, J. Li, F. M. Peeters and J. Wu, *Nat Commun*, 2014, **5**.
23. S. Ishiwata, Y. Shiomi, J. S. Lee, M. S. Bahramy, T. Suzuki, M. Uchida, R. Arita, Y. Taguchi and Y. Tokura, *Nat Mater*, 2013, **12**, 512-517.
24. T. Nilges, S. Lange, M. Bawohl, J. M. Deckwart, M. Janssen, H.-D. Wiemhofer, R. Decourt, B. Chevalier, J. Vannahme, H. Eckert and R. Weihrich, *Nat Mater*, 2009, **8**, 101-108.
25. C. Xiao, Z. Li, K. Li, P. Huang and Y. Xie, *Acc. Chem. Res.*, 2014, **47**, 1287-1295.
26. C. Xiao, X. Qin, J. Zhang, R. An, J. Xu, K. Li, B. Cao, J. Yang, B. Ye and Y. Xie, *J. Am. Chem.Soc.*, 2012, **134**, 18460-18466.
27. M. Lazzeri and F. Mauri, *Phys. Rev. Lett.*, 2003, **90**, 036401.
28. T. A. Nguyen, J.-U. Lee, D. Yoon and H. Cheong, *Sci. Rep.*, 2014, **4**, 4630.
29. D. J. Late, S. N. Shirodkar, U. V. Waghmare, V. P. Dravid and C. N. R. Rao, *ChemPhysChem*, 2014, **15**, 1592-1598.
30. N. Peimyoo, J. Shang, W. Yang, Y. Wang, C. Cong and T. Yu, *Nano Research*, 2014, 1-12.
31. S. Bertolazzi, J. Brivio and A. Kis, *ACS Nano*, 2011, **5**, 9703-9709.

32. A. Das, S. Pisana, B. Chakraborty, S. Piscanec, S. K. Saha, U. V. Waghmare, K. S. Novoselov, H. R. Krishnamurthy, A. K. Geim, A. C. Ferrari and A. K. Sood, *Nat Nano*, 2008, **3**, 210-215.

33. A. Berkdemir, H. R. Gutierrez, A. R. Botello-Mendez, N. Perea-Lopez, A. L. Elias, C.-I. Chia, B. Wang, V. H. Crespi, F. Lopez-Urias, J.-C. Charlier, H. Terrones and M. Terrones, *Sci. Rep.*, 2013, **3**.

34. C. Lee, H. Yan, L. E. Brus, T. F. Heinz, J. Hone and S. Ryu, *ACS Nano*, 2010, **4**, 2695-2700.

35. H. Sahin, S. Tongay, S. Horzum, W. Fan, J. Zhou, J. Li, J. Wu and F. M. Peeters, *Phys. Rev. B*, 2013, **87**, 165409.

36. M. Yamamoto, S. T. Wang, M. Ni, Y.-F. Lin, S.-L. Li, S. Aikawa, W.-B. Jian, K. Ueno, K. Wakabayashi and K. Tsukagoshi, *ACS Nano*, 2014, **8**, 3895-3903.

37. N. A. Lanzillo, A. Glen Birdwell, M. Amani, F. J. Crowne, P. B. Shah, S. Najmaei, Z. Liu, P. M. Ajayan, J. Lou, M. Dubey, S. K. Nayak, apos and T. P. Regan, *Appl. Phys. Lett.*, 2013, **103**, 093102.

38. G. Lucazeau, *J. Raman Spectrosc.*, 2003, **34**, 478-496.

39. P. G. Klemens, *Phys. Rev.*, 1966, **148**, 845-848.

CHAPTER 4.2

Electronic and thermal transport properties of anion-deficient $MoTe_2$*

Summary

We have studied the high-temperature electronic and thermal transport properties of polycrystalline anion-deficient 2H- and 1T'-$MoTe_2$. Electron transport measurements in the temperature range of 300-673 K show that 2H-$MoTe_{2-x}$ exhibits two regimes of activated conduction: conduction in defect-induced localized states at lower temperatures and an extended state conduction at higher temperatures. Its Seebeck coefficient changes from p-type to n-type around 497 K peaking near 370 K which is ascribed to the mixed conduction of holes and electrons. In contrast, 1T'-$MoTe_{2-x}$ exhibits metallic conduction up to 300 K beyond which conductivity slightly increases due to the contribution from thermally excited carriers; its Seebeck coefficient remains positive throughout the temperature range investigated implying a dominant hole-contribution. 2H- and 1T' forms of $MoTe_{2-x}$ exhibit thermal conductivity with opposite temperature-dependence due to considerable electronic thermal conductivity in the latter. The localized states induced by non-stoichiometry are crucial to understanding the observed trends in the temperature-dependent electron-transport properties, especially of 2H-$MoTe_{2-x}$. Interestingly, there is no sign of an expected first order structural phase transition from 1T' to Td structure at low temperatures (ca. 250 K) either from electrical conductivity or Raman spectroscopy, suggesting a possible role of vacancies in the present samples.

*A paper based on this study has appeared in **Z. Anorg. Allg. Chem.**, 2016, *642*, 1386.

4.2.1 Introduction

Group VI transition metal dichalcogenides (TMDCs) such as MoS_2 and WS_2 can exist as semiconducting 2H- and metallic 1T-polytypes.[1-6] Most studies have been on the thermodynamically stable semiconducting hexagonal (2H) phase because the 1T-phases which are usually obtained by chemical exfoliation are metastable.[2, 5] While phase engineering of MoS_2 and related TMDCs to achieve coherent metal-semiconductor heterojunctions in a chemically homogeneous sample is attractive, it is challenging due to the transient nature of the 1T phases.[5]

Unlike MoS_2, $MoTe_2$ exhibits a thermally induced structural transition around 900 °C from the semiconducting 2H phase to semimetallic 1T' phase[7]. The 1T' phase with the monoclinic crystal structure can be interpreted as a distortion of the centrosymmetric 1T phase by the formation of in-plane Mo-Mo bonds resulting in pseudo-hexagonal layers with zigzag Mo-chains. First-principles calculations reveal 2H-$MoTe_2$ to be the more stable form. However, the energy difference between 2H- and 1T'-$MoTe_2$ is small (ca. 35 meV) and can allow for the selective synthesis of 1T'- and 2H-$MoTe_2$ [8, 9]. With a strong spin-orbit coupling and a narrow band gap (ca. 1 eV), 2H-$MoTe_2$ is useful in semiconductor-electronics[10-13] and valleytronics[14]. A field-effect transistor with mobility as high as ca. 40 $cm^2\ V^{-1}s^{-1}$ has been fabricated with a channel made of few-layer 2H-$MoTe_2$ [9]. Bulk single crystal of 1T'-$MoTe_2$ exhibits a giant magnetoresistance (MR) of 16,000% in a magnetic field of 14 T at 1.8 K [9]. Recently pressure-driven superconductivity has been reported in single crystals of orthorhombic Td-$MoTe_2$, a low-temperature polymorph of 1T'-$MoTe_2$, with a maximum critical temperature of 8.2 K at 11.7 GPa[15]. The Td-structure is similar to the 1T'-phase but with its layers stacked differently, resulting in a higher symmetry orthorhombic structure.

By virtue of the low energy-difference between 1T'- and 2H-polymorphs, $MoTe_2$ provides a unique opportunity for phase engineering. Recently, laser-induced phase patterning has been used to fabricate an ohmic heterojunction between semiconducting 2H- and metallic 1T'-$MoTe_2$ that is stable up to 300

°C [8]. Such heterojunctions increase the carrier mobility of the $MoTe_2$ transistor by a factor of about 50 while retaining a high on/off current ratio of 10^6. The phase transition from 2H to 1T' phase of $MoTe_2$ originates from the Te-vacancies induced by laser irradiation at elevated temperatures. Based on density-functional theoretical (DFT) calculations, a Te-vacancy concentration more than 3% is shown to cause the 1T' phase to be more stable than the 2H phase [8].

In chapter 4.1, we have studied the structural, vibrational and thermoelectric properties of WTe_2 that exists only in the Td-structure, a distorted variant of *c*1T structure found in MoS_2. In the present chapter, we have studied 2H as well as 1T' phases of polycrystalline $MoTe_2$, with particular emphasis on the electron transport properties. While there are reports on the effects of defects on TMDCs such as MoS_2,[16-21] studies on the influence of point defects in $MoTe_2$ are limited.[22] We have investigated the nature of defect states in $MoTe_2$ specifically associated with the Te-vacancies using the first-principles calculations. These defect states are found to govern the observed temperature-dependence of electron transport properties of $MoTe_2$. The present work also reflects the possible influence of Te-vacancies on the relative stabilities of 1T' and Td phases of $MoTe_2$ as indicated by the absence of a first-order phase transition from 1T' to Td phase at low temperatures in our nonstoichiometric samples.

4.2.2 Methods

4.2.2.1 Synthesis

I have prepared the samples by a solid state synthesis. To obtain 1T'-$MoTe_2$, finely ground stoichiometric amounts of elemental Mo and Te were sealed in evacuated quartz tubes (10^{-5} torr), heated at 650 °C for 12 hr and then at 1200 °C for 15 hr followed by quenching in ice-cooled water. Annealing this compound at 700 °C for 24 hr yields 2H-$MoTe_2$.

4.2.2.2 Characterizations

Powder X-ray diffraction (PXRD) patterns were recorded on Bruker D8 diffractometer using Cu Kα (λ= 1.5406 Å) radiation to confirm the phase

purity of monoclinic 1T'-$MoTe_{2-x}$ (space group $P12_1/m1$) and hexagonal 2H-$MoTe_{2-x}$ (space group $P6_3/mmc$). Raman spectra were recorded on LabRam HR microscope using Ar-laser (514.5 nm) excitation in a backscattering configuration. Temperature-dependent Raman spectra were recorded with a THMS600 stage equipped with a liquid-N_2 cryostat. Optical band gaps were estimated from diffuse reflectance spectroscopy at room temperature using Perkin Elmer Lambda 25 UV-Vis spectrophotometer. Absorption (α/S) data were calculated from the reflectance data using the Kubelka−Munk function, $\alpha/S=(1-R)^2/(2R)$, where R is the reflectance; α, the absorption coefficient and S, the scattering coefficient. The optical band gaps were determined from α/S vs. E (eV) plots. Core-electron X-ray photoelectron spectroscopy was carried out on powder samples using Omicron nanotechnology ESCA instrument (model: EAC 2000 SPHERA 547) with monochromatic Mg Kα ($h\nu$ = 1253.6 eV) X-ray source. Mo-3d and Te-3d XPS spectra were obtained with a pass energy of 25 eV and resolution of 0.5 eV.

4.2.2.3 Transport measurements

For measuring the electrical transport properties, the as-synthesized polycrystalline samples were finely ground and cold-compacted into bar-, cylinder- and disc-shaped samples at 30 MPa and annealed in evacuated quartz tubes (10^{-5} torr) at 1200 °C in the case of 1T'-phase and at 700 °C in the case of 2H-phase. The resultant samples were found to be 00*l*-oriented along the pressing-direction. After annealing, the average elemental compositions as estimated by the energy-dispersive X-ray spectroscopy were found to be $MoTe_{1.92}$ and $MoTe_{1.85}$ for the 2H- and 1T'-phases respectively. Electrical conductivity (σ) and Seebeck coefficient (S) were simultaneously measured for rectangular bar- ($\perp$ to pressing-direction) and cylinder-shaped (// to pressing-direction) samples between room temperature (RT) and 673 K under He-atmosphere by a four-probe method using ULVAC-RIKO ZEM3 instrument (refer to part 1 for more details). Low-temperature electrical resistivity was measured along the length of the bar-shaped sample between 3 K and 300 K by a four-probe method using PPMS instrument. The thermal diffusivity (D) for the disc-shaped samples was measured along the pressing-direction between

room temperature and 673 K using laser flash diffusivity method in Netzsch LFA-457 instrument. Total thermal conductivity along with the lattice and electronic contributions is calculated as detailed in part 1.

4.2.2.4 Computational details

The present first-principles simulations are carried out in collaboration with Prof. Umesh Waghmare's group at JNCASR, Bangalore. They are based on density functional theory (DFT) as implemented in QUANTUM ESPRESSO (QE) package. Local density approximation (LDA) with the Perdew-Zunger (PZ) form of the exchange correlation energy functional and norm-conserving pseudopotentials to represent the interaction between ionic cores and valence electrons were used. Spin-orbit coupling (SOC)[23] was used through the use of relativistic pseudopotentials using a second variational procedure, and van der Waals (vdW) interaction with the implementation of Grimme parameterized scheme[24]. The plane wave basis sets for representation of Kohn-Sham wave-functions and charge density have been truncated with energy cut-off of 80 Ry and 320 Ry respectively. Convergence to self-consistency was aided by using Fermi-Dirac distribution function to smear occupation numbers with a width of 0.003 Ry.

In the structural optimization and total energy calculations of pristine $MoTe_2$, conventional unit cells containing 6 and 12 atoms were used for 2H-$MoTe_2$ and 1T'-$MoTe_2$ respectively. Integrations over Brillouin zone were sampled on uniform grids of 12×12×3 k-points for 2H-$MoTe_2$ and 20×10×5 k-points for 1T'-$MoTe_2$. For modeling 3% Te vacancies in 2H-$MoTe_2$, a 2×2×2 periodic supercell (48 atoms) was used with one Te atom removed from the supercell. To simulate Te-vacancies in 1T'-$MoTe_2$, a 1×2×2 supercell with 48 atoms was constructed. 6% Te vacancies were modeled in 2H-$MoTe_2$ and 1T'-$MoTe_2$ using 1×2×2 and 1×1×2 supercells (24 atoms) respectively with the removal of one Te atom from the supercell. Boltztrap code[25] was used for calculating electronic transport properties. Boltztrap is a program based on the semiclassical Boltzmann theory of transport and uses a smoothened Fourier interpolation of the electronic bands obtained from first-principles.

4.2.3 Results & discussion

4.2.3.1 Structural aspects

$MoTe_2$ occurs in three forms: 2H-$MoTe_2$, 1T'-$MoTe_2$ and Td-$MoTe_2$. The 2H-$MoTe_2$ has a hexagonal crystal structure (space group $P6_3/mmc$) where layers of covalently bonded Te-Mo-Te atomic planes are stacked along crystallographic *c*-axis via weak van der Waals interactions. Each Mo atom has six Te neighbors forming trigonal prisms that are slightly elongated along *c*-axis, the stacking sequence being AbA BaB where the capital and lower case letters denote chalcogen and metal atoms respectively (Figure 4.2.1(a)).

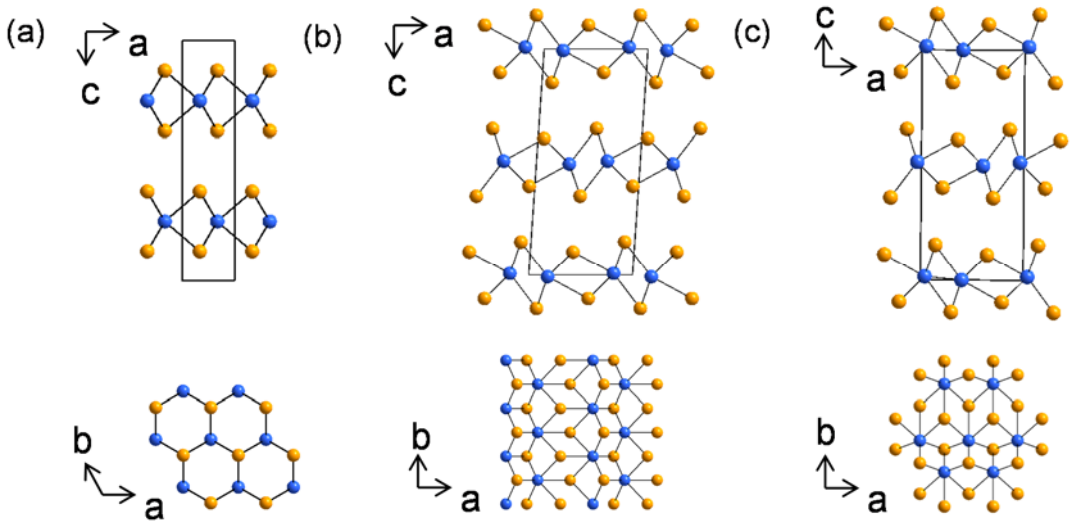

Figure 4.2.1 *Crystal structures of a) 2H-$MoTe_2$, b) 1T'-$MoTe_2$ and c) Td-$MoTe_2$. Blue and yellow spheres denote Mo and Te respectively.*

1T'-$MoTe_2$ is the high-temperature polymorph of $MoTe_2$ crystallizing in a monoclinic structure (space group $P12_1/m1$). The layered structure of 2H-$MoTe_2$ is preserved in 1T'-$MoTe_2$ except that the metal atoms are octahedrally coordinated by Te atoms. The $MoTe_6$ octahedra are strongly distorted due to off-centering of Mo atoms as the latter move towards each other forming weakly buckled Mo-Mo zigzag chains along *a*-axis. The resultant stacking sequence is AbC BcD EdF where the capital and lower case letters denote chalcogen and metal atoms respectively (Figure 4.2.1(b)). Consequently, 1T'-$MoTe_2$ exhibits metallic bonding with a Mo-Mo bond distance of 2.90 Å which is only about 0.18 Å longer than that in the elemental bcc Mo.[7] 1T'-$MoTe_2$ undergoes a first-order phase-transition upon cooling (below 250 K)[26] wherein the layers

shift quasi-continuously to form orthorhombic Td-$MoTe_2$. With decreasing temperature, the *c*-lattice parameter first increases and then decreases as the layers lock into a new orientation wherein the monoclinic angle of 93° reduces to the orthorhombic structure with the angle of 90°.[27] Thus, Td-$MoTe_2$ manifests a weakly bonded layered structure with each Mo atom surrounded by eight Te-neighbours (Figure 4.2.1(c)). The room temperature PXRD patterns collected from powders and pellets of the as-synthesized 2H-$MoTe_{2-x}$ (Figure 4.2.2(a)) and 1T'-$MoTe_{2-x}$ (Figure 4.2.2(b)) samples can be indexed on hexagonal and monoclinic structures respectively. The relatively intense (00*l*) peaks for the pellets of both the phases arise from the preferred stacking of the Te-Mo-Te layers along the pressing-direction during compaction.

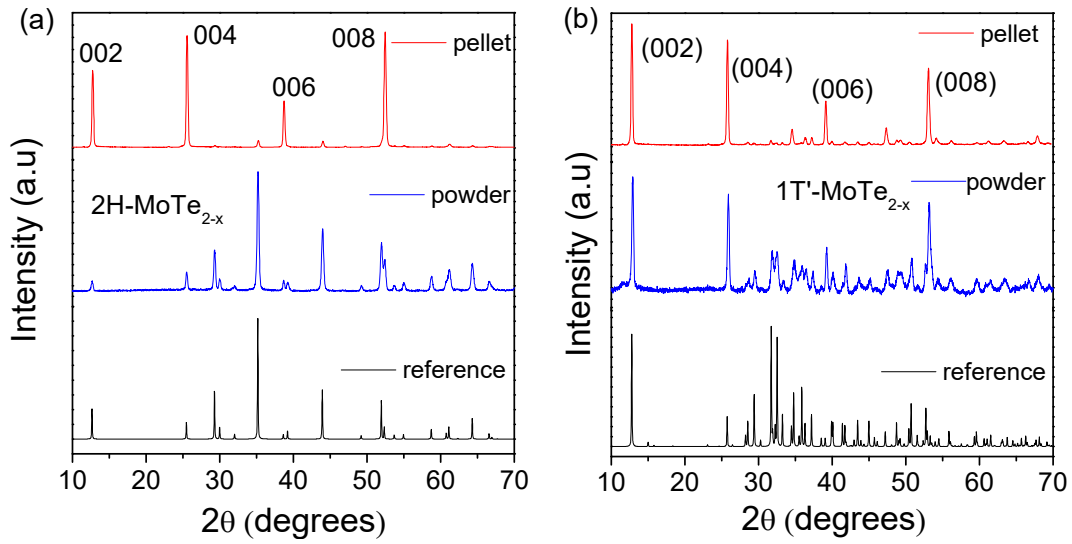

Figure 4.2.2 *XRD patterns of polycrystalline bulk a) 2H-$MoTe_{2-x}$ and b) 1T'-$MoTe_{2-x}$ in powder and pellet forms.*

4.2.3.2 Raman spectroscopy

The Raman spectrum of bulk 2H-$MoTe_{2-x}$ excited with a 514.4 nm laser exhibits three distinct bands centered around 121, 175, 236 cm^{-1} which are assigned to E_{1g}, A_{1g} and E^1_{2g} vibrational modes respectively (Figure 4.2.3(b)).[28-30] The Raman spectrum of 1T'-$MoTe_2$, on the other hand, reveals three bands centered around 110, 129 and 164 cm^{-1} which are assigned to A_u, A_g and B_g modes respectively (Figure 4.2.3 (a)).[9, 29-31] A weak hump observed in 245-260 cm^{-1} region is associated with A_g mode of vibration while the band

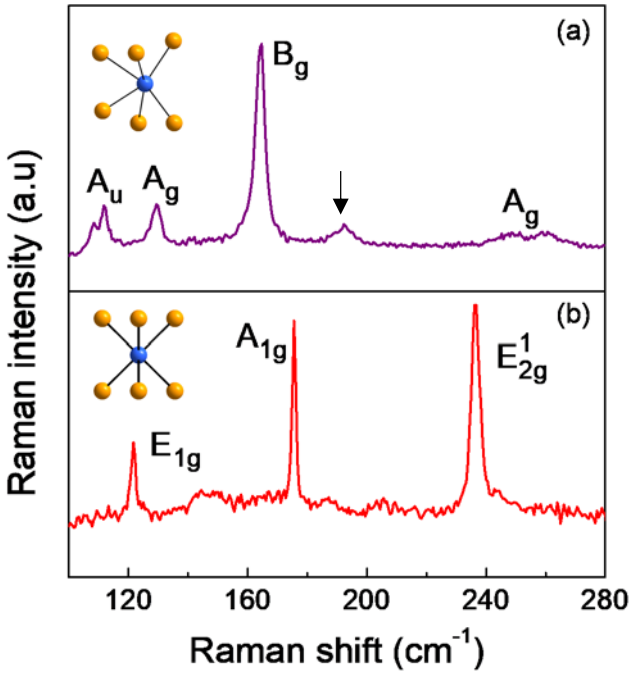

Figure 4.2.3 *Raman spectra of a) 1T'-$MoTe_{2-x}$ and b) 2H-$MoTe_{2-x}$ recorded at room temperature using Ar- laser (514.4 nm) excitation. The Raman band in (a) indicated by an arrow is unassigned.*

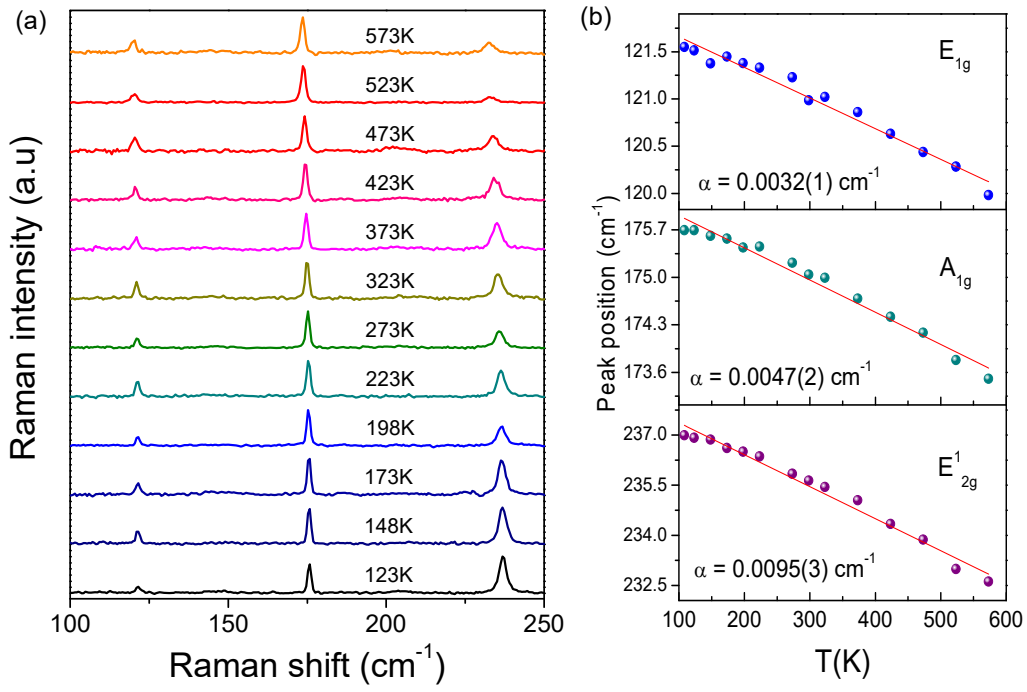

Figure 4.2.4 *a) Raman spectra of bulk 2H-$MoTe_{2-x}$ recorded at various temperatures under Ar- laser (514.4 nm) excitation and b) temperature-dependence of peak frequencies. Solid lines are linear fits according to equation 4.2.1.*

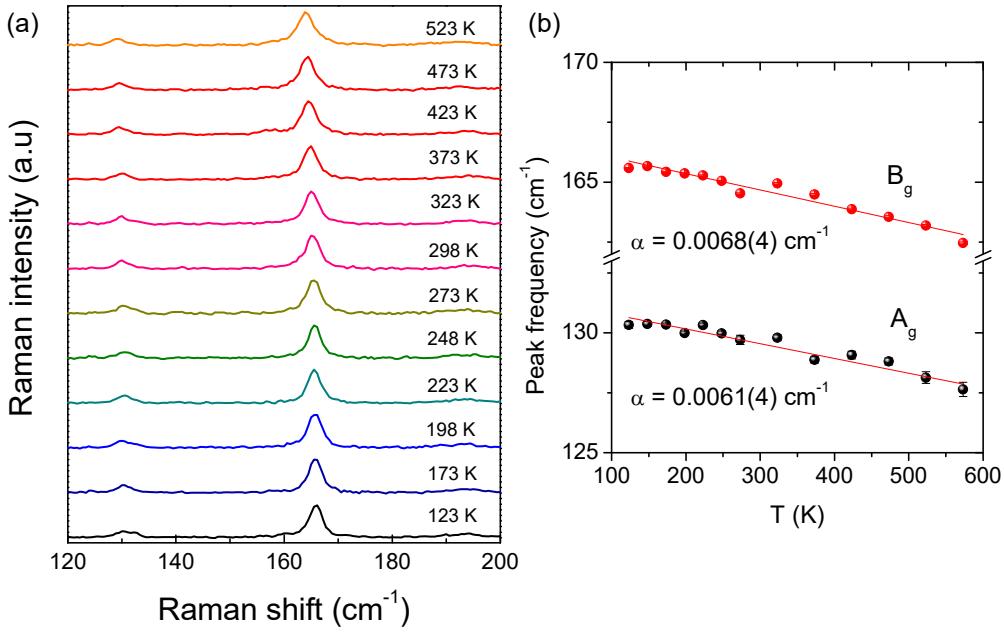

Figure 4.2.5 *a) Raman spectra of bulk 1T'-$MoTe_{2-x}$ recorded at various temperatures under Ar- laser (514.4 nm) excitation and b) temperature-dependence of peak frequencies. Solid lines are linear fits according to equation 4.2.1.*

centered about 192 cm^{-1} has not been assigned.[9, 29-31] To estimate the thermally induced shifts in band-positions, Raman spectra were recorded in the temperature range of 123-573 K. The Raman spectra of 2H-$MoTe_{2-x}$ recorded at various temperatures are shown in figure 4.2.4(a). The data points were fitted using the linear anharmonic model:

$$\omega(T) = \omega(0) - \alpha T \qquad 4.2.1$$

All the three modes soften with temperature, and the linear temperature coefficients ($\alpha = d\omega/dT$) are 0.0032(1), 0.0047(2) and 0.0095(3) $cm^{-1}K^{-1}$ for E_{1g}, A_{1g} and E^1_{2g} bands respectively (figure 4.2.4(b)). Figure 4.2.5(a) shows the Raman spectrum of 1T'-$MoTe_{2-x}$ recorded at various temperatures. Figure 4.2.5(b) shows the temperature-dependence of corresponding peak frequencies with linear temperature coefficients (α) being 0.0068(4) and 0.0061(4) $cm^{-1}K^{-1}$ respectively, for the bands centered around 129 cm^{-1} and 164 cm^{-1} (B_g). Interestingly, there is no sign of a first order phase-transition from 1T' to Td-phase in the temperature-dependent Raman spectra of 1T'-$MoTe_{2-x}$ even down to 123 K. The 1T' to Td phase-transition was previously reported to occur around 250 K in the single crystalline 1T'-$MoTe_2$. [7, 26]

4.2.3.3 X-ray photoelectron spectroscopy

The core level X-ray photoelectron spectra of 2H- and 1T'-$MoTe_{2-x}$ powders are given in figure 4.2.6. The Te-3d and Mo-3d signals appear as doublets due to $3d_{3/2}$ and $3d_{5/2}$ states. Weak humps (indicated by arrows) in the Te-3d spectra are due to traces of TeO_2. Mo-3d spectra, on the other hand, do not show such humps suggesting that the oxidation is confined to the outer Te-planes at the surface.

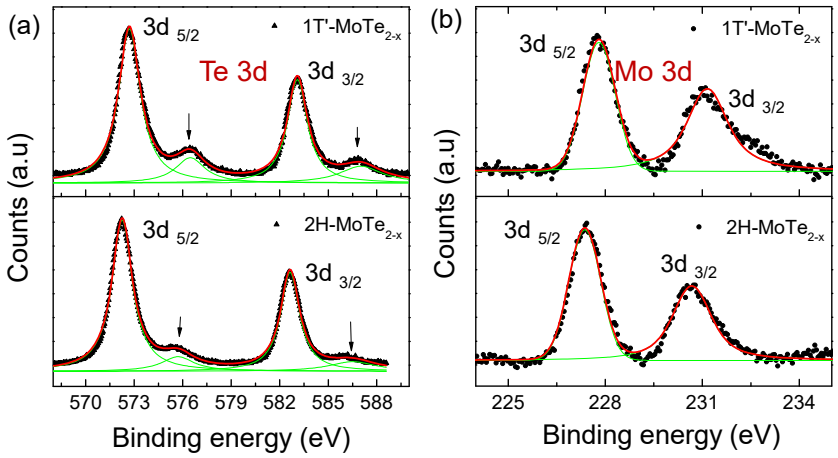

Figure 4.2.6 *Core level a) Te-3d and b) Mo-3d X-ray photoelectron spectra of 1T'-$MoTe_{2-x}$ and 2H-$MoTe_{2-x}$ recorded at room temperature.*

4.2.3.4 Electron transport properties

Invariably, the as-prepared samples were found to be anion-deficient after thermal annealing, and the average elemental compositions were estimated by energy-dispersive X-ray spectroscopy to be $MoTe_{1.92}$ and $MoTe_{1.85}$ for the 2H- and 1T'-phases respectively. Figure 4.2.7 presents the electron transport properties of polycrystalline 2H-$MoTe_{2-x}$ measured between 300 and 673 K. The electrical conductivity (σ) and seebeck coefficient (S) measured along the directions parallel and perpendicular to the stacking direction, are shown in figures 4.2.7 (a) and (c) respectively. The electrical conductivity is very low (3E-3 S cm^{-1}) at ca. 300 K but increases by up to three orders at 660 K due to thermal excitation of carriers. At elevated temperatures, σ normal to the stacking direction ($\sigma_{\perp}$) is higher than that along the stacking direction ($\sigma_{\parallel}$), and vice versa in the case of the Seebeck coefficient. This anisotropy is caused

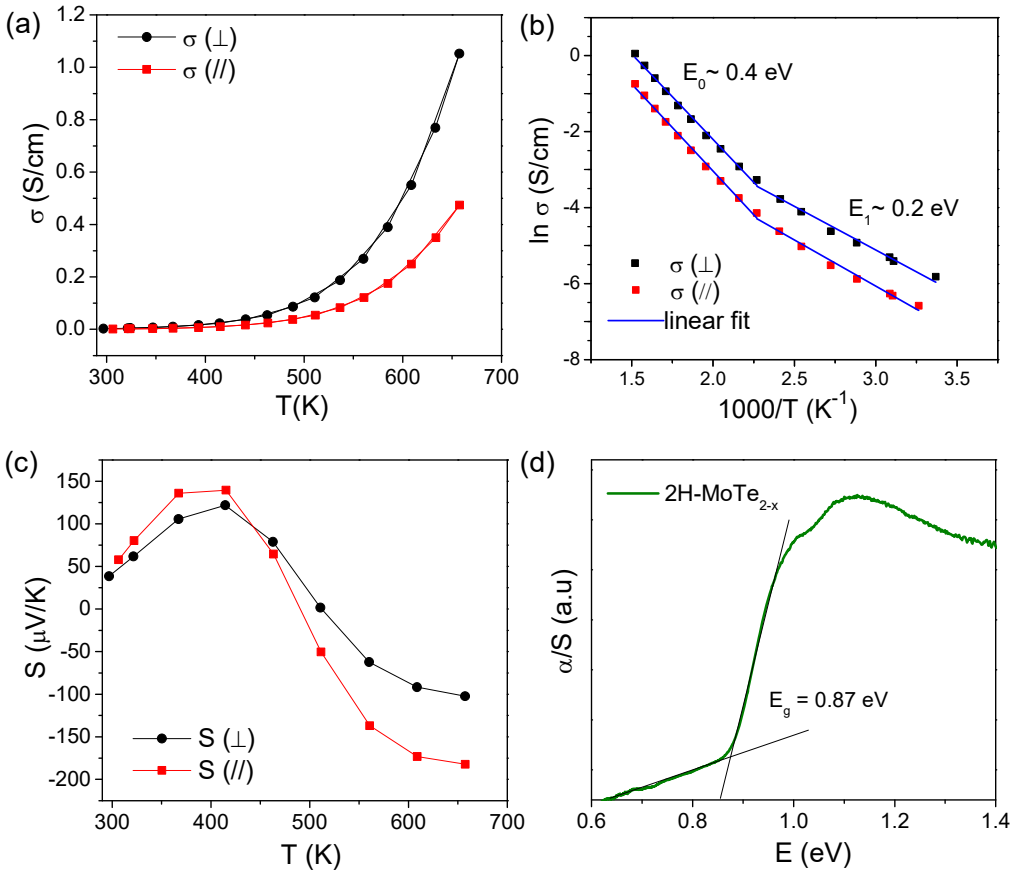

Figure 4.2.7 *(a) Electrical conductivity (σ), b) Arrhenius fits to electrical conductivity showing two activated regimes at lower and higher temperatures, (c) Seebeck coefficient (S) of 2H-$MoTe_{2-x}$ measured along directions, parallel and normal to the stacking direction and d) Kubelka-Munk absorption spectrum of 2H-$MoTe_{2-x}$.*

by the energy-barriers at the interfaces, which filter the low-energy electrons thereby decreasing σ and increasing S along the stacking direction[32].

Temperature-dependent (300-623 K) electrical conductivity (σ) of 2H-$MoTe_{2-x}$ range can be described with the Arrhenius equation:[33]

$$\sigma = \sigma_0 exp(-E_0/k_B T) \; + \; \sigma_1 exp(-E_1/k_B T) \qquad 4.2.2$$

where E_0 and E_1 are the respective activation energies associated with the two conduction mechanisms, k_B is the Boltzmann constant and T is the absolute temperature. The first term describes conduction of carriers excited beyond the mobility edge into extended states in conduction or valence bands at higher temperatures whereas the second term describes conduction of carriers across localized states at lower temperatures. σ_0 and σ_1 are the corresponding pre-exponential factors; σ_1 is expected to be smaller than σ_0 by several orders due

to lower effective density of states (DOS) and lower mobility of the localized states.[33]

In the high-temperature regime (> 450 K), a thermal activation energy (E_0) of ca. 0.4 eV is estimated along both the directions from the slope of linear ln σ vs. 1/T plots shown in figure 4.2.7(b). The value of E_0 agrees roughly with one half of the optical energy gap (ca. 0.9 eV) measured from diffuse reflectance spectroscopy (Figure 4.2.7(d)) and hence, is associated with intrinsic conduction in extended states at high temperatures. The estimated value of $E_1 \sim 0.2$ eV (along both the directions) in 300-450 K range is much smaller than the optical band gap and suggests the hopping conduction of carriers in the mid-gap defect states. When there is a finite density of states (DOS) at the Fermi level (E_F) due to localized defect states and for temperatures such that k_BT is smaller than the bandwidth, hopping of carriers across the localized states is expected. Therefore, the electrical conductivity in this temperature range is indeed governed by defect-induced localization of charge carriers, the defects arising from dangling bonds at the point-defects such as Te-vacancies.

The Seebeck coefficient ($S_\perp$) measured normal to the stacking direction varies from 38 µV/K at ca. 300 K to -108 µV/K at 660 K with a maximum value of 121 µV/K at 415 K (Figure 4.2.7(c)). The Seebeck coefficient ($S_\parallel$) measured parallel to the stacking direction varies from 57 µV/K at ca. 300 K to -182 µV/K at ca. 660 K with a maximum value of 140 µV/K at ca. 415 K. Both $S_\perp$ and $S_\parallel$ exhibit a sign-change from p-type to n-type in 490-515 K range. The sign-change of *S(T)* indicates mixed conduction of holes and electrons and a two-carrier model can be used to describe S qualitatively as:[34]

$$S = (S_h - \left(\frac{\sigma_e}{\sigma_h}\right)|S_e|)/(1+\frac{\sigma_e}{\sigma_h}) \qquad 4.2.3$$

where S_e and S_h are partial Seebeck coefficients of electrons and holes, and σ_h and σ_e are the conductivities of holes and electrons respectively. At lower temperatures (300-515 K), the dominant contribution is from holes and hence the value of S is positive. The maximum in S corresponds to the onset of mixed conduction. When S equals zero, both electrons and holes contribute equally.

At higher temperatures where $S >> S_{max}$, dominant contribution to overall S comes from thermally excited electrons in the conduction band.

In the temperature range investigated, it is reasonable to consider a mixed scattering of carriers by ionized impurities and acoustic phonons. The ionized impurities can arise due to defects such as Te-vacancies. For parabolic bands, the Seebeck coefficient as a function of the reduced chemical potential, $\eta = E_F/k_BT$ is given by:[35]

$$S = -\frac{k_B}{e}\left(\frac{\Phi_4(\eta, a)}{\Phi_3(\eta, a)} - \eta\right) \qquad 4.2.4$$

where a is the scattering parameter (a=1 for mixed scattering [35, 36]) associated with energy dependent carrier relaxation time, e is the absolute electronic charge, and $\Phi_{\mathrm{m}}(\eta, a)$ is similar to Fermi integral given by [35]

$$\Phi_{\mathrm{m,integer}}(\eta, a) = \int_0^\infty \frac{x^{\mathrm{m}}\exp(x-\eta)}{(x^2+a^2)[1+\exp(x-\eta)]^2}\, dx \qquad 4.2.5$$

Room temperature η, obtained from least square fitting of the measured Seebeck coefficient with calculated Seebeck coefficient (Equation 4.2.4), is positive implying a finite DOS at E_F near room temperature plausibly arising due to mid-gap states associated with defects such as Te-vacancies. The positive value of room temperature η does suggest that electrical conductivity near room temperature is indeed governed by conduction in mid-gap states near E_F. Similar analysis assuming the parabolic dispersion of bands and only acoustic scattering to be dominant scattering mechanism also yields a positive η at room temperature (see part 1 for relevant equations).

The low-temperature electrical conductivity of bulk 1T'-$MoTe_{2-x}$ measured between 2 and 300 K exhibits a typical metal-like behavior (Figure 4.2.8) with no sign of anomaly corresponding to a 1T' to Td phase transition down to 2 K, in agreement with the temperature-dependent Raman spectra. High-temperature electrical conductivity measured along directions normal and parallel to the stacking direction in the temperature range of 300-673 K is presented in figure 4.2.9(a). The electrical conductivity near 300 K is much higher compared to that of 2H-$MoTe_{2-x}$ owing to metallic nature of 1T'-$MoTe_{2-}$

$_x$. The value of $\sigma_\perp$ near 300 K is ca. 1911 S cm^{-1}, which slightly increases to ca. 1937 S cm^{-1} near 660 K with a minimum of ca. 1887 S cm^{-1} near 370 K. The value of $\sigma_\parallel$, on the other hand, varies from ca. 1195 S cm^{-1} near 300 K to ca. 1257 S cm^{-1} near 660 K with a minimum of ca. 1189 S cm^{-1} near 370 K. $\sigma_\perp$ is

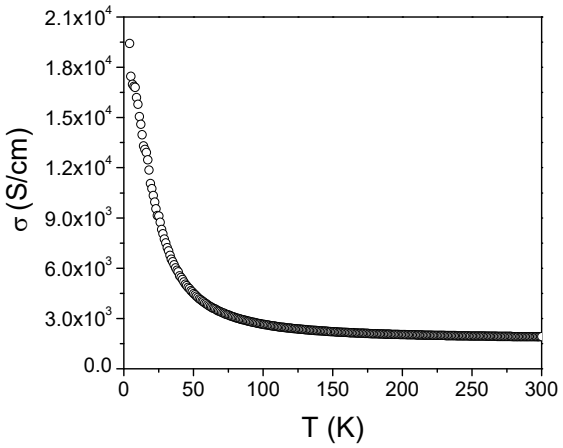

Figure 4.2.8 *Low-temperature electrical conductivity of 1T'-$MoTe_{2-x}$*

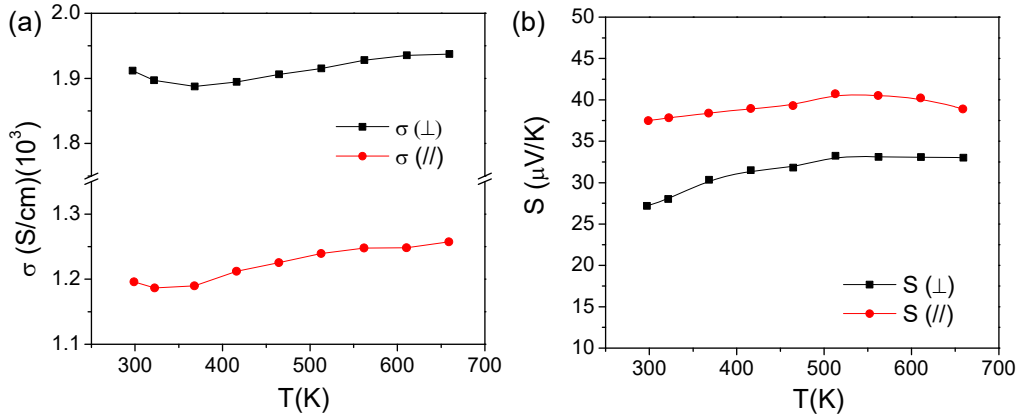

Figure 4.2.9 *High-temperature a) electrical conductivity (σ) and b) Seebeck coefficient (S) of bulk 1T'-$MoTe_{2-x}$ measured along directions parallel and normal to the stacking direction.*

greater than $\sigma_\parallel$ due to filtering of low-energy carriers at the energy barriers induced by interfaces along the stacking direction. For the same reason, $S_\perp$ is smaller than $S_\parallel$ throughout the temperature range investigated (Figure 4.2.9(b)). As a result, $S_\perp$ near 300 K is ca. 27 μV/K which plateaus at ca. 33 μV/K above 512 K, while $S_\parallel$ varies slightly from ca. 37 μV/K near 300 K to ca. 39 μV/K near 660 K with a maximum of ca. 40 μV/K near 512 K. The Seebeck coefficient is positive throughout the temperature range investigated suggesting that p-type carriers are the majority carriers. The observed

minimum in σ and maximum in S are caused by weak bipolar conduction due to thermal excitation of minority carriers at elevated temperatures.

4.2.3.5 Thermal conductivity

Figure 4.2.10 shows thermal transport in 2H-$MoTe_{2-x}$ and 1T'-$MoTe_{2-x}$ in the temperature range of 300-623 K. Thermal diffusivity (D) is measured normal to the stacking direction. The lattice (κ_{Lat}) and electronic (κ_{el}) contributions to the total thermal conductivity (κ) were extracted by using the Wiedemann-Franz law (refer to part 1 for details). For 2H-$MoTe_{2-x}$, κ_{Lat} is nearly equal to κ as κ_{el} is negligible owing to low electrical conductivity. κ_{Lat} decays from 2.8 $Wm^{-1}K^{-1}$ at 300 K to 1.5 $Wm^{-1}K^{-1}$ at 623 K with nearly $T^{-1/2}$ dependence suggesting that the phonon-transport is dominated by phonon-phonon Umklapp scattering processes at higher temperatures. For 1T-$MoTe_{2-x}$, κ varies from 2.3 $Wm^{-1}K^{-1}$ at 300 K to 2.7 $Wm^{-1}K^{-1}$ at 623 K. κ_{Lat} decreases from 1.8 $Wm^{-1}K^{-1}$ at 300 K to 1.5 $Wm^{-1}K^{-1}$ at 623 K with $T^{-1/2}$ dependence. κ_{el}, however, increases from 0.5 $Wm^{-1}K^{-1}$ at 300 K to 1.2 $Wm^{-1}K^{-1}$ at 623 K due to increasing contribution from thermally excited minority carriers as is also evident in the bipolar electrical transport at elevated temperatures.

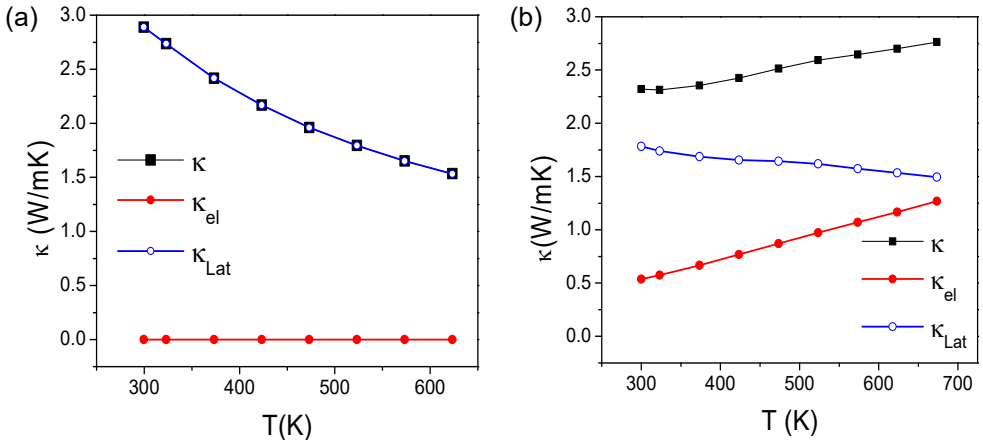

Figure 4.2.10 *Temperature-dependent total thermal conductivity (κ) along with lattice (κ_{Lat}) and electronic (κ_{el}) thermal conductivities of bulk (a) 2H-$MoTe_{2-x}$ and (b) 1T'-$MoTe_{2-x}$.*

4.2.3.6 Electronic structures of pristine $MoTe_2$

The calculated electronic structure and projected density of states of 2H- and 1T'- $MoTe_2$ (Figures 4.2.11(a) and (b)) show that the valence bands (VBs) of both the structural forms involve strong hybridization between Te 5p and Mo

4d states. On the other hand, the Mo 4d orbitals primarily contribute to the peaks in the conduction band (CB) with a weaker contribution of Te 5p and 4d states as expected from the ionic charges and bonding in $MoTe_2$. Valence bands deeper in energy comprise largely of p-orbitals of Te. The electronic structure of pristine 2H-$MoTe_2$ exhibits an indirect gap of 0.56 eV between valence band maximum (VBM) and conduction band minimum (CBM) along Γ-K (Figure 4.2.11(a)) direction. Our theoretical band gap is underestimated, as typical of LDA-DFT calculations, in comparison with the reported value of 1.1 eV for the single crystalline 2H-$MoTe_2$.[6, 7] To improve the band gap of 2H-$MoTe_2$, the structure has been optimized with non-local vdW interactions using vdw-df2-b86r functional [37-40] and as a result, the indirect band gap of 2H-$MoTe_2$ is enhanced from 0.56 eV to 0.75 eV. Further, when HSE06 functional is used in the calculations,[41, 42] an indirect band gap of 1.5 eV (refer to table 4.2.1) is obtained which is overestimated by 0.4 eV with respect to the literature value. The pristine 1T'-$MoTe_2$, on the other hand, has a semi-metallic electronic structure (Figure 4.2.11(b)).

4.2.3.7 Electronic structures of Te-deficient $MoTe_2$

To determine the effect of defects specifically associated with the Te vacancies, We have simulated 3% and 6% Te vacancies within supercells containing 48 atoms (32 Te atoms and 16 Mo atoms) and 24 atoms (16 Te atoms and 8 Mo atoms) respectively. The defect formation energy is estimated using $\delta E = E_v - E_b + E_{Te}$, where E_v, E_b and E_{Te} are the total energies of supercell containing a Te vacancy, bulk crystal (with the same number of atoms as in the defective structure), and an isolated Te atom respectively. Our estimates of the vacancy energies with 3% concentration of Te-vacancies in 2H-, 1T'- and Td-$MoTe_2$ are 7.18, 6.49 and 6.51 eV per vacancy respectively whereas those for 6% concentration of Te vacancies are 7.18, 6.72 and 6.57 eV per vacancy respectively suggesting a relatively weak interaction between the periodic images of vacancies in the 2H- and Td-forms. As the difference in energies of pristine $MoTe_2$ in 1T' and 2H structures is 0.165 eV/cell, these results suggest that the Te vacancies play an important role in their relative stability, in accordance with reference 8.

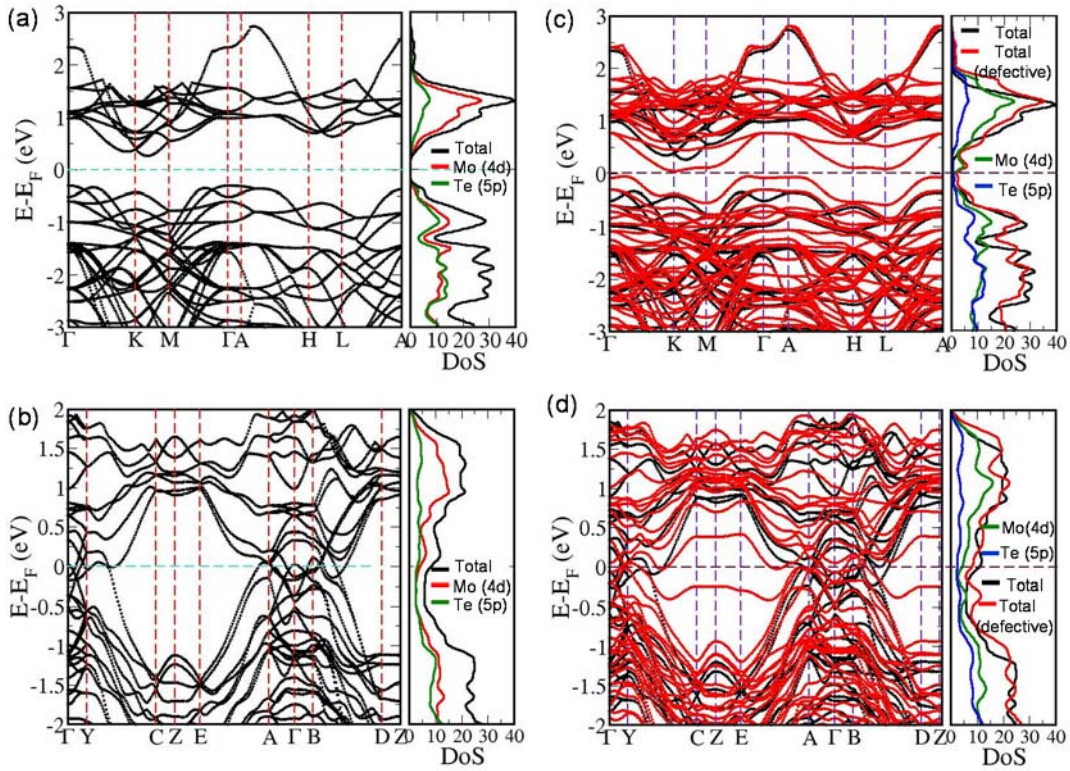

Figure 4.2.11 *Electronic structures and projected density of states (PDoS) of bulk pristine (a) 2H-$MoTe_2$ and (b) 1T'-$MoTe_2$, and of 6% Te-deficient (c) 2H-$MoTe_{2-x}$ and (d) 1T'-$MoTe_{2-x}$. Note that electronic band structures of Te-deficient $MoTe_2$ in (c) and (d) are superimposed on those of pristine bulk $MoTe_2$ shown in (a) and (b).*

Table 4.2.1 *The calculated electronic band gaps of bulk pristine and anion deficient 2H-$MoTe_2$*

2H-$MoTe_2$	E_g (eV)		
	LDA+ vdW (Grimme)	LDA+ non-local vdW (vdw-df2-b86r)	LDA+ non-local vdW+ HSE06
Bulk	0.576	0.753	1.5
3% Te Vacancies	0.134	0.1907	0.797
6% Te vacancies	0.099	0.1694	0.771

In the electronic structure of $MoTe_2$ with Te vacancies, bands associated with the defect states appear at the top of VB and the bottom of CB. The indirect gap for 2H-$MoTe_2$ reduces to 0.134 eV and 0.099 eV with 3% and 6% Te-vacancies respectively (Figure 4.2.11(c)). The estimates of indirect band gap with inclusion of non-local vdW interactions are 0.19 eV and 0.16 eV at

3% and 6% concentration of Te-vacancies respectively. As the HSE06 calculations are computationally expensive for large supercell, we used it to determine the gap at Γ-point and applied the corrections in VBM and CBM at other k-points to estimate the indirect band gap values. Resulting indirect gaps with 3% and 6% Te vacancies are 0.797 eV and 0.771 eV respectively (Table 4.2.1). On the other hand, the electronic structure of 1T'-$MoTe_2$ with Te-vacancies becomes more metallic, with an increase in the overlap between valence and conduction bands at the Fermi level (Figure 4.2.11(d)). Te vacancy related bands result in a reduction of the pseudo gap between the VBs and CBs (along Y-A and B-Z directions for 1T' structure), i.e., the density of states at Fermi level increases. From the electronic density of states (DOS) of Te-deficient 2H-$MoTe_2$, we find a new peak below CBM and identify it as the defect peak. This peak is contributed by Mo 4d states. For 1T'-$MoTe_2$, we observe a redistribution of DOS near E_F.

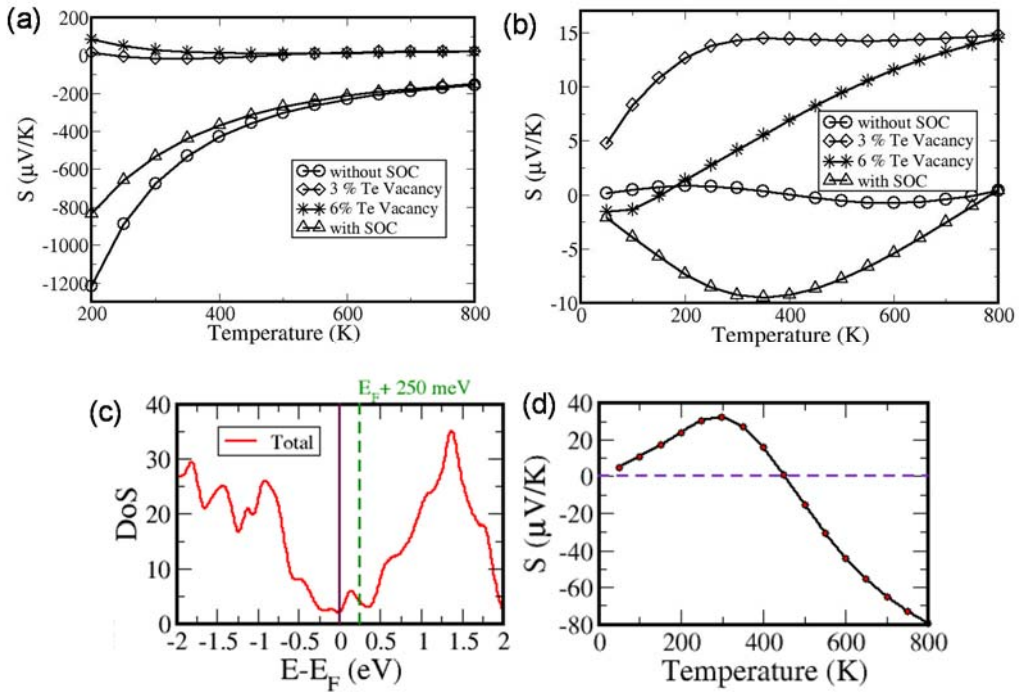

Figure 4.2.12 *Calculated Seebeck coefficient (S) as a function of temperature for (a) 2H-$MoTe_2$ and (b) 1T'-$MoTe_2$ with and without spin-orbit coupling, and with Te-vacancies. (c) The total electronic DOS of 6% Te-deficient 2H-$MoTe_2$. Note that the green dashed line shows the Fermi level shifted by 250 meV into the defect band. (d) Calculated temperature-dependent Seebeck coefficient for the 6% Te-deficient 2H-$MoTe_2$ with a 250 meV shift in Fermi level.*

To qualitatively interpret the experimental results presented earlier, we have determined the temperature-dependence of electronic transport properties of pristine 2H- and 1T'-$MoTe_2$ within semi-classical framework using the Boltztrap code with the input of first-principles electronic structures.[25, 43] The calculated trends, however, do not entirely agree with experiments. For the pristine 2H-$MoTe_2$, the calculated S is negative (with or without the inclusion of spin-orbit coupling (SOC)) in the entire temperature range studied (Figure 4.2.12(a)) whereas experiments show a p- to n-type cross-over around 415 K. For the pristine 1T'-$MoTe_2$, calculated S remains either negative or close to zero respectively with or without SOC (Figure 4.2.12(b)) whereas experiments show a p-type S throughout the temperature range studied. It is also noted that SOC has a stronger effect on the transport properties of 1T'-$MoTe_2$ than on those of 2H-$MoTe_2$.

The calculated temperature-dependence of S for the Te-deficient 2H-$MoTe_2$ (Figure 4.2.12(a)) is quite different from that for the pristine 2H-$MoTe_2$. Te-vacancies change the character of S in pristine 2H-$MoTe_2$ from otherwise n-type to p-type. By moving the Fermi level (E_F) by +250 meV into the defect-associated band in 2H-$MoTe_{2-x}$ with 6% Te-vacancies (see figure 4.2.12(c)), we find that the calculated temperature-dependence of S is in qualitative agreement with the experiments exhibiting a p- to n-type cross-over (see figure 4.2.12(d)). On the other hand, the calculated S is of p-type for the Te-deficient 1T'-$MoTe_{2-x}$, and its temperature-dependence also agrees reasonably well with the experiments (see figure 4.2.12(b)). We, however, note a discrepancy in magnitude of $|S|$ in calculations and experiment which can arise from the errors in band-structure (particularly associated with d-states near the Fermi energy, compounded with the errors in lattice constants) and concentration of Te-vacancies incorporated, doping, and possibly other intrinsic defects in real polycrystalline samples. Moreover, the Boltztrap code does not account for all the possible carrier scattering mechanisms and hence cannot reproduce the experiments quantitatively although it does capture the experimental trends qualitatively, asserting the influence of defects such as Te-vacancies on the observed transport properties.

4.2.4 Conclusions

I have measured the electron and thermal transport properties of polycrystalline anion-deficient 2H- and 1T'-$MoTe_{2-x}$ between 300 and 673 K. The electrical conductivity of 2H-$MoTe_{2-x}$ exhibits two regimes corresponding to conduction in localized states ($<$ 450 K) and an intrinsic extended state conduction ($>$ 450 K). Bipolar conduction is evident from the sign-change of Seebeck coefficient, marking p-type to n-type cross-over with a maximum at ca. 370 K. 1T'-$MoTe_2$ exhibits metallic conduction up to 300 K beyond which the conductivity increases slightly due to weak bipolar conduction. The thermal conductivities of 2H-$MoTe_{2-x}$ and 1T'-$MoTe_{2-x}$ exhibit opposite trends with temperature due to considerable electronic contribution to thermal transport in the latter. The observed trends in the transport properties, especially for 2H-$MoTe_{2-x}$ can be qualitatively understood using theory only by taking into account Te-vacancies.

Furthermore, there is no phase-transition from 1T' to Td phase even at very low temperatures as evident from the electrical conductivity and Raman spectroscopy. It appears that Te vacancies determine the relative stabilities (energies) of 1T' versus Td phases of $MoTe_2$ which, however, needs to be validated by studying a series of Te-deficient compositions. Varying the stoichiometry in a controlled fashion in the present polycrystalline samples is not trivial. Controlled evaporation of Te in the stoichiometric single crystals of $MoTe_2$ grown either by chemical vapor transport or flux method can provide a solution. In future, we wish to undertake the above to investigate in detail the effect of Te vacancies on the 1T'-Td phase transition which is important especially given that the Td-$MoTe_2$ is a potential candidate for a Type-II Weyl semimetal.

4.2.5 References

1. S. Bhattacharyya and A. K. Singh, *Phy. Rev. B*, 2012, **86**, 075454.
2. G. Eda, T. Fujita, H. Yamaguchi, D. Voiry, M. Chen and M. Chhowalla, *ACS Nano*, 2012, **6**, 7311-7317.
3. U. Gupta, B. S. Naidu, U. Maitra, A. Singh, S. N. Shirodkar, U. V. Waghmare and C. N. R. Rao, *APL Mat.*, 2014, **2**, 092802.
4. A. P. Nayak, S. Bhattacharyya, J. Zhu, J. Liu, X. Wu, T. Pandey, C. Jin, A. K. Singh, D. Akinwande and J.-F. Lin, *Nat Commun*, 2014, **5**, 3731.
5. D. Voiry, A. Mohite and M. Chhowalla, *Chem. Soc. Rev.*, 2015, **44**, 2702-2712.
6. D. Voiry, H. Yamaguchi, J. Li, R. Silva, D. C. B. Alves, T. Fujita, M. Chen, T. Asefa, V. B. Shenoy, G. Eda and M. Chhowalla, *Nat. Mater*, 2013, **12**, 850-855.
7. B. Brown, *Acta Cryst.*, 1966, **20**, 268-274.
8. S. Cho, S. Kim, J. H. Kim, J. Zhao, J. Seok, D. H. Keum, J. Baik, D.-H. Choe, K. J. Chang, K. Suenaga, S. W. Kim, Y. H. Lee and H. Yang, *Science*, 2015, **349**, 625-628.
9. D. H. Keum, S. Cho, J. H. Kim, D.-H. Choe, H.-J. Sung, M. Kan, H. Kang, J.-Y. Hwang, S. W. Kim, H. Yang, K. J. Chang and Y. H. Lee, *Nat Phys*, 2015, **11**, 482-486.
10. S. Fathipour, N. Ma, W. S. Hwang, V. Protasenko, S. Vishwanath, H. G. Xing, H. Xu, D. Jena, J. Appenzeller and A. Seabaugh, *Appl. Phys. Lett.*, 2014, **105**, 192101.
11. Y.-F. Lin, Y. Xu, S.-T. Wang, S.-L. Li, M. Yamamoto, A. Aparecido-Ferreira, W. Li, H. Sun, S. Nakaharai, W.-B. Jian, K. Ueno and K. Tsukagoshi, *Adv. Mater.*, 2014, **26**, 3263-3269.
12. S. Nakaharai, M. Yamamoto, K. Ueno, Y.-F. Lin, S.-L. Li and K. Tsukagoshi, *ACS Nano*, 2015, **9**, 5976-5983.
13. N. R. Pradhan, D. Rhodes, S. Feng, Y. Xin, S. Memaran, B.-H. Moon, H. Terrones, M. Terrones and L. Balicas, *ACS Nano*, 2014, **8**, 5911-5920.
14. J. Qi, X. Li, Q. Niu and J. Feng, *Phys. Rev. B*, 2015, **92,** , 121403.

15. Y. Qi, P. G. Naumov, M. N. Ali, C. R. Rajamathi, O. Barkalov, Y. Sun, C. Shekhar, S.-C. Wu, V. Süß, M. Schmidt, E. Pippel, P. Werner, R. Hillebrand, T. Förster, E. Kampertt, W. Schnelle, S. Parkin, R. J. Cava, C. Felser, B. Yan and S. A. Medvedev, *Nat Commun*, 2016, **7**, 11038.
16. C. Ataca, H. Şahin, E. Aktürk and S. Ciraci, *J. Phys. Chem. C*, 2011, **115**, 3934-3941.
17. M. Bar-Sadan, A. N. Enyashin, S. Gemming, R. Popovitz-Biro, S. Y. Hong, Y. Prior, R. Tenne and G. Seifert, *J. Phys. Chem. B*, 2006, **110**, 25399-25410.
18. A. N. Enyashin, M. Bar-Sadan, L. Houben and G. Seifert, *J. Phys. Chem. C*, 2013, **117**, 10842-10848.
19. M. Ghorbani-Asl, A. N. Enyashin, A. Kuc, G. Seifert and T. Heine, *Phys. Rev. B*, 2013, **88**, 245440.
20. H.-P. Komsa, S. Kurasch, O. Lehtinen, U. Kaiser and A. V. Krasheninnikov, *Phys. Rev. B*, 2013, **88**, 035301.
21. S. McDonnell, R. Addou, C. Buie, R. M. Wallace and C. L. Hinkle, *ACS Nano*, 2014, **8**, 2880-2888.
22. T. Böker, R. Severin, A. Müller, C. Janowitz, R. Manzke, D. Voß, P. Krüger, A. Mazur and J. Pollmann, *Phys. Rev. B*, 2001, **64**, 235305.
23. J. P. Perdew and A. Zunger, *Phys. Rev. B*, 1981, **23**, 5048-5079.
24. S. Grimme, *J. Comput. Chem*, 2004, **25**, 1463-1473.
25. G. K. H. Madsen and D. J. Singh, *Comp. Phys. Comm.*, 2006, **175**, 67-71.
26. J. Joshi, I. R. Stone, R. Beams, S. Krylyuk, I. Kalish, A. V. Davydov and P. M. Vora, *App. Phys. Lett.*, 2016, **109**, 031903.
27. W. G. Dawson and D. W. Bullett, *J. Phys. C: Solid State Phys.*, 1987, **20**, 6159-6174.
28. H. Guo, T. Yang, M. Yamamoto, L. Zhou, R. Ishikawa, K. Ueno, K. Tsukagoshi, Z. Zhang, M. S. Dresselhaus and R. Saito, *Phys. Rev. B*, 2015, **91**, 205415.
29. L. Zhou, K. Xu, A. Zubair, A. D. Liao, W. Fang, F. Ouyang, Y.-H. Lee, K. Ueno, R. Saito, T. s. Palacios, J. Kong and M. S. Dresselhaus, *J. Am. Chem. Soc.*, 2015, **137**, 11892-11895.

30. J. C. Park, S. J. Yun, H. Kim, J.-H. Park, S. H. Chae, S.-J. An, J.-G. Kim, S. M. Kim, K. K. Kim and Y. H. Lee, *ACS Nano*, 2015, **9**, 6548-6554.

31. M. Kan, H. G. Nam, Y. H. Lee and Q. Sun, *Phys. Chem. Chem. Phys.*, 2015, **17**, 14866-14871.

32. A. Soni, Y. Shen, M. Yin, Y. Zhao, L. Yu, X. Hu, Z. Dong, K. A. Khor, M. S. Dresselhaus and Q. Xiong, *Nano Letters*, 2012, **12**, 4305-4310.

33. N. F. Mott and E. A. Davis, *Clarendon-Press, Oxford 1971 437*, 1972.

34. T. C. Chasapis, D. Koumoulis, B. Leung, N. P. Calta, S.-H. Lo, V. P. Dravid, L.-S. Bouchard and M. G. Kanatzidis, *APL Mater.*, 2015, **3**, 083601.

35. J. S. Dyck, W. Chen, C. Uher, L. Chen, X. Tang and T. Hirai, *J. Appl. Phys.*, 2002, **91**, 3698-3705.

36. S. Wang, J. Yang, L. Wu, P. Wei, J. Yang, W. Zhang and Y. Grin, *Chem. Mater.*, 2015, **27**, 1071-1081.

37. T. Thonhauser, S. Zuluaga, C. A. Arter, K. Berland, E. Schröder and P. Hyldgaard, *Phys. Rev. Lett.*, 2015, **115**, 136402.

38. D. C. Langreth, B. I. Lundqvist, S. D. Chakarova-Käck, V. R. Cooper, M. Dion, P. Hyldgaard, A. Kelkkanen, J. Kleis, K. Lingzhu, L. Shen, P. G. Moses, E. Murray, A. Puzder, H. Rydberg, E. Schröder and T. Thonhauser, *J. Phys.: Condens. Matter*, 2009, **21**, 084203.

39. B. Kristian, R. C. Valentino, L. Kyuho, S. Elsebeth, T. Thonhauser, H. Per and I. L. Bengt, *Rep. Prog. Phys.*, 2015, **78**, 066501.

40. T. Thonhauser, V. R. Cooper, S. Li, A. Puzder, P. Hyldgaard and D. C. Langreth, *Phys. Rev. B*, 2007, **76**, 125112.

41. J. Heyd, G. E. Scuseria and M. Ernzerhof, *J. Chem. Phys.*, 2003, **118**, 8207-8215.

42. J. Heyd, G. E. Scuseria and M. Ernzerhof, *J. Chem. Phys.*, 2006, **124**, 219906 *(erratum)*.

43. A. Ishida, T. Yamada, T. Nakano, Y. Takano and S. Takaoka, *Jpn. J. Appl. Phys.*, 2011, **50**, 031302.

PART 5

Origin of low lattice thermal conductivity in Zintl-type $AInTe_2$ ($A=Tl^+/In^+$) compounds.

CHAPTER 5.1

Intrinsic rattler-induced low thermal conductivity in Zintl-type $TlInTe_2$*

Summary

Understanding the nature of chemical bonding and lattice dynamics together with their influence on phonon-transport is essential to explore and design crystalline solids with ultralow thermal conductivity for various applications including thermoelectrics. $TlInTe_2$ with interlocked rigid and weakly bound substructures, exhibits lattice thermal conductivity as low as ca. 0.5 W/mK near room temperature, owing to rattling dynamics of weakly bound Tl^+ cations. Large displacements of Tl^+ cations along the c-axis, plausibly driven by localized spherical electron clouds on Tl atoms, are akin to those of rattling guests in caged-systems. The heat capacity of $TlInTe_2$ exhibits a broad peak at low-temperatures due to contribution from Tl-induced low-frequency Einstein modes as also evidenced from THz time domain spectroscopy. The phonon dispersion reveals a strong coupling between large-amplitude coherent optic vibrations of Tl-rattlers and acoustic phonons. The ensuing low acoustic cut-off frequencies and sound velocities together with strong anharmonicity lead to low lattice thermal conductivity in $TlInTe_2$.

A paper based on this study has appeared in* ***J. Am. Chem. Soc.,* 2017, *139,* 4350.

5.1.1 Introduction

Crystalline solids exhibiting ultralow thermal conductivity are centric to the development of thermoelectrics, refractories and thermal insulators for efficient energy-management. Thermal transport is indeed reckoned to be a limiting factor for realizing efficient thermoelectric (TE) materials which can convert waste-heat into electricity.[1] Extrinsic strategies such as alloying and nanostructuring[2, 3] have been proven effective to suppress the lattice thermal conductivity, (κ_{Lat}) but may also deteriorate electrical mobility. Solids with intrinsically low κ_{Lat} are, therefore, practically attractive being capable of offering nearly independent control over electrical transport.

Investigations on minimal κ_{Lat} in certain TE solids have unveiled non-traditional phonon-scattering mechanisms viz. resonant phonon-scattering in filled-skutterudites[4] and clathrates[5] with randomly rattling guest-fillers, and thermal damping due to liquid-like atomic dynamics in Cu_3SbSe_3[6] and Cu_2Se[7]. A common characteristic of the above materials is the crystallographic heterogeneity with coexisting rigid and fluctuating sublattices. Intrinsically low κ_{Lat} in rock-salt I-V-VI chalcogenides[8-10] and $PbCuSbS_3$[11] was ascribed to the strong lattice-anharmonicity induced by electrostatic repulsions due to cationic ns^2 lone pair electrons. Other intrinsic phenomena leading to low κ_{Lat} include resonant bonding,[12] rattling-modes,[13, 14] multicentre bonding[15, 16] and layered structure with significant anharmonicity.[17] A microscopic understanding of the underlying correlation amongst structure, chemical bonding, and lattice dynamics together with their impact on phonon transport is not only of fundamental interest but also indispensable to explore and design new materials with ultralow thermal conductivity.

In the present chapter, we report an ultra-low κ_{Lat} (< 0.5 W/mK) in Zintl type $TlInTe_2$ in the 300-673 K range, which remains close to its theoretical minimum limit (κ_{min}). We have investigated the aspects of structure and lattice dynamics responsible for the low κ_{Lat} in $TlInTe_2$ through low-temperature heat capacity and THz time-domain spectroscopy, combined with first-principles calculations. $TlInTe_2$ exhibits rattling dynamics of Tl^+

cations inside the cage-like Thompson cubes formed by surrounding Te atoms. The ensuing low-frequency optical phonons scatter the acoustic phonons, thereby causing low κ_{Lat} in $TlInTe_2$. The latter represents a class of solids with relatively simple unit cells yet exhibiting intrinsically low κ_{Lat} due to hierarchical bonds and strong lattice anharmonicity.

5.1.2 Methods

5.1.2.1 Synthesis and characterizations

Polycrystalline ingots of $TlInTe_2$ were prepared by melting stoichiometric quantities of high-purity elemental thallium (Tl, 99.99 % metals basis), indium (In, 99.99 %) and tellurium (Te, 99.999 % metals basis) weighing a total of 6 g in sealed carbon-coated quartz ampoules evacuated at a high vacuum of 10^{-5} torr. The contents were heated up to 1123 K in 7 hr, soaked at this temperature for 10 hr and cooled to room temperature in 15 hr. Ampoules were periodically shaken to ensure homogeneity of the melt. Powder X-ray diffraction (PXRD) patterns were recorded on Bruker D8 diffractometer using Cu Kα (λ= 1.54 Å) radiation. Structure refinement was carried out using GSAS crystallographic analysis program.[18]

5.1.2.2 Rapid induction hot-pressing

The as-obtained ingots were brittle and difficult to be cut and polished directly. To prepare samples for electrical and thermal characterization, ingots were finely ground, and an appropriate amount of powdered sample was loaded into a cylindrical graphite die (10 mm inner diameter), ramped up to 723 K in 150 sec in an induction-furnace with Ar atmosphere, uniaxially pressed under ca. 47 MPa for five minutes and subsequently cooled to room temperature. The as-obtained cylinder- (ca. 9×10 mm^2) and coin- (ca. 10×2.5 mm^2) shaped samples were used for electrical and thermal transport measurements respectively (see figure 5.1.2(a)). The density of samples, measured using Archimedes method, is more than 98 % of the theoretical density of $TlInTe_2$ (7.3 g/cm^{-3}).

5.1.2.3 Thermoelectric measurements

Electrical transport: Electrical conductivity (σ) and Seebeck coefficient (S) were measured as a function of temperature from 300 K up to 673 K under He-atmosphere in a four-probe configuration using ULVAC-RIKO ZEM-3 instrument. The rectangular bar shaped samples (ca. 2×2×8 mm^3) cut from cylindrical samples were used for the electrical measurements.

Thermal transport: Coin-shaped pellets with dimensions of ca. 10 mm diameter and 2.5 mm thickness were used for thermal transport measurement. The thermal diffusivity was measured along the same direction as that for electrical transport measurement, i.e., along the hot-pressing direction. Total thermal conductivity (κ_{tot}) was then estimated using the relation, $\kappa_{tot} = D.C_p.\rho$, where ρ is the sample's density determined by Archimedes method and C_p is the specific heat capacity, derived indirectly from a standard reference (pyroceram). Lattice thermal conductivity (κ_{Lat}) is extracted by subtracting the electronic thermal conductivity (κ_{el}) from total thermal conductivity. κ_{el} is calculated using the Wiedemann Franz law, $\kappa_{el} = L\sigma T$, where σ is the electrical conductivity and L is the temperature-dependent Lorentz number. For more details, refer to the methods section in part 1. Due to very low σ, $\kappa_{Lat} \approx \kappa_{tot}$ for $TlInTe_2$. Owing to the instrumental factors, the percent error in the measured data is 5% each for electrical conductivity, Seebeck coefficient and thermal diffusivity.

5.1.2.4 Terahertz Time-Domain Spectroscopy

To probe the low-energy optical phonons in $TlInTe_2$, we have carried out Terahertz (THz) Time-Domain Spectroscopy (TDS) on $TlInTe_2$ in collaboration with Dr. Pankaj Mandal's group at IISER, Pune. A coin-shaped sample of ca. 7 mm diameter and 480 µm thickness is used. THz-TDS is a non-contact way of measuring a material's dielectric response.[19, 20] The THz time-domain spectrometer is based on an amplified ultrafast laser system, consisting of a Ti: Sapphire oscillator (Spectra Physics Tsunami) and regenerative amplifier (Spectra Physics Spitfire Pro). The amplifier output has a peak wavelength at 800 nm, a pulse duration of 50 fs, 1 K Hz repetition rate and 4 W of total power. Half of the laser power is used for generation and coherent

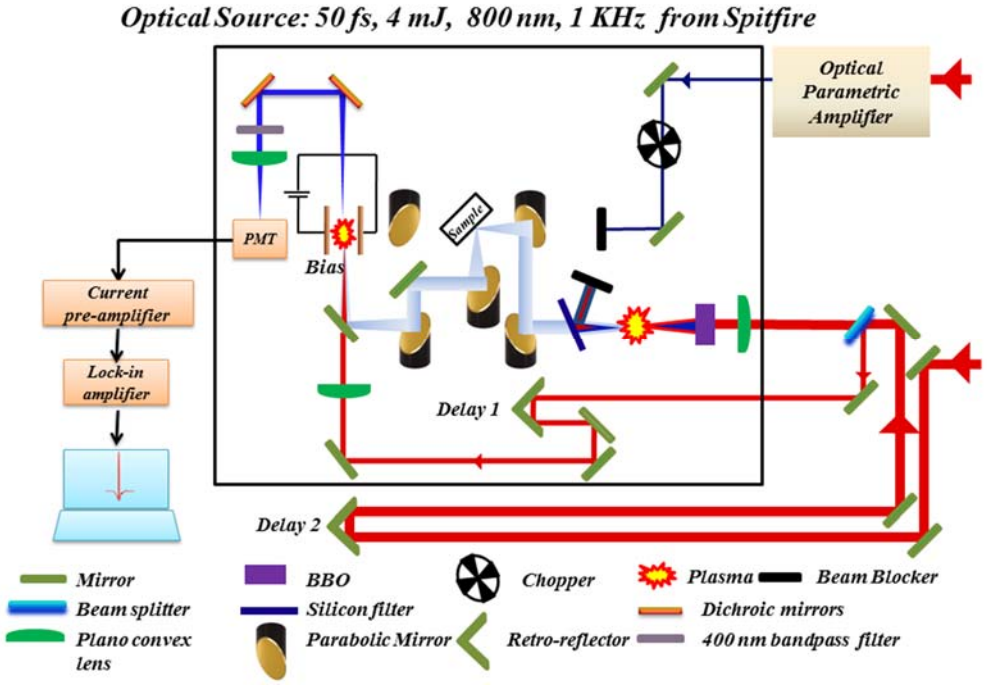

Figure 5.1.1. *Schematic of THz-spectrometer*

detection of THz radiation using air photonics.[21, 22] The schematic of the setup is shown in figure 5.1.1, and the details are described elsewhere.[23] The entire THz path is enclosed and continuously purged with dry nitrogen to avoid THz absorption by water vapor. All THz data were collected at room temperature. Because of the very high absorption coefficient of the sample at the concerned spectral range (0.1-15 THz), THz-TDS in transmission mode shows very little THz transmission through the sample. Hence, we have collected the THz-TDS in reflection geometry with an incidence angle of 45°. Time domain THz electric fields reflected from the reference ($E_{Si}(t)$) and sample ($E_{sam}(t)$) were collected. High resistivity silicon wafer was used as a reference. The ratio of the Fourier transforms of time-domain signals from the sample and reference is related to the refractive indices of sample and reference according to the following Fresnel equation for reflection:[24, 25]

$$(\omega) = \frac{\tilde{E}_{sam}(\omega)}{\tilde{E}_{ref}(\omega)} = \frac{\tilde{n}_{sam}^2 cos\theta - n_{air}\sqrt{\tilde{n}_{sam}^2 - n_{air}^2\, sin^2\,\theta}}{\tilde{n}_{sam}^2 cos\theta + n_{air}\sqrt{\tilde{n}_{sam}^2 - n_{air}^2\, sin^2\,\theta}} \Big/ \frac{\tilde{n}_{si}^2 cos\theta - n_{air}\sqrt{\tilde{n}_{si}^2 - n_{air}^2\, sin^2\,\theta}}{\tilde{n}_{si}^2 cos\theta + n_{air}\sqrt{\tilde{n}_{si}^2 - n_{air}^2\, sin^2\,\theta}} \qquad (5.1.1)$$

Complex refractive index ($\tilde{n}_{sam} = n + ik$) of the sample was calculated numerically. Refractive indices of silicon ($n_{Si} = 3.45$) and air ($n_{air} = 1$) are

almost constant over the entire range of detected THz frequencies. Real part (n) of complex refractive index is the actual refractive index of sample while imaginary part, extinction coefficient (k), is related to the absorption coefficient (α) as: $\alpha = 2\omega k/c$, where ω is angular frequency, and c is the speed of light. Since the absorption by the sample is very high above 5 THz even in reflection mode, the optical parameters (n and α) obtained may not be reliable beyond this frequency range.

5.1.2.5 Computational details

To investigate the phonons in $TlInTe_2$, we have collaborated with Prof. Waghmare's group at JNCASR, Bangalore, to carry out the density functional theory (DFT) based first-principles calculations using Quantum espresso (QE) code.[26] The latter uses plane wave basis to represent wavefunctions and charge density and pseudopotentials to capture the effect of potential arising from the nucleus and core electrons of an atom. Norm-conserving pseudopotentials were used in the calculations. The exchange and correlation energy of the electrons were treated with a generalized gradient approximated (GGA) functional [27] as parametrized by Perdew, Burke, and Ernzerhof.[28] The expansion of electronic wave function and charge density in plane wave basis was truncated with cut-off energies of 60 Ry and 240 Ry respectively. Brillouin Zone (BZ) integrations were sampled on a uniform mesh of 8×8×8 k-points. The discontinuity in the occupations number of electronic states near the gap was smeared with Fermi-Dirac distribution functions with a broadening of $\kappa_B T = 0.003$ Ry. Fully optimized lattice constants of $TlInTe_2$ agree quite well with that of its experimental values. The electronic structure and lattice dynamical properties were determined for the optimized crystal structure of $TlInTe_2$. QE implementation of density functional perturbation theory (DFPT) [29] was used to obtain phonon dispersion of $TlInTe_2$. In this, the interatomic force constant matrices were first obtained on a 2×2×2 mesh of q-points in the BZ, and were Fourier interpolated at an arbitrary q-vector. Grüneisen parameter (γ) measures the degree of anharmonicity of phonons in a material. Mode Grüneisen parameter (γ_i) of each of the phonon modes is estimated using finite

difference formula ($\gamma_i = -\frac{V}{\omega_i} d\omega_i/dV$) and taking phonon dispersion calculated at two volumes (V_0 and $0.96V_0$, V_0 being the equilibrium volume at 0 GPa).

5.1.3 Results & discussion

5.1.3.1 Structure and bonding

Figure 5.1.2(a) shows the Rietveld refinement of PXRD data from an as-synthesized sample, based on the tetragonal (I/4mcm) crystal structure. The structural parameters of Rietveld refinement are tabulated in Table 5.1.1. $TlInTe_2$ has a tetragonal crystal structure (I/4mcm space group) which constitutes anionic $(InTe_2)_n^{-n}$ chains alternating with chains of Tl^+ cations (Figure 5.1.2(b)).[30] Each In makes four covalent (sp^3) bonds with four Te atoms forming tetrahedrons; the latter share their horizontal edges to form columnar anionic substructure along the crystallographic c-axis. The covalent bond distance between In and Te is about 2.81 Å being close to the sum of covalent radii of In (1.44 Å) and Te (1.35 Å). Each Tl is surrounded by eight Te atoms (of the anionic substructure) in a distorted square antiprismatic arrangement forming skewed cages referred to as 'Thompson cubes'. The latter share square-faces along the c-axis forming cationic substructure (Figures 5.1.2(b) and 5.1.3(c)). The Tl-Te distance of 3.59 Å is close to the sum of ionic radii of Tl^+ (1.59 Å) and Te^{2-} (2.21 Å).

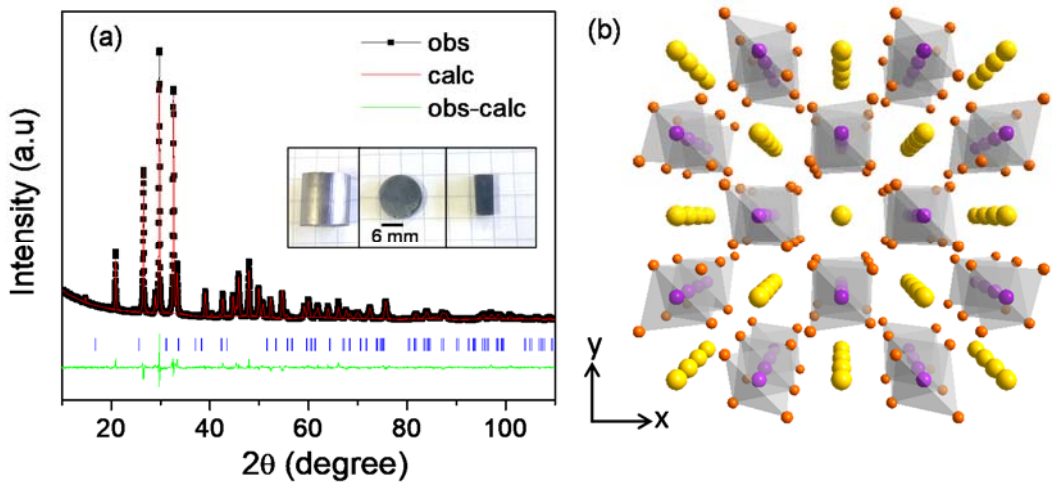

Figure 5.1.2 *(a) Rietveld refinement of powder XRD pattern of $TlInTe_2$ with tetragonal (I/4mcm) structural model. The inset shows hot-pressed specimens used for thermoelectric measurements. (b) Crystal structure of $TlInTe_2$ viewed down the z-axis. Yellow, violet and orange atoms denote Tl, In and Te atoms, respectively.*

Table 5.1.1 *Structural parameters of Rietveld refinement.*

Space group: I4/mcm; $a = b = 8.47980(27)$; $c = 7.18894(28)$; unit cell volume = 516.94(5)

Atom	Wyck.	x/a	y/b	z/c	U_{iso}		
In	4b	0	0.5	0.25	0.016		
Te	8h	0.18098	0.68098	0	0.023		
					U_{11}	U_{22}	U_{33}
Tl	4a	0	0	0.25	0.027	0.027	0.074

Reduced χ^2=5.6; Rp = 0.0246; wRp=0.0347

$TlInTe_2$ is structurally analogous to Zintl compounds such as Ca_3AlSb_3, $Ca_5Al_2Sb_6$ and Sr_3GaSb_3 constituting 1D anionic chains.[31-33] The latter exhibit low κ_{Lat} owing to complex unit cells (26-56 atoms per unit cell). Zintl-type structures with cationic and anionic substructures are adopted by electron-deficient compounds which cannot form all two-center-two-electron (2c-2e) covalent bonds. Electrons are transferred from the more electropositive cations to the anionic substructure where they are used to form 2c-2e covalent bonds.[34, 35] $TlInTe_2$ adopts a Zintl-like structure as the sp^3 hybridized In has only three valence electrons and hence, cannot form four 2c-2e bonds with Te atoms. Based on Zintl-Klemm rules of valence-counting,[36] the more electropositive Tl atom in $TlInTe_2$ donates one valence electron to the anionic chain and leaves behind its $6s^2$ lone pair to attain a formal valence of +1. Treating In as a part of anionic substructure, In being bonded to four Te atoms has a formal valence of -1, whereas Te being shared between two tetrahedra has a formal valence of 0. Accordingly, $TlInTe_2$ is a valence compound described as $Tl^{+}In^{-1}Te_2^{0}$ and exhibits semiconducting properties in agreement with our electrical transport measurements. It is interesting that $TlInTe_2$, with only 16 atoms per unit cell, is simple relative to the aforementioned 1D Zintl compounds yet exhibits low κ_{Lat} (ca. 0.5 W/m.K at 300 K) owing to distinct lattice dynamics thereof as discussed below.

As $TlInTe_2$ consists of covalent as well as ionic substructures, we expect the chemical bonding in $TlInTe_2$ to be different from solids with crystallographic homogeneity. We have examined the bonding environments in $TlInTe_2$ with the aid of real-space descriptors such as charge density and

electron localization function (ELF) calculated using the DFT. The calculated total charge density of $TlInTe_2$ reveals overlapping charge densities of In and Te atoms within the $InTe_4$ tetrahedra signifying a strong covalent bonding between them (Figure 5.1.3(a)). On the other hand, the more electropositive Tl is surrounded by non-overlapping, nearly spherical charge density due to $6s^2$ electron lone pair of Tl (Figure 5.1.3(a)) implying the interaction between Tl and the surrounding Te atoms to be electrostatic. ELF estimates the degree of electron localization in a solid taking into account the local influence of the Pauli repulsion. As seen from the ELF map shown in Figure 5.1.3(b), a spherical electron localization around Tl is associated with its $6s^2$ lone pair, whereas a lobe-shaped asymmetrically distributed electron cloud around Te arises from the $5s^2$ lone pair of Te, partially hybridized as permitted by its site symmetry.

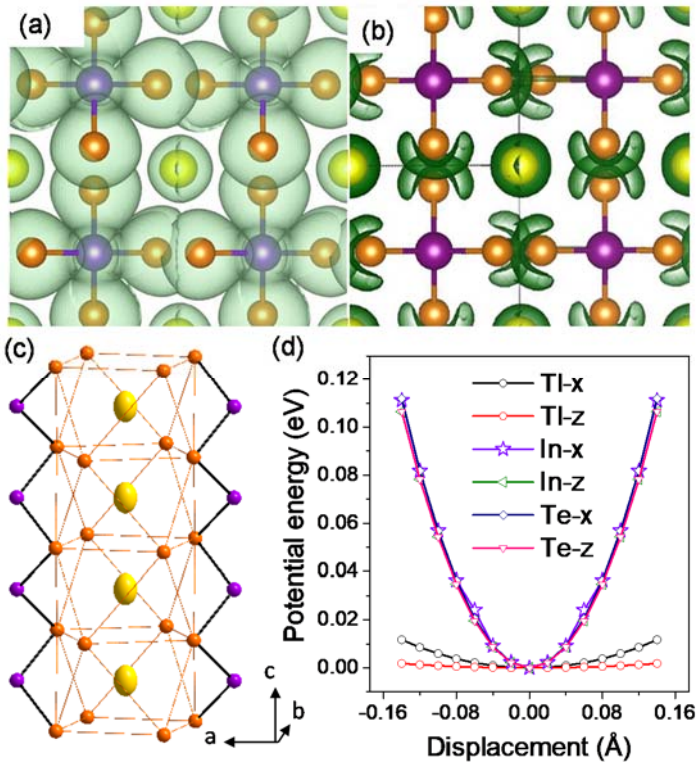

Figure 5.1.3 *Plots of (a) total charge density and (b) electron localization function (ELF); (c) ADPs of all the atoms plotted as 80% probability ellipsoids. Yellow, violet, and orange atoms denote Tl, In and Te atoms respectively; (d) potential energy vs. displacement along crystallographic x- and z-directions of the tetragonal unit cell.*

The atomic displacement parameter (ADP) measures the mean-square displacement of an atom about its equilibrium position in a crystal. ADPs were obtained from the atom-refinement of PXRD pattern (see table 5.1.1). In and

Te atoms are associated with isotropic ADPs whereas Tl is associated with a large anisotropic ADP ($U_{3,3} \sim 0.07$ Å^2 at 300 K) with its maximum displacement being along the c-axis (Figure 5.1.3(c) and table 5.1.1). Large ADP implies a weak bonding and is characteristic of rattlers, for instance, in filled-skutterudites.[4, 37] Tl can, therefore, be regarded as a rattler in $TlInTe_2$ with the surrounding Thompson cage of Te-atoms resembling the over-sized cages in filled-skutterudites and clathrates. Given the large ADP of Tl^+ cations, it is interesting to investigate the phonon scattering mechanism causing an exceptionally low κ_{Lat} in $TlInTe_2$.

To get further insight into atomic-level dynamics, we have calculated the potential energy curves by off-centering the atoms relative to their static equilibrium positions along the x- and z-directions. It is clear from figure 5.1.3(d) that In and Te atoms are confined in steep potential wells whereas Tl is located in a flat potential well suggesting that Tl atoms would easily rattle within hallow Thompson cages with large amplitudes, especially along the z-axis (c-axis). The flat potential well of Tl is consistent with its large ADP and induces low-energy optical modes which scatter the heat-carrying acoustic phonons. It is important to note that the large anisotropic ADP of Tl^+ cation is in contrast with small (< 0.015 Å^2) and isotropic ADPs associated with the cations in other 1D Zintl compounds such as Ca_3AlSb_3 $Ca_5Al_2Sb_6$ and Sr_3GaSb_3.[38] Besides thermal energy, two factors viz. a) the electrostatic repulsion between the localized electrons (lone pair) of Tl and the surrounding Te ions and b) the propensity of $6s^2$ lone pair of Tl to stereochemically express itself, plausibly augment the displacements of Tl along the c-axis, which show up as large ADPs in powder Bragg refinement. This also avoids dimerization of Tl^+ and collective motion of Tl^+ ions belonging to Tl-chain along the c-axis. It has been shown previously that a spherically distributed lone pair tends to be unstable and forms a localized lobe by driving a structural distortion in the extreme case, for instance, in perovskite $BiMnO_3$.[39] Lone-pair induced local cation off-centering has also been observed in rock-salt PbTe.[40] On the other hand, in filled-skutterudites, the guest atoms are too small for the oversized structural voids and do not interact with the host lattice thereby causing them

to randomly rattle within the voids under thermal agitation. It is important to note that in the absence of a lone-pair induced structural distortion, the phonons become highly anharmonic as shown in the rocksalt I-V-VI compounds.[10] The latter adopt rhombohedral phases as a consequence of strong lone-pair (of group V element) induced distortion in the rocksalt structure; when they are marginally stable in the rocksalt phase, the phonons become highly anharmonic.

5.1.3.2 Experimental heat capacity

The large ADPs and flat potential wells of Tl^{+} cations prompted us to investigate the low-temperature specific heat capacity, C_p, of $TlInTe_2$ between 2 and 30 K. To quantitatively interpret the experimental heat capacity of $TlInTe_2$, I have employed a combined Debye-Einstein model. Figure 5.1.4(a) shows the low-temperature C_p of $TlInTe_2$ in the range of 2-30 K. The plot of C_p/T vs. T^2 can be well fitted by using the combined Debye-Einstein model:[41]

$$\frac{C_p}{T} = \gamma + \beta T^2 + \sum_n \left(A_n (\Theta_{En})^2 . (T^2)^{-\frac{3}{2}} . \frac{e^{\frac{\Theta_{En}}{T}}}{\left(e^{\frac{\Theta_{En}}{T}} - 1\right)^2} \right) \qquad (5.1.2)$$

In the above equation, the first term denotes the electronic contribution and the second term, to the Debye lattice contribution with $\beta = C.(12\pi^4 N_A k_B/5).(\Theta_D^{-3})$ where N_A, k_B and Θ_D denote Avogadro number, Boltzmann constant and characteristic Debye temperature respectively. The parameter C is given as $C = 1 - \sum_n A_n/3NR$, where N is the number of atoms per formula unit and R is the gas constant (8.314 J/mol.K). The third term represents the contribution from Einstein oscillator modes where A_n is the pre-factor of the n^{th} Einstein oscillator mode. The various fitting parameters are listed in Table 5.1.2. A minimum of three Einstein modes are required to adequately model the temperature-dependence of C_p, whose characteristic temperatures were estimated though fitting to be $\Theta_{E1} = 24.8 \pm 3.9$ K, $\Theta_{E2} = 44.5 \pm 4.1$ K, and $\Theta_{E3} = 79.8 \pm 5.1$ K. The estimated Debye temperature (Θ_D) of $TlInTe_2$ is 250 K. At low temperatures, C_p exhibits a broad peak in the 5-15 K range as seen clearly in the C_p/T^3 vs. T plot (Figure 5.1.4(b)); the broad peak can be fitted only by using combined Debye-Einstein model as Debye model (green line)

alone cannot suffice to reproduce the observed C_p data asserting the contribution from Einstein oscillators. This broad peak resembles the Boson-like hump observed in the low-T C_p of disordered glasses while in clathrates and skutterudites, it was ascribed to the excess phonon density of states (DOS) resulting from guest-induced low-lying optical modes.[5] In $TlInTe_2$, an excess contribution to C_p at low temperatures arises due to low-energy optical modes originating from weakly bound Tl-rattlers, which manifest as the Einstein oscillators. These low-lying optical modes can couple with the heat-carrying acoustic modes decreasing the group velocities of the latter and thereby suppressing κ_{Lat}.

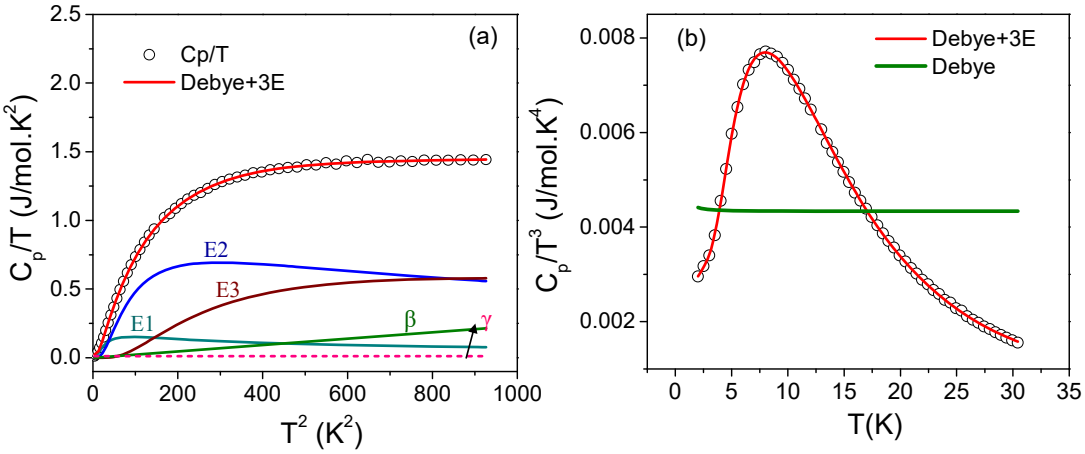

Figure 5.1.4 *(a) Cp/T vs. T^2 plot in 2–30 K range. The red solid line is calculated using combined Debye–Einstein model. The individual contributions from electronic (γ), Debye (β) and the three Einstein terms (E1, E2, E3) are also plotted. b) Cp/T^3 vs. T plot showing a broad peak that can be fitted only with combined Debye–Einstein model (red solid line) and not the Debye model alone (green solid line).*

Table 5.1.2 *Fitting parameters for modeling C_p/T vs. T^2 plot*

Parameter	Value
γ /10^{-3} J mol^{-1} K^{-2}	11.920 ± 4.300
β /10^{-4} J mol^{-1} K^{-2}	2.312 ± 0.265
Θ_{E1}/K	24.803 ± 3.922
Θ_{E2}/K	44.506 ± 4.132
Θ_{E3}/K	79.823 ± 5.130
Θ_D (K)	250
R^2	0.99992

5.1.3.3 Experimental lattice thermal conductivity

Figure 5.1.5(a) shows the temperature-dependent lattice thermal conductivity (κ_{Lat}) of hot-pressed $TlInTe_2$ in the 300-673 K range. It varies slightly from about 0.46 W/mK at 300 K to 0.31 W/mK at 673 K. The solid line shows 1/T dependence of κ_{Lat}, suggesting a dominant Umklapp phonon scattering. The dotted horizontal line corresponds to the theoretical minimum (κ_{min}) of $TlInTe_2$ estimated using Cahill's model (Equation 1.15, part 1) which assumes a random walk of energy between localized oscillators of varying sizes and frequencies.[42] κ_{min} of $TlInTe_2$ is estimated to be about 0.28 W/mK by using a number density of ca. 3.1×10^{22} cm^{-3}, and calculated values of sound velocities (v_i) and mode Debye temperatures ($\theta_i = \hbar\omega_{max}/k_B$) (see table 5.1.3). It is interesting to note that κ_{Lat} of $TlInTe_2$ is close to the estimated κ_{min} throughout the temperature range investigated. Figure 5.1.5(b) compares the κ_{Lat} of $TlInTe_2$ with that of PbTe, a leading thermoelectric material, and that of aforementioned 'complex' Zintl compounds with columnar anionic substructures, viz. Ca_3AlSb_3, $Ca_5Al_2Sb_6$ and Sr_3GaSb_3. It is noteworthy that κ_{Lat} of $TlInTe_2$ is lower than that of all the above compounds throughout the temperature range investigated.

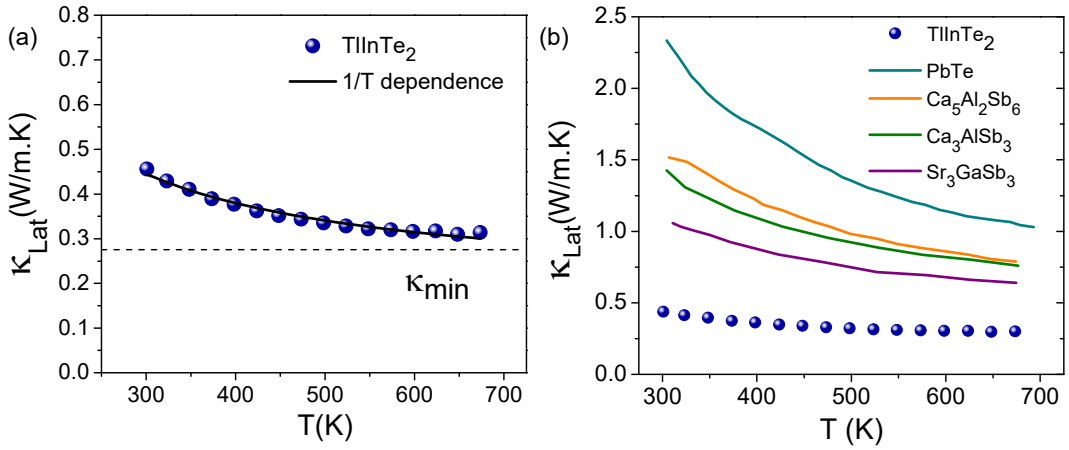

Figure 5.1.5 *(a) κ_{Lat} of $TlInTe_2$ measured between 300 and 673 K. The solid black curve is the T^{-1} fit of κ_{Lat}. The horizontal dashed line is the theoretical κ_{min} of $TlInTe_2$ calculated using Cahill's model. b) Comparison of κ_{Lat} of $TlInTe_2$ with that of structurally analogous Zintl compounds viz. $Ca_5Al_2Sb_3$, Ca_3AlSb_3 and Sr_3GaSb_3, and that of rocksalt PbTe.*

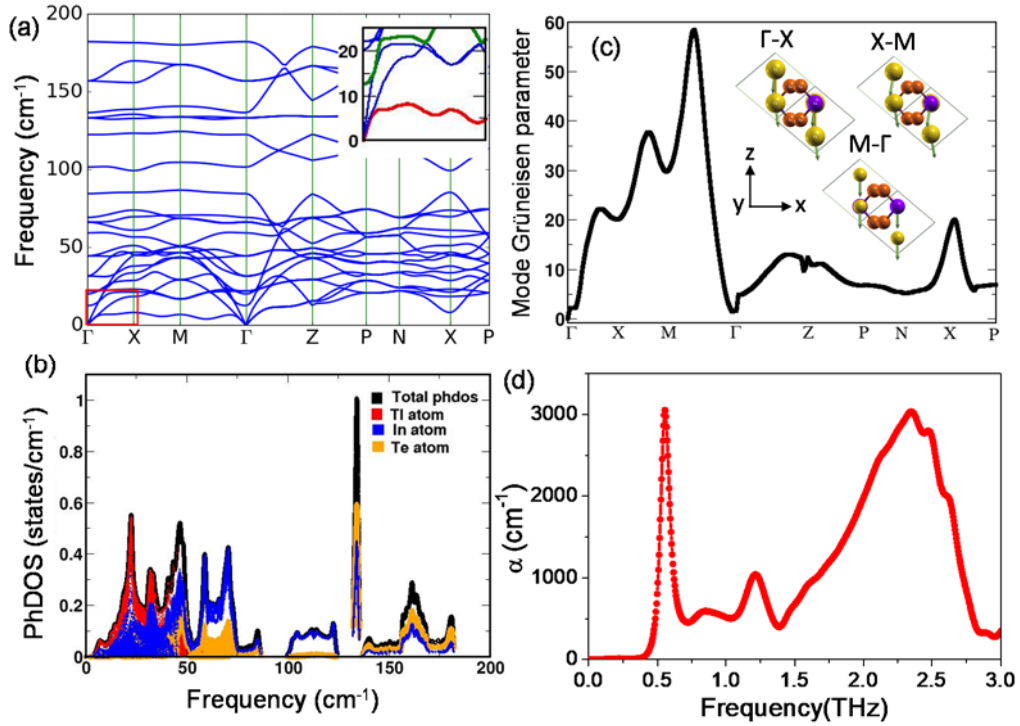

Figure 5.1.6 *(a) Calculated phonon dispersion of $TlInTe_2$. The inset shows an avoided-crossing between green and red branches near the Γ-point due to optical–acoustic coupling. (b) Phonon DOS showing the dominant contribution of Tl atom in the low-frequency region. (c) Dispersion of mode Grüneisen parameter along various k-points for the lowest flat branch. The inset shows eigen displacements along the Γ-X-M-Γ path. Yellow, violet and orange spheres denote Tl, In and Te atoms respectively. (d) The absorption coefficient of $TlInTe_2$ as a function of THz frequency at room temperature.*

5.1.3.4 Phonon dispersion

The calculated phonon dispersion (Figure 5.1.6(a)) exhibits several low-frequency phonon modes starting from ca. 12.4 cm^{-1} at the Γ-point and dispersing to higher frequencies along high-symmetry directions in the Brillouin zone. The calculated phonon-frequencies at the Γ-point are listed in table 5.1.4. A striking feature of phonon dispersion plot is the presence of a nondispersive branch along Γ-X-M-Γ path. The corresponding eigen-displacements viewed along the Γ-X-M-Γ path essentially constitute large-amplitude coherent vibration of Tl atoms along the c-axis (see inset, Figure 5.1.6(c)). Beyond the Γ-point, the optic-acoustic coupling is discernible from the avoided-crossing feature of the phonon dispersion (inset of figure 5.1.6(a)). The cut-off frequencies of acoustic phonons lie below 45 cm^{-1}, and the average sound velocities are quite low (Table 5.1.3). Atom-projected phonon DOS in figure 5.1.6(b) shows that the dominant contribution in the low-energy region ($<$ 50

cm^{-1}) comes from Tl atom further indicating that the low-energy phonons are mainly dictated by Tl-vibrations. The visuals of three lowest zone-center optical phonon modes indeed show dominant vibrations of Tl^{+} cations. The lowest optical phonon at 12.4 cm^{-1} is in reasonable agreement with the lowest

Table 5.1.3 *Calculated Phonon sound velocities in the vicinity of Brillouin zone center (v_{TA1}, v_{TA2}, v_{LA}), and cut-off frequencies for longitudinal (LA) and transverse acoustic phonon branches (TA1, TA2) along the Γ-X, Γ -Z and Γ-M directions in the Brillouin zone. The cut-off frequency (ω_{max}) is the highest acoustic frequency along a given direction.*

Direction	v_{LA} (m/s)	v_{TA1} (m/s)	v_{TA2} (m/s)	ω_{max} (cm^{-1}) LA	ω_{max} (cm^{-1}) TA1	ω_{max} (cm^{-1}) TA2
Γ-X	2222	1009	1042	45	6.7	17.9
Γ-M	2195	1105	1158	32.7	6.4	29
Γ-Z	2648	1166	1166	43	11	11
Average	2355	1093	1122	40.23	8.3	19.3

Table 5.1.4 *Calculated phonon frequencies of zone center optical phonons in $TlInTe_2$.*

S. No	Mode	Frequency in cm^{-1}
1	A_{2u}	12.4
2	A_{2g}	19.8
3	E_g	21.8
4	E_u	31.2
5	E_g	44.2
6	A_{2g}	59.2
7	E_u	66.1
8	B_{1g}	69.1
9	B_{2g}	84.3
10	B_{1u}	101.6
11	A_{1g}	122.3
12	E_g	133.1
13	A_{2u}	136.5
14	E_u	156.8
15	B_{2g}	182.1

Einstein mode (Θ_{E1} = 24.8 K) obtained from the fitting-analysis of low-T C_p. It is also lower than the lowest optical phonon in low-κ α-MgAgSb (κ_{Lat}=0.6 W m^{-1}K^{-1} at 300 K).[16] In α-MgAgSb, the low-frequency optical phonons arise from weak multicenter bonding interactions and reduce the κ_{Lat} through resonant phonon scattering. Similar low-frequency optic modes have been shown to cause low κ_{Lat} in filled-skutterudites, clathrates and Cu-based chalcogenides.[41, 43] In $TlInTe_2$, the low-frequency optical modes arise from rattling Tl atoms and couple with the heat-carrying acoustic phonons through symmetry-allowed interactions as clearly evident from the avoided-crossing in the phonon dispersion. Secondly, the flat non-dispersive nature of optical branch suggests that the coupling exists at all wavelengths of optic mode (inset of figure 5.1.6(a)). It is thus clear from the low-T C_p and first-principles analysis that Tl-induced low-energy optical modes play an important role in causing low κ_{Lat}.

5.1.3.5 Dispersion of mode Grüneisen parameters

As discussed in part 1, Grüneisen parameter (γ) quantifies the strength of anharmonicity in a solid. The Gruneisen parameter strongly affects the phonon-phonon interactions. When atoms in an anharmonic solid are displaced by a wave, the elastic properties of the medium as seen by another wave vary along the path of the first wave, resulting in strong interactions. Because γ quantifies by how much the bond stiffness is affected by changes in the interatomic distances, the probability of phonon-phonon interactions is proportional to γ^2. We have determined the k-dispersion of mode Grüneisen parameters (γ_i) for the three lowest branches using phonon dispersions calculated at two different volumes in a finite-difference method (Figure 5.1.6(c)). γ_i is high for all the branches and notably, the aforementioned flat phonon branch shows an anomalously high γ_i of ~ 60 along M-Γ path; the high γ_i may arise due to a) flat potential well of Tl (low phonon frequency) and b) dependence of restoring force on volume via electrostatic repulsion between Tl and the surrounding Te ions. At high-temperatures where the Umklapp phonon scattering is dominant, κ_{Lat} decays as γ_i^2.[8] Therefore, such a high value of γ_i indeed reflects strong anharmonicity and phonon-phonon interactions in

$TlInTe_2$[10] and also confirms the dominant role of localized and low-frequency rattling mode of Tl cations in the reduction of κ_{Lat} in $TlInTe_2$.

5.1.3.6 Terahertz Time-Domain Spectroscopy

To experimentally verify the presence of low-frequency optical modes, we have carried out Terahertz Time-Domain Spectroscopy (THz-TDS).[19, 20] Figure 5.1.6(d) shows the plot of absorption coefficient as a function of THz frequency, obtained at 300 K. There are three distinct peaks below 1.5 THz in the THz absorption plot at about 0.5, 0.9 and 1.2 THz which are in reasonable agreement with the three aforementioned Einstein modes from specific heat capacity and the calculated low-energy optical phonons (Table 5.1.4).

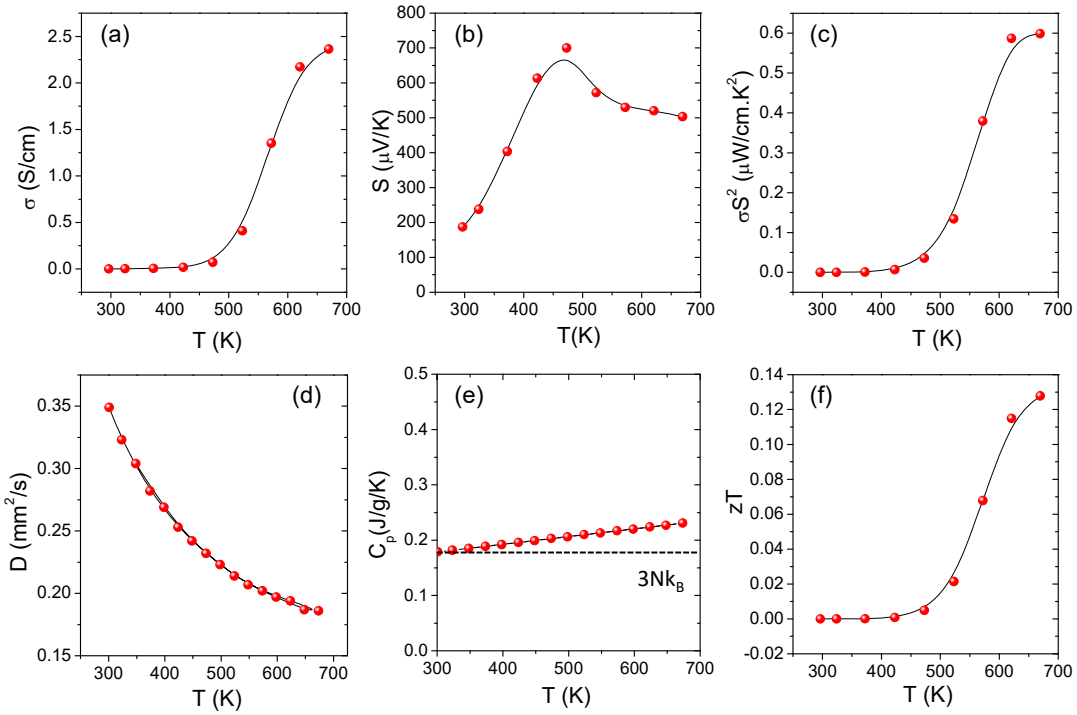

Figure 5.1.7 *High-temperature electrical and thermal transport properties. a) Electrical conductivity (σ), b) Seebeck coefficient (S), c) power factor (σS^2), d) Diffusivity (D), e) specific heat capacity (C_p) and f) thermoelectric figure of merit (zT) of $TlInTe_2$.*

5.1.3.7 Figure of merit, *zT*

Figures 5.1.7(a-c) show the temperature-dependent σ, S and power factor (σS^2) respectively, between 300 and 673 K. Figures 5.1.7(d-f) show temperature-dependent diffusivity (D), C_p and dimensionless thermoelectric figure of merit ($zT = \sigma S^2 T/\kappa$) respectively, between 300 and 673 K. σ and S

exhibit typical semiconducting behaviour with thermal activation at high temperatures. However, due to very low σ of $TlInTe_2$, the maximum power factor is less than unity thereby limiting the maximum zT to ca. 0.15 at 673 K.

5.1.4 Conclusions

$TlInTe_2$ manifests hierarchical chemical bonding with a rigid covalently bound anionic framework interlocked with weakly bound cationic substructure comprising of Tl^+ cations. The latter act as intrinsic rattlers akin to guest-rattlers in filled-skutterudites. The large displacements of Tl atoms along the c-axis are caused by spherically distributed $6s^2$ lone pairs of Tl. Low-T C_p, as well as THz-TDS spectroscopy reveal low-energy optical phonons resulting from the weakly bound Tl-rattlers as also confirmed by first-principles calculations. The latter also reveal a strong optical-acoustic coupling that results in anharmonic damped vibration of Tl-cations along the c-axis. Strong anharmonicity together with low sound velocities and cut-off frequencies leads to κ_{Lat} as low as ca. 0.5 W/mK at 300 K. Due to very low electrical conductivity, however, pristine $TlInTe_2$ is not a good thermoelectric material and requires an extensive carrier-engineering to realize promising thermoelectric efficiency. But it does lead to an important conclusion that large ADPs associated with a specific set of atoms (i.e., hierarchical bonding) and spherical lone pairs will serve as good indicators of anharmonicity and low κ_{Lat} in the search for new thermoelectric materials.

5.1.5 References

1. J. R. Sootsman, D. Y. Chung and M. G. Kanatzidis, *Angew. Chem. Int. Ed.*, 2009, **48**, 8616-8639.
2. K. Biswas, J. He, I. D. Blum, C.-I. Wu, T. P. Hogan, D. N. Seidman, V. P. Dravid and M. G. Kanatzidis, *Nature*, 2012, **489**, 414-418.
3. B. Poudel, Q. Hao, Y. Ma, Y. Lan, A. Minnich, B. Yu, X. Yan, D. Wang, A. Muto, D. Vashaee, X. Chen, J. Liu, M. S. Dresselhaus, G. Chen and Z. Ren, *Science*, 2008, **320**, 634-638.
4. X. Shi, J. Yang, J. R. Salvador, M. Chi, J. Y. Cho, H. Wang, S. Bai, J. Yang, W. Zhang and L. Chen, *J. Am. Chem. Soc.*, 2011, **133**, 7837-7846.
5. T. Takabatake, K. Suekuni, T. Nakayama and E. Kaneshita, *Rev. Mod. Phys.*, 2014, **86**, 669-716.
6. W. Qiu, L. Xi, P. Wei, X. Ke, J. Yang and W. Zhang, *Proc. Natl. Acad. Sci.*, 2014, **111**, 15031-15035.
7. H. Liu, X. Shi, F. Xu, L. Zhang, W. Zhang, L. Chen, Q. Li, C. Uher, T. Day and G. J. Snyder, *Nat Mater*, 2012, **11**, 422-425.
8. D. T. Morelli, V. Jovovic and J. P. Heremans, *Phys. Rev. Lett.*, 2008, **101**, 035901.
9. S. N. Guin, A. Chatterjee, D. S. Negi, R. Datta and K. Biswas, *Energy Environ. Sci.*, 2013, **6**, 2603-2608.
10. M. D. Nielsen, V. Ozolins and J. P. Heremans, *Energy Environ. Sci.*, 2013, **6**, 570-578.
11. Y. Dong, A. R. Khabibullin, K. Wei, J. R. Salvador, G. S. Nolas and L. M. Woods, *ChemPhysChem*, 2015, **16**, 3264.
12. S. Lee, K. Esfarjani, T. Luo, J. Zhou, Z. Tian and G. Chen, *Nat. Commun.*, 2014, **5**, 3525.
13. D. J. Voneshen, K. Refson, E. Borissenko, M. Krisch, A. Bosak, A. Piovano, E. Cemal, M. Enderle, M. J. Gutmann, M. Hoesch, M. Roger, L. Gannon, A. T. Boothroyd, S. Uthayakumar, D. G. Porter and J. P. Goff, *Nat Mater*, 2013, **12**, 1028-1032.

14. M. K. Jana, K. Pal, U. V. Waghmare and K. Biswas, *Angew. Chem. Int. Ed.*, 2016, **55**, 7792-7796.
15. S. Wang, J. Yang, L. Wu, P. Wei, J. Yang, W. Zhang and Y. Grin, *Chem. Mater.*, 2015, **27**, 1071-1081.
16. P. Ying, X. Li, Y. Wang, J. Yang, C. Fu, W. Zhang, X. Zhao and T. Zhu, *Adv. Funct. Mater.*, 2017, **27**, 1604145.
17. L.-D. Zhao, S.-H. Lo, Y. Zhang, H. Sun, G. Tan, C. Uher, C. Wolverton, V. P. Dravid and M. G. Kanatzidis, *Nature*, 2014, **508**, 373-377.
18. B. Toby, *J. Appl. Cryst.*, 2001, **34**, 210-213.
19. M. C. Beard, G. M. Turner and C. A. Schmuttenmaer, *J. Phys. Chem. B*, 2002, **106**, 7146-7159.
20. P. U. Jepsen, D. G. Cooke and M. Koch, *Laser & Photon. Rev.*, 2011, **5**, 124-166.
21. J. B. Baxter and G. W. Guglietta, *Anal. Chem.*, 2011, **83**, 4342-4368.
22. B. Clough, J. Dai and X.-C. Zhang, *Mater. Today*, 2012, **15**, 50-58.
23. G. R. Yettapu, D. Talukdar, S. Sarkar, A. Swarnkar, A. Nag, P. Ghosh and P. Mandal, *Nano Lett.*, 2016, **16**, 4838-4848.
24. P. U. Jepsen, J. K. Jensen and U. Møller, *Opt. Express*, 2008, **16**, 9318-9331.
25. P. U. Jepsen, U. Møller and H. Merbold, *Opt. Express*, 2007, **15**, 14717-14737.
26. P. Giannozzi, S. Baroni, Nicola Bonini, Matteo Calandra, Roberto Car, C. Cavazzoni, Davide Ceresol, Guido L Chiarotti, Matteo Cococcioni, Ismaila Dabo, Andrea Dal Corso, Stefano de Gironcoli, Stefano Fabris, Guido Fratesi, Ralph Gebauer, Uwe Gerstmann, Christos Gougoussis, Anton Kokalj, Michele Lazzeri, Layla Martin-Samos, Nicola Marzari, Francesco Mauri, Riccardo Mazzarello, Stefano Paolini, Alfredo Pasquarello, Lorenzo Paulatto, Carlo Sbraccia, Sandro Scandolo, Gabriele Sclauzero, Ari P Seitsonen, Alexander Smogunov, P. Umari and R. M. Wentzcovitch, *J. Phys.: Condens. Matter*, 2009, **21**, 395502.
27. X. Hua, X. Chen and W. A. Goddard, *Phys. Rev. B*, 1997, **55**, 16103-16109.

28. J. P. Perdew, K. Burke and M. Ernzerhof, *Phys. Rev. Lett.*, 1996, **77**, 3865-3868.

29. S. Baroni, S. de Gironcoli, A. Dal Corso and P. Giannozzi, *Rev. Mod. Phys.*, 2001, **73**, 515-562.

30. A. M. Panich, *J. Phys.: Condens. Matter*, 2008, **20**, 293202.

31. A. Zevalkink, E. S. Toberer, W. G. Zeier, E. Flage-Larsen and G. J. Snyder, *Energy Environ. Sci.*, 2011, **4**, 510-518.

32. A. Zevalkink, W. G. Zeier, G. Pomrehn, E. Schechtel, W. Tremel and G. J. Snyder, *Energy Environ. Sci.*, 2012, **5**, 9121-9128.

33. E. S. Toberer, A. Zevalkink, N. Crisosto and G. J. Snyder, *Adv. Funct. Mater.*, 2010, **20**, 4375-4380.

34. S. M. Kauzlarich, in *Encyclopedia of Inorganic Chemistry*, John Wiley & Sons, Ltd, 2006.

35. S. M. Kauzlarich, S. R. Brown and G. Jeffrey Snyder, *Dalton Trans.*, 2007, DOI:10.1039/b702266b, 2099-2107.

36. E. S. Toberer, A. F. May and G. J. Snyder, *Chem. Mater.*, 2010, **22**, 624-634.

37. B. C. Sales, D. G. Mandrus and B. C. Chakoumakos, in *Semicond. and Semimet.*, ed. M. T. Terry, Elsevier, 2001, pp. 1-36.

38. G. Cordier, H. Schafer and M. Stelter, *Z. Naturforsch. B*, 1984, **39**, 727-732.

39. R. Seshadri and N. A. Hill, *Chem. Mater.*, 2001, **13**, 2892-2899.

40. E. S. Božin, C. D. Malliakas, P. Souvatzis, T. Proffen, N. A. Spaldin, M. G. Kanatzidis and S. J. L. Billinge, *Science*, 2010, **330**, 1660.

41. H. Liu, J. Yang, X. Shi, S. A. Danilkin, D. Yu, C. Wang, W. Zhang and L. Chen, *J. Materiomics*, 2016, **2**, 187-195.

42. D. G. Cahill, S. K. Watson and R. O. Pohl, *Phys. Rev. B*, 1992, **46**, 6131-6140.

43. H. Euchner, S. S. Pailhès, L. T. K. Nguyen, W. Assmus, F. Ritter, A. Haghighirad, Y. Grin, S. Paschen and M. de Boissieu, *Phys. Rev. B*, 2012, **86**, 224303.

CHAPTER 5.2

Intrinsically low thermal conductivity in InTe, and enhanced thermoelectric performance through carrier-engineering*

Summary

Understanding the origin of intrinsically low thermal conductivity is fundamentally important to the development of high-performance thermoelectric materials which can convert waste-heat into electricity. Herein, we demonstrate an ultralow lattice thermal conductivity (ca. 0.4 W/mK) in mixed valent InTe [i.e., $In^{+}In^{3+}Te_2$] which exhibits an intrinsic bonding asymmetry with coexistent covalent and ionic substructures. The phonon dispersion of InTe exhibits, in addition to low-energy flat branches, weak instabilities associated with the rattling vibrations of In^{+} cations along the columnar ionic substructure. These weakly unstable phonons originate from the $5s^2$ lone pair of In^{+} cation and are strongly anharmonic, which scatter the heat carrying acoustic phonons through strong anharmonic phonon-phonon interactions as evident in anomalously high mode Grüneisen parameters. A maximum thermoelectric figure of merit (zT) of ca. 0.9 is achieved at 600 K for the 0.3 mol.% In-deficient sample making InTe a promising material for mid-temperature thermoelectric applications.

A paper based on this study has appeared in* ***Angew. Chem. Int. Ed.,* 2016, *55*, 7792.

5.2.1 Introduction

Thermoelectric materials can convert waste-heat into useful electricity, and constitute a viable means to efficient energy management. The dimensionless figure of merit, $zT = S^2\sigma T/(\kappa_{Lat} + \kappa_e)$, determines their conversion-efficiency and is derived from interdependent electrical conductivity (σ), Seebeck coefficient (S), lattice (κ_{Lat}) and electronic (κ_e) thermal conductivities, where T is the absolute temperature. The fundamental challenge in developing high-performance thermoelectric materials has been to achieve a simultaneous enhancement in power factor ($S^2\sigma$) and reduction in κ_{Lat}.[1, 2] Significant reduction in κ_{Lat} of a material has been achieved through all-scale hierarchical architectures[3, 4] and endotaxial nanostructuring.[5, 6] On the other hand, intrinsically low κ_{Lat} originating in solids with complex crystal structures,[7, 8] part-crystalline part-liquid state,[9] rattling modes,[10-13] soft phonon modes,[14] superionic substructure with liquid-like cation disordering,[15-17] resonant bonding,[18] and anisotropic layered crystal structure,[19] is of practical interest due to its robustness against grain size and other structural variations.

Lattice anharmonicity and strong phonon–phonon interactions in specific materials can engender intrinsically low κ_{Lat} while preserving the carrier mobility.[20, 21] The origin of lattice anharmonicity and the ensuing ultralow κ_{Lat} in the I-V-VI_2 chalcogenides such as $AgSbSe_2$,[22] $AgBiSe_2$,[23-25] $AgBiS_2$ [26] and AgBiSeS [27] has been traced to the electrostatic repulsion between the stereochemically active ns^2 lone pair of group V cations and the valence p-orbital of group VI anions. Intrinsically low κ_{Lat} has also been evidenced in $Cu_{12}Sb_4S_{13}$[28] and $PbCuSbS_3$[29] due to the bond anharmonicity caused by stereochemically active $5s^2$ lone pair of Sb. The deformation of weak multicenter bonds in an electron-poor CdSb has been recently shown to cause lattice anharmonicity and thereby, a low κ_{Lat}.[30] The concept of phonon glass electron crystal (PGEC) has been demonstrated earlier in some host/guest frameworks as exemplified by clathrates [31] and filled skutterudites.[13, 32] In these compounds, a guest atom rattles within oversized structural cages and scatters the heat-carrying acoustic phonons thereby significantly lowering κ_{Lat}. The exploration of new materials with intrinsically low κ_{Lat} along with a

microscopic understanding of the underlying correlations among bonding, lattice dynamics and phonon transport is fundamentally important towards designing promising thermoelectric materials.

In chapter 5.1, I have shown $TlInTe_2$ to exhibit ultralow κ_{Lat} but the thermoelectric figure of merit (zT) is very low due to its poor electrical conductivity. In the present chapter, we report an ultralow κ_{Lat} (ca. 0.4 W/mK) in Zintl-type InTe (i.e. $In^{+}In^{3+}Te_2$) which is isostructural to $TlInTe_2$. In order to improve the electrical properties of InTe, I have increased the hole-carrier concentration though optimal In-deficiencies. Thereby, the power factor ($S^2\sigma$) has been enhanced to achieve a maximum zT of ca. 0.9 at 600 K in the nominal $In_{0.997}Te$ sample, which is significantly higher than that of pristine InTe. Furthermore, using first principles studies, we also assert the presence of strongly anharmonic phonons in InTe, originating from rattling vibrations of In^{+} cations, which couple with the heat-carrying acoustic modes and lead to an ultralow κ_{Lat}.

5.2.2 Methods

5.2.2.1 Synthesis

To synthesize polycrystalline ingots of pristine InTe and $In_{1-x}Te$ (x= 0.003 or 0.005), appropriate ratios of high-purity In and Te (total weight of 6 g) were taken in carbon-coated quartz ampoules, evacuated at a high vacuum of 10^{-5} torr and then sealed under vacuum. The contents were heated up to 1073 K for 7 hr, and soaked at this temperature for 10 hr followed by cooling to room temperature over 15 hr.

5.2.2.2 Characterizations

Powder X-ray diffraction (PXRD) patterns for all the samples were recorded on Bruker D8 diffractometer using Cu Kα (λ= 1.5406 Å) radiation. To estimate the optical band gap of InTe, diffuse reflectance spectroscopy was carried out on disc-shaped pellets at room temperature using FT-IR Bruker IFS 66 V/S spectrometer (2 cm^{-1} resolution) in a frequency range of 4000—400 cm^{-1} with 100 acquisition scans. Absorption (α/s) data were calculated from the reflectance data using Kubelka—Munk function, $\alpha/s = (1-R)^2/(2R)$, where

R is the reflectance, and α and s being the absorption and the scattering coefficients respectively. The energy band gaps were determined from the x-axis intercept of α/s vs. E (eV) plot. X-ray photoelectron spectroscopy (XPS) was carried out on Omicron nanotechnology ESCA instrument (model: EAC 2000 SPHERA 547) using monochromatic Mg Kα (hν = 1253.6 eV) X-ray source. Spectra for In-3d were obtained with a pass energy of 25 eV and resolution of 0.5 eV.

5.2.2.3 Thermoelectric measurements

The as-obtained ingots (200 mm long and 8 mm wide) are hard enough to be directly cut by a rotating diamond blade and polished into required dimensions for electrical and thermal transport measurements.

Electrical transport: Electrical conductivity (σ) and Seebeck coefficient (S) were simultaneously measured between 300 and 673 K along the ingot's growth direction (longer direction) under He-atmosphere using ULVAC-RIKO ZEM-3 instrument (refer to part 1 for more details). For the electrical measurements, rectangular bar-shaped samples with typical dimensions of ca. 2×2×8 mm^3 were cut and polished from the ingots. Heating and cooling cycles of measurement gave consistent data for all the samples.

Hall-coefficients (R_H) for all the samples (bar-shaped samples used for electrical transport measurements) were measured in a 5-point geometry at room temperature using PPMS (Physical Property Measurement System, Quantum design) with a variable magnetic field up to 5 Tesla. Hall carrier concentrations (n_H) were estimated from the Hall-coefficients (R_H) using the relation, $n_H = 1/eR_H$ cm^{-3}, where e is the absolute electronic charge. The Hall carrier concentration is related to the true carrier concentration, n as $n = n_H . r_H$ where r_H is the Hall factor which is generally equal to 1 in metals or degenerate semiconductors with single parabolic band conduction. Given that the present samples are all degenerate p-type semiconductors, $n_H \approx n$.

Thermal conductivity: The thermal diffusivity, D, was measured between 300 K and 673 K using laser flash diffusivity technique in Netzsch LFA-457 instrument. The thermal diffusivity was measured along the same direction as

that for electrical transport measurement, i.e., along the ingot's growth-direction. Coins with ca. 8 mm diameter and 2 mm thickness were used for the measurement. Total thermal conductivity (κ) was calculated using the relation, $\kappa = D \times C_p \times \rho$, where ρ is the density of the sample and C_p is the specific heat capacity, derived from pyroceram reference. More details are given in part 1. The density of all the pellets, measured using Archimedes method, is close to ca. 97% of the theoretical density (6.02 g/cm^{-3}).

5.2.2.4 Computational details

To investigate the electronic structure and phonon dispersion in InTe, we have collaborated with Prof. Umesh Waghmare's group at JNCASR, Bangalore to carry out first-principles calculations based on density functional theory (DFT) with Quantum espresso (QE) implementation.[33] Integrations over the Brillouin zone are sampled on 9×9×9 uniform mesh of k-points. Lattice constants and atomic positions were optimized in simulations at 3 GPa. To determine the phonon dispersion, the force constant matrices are obtained on a 2×2×2 mesh of q-points. A primitive unit cell with eight atoms is used to determine the electronic structure and phonon dispersion along high symmetry lines in its Brillouin zone. For more details, refer to methods section of chapter 5.1.

5.2.3 Results & discussion

5.2.3.1 Structure and bonding

InTe, (i.e. $In^{+}In^{3+}Te_2$), is a mixed valent compound belonging to tetragonal I4/mcm space group with a chain-type structure similar to $TlInTe_2$ and TlSe.[34-36] The structure features coexistent ionic and covalent substructures. The In^{+} and In^{3+} cations are crystallographically inequivalent with distinct bonding environment. The trivalent In^{3+} cations form covalent (sp^3) In-Te bonds which construct $In^{3+}Te_4^{2-}$ tetrahedra.[34, 35] These tetrahedra share the horizontal edges to form covalently bonded anionic substructure with a chain-like topology along the crystallographic *z*-axis (Figure 5.2.1(a)). The In^{3+}-Te bond distance of 2.81 Å is close to the sum of covalent radii of In (1.44 Å) and Te (1.35 Å) [34, 35]. On the other hand, each monovalent In^{+} cation is surrounded by eight Te atoms in a distorted square antiprismatic arrangement to form skewed

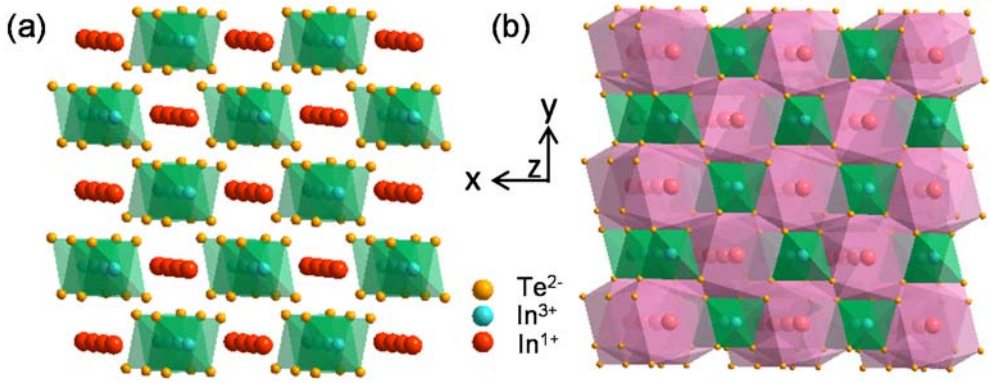

Figure 5.2.1 *Crystal structure of InTe showing a) chains of covalently bound, edge-sharing $In^{3+}Te_4^{2-}$ tetrahedra (blue) alternating with b) chains of face-sharing distorted Thompson cubes (pink) along the z-axis.*

Thompson cubes. [34, 35] These cubes share common square faces and form one-dimensional columnar ionic substructure along the *z*-axis (Figure. 5.2.1(b)). The In^+-Te distance of 3.57 Å is close to the sum of ionic radii of In^+ (1.32 Å) and Te^{2-} (2.21 Å).[37] These chains of In^+ cations hold together the chains of $In^{3+}Te_4^{2-}$ tetrahedra via weak electrostatic interactions (Figure 5.2.1(b)). Along the chain-direction (down the [001] axis), In^+ - In^+ and In^{3+} - In^{3+} distances are 3.57 Å while the distance between In^+ and In^{3+} cations in the a-b plane is 4.23 Å. [34, 35]

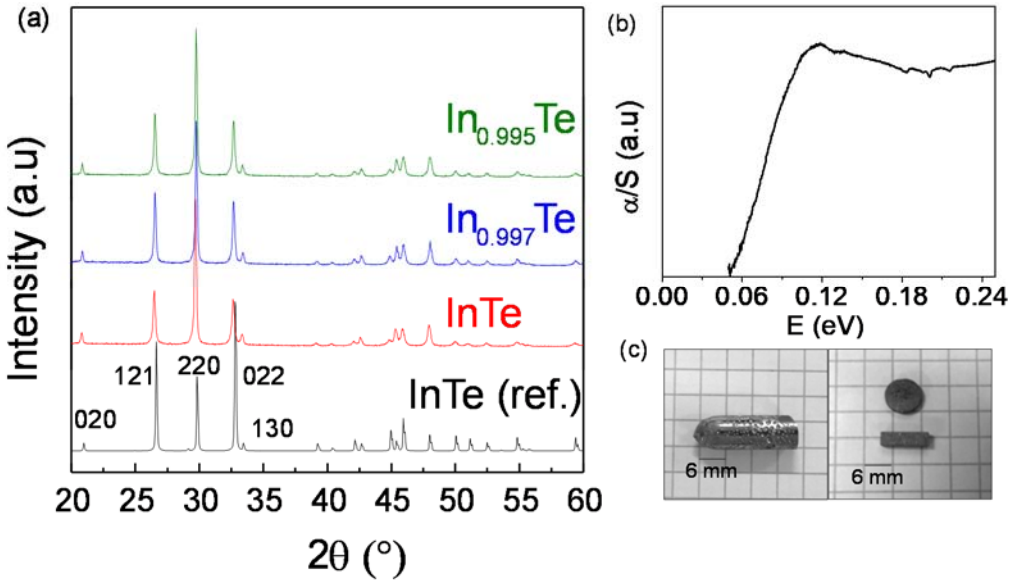

Figure 5.2.2 *a) Powder XRD patterns of nominal InTe, $In_{0.997}Te$ and $In_{0.995}Te$ samples, b) optical absorption spectrum of InTe and c) photograph of a typical as-grown polycrystalline ingot (left) which is cut and polished into a bar- and coin-shaped samples (right) for thermoelectric measurements.*

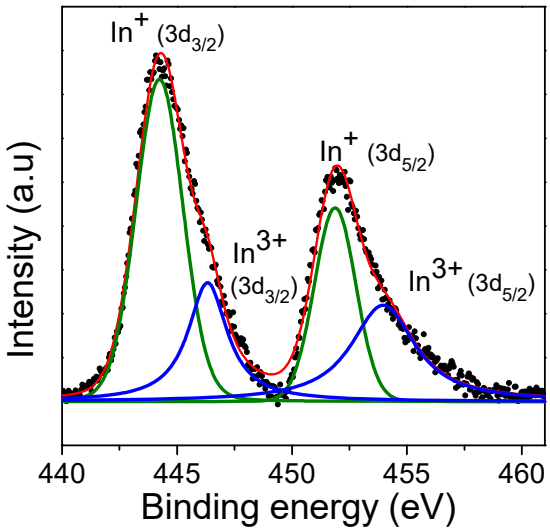

Figure 5.2.3 *In-3d X-ray photoelectron spectrum*

The PXRD patterns of all the samples (Figure 5.2.2(a)) can be indexed on the pure tetragonal I4/mcm structure. From diffuse reflectance spectroscopy, an optical energy gap of about ca. 0.06 eV was estimated for the nominally pristine InTe, (Figure 5.2.2(b)) whereas no energy gaps were apparent for the In-deficient samples, plausibly due to their highly degenerate semiconducting behavior. The XPS In-3d spectra of InTe samples reveal asymmetrically broadened doublet ($3d_{3/2}$ and $3d_{5/2}$), which can be deconvoluted into two pairs of Gaussian peaks separated by ca. 2 eV corresponding to the In^{+} and In^{3+} cations in InTe (Figure 5.2.3).

5.2.3.2 Electrical transport properties

Figure 5.2.4(a) shows the temperature-dependent (300-673 K) electrical conductivity (σ) of InTe and $In_{1-x}Te$ (x= 0.003, 0.005) samples, measured along the ingot's growth-direction (see figure 5.2.2(c)). σ decreases with temperature for all the samples, which is characteristic of heavily doped (degenerate) semiconductors. Typically, for the pristine InTe, σ decreases from about 50 Scm^{-1} at 300 K to 18 Scm^{-1} at 600 K. σ near 300 K increases significantly to about 485 Scm^{-1} for the nominal $In_{0.997}Te$ sample. For $In_{0.995}Te$, σ lowers to about 164 Scm^{-1} at 300 K due to reduction in the Hall carrier mobility (μ_H).

The room temperature Hall coefficients (R_H) are positive for all the samples due to dominant *p*-type conduction. The hole-concentrations (n_H) at 300 K were determined by using the equation, $n_H = 1/eR_H$. n_H increases from

ca. 5.8x10^{18} cm^{-3} in pristine InTe to ca. 2.8×10^{19} cm^{-3} and 3.4×10^{20} cm^{-3} in $In_{0.997}Te$ and $In_{0.995}Te$ samples respectively. Room temperature Hall carrier mobilities (μ_H), were determined using $\mu_H = \sigma/n_H e$. μ_H increases from ca. 58 cm^{2}V^{-1}s^{-1} in pristine InTe to ca. 108 cm^{2}V^{-1}s^{-1} in $In_{0.997}Te$ sample and then drastically reduces to ca. 3 cm^{2}V^{-1}s^{-1} in $In_{0.995}Te$ sample.

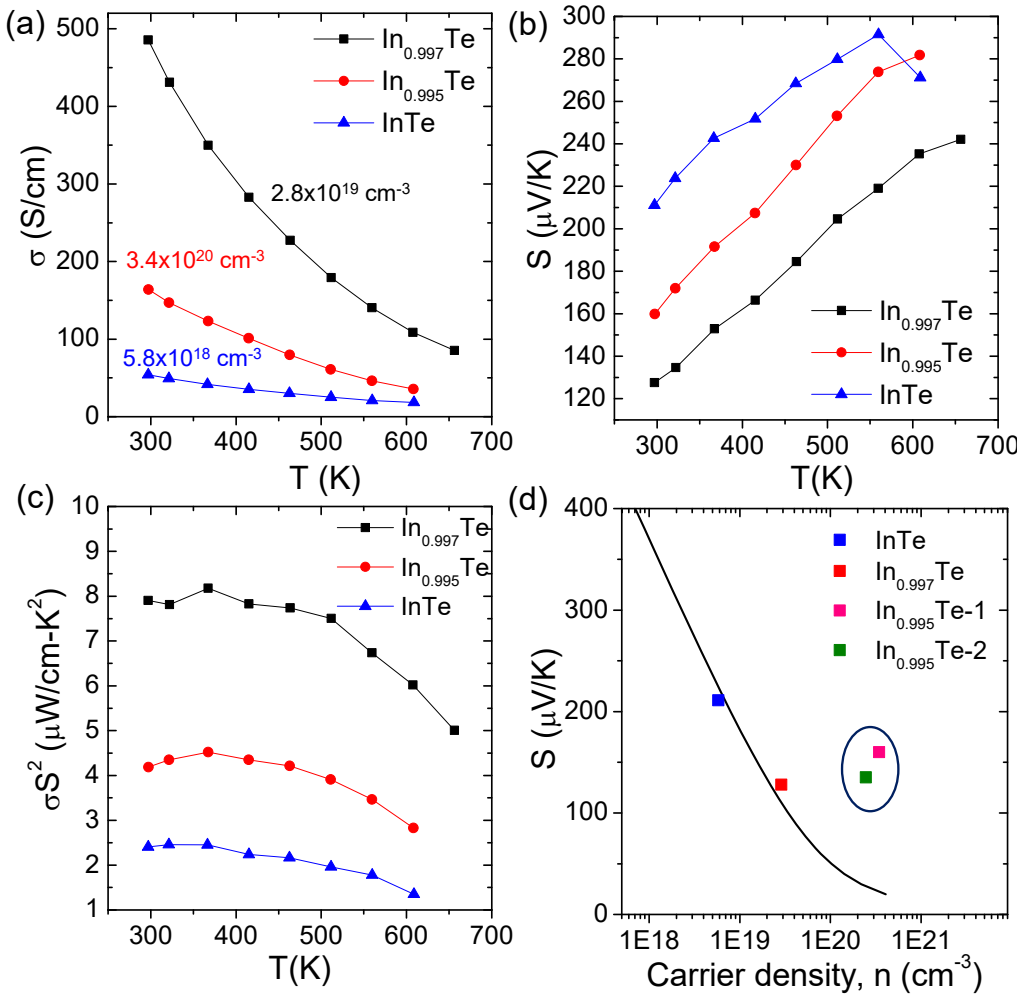

Figure 5.2.4 *Temperature-dependent a) electrical conductivity (σ), b) Seebeck coefficient (S) and c) power factor (σS^2) of $In_{1-x}Te$ (x=0, 0.003 and 0.005) samples. d) Theoretical Pisarenko curve (solid line) generated using single parabolic band model with a density-of-states effective mass (m*) of 0.6 m_e. The black points are experimental S vs. n_H data. The circled data points correspond to two different batches of nominal $In_{0.995}Te$.*

Figure 5.2.4(b) shows the temperature-dependent Seebeck coefficient (S) of $In_{1-x}Te$ samples. S is positive for all the samples due to p-type conduction. For the pristine InTe, S varies from about 211 μV/K at 300 K to 271 μV/K at 608 K peaking at a value of about 291 μV/K at 560 K which is

suggestive of bipolar conduction in InTe. For the In-deficient samples, bipolar conduction is suppressed due to increased hole-carrier concentrations. The values of S near 300 K for nominal $In_{0.997}Te$ and $In_{0.995}Te$ samples are about 127 µV/K and 159 µV/K respectively.

The electron transport of pristine InTe and $In_{0.997}Te$ samples can be described using single parabolic band (SPB) model assuming the acoustic phonon scattering to be dominant. Seebeck coefficient (S), carrier concentration (n_H) and Lorentz number (L) can be calculated using the following SPB equations: [3, 8, 38]

$$S = \frac{k_B}{e}\left(\frac{2F_1(\eta)}{F_0(\eta)} - \eta\right) \tag{5.2.1}$$

$$n = 4\pi \left(\frac{2m^* k_b T}{h^2}\right)^{3/2} F_{1/2}(\eta) \tag{5.2.2}$$

$$L = \left(\frac{k_b}{e}\right)^2 \frac{3F_0(\eta)F_2(\eta) - 4F_1(\eta)^2}{F_0(\eta)^2} \tag{5.2.3}$$

$$F_j(\eta) = \int_0^\infty \frac{x^j}{1 + e^{x-\eta}}\, \mathrm{d}x \tag{5.2.4}$$

where m^* is the density of states effective mass; η, the reduced Fermi energy (E_F/k_BT); $F_j(\eta)$, the j$^{\text{th}}$ order Fermi integral; k_B, the Boltzmann constant; e, the absolute electron charge; h, the Planck constant, and x, the reduced carrier energy. Figure 5.2.4(d) shows the theoretical Pisarenko curve (S vs. n) calculated using equations 5.2.1 and 5.2.2 with m^* value of 0.6 m_e. The experimental S vs. n_H data points of nominal pristine InTe and $In_{0.997}Te$ fall close to the Pisarenko curve corresponding to a m^* value of 0.6 m_e. However the experimental S vs. n_H data points of nominal $In_{0.995}Te$ samples, deviate far above the theoretical Pisarenko curve suggesting an increased m^* in the latter, which results in reduced mobility and enhanced S.[39, 40] Figure 5.2.5(a) shows the calculated electronic structure of InTe which reveals two important features: (a) two nearly degenerate valence band valleys at M- and Z-points, and (b) valence band at each of these points exhibits an inverted double well or "M"-shaped sub-valley structure. We speculate that high density p-type carriers resulting from heavy doping in $In_{0.995}Te$ ($n_H \sim 3.4\times10^{20}$ cm^{-3}) populate

the multiple valence bands, giving rise to a higher m^* and therefore an enhanced S in this sample.[22, 39]

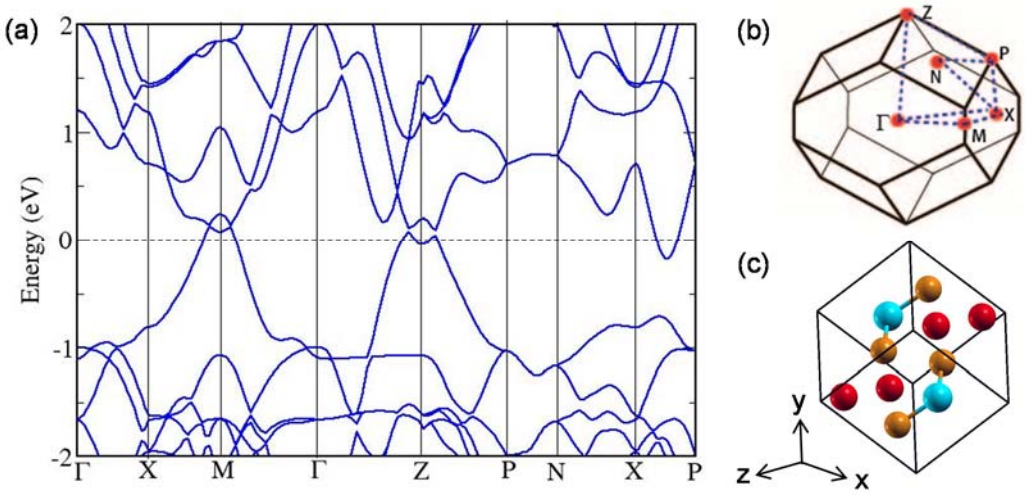

Figure 5.2.5 *(a) Electronic structure of InTe at the high symmetry points in the Brillouin zone (shown in (b)) calculated at the experimental lattice constant for the primitive unit cell shown in (c). The blue, red and yellow spheres denote In^{3+}, In^{+}, and Te^{2-} atoms respectively.*

Figure 5.2.4(c) shows the temperature dependent power factor ($S^2\sigma$) for all the samples. A maximum power factor of ca. 8 μWcm^{-1}K^{-2} is obtained at 373 K for the $In_{0.997}Te$ sample, which maintains in excess of 5 μWcm^{-1}K^{-2} up to 650 K. The higher power factor in this sample is attributed to higher carrier mobility and an optimized hole-concentration.

5.2.3.3 Thermal conductivity

Figures 5.2.6(a) and (b) show respectively, the thermal diffusivity (D) and specific heat capacity (C_p) of InTe and $In_{1-x}Te$ (x=0.03 and 0.05) samples measured between 300 and 673 K. Figure 5.2.6(c) shows the temperature-dependent (300-673 K) total thermal conductivity (κ) of all the samples, measured along the ingot's growth-direction. At 300 K, the pristine InTe exhibits a low κ value of ca. 0.76 Wm^{-1}K^{-1} which decays to ca. 0.5 Wm^{-1}K^{-1} at 673 K. For $In_{0.997}Te$ sample, κ varies from ca. 0.68 Wm^{-1}K^{-1} at 300 K to ca. 0.36 Wm^{-1}K^{-1} at 673 K. For $In_{0.995}Te$ sample, κ varies from ca. 0.76 Wm^{-1}K^{-1} at 300 K to ca. 0.45 Wm^{-1}K^{-1} at 673 K. To calculate the lattice thermal conductivity ($\kappa_{Lat} = \kappa - \kappa_e$), the electronic thermal conductivity, κ_e, was extracted using Wiedemann-Franz law, $\kappa_e = L\sigma T$ where L is the temperature-

dependent Lorentz Number. For the pristine and $In_{0.997}Te$ samples, L was calculated using SPB model (see equation 5.2.3), whereas a degenerate value of L= 2.45×10^{-8} $W\Omega K^{-2}$ was used for the $In_{0.995}Te$ sample given its high carrier density.

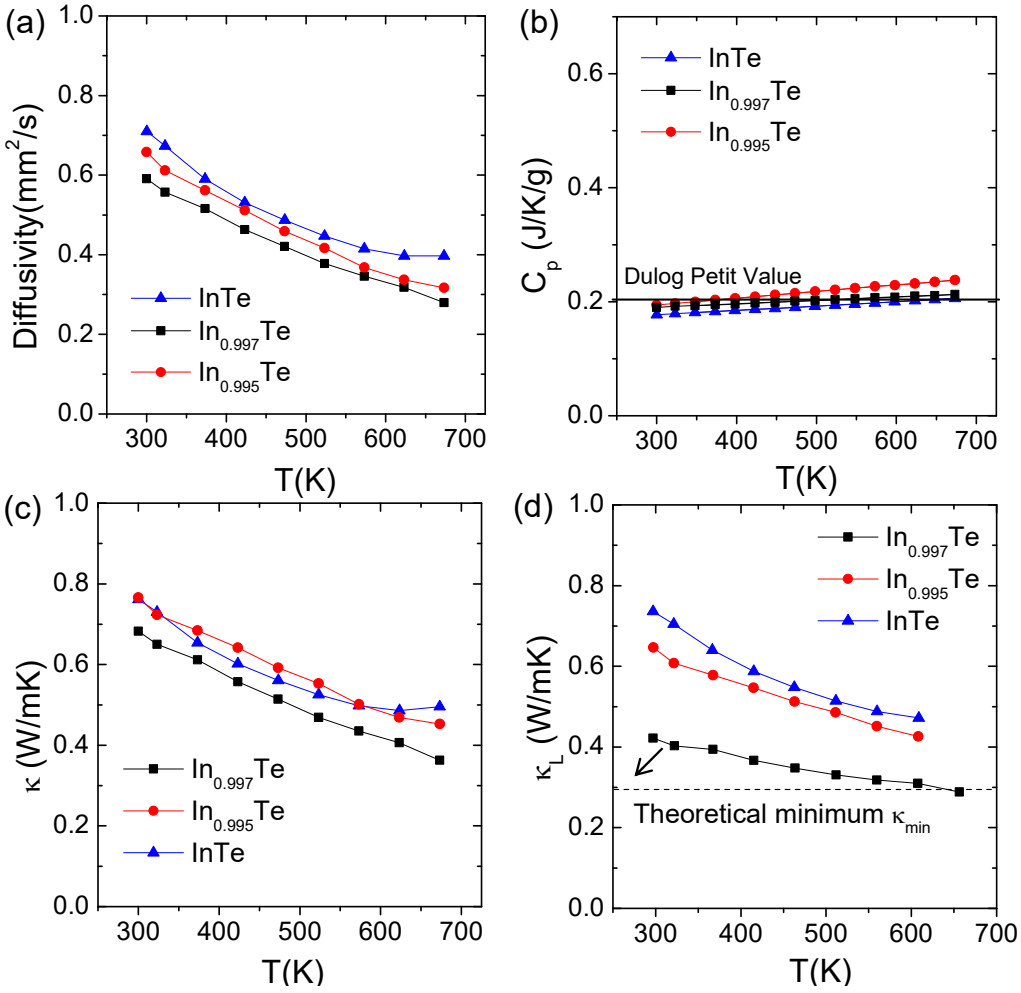

Figure 5.2.6 *Temperature-dependent a) thermal diffusivity (D), b) specific heat capacity (C_p), c) total thermal conductivity (κ) and d) lattice thermal conductivity (κ_{Lat}) of $In_{1-x}Te$ (x=0, 0.003 and 0.005) samples.*

Figure 5.2.6(d) shows the κ_{Lat} of $In_{1-x}Te$ samples as a function of temperature. For all the samples, κ_{Lat} follows T^{-1} dependence indicating the Umklapp phonon-phonon scattering to be dominant. For the pristine InTe, due to low electrical conductivity, κ_e is minimal and the total κ is dominated by κ_{Lat} which varies from ca. 0.73 $Wm^{-1}K^{-1}$ at 300 K to ca. 0.47 $Wm^{-1}K^{-1}$ at 600 K. For the $In_{0.997}Te$ sample, κ_{Lat} at 300 K decreases to ca. 0.43 $Wm^{-1}K^{-1}$ which further decays to as low as ca. 0.3 $Wm^{-1}K^{-1}$ at 673 K. The reduction in κ_{Lat} with respect to the pristine InTe is expected to arise from phonon-scattering

at the vacancies which act as point-defects. In principle, increased point defects in $In_{0.995}Te$ sample are expected to further lower κ_{Lat} value. However, κ_{Lat} of $In_{0.995}Te$ is higher than that of $In_{0.997}Te$. Heavily doped semiconductor ($n \sim 10^{20}$ cm^{-3}) with multiple valence band valleys coexistent at the Fermi level is known to show an interband carrier-transfer which causes an excess κ_e due to associated changes in energy.[41] The excess thermal conductivity during interband scattering cannot be accounted by the simple degenerate L value of 2.45×10^{-8} WΩK^{-2}, leading to an underestimation of the total κ_e as in the case of $In_{0.995}Te$. Thus, an increase of κ_{Lat} in $In_{0.995}Te$ ($n_H \sim 3.4\times10^{20}$ cm^{-3}) compared to that in $In_{0.997}Te$ ($n_H \sim 2.8\times10^{19}$ cm^{-3}) is probably due to an underestimation of κ_e in $In_{0.995}Te$ caused by phonon-mediated interband carrier-transfer. First-principles calculation of electron-phonon interaction indeed reveals that two low-frequency phonon modes (around 21 and 71 cm^{-1}) at wave vector $q = q_M - q_Z$ strongly couple to the carriers, which indeed facilitate the interband scattering between M and Z valence band valleys at increased concentrations of p-type carriers. Such an interband scattering has been observed earlier in heavily doped p-type PbTe where the κ_{Lat} value was relatively larger than that of undoped PbTe due to an underestimation of κ_e caused by using the simple degenerate L.[42] The rapid decrease in carrier mobility for the $In_{0.995}Te$ sample does suggest an interband scattering of carriers that causes the anomaly in its calculated κ_{Lat}.

By using the calculated average sound velocities of three acoustic modes (see table 5.2.1) and an atom number density of ca. 3.11×10^{22} cm^{-3} for InTe, minimum thermal conductivity (κ_{min}) of InTe is estimated to be about 0.3 Wm^{-1}K^{-1} using Cahill's model[43] (refer to part 1 for details), and is shown as a dashed line in figure 5.2.6(d). The experimental κ_{Lat} for the $In_{0.997}Te$ sample is remarkably low and decays to the amorphous limit of 0.3 Wm^{-1}K^{-1} at ca. 673 K. The low overall κ and κ_{Lat} values are highly desirable for thermoelectrics and are comparable to those of I-V-VI_2 chalcogenides such as $AgSbSe_2$ and $AgBiS_2$ where the ns^2 lone pair of group V cations causes a strong lattice anharmonicity and thereby a low κ_{Lat}.[20-22]

5.2.3.4 Phonon dispersion

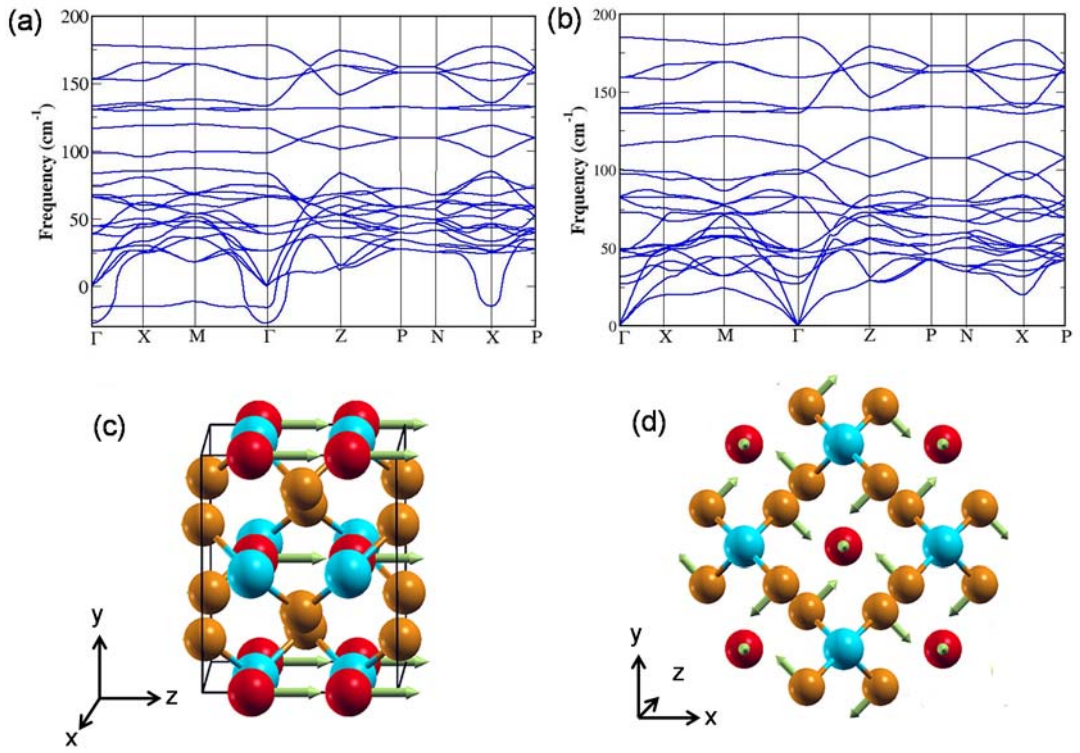

Figure 5.2.7 *(a) Phonon dispersion of InTe revealing two negative phonon branches with frequencies at -16 cm^{-1} and -28 cm^{-1} near the Γ point; the associated atomic vibrations are shown respectively in (c) and (d) in the conventional tetragonal unit cell. Blue, red and yellow spheres denote In^{3+}, In^{+} and Te^{2-} atoms respectively; b) Phonon dispersion of InTe at 3 GPa showing no negative frequency modes.*

To uncover the precise origin of low κ_{Lat}, phonon dispersion of InTe was determined using first-principles density functional calculations. Phonon dispersion of InTe calculated at its experimental lattice constant reveals a flat branch containing modes of imaginary frequencies (around -16 cm^{-1} at Γ point) along Γ-X-M-Γ directions of the Brillouin zone (Figure 5.2.7(a)), which involve the displacement of only In^{+} cations along z-direction (Figure 5.2.7(c)). Another branch containing imaginary frequency (-28 cm^{-1}) occurs at the Γ point, which involves anti-parallel displacements of In^{+} cations along the (±) z-direction and rotation of $In^{3+}Te_4^{2-}$ tetrahedra around z-axis through displacements of Te^{2-} anions in the xy-plane (Figure 5.2.7(d)). These unstable modes necessarily involve collective rattling vibrations of In^{+} atoms (parallel to z-axis) within the columnar ionic substructure. The region of these instabilities in the Brillouin zone implies that (a) rattling motion involves

displacement of about six In^+ cations along the chain-direction, and (b) the In^+ displacements in adjacent chains are random. Single crystal refinement of InTe shows the atomic displacement parameters (ADPs) of In^+ to be significantly larger than those of In^{3+} and Te^{2-} and to be highly anisotropic with the maximum of vibration ellipsoid occurring in the z-direction towards the adjacent In^+ atoms ($U_{11} = U_{22} = 0.045$ Å^2 and U_{33}=0.081 Å^2).[34] The large anisotropic ADPs indeed suggest In^+ atoms to behave as rattlers in InTe similar to Tl^+ cations in $TlInTe_2$ (see chapter 5.1).

Table 5.2.1 *Phonon sound velocities in the vicinity of Brillouin zone center (v_{TA1}, v_{TA2}, v_{LA}), mode Debye temperatures ($\Theta_{TA1}, \Theta_{TA2}, \Theta_{LA}$) and mode Grüneisen parameters for transverse acoustic phonon branches (TA1, TA2) and longitudinal acoustic phonon (LA) branches along the Γ-X, Γ -Z and Γ-M directions. The mode Debye temperatures are calculated using $\Theta_i = \hbar\omega_{max}/k_B$ where ω_{max} is the largest acoustic frequency of i^{th} mode (TA1 or TA2 or LA) along a given direction. Mode-Gruneisen parameter, γ of each acoustic branch is evaluated from the root-mean-square value of γ_i : $\gamma = \sqrt{(<\gamma_i{}^2>)}$ where $\gamma_i = -V/\omega_i \frac{d\omega_i}{dV}$*

Direction	v_{TA1} (m/s)	v_{TA2} (m/s)	v_{LA} (m/s)	γ_{TA1}	γ_{TA2}	γ_{LA}	Θ_{TA1} (K)	Θ_{TA2} (K)	Θ_{LA} (K)
Γ-X	1671	1255	2187	5.2	1.64	1.74	34	37	50
Γ-Z	2111	911	3072	4.8	6	6	15	15	82
Γ-M	1533	1282	2167	0.41	1.7	2.1	34	28	50
Average	1771	1149	2475	3.47	3.11	3.28	28	27	60

5.2.3.5 Charge density and electron localization

The total charge density of InTe at the experimental lattice constant (Figure 5.2.8(a)) reveals strongly covalent In-Te bonds within the $InTe_4{}^{2-}$ tetrahedron, as evident from its directionality between the In^{3+} cation and the surrounding four Te^{2-} anions. The centrally inactive In^+ cation is surrounded by a uniform spherical charge density arising from the $5s^2$ lone pair at the body center of the conventional tetragonal cell. To confirm the presence of a lone pair on In^+ cation, we examine the electron localization function (ELF) of InTe (Figure 5.2.8(b)). ELF measures the degree of electron localization in a molecule or a solid with information of local influence of the Pauli repulsion. The ELF

analysis shows a spherical electron localization around In^{+} atoms, which is due to the $5s^2$ lone pair of In^{+}, and a lobe-shaped asymmetrically localized electron cloud around Te^{2-}, which constitutes the $5s^2$ lone pair of Te^{2-}, hybridized partially as permitted by its site symmetry. The spherical shape of a lone pair of an ion is known to cause its off-centering instability in a system.[44] Thus, the weak instabilities in the phonon spectrum originate from the $5s^2$ lone pair around In^{+} ions. On the other hand, the lobe-shaped lone pair on Te^{2-} ions causes their movement in the xy-plane giving the rotational instability. By shifting the atoms away from equilibrium positions (along x- and z-directions), we find that the energy well of an off-centered In^{+} atom is very flat unlike In^{3+} and Te^{2-} atoms which sit in deep potential wells (Figure 5.2.8(c)). Thus the loosely bound In^{+} cations behave as rattlers possessing large ADPs.

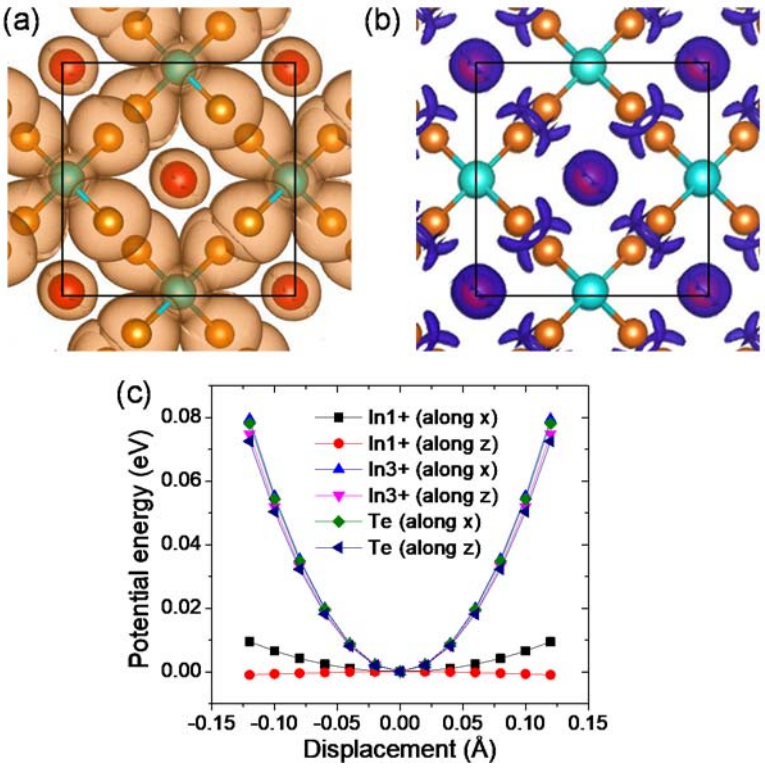

Figure 5.2.8 *(a) Iso-surfaces of total charge density showing covalent bonding within the $In^{3+}Te_4^{2-}$ tetrahedron, and isolated In^{+} cations at the body-center of the conventional tetragonal unit cell; (b) ELF map (plotted at an iso-value of 0.88) reveals a nearly spherical charge density around In^{+} cation corresponding to its $5s^2$ electron lone pair. Blue, red and yellow spheres denote In^{3+}, In^{+} and Te^{2-} atoms respectively; c) calculated potential energy curves for all the atom types (In^{+}, In^{3+} and Te^{2-}) as a function of displacement about the equilibrium positions, along x- and z- directions.*

5.2.3.6 Anharmonic phonon interactions

The lattice thermal conductivity (κ_{Lat}) of a material is given by $\kappa_{Lat} = 1/3C_v v^2 \tau$, where C_v, v and τ are specific heat capacity, sound velocity and relaxation time respectively (refer to part 1 for details). Our calculations show that the frequencies of acoustic modes are less than 50 cm^{-1} suggesting soft bonding in InTe. The zone centre group velocities of acoustic branches, calculated along Γ-X, Γ-Z and Γ-M directions (Table 5.2.1) are very low, and hence their contribution to κ_{Lat} is weak. The ionic substructure with weakly bound In^+ atoms results in anomalously large mode Grüneisen parameters (γ_i) (Table 5.2.1). Given the Umklapp (U) and normal (N) phonon scattering rates are proportional to γ^2 ,[9] large values of γ_i reflect strong anharmonic phonon-phonon interactions in InTe.[21] Moreover the optical phonon instabilities ($\omega^2 < 0$) disappear in the phonon dispersion determined at a pressure of 3 GPa (Figure 5.2.7(b)), showing that the rattling optical modes are strongly anharmonic, and can scatter the heat-carrying acoustic phonons through phonon-phonon interactions to effectively reduce τ and κ_{Lat} of InTe.

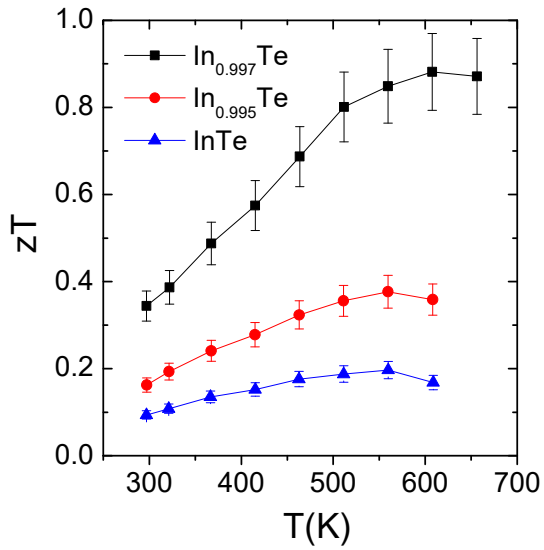

Figure 5.2.9 *(a) Temperature-dependent thermoelectric figure of merit (zT) of $In_{1-x}Te$ (x=0, 0.003, 0.005) samples, with 10% error bars.*

5.2.3.7 Thermoelectric figure of merit, *zT*

Figure 5.2.9 shows the temperature dependence of zT for all the samples. In-deficiencies effectively increase power factor and give rise to a maximum zT of ca. 0.9 at 600 K in the nominal $In_{0.997}Te$ sample, which is particularly attractive

given its relatively non-toxic constituent elements, and may be practically useful for mid-temperature thermoelectric applications. Thermoelectric properties and zT of the $In_{0.997}Te$ sample are well reproducible over heating-cooling cycles as shown in figure 5.2.10.

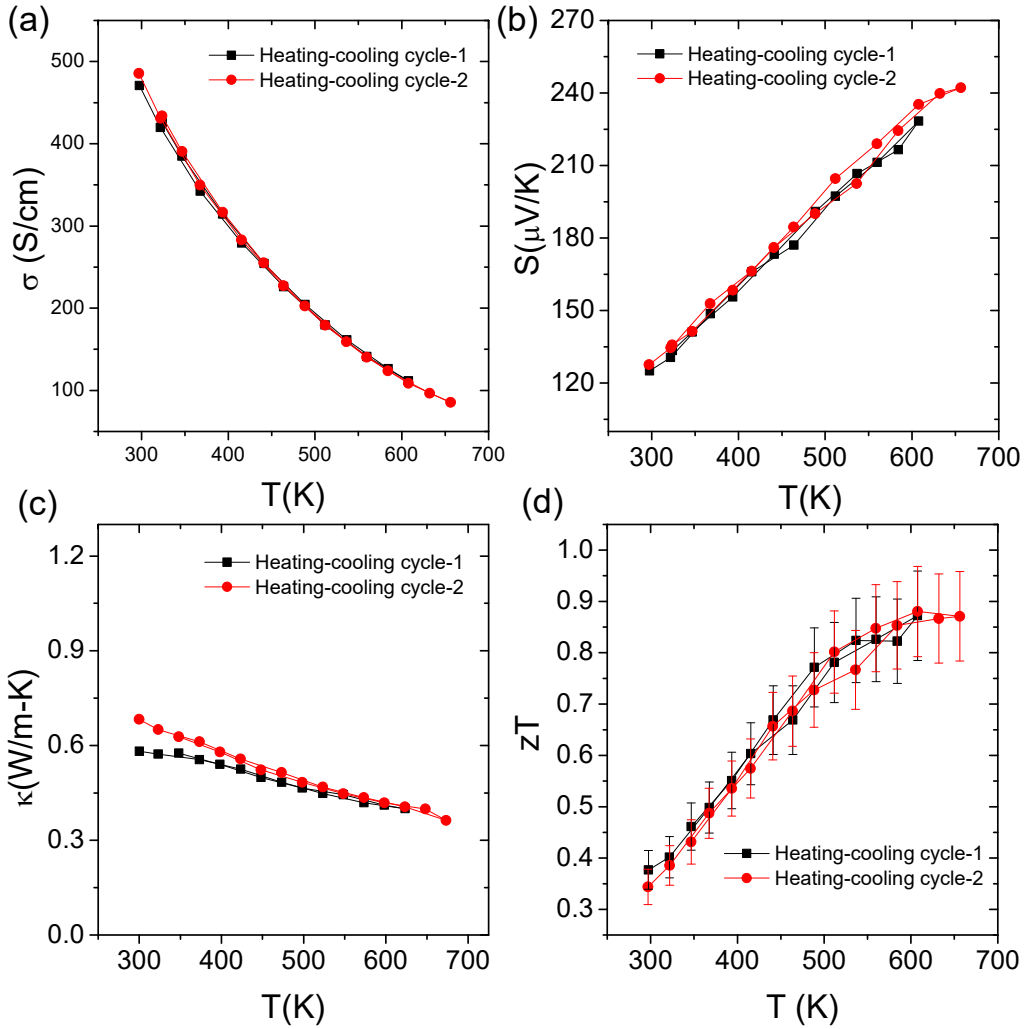

Figure 5.2.10 *Heating-cooling cycles of the $In_{0.997}Te$ sample showing the reproducibility of temperature-dependent thermoelectric properties during cycling.*

5.2.4 Conclusions

InTe exhibits an ultralow lattice thermal conductivity approaching the theoretical minimum limit at elevated temperatures, which is attributed to the bonding asymmetry and lattice anharmonicity; In^{3+} cations covalently bond to Te atoms to form a rigid anionic substructure whereas weakly bound In^{+} cations rattle along the ionic substructure due to lone pair induced off-centering. The collective rattling vibrations of In^{+} cations manifest as weakly

localized branches with imaginary frequencies in the phonon dispersion; they are strongly anharmonic and scatter the heat-carrying acoustic phonons to effectively lower κ_{Lat}. The ionic substructure with rattling In^+ cations leads to an intrinsically low κ_{Lat} while the covalently bonded rigid substructure maintains the electrical conductivity, reflecting the 'phonon-glass electron-crystal' nature of InTe. A maximum zT of ca. 0.9 is achieved at 600 K in the nominal $In_{0.997}Te$ sample, making InTe a promising material for mid-temperature thermoelectric applications.

5.2.5 Future outlook

In chapters 5.1 and 5.2, I have shown the influence of intrinsic rattling dynamics of Tl^+/In^+ cations on the κ_{Lat} of Zintl type $AInTe_2$ ($A=Tl^+/In^+$) compounds. We believe that the spherical lone-pair of these cations tends to express stereochemically driving large displacements of these cations, and induces anharmonic terms in the lattice potential thereby resulting in high γ_i and thereby, low κ_{Lat}. No structural distortion is, however, apparent in the 2-673 K range both from heat capacity and thermal conductivity measurements. Local distortions can, however, exist especially given the large ADPs associated with these cations. In future, we wish to investigate any possible lone-pair induced local off-centering of Tl^+/In^+ cations through analysis of local structure using atomic Pair Distribution Function (PDF) or Extended X-ray Absorption Spectroscopy (EXAFS). This will also help us establish that compounds where the spherical ns^2 lone pairs lead to local dynamic disorder rather than a complete structural distortion, should exhibit strong lattice anharmonicity and hence low κ_{Lat}.

5.2.6 References

1. J. R. Sootsman, D. Y. Chung and M. G. Kanatzidis, *Angew. Chem. Int. Ed.*, 2009, **48**, 8616-8639.
2. L.-D. Zhao, V. P. Dravid and M. G. Kanatzidis, *Energy Environ. Sci.*, 2014, **7**, 251-268.
3. K. Biswas, J. He, I. D. Blum, C.-I. Wu, T. P. Hogan, D. N. Seidman, V. P. Dravid and M. G. Kanatzidis, *Nature*, 2012, **489**, 414-418.
4. B. Poudel, Q. Hao, Y. Ma, Y. Lan, A. Minnich, B. Yu, X. Yan, D. Wang, A. Muto, D. Vashaee, X. Chen, J. Liu, M. S. Dresselhaus, G. Chen and Z. Ren, *Science*, 2008, **320**, 634-638.
5. K. Biswas, J. He, Q. Zhang, G. Wang, C. Uher, V. P. Dravid and M. G. Kanatzidis, *Nat Chem*, 2011, **3**, 160-166.
6. L.-D. Zhao, S. Hao, S.-H. Lo, C.-I. Wu, X. Zhou, Y. Lee, H. Li, K. Biswas, T. P. Hogan, C. Uher, C. Wolverton, V. P. Dravid and M. G. Kanatzidis, *J. Am. Chem. Soc.*, 2013, **135**, 7364-7370.
7. G. J. Snyder and E. S. Toberer, *Nat Mater*, 2008, **7**, 105-114.
8. A. Zevalkink, E. S. Toberer, W. G. Zeier, E. Flage-Larsen and G. J. Snyder, *Energy Environ. Sci.*, 2011, **4**, 510-518.
9. W. Qiu, L. Xi, P. Wei, X. Ke, J. Yang and W. Zhang, *Proc. Natl. Acad. Sci.*, 2014, **111**, 15031-15035.
10. H. Euchner, S. S. Pailhès, L. T. K. Nguyen, W. Assmus, F. Ritter, A. Haghighirad, Y. Grin, S. Paschen and M. de Boissieu, *Phys. Rev. B*, 2012, **86**, 224303.
11. W. Schweika, R. P. Hermann, M. Prager, J. Perßon and V. Keppens, *Phys. Rev. Lett.*, 2007, **99**, 125501.
12. D. J. Voneshen, K. Refson, E. Borissenko, M. Krisch, A. Bosak, A. Piovano, E. Cemal, M. Enderle, M. J. Gutmann, M. Hoesch, M. Roger, L. Gannon, A. T. Boothroyd, S. Uthayakumar, D. G. Porter and J. P. Goff, *Nat Mater*, 2013, **12**, 1028-1032.
13. X. Shi, J. Yang, J. R. Salvador, M. Chi, J. Y. Cho, H. Wang, S. Bai, J. Yang, W. Zhang and L. Chen, *J. Am. Chem. Soc.*, 2011, **133**, 7837-7846.

14. L. Bjerg, B. B. Iversen and G. K. H. Madsen, *Phys. Rev. B*, 2014, **89**, 024304.
15. S. N. Guin, J. Pan, A. Bhowmik, D. Sanyal, U. V. Waghmare and K. Biswas, *J. Am. Chem. Soc.*, 2014, **136**, 12712-12720.
16. Y. He, T. Day, T. Zhang, H. Liu, X. Shi, L. Chen and G. J. Snyder, *Adv. Mater.*, 2014, **26**, 3974-3978.
17. H. Liu, X. Shi, F. Xu, L. Zhang, W. Zhang, L. Chen, Q. Li, C. Uher, T. Day and G. J. Snyder, *Nat Mater*, 2012, **11**, 422-425.
18. S. Lee, K. Esfarjani, T. Luo, J. Zhou, Z. Tian and G. Chen, *Nat. Commun.*, 2014, **5**, 3525.
19. L.-D. Zhao, S.-H. Lo, Y. Zhang, H. Sun, G. Tan, C. Uher, C. Wolverton, V. P. Dravid and M. G. Kanatzidis, *Nature*, 2014, **508**, 373-377.
20. D. T. Morelli, V. Jovovic and J. P. Heremans, *Phys. Rev. Lett.*, 2008, **101**, 035901.
21. M. D. Nielsen, V. Ozolins and J. P. Heremans, *Energy Environ. Sci.*, 2013, **6**, 570-578.
22. S. N. Guin, A. Chatterjee, D. S. Negi, R. Datta and K. Biswas, *Energy Environ. Sci.*, 2013, **6**, 2603-2608.
23. S. N. Guin, V. Srihari and K. Biswas, *J. Mater. Chem. A*, 2015, **3**, 648-655.
24. L. Pan, D. Bérardan and N. Dragoe, *J. Am. Chem. Soc.*, 2013, **135**, 4914-4917.
25. C. Xiao, X. Qin, J. Zhang, R. An, J. Xu, K. Li, B. Cao, J. Yang, B. Ye and Y. Xie, *J. Am. Chem. Soc.*, 2012, **134**, 18460-18466.
26. S. N. Guin and K. Biswas, *Chem. Mater.*, 2013, **25**, 3225-3231.
27. Y.-L. Pei, H. Wu, J. Sui, J. Li, D. Berardan, C. Barreteau, L. Pan, N. Dragoe, W.-S. Liu, J. He and L.-D. Zhao, *Energy Environ. Sci.*, 2013, **6**, 1750-1755.
28. W. Lai, Y. Wang, D. T. Morelli and X. Lu, *Adv. Funct. Mater.*, 2015, **25**, 3648-3657.
29. Y. Dong, A. R. Khabibullin, K. Wei, J. R. Salvador, G. S. Nolas and L. M. Woods, *ChemPhysChem*, 2015, **16**, 3264.

30. S. Wang, J. Yang, L. Wu, P. Wei, J. Yang, W. Zhang and Y. Grin, *Chem. Mater.*, 2015, **27**, 1071-1081.

31. M. Beekman and G. S. Nolas, *J. Mater. Chem.* , 2008, **18**, 842-851.

32. G. S. Nolas, D. T. Morelli and T. M. Tritt, *Annu. Rev. Mater. Sci.*, 1999, **29**, 89-116.

33. P. Giannozzi, S. Baroni, Nicola Bonini, Matteo Calandra, Roberto Car, C. Cavazzoni, Davide Ceresol, Guido L Chiarotti, Matteo Cococcioni, Ismaila Dabo, Andrea Dal Corso, Stefano de Gironcoli, Stefano Fabris, Guido Fratesi, Ralph Gebauer, Uwe Gerstmann, Christos Gougoussis, Anton Kokalj, Michele Lazzeri, Layla Martin-Samos, Nicola Marzari, Francesco Mauri, Riccardo Mazzarello, Stefano Paolini, Alfredo Pasquarello, Lorenzo Paulatto, Carlo Sbraccia, Sandro Scandolo, Gabriele Sclauzero, Ari P Seitsonen, Alexander Smogunov, P. Umari and R. M. Wentzcovitch, *J. Phys.: Condens. Matter*, 2009, **21**, 395502.

34. J. H. C. Hogg and H. H. Sutherland, *Acta Cryst.*, 1976, **32**, 2689-2690.

35. A. M. Panich, *J. Phys.: Condens. Matter*, 2008, **20**, 293202.

36. Ş. Ellialtıoğlu, E. Mete, R. Shaltaf, K. Allakhverdiev, F. Gashimzade, M. Nizametdinova and G. Orudzhev, *Phys. Rev. B*, 2004, **70**, 195118.

37. R. E. Jones and D. H. Templeton, *Acta Cryst.*, 1955, **8**, 847.

38. Z. Liu, H. Geng, J. Shuai, Z. Wang, J. Mao, D. Wang, Q. Jie, W. Cai, J. Sui and Z. Ren, *J. Mater. Chem. C*, 2015.

39. Y. Pei, X. Shi, A. LaLonde, H. Wang, L. Chen and G. J. Snyder, *Nature*, 2011, **473**, 66-69.

40. J. P. Heremans, V. Jovovic, E. S. Toberer, A. Saramat, K. Kurosaki, A. Charoenphakdee, S. Yamanaka and G. J. Snyder, *Science*, 2008, **321**, 554-557.

41. N. V. Kolomoets, *Sov. Phys. Solid State*, 1966, **8**, 799.

42. J. Androulakis, I. Todorov, D.-Y. Chung, S. Ballikaya, G. Wang, C. Uher and M. Kanatzidis, *Phys. Rev. B*, 2010, **82**, 115209.

43. D. G. Cahill, S. K. Watson and R. O. Pohl, *Phys. Rev. B*, 1992, **46**, 6131-6140.

44. R. Seshadri and N. A. Hill, *Chem. Mater.*, 2001, **13**, 2892-2899.

BIOGRAPHY

Manoj Kumar Jana graduated with honors in chemistry in 2010 and later received his Master's degree in chemistry in 2012 from Sri Sathya Sai Institute of Higher Learning, Puttaparthi, Andhra. He joined as a Ph.D. student in 2012 in materials science at the New Chemistry Unit, Jawaharlal Nehru Center for Advanced Scientific Research (JNCASR), Bangalore, India under the research supervision of Bharat Ratna Prof. C. N. R. Rao, FRS, and Dr. Kanishka Biswas. His Ph.D. research pertains to a study of structure-property relationships in transition metal dichalcogenides, and thermoelectric materials with ultra low thermal conductivity. He secured All-India 14th Rank in the CSIR-UGC NET exam (2011) and 20th Rank in the GATE exam (2012). He was a recipient of the best-talk award at the 8th JNC Research Conference on the Chemistry of Materials (2013), Kerala, India and the best-poster award at the Annual In-house Symposium (2014) at JNCASR, India.